# Thermo-Hydro-Mechanical Behaviour of the Callovo-Oxfordian Clay Rock

Final Report

GRS - 266

Gesellschaft für Anlagen-
und Reaktorsicherheit
(GRS) mbH

# Thermo-Hydro-Mechanical Behaviour of the Callovo-Oxfordian Clay Rock

within the Framework of GRS/ANDRA Cooperation Programme and the EC TIMODAZ Project

Final Report

Chung-Liang Zhang
Oliver Czaikowski
Tilmann Rothfuchs

December 2010

**Remark:**

This report was prepared under contract No. 02 E 10045 with the German Federal Ministry of Economics and Technology (BMWi) and under contract No. F16W - FP6 - 036449 with the Commission of the European Communities in the sixth framework programme research and training in the field of nuclear energy (2002 – 2006).

The work was conducted by the Gesellschaft für Anlagen- und Reaktorsicherheit (GRS) mbH.



**GRS - 266**
**ISBN 978-3-939355-42-7**

**Keywords:**
Clay Rock, Damage, Deformation, Field Observation, Laboratory Experiment, Permeability, Self-sealing, Strength, Swelling, Theoretical Modelling, Thermal Effects, THM Behaviour

## Foreword

Clay formations are being world-widely investigated as host medium for the disposal of radioactive waste because of their favourable properties such as very slow transport of fluids and high sorption capacity for most radionuclides. In accordance with the R&D programme defined by the German Federal Ministry of Economics and Technology (BMWi), site-independent basic research on indurated clays for disposal of high-level radioactive waste is in progress in Germany. The German research work has been mostly carried out by participation in international research projects conducted in underground research laboratories in clay formations.

Since 2000, the Meuse/Haute-Marne Underground Research Laboratory (MHM-URL) has been built close to the village of Bure in eastern France to study the suitability of the Callovo-Oxfordian argillaceous formation (COX) to host a repository for high-level and long-lived radioactive waste. A large number of *in situ* experiments has been conducted there. In the framework of a co-operation agreement between BMWi and ANDRA (the French Agence Nationale Pour la Gestion de Déchets Radioactifs), GRS has contributed to ANDRA's research programme with laboratory investigations, field measurements, and numerical modelling. The work of GRS was co-funded by BMWi and the European Commission (EC) within several projects such as

– MODEX-REP (2000 – 2005) for the development and validation of constitutive models describing the coupled hydro-mechanical processes in the COX clay rock during shaft sinking;

– BURE-PRE (2001 – 2003) for the preparation of future collaboration between ANDRA and GRS;

– HE-D (2003 – 2005) heating experiment jointly performed by ANDRA and GRS at the Mont Terri Rock Laboratory;

– NF-PRO (2005 – 2007) for the investigation on self-sealing properties of indurated clays;

– BURE-HAUPT & TIMODAZ (2005 – 2010) for the investigation of thermal impact on development of excavation damaged zones in clay formations.

Within the most recent projects BURE-HAUPT & TIMODAZ, which were co-funded by BMWi under contract No. 02E10045 and by EC under contract No. F16W-FP6-036449, the thermo-hydro-mechanical behaviour of the COX clay rock was experimentally investigated and numerically simulated. The experimental programme focused on examination of short- and long-term deformation response to mechanical loads, swelling and shrinkage induced by variations of environmental moisture, permeability changes caused by damage and re-compaction, and thermal effects on the hydro-mechanical properties of the COX clay rock. The purpose of the modelling exercises was to validate the capabilities of constitutive models for analysis of coupled THM processes in clay host rocks, particularly the predictability of the development and recovery of excavation damaged zones around repositories in clay formations. The model validation was conducted by simulation of laboratory tests on large COX hollow cylinders and *in situ* shaft sinking as well as heating experiments performed in the MHM-URL.

The results and conclusions achieved from the GRS's work within both the BURE-HAUPT and TIMODAZ projects are summarized in this report.

## Table of Contents

# 1 Introduction

Clay formations are being world-widely investigated as host medium for the disposal of radioactive waste because of their favourable properties such as very slow transport of fluids and high sorption capacity for most radionuclides. In order to prove the feasibility of the disposal concepts proposed by countries like for instance France /AND 05/ and Switzerland /NAG 02/, underground research laboratories were constructed in the over-consolidated Callovo-Oxfordian (COX) clay rock at the Meuse/Haute-Marne Underground Research Laboratory (MHM-URL) close to the village of Bure in France and the Opalinus clay (OPA) at Mont Terri Underground Research Laboratory (MT-URL) in Switzerland. In these URLs, most important scientific activities are the conduction of large and full-scale experiments to study the coupled thermo-hydro-mechanical-chemical (THMC) behaviour of the host clay rocks and of the backfill/buffer materials under realistic repository conditions. The *in situ* experiments are supported by laboratory tests under well-controlled conditions for characterization of the material properties and for gaining a better understanding of the observed processes. Within the framework of long-term performance and safety assessments of a potential repository, the complex THMC processes prevailing in the geological barrier system are to be predicted by numerical simulations using adequate codes and theoretical models. Their suitability and predictive capability must be validated in a robust way, for instance, by comparison with the measurement data of laboratory and *in situ* experiments.

Since a decade, site-independent basic research on indurated clays for the disposal of high-level radioactive waste (HLW) has been in progress in Germany, in accordance with the R&D programme defined by the German Federal Ministry of Economics and Technology (BMWi). The German research work has been mostly carried out by participation in international research projects conducted in the above-mentioned URLs.

Among others, GRS has participated in ANDRA's research programme in the MHM-URL /AND 00/, /AND 03/, /AND 05/, /DEL 07/, in the framework of a co-operation agreement between BMWi and ANDRA (the French Agence Nationale Pour la Gestion de Déchets Radioactifs). The main objective of ANDRA's research programme was the characterization of the isolating properties of the COX clay rock through a large number of *in situ* experiments with specific purposes. Tab. 1.1 gives an overview of the experiments performed so far. The most important outcomes from the experiments performed during the time period from 1999 to 2005 have been published in the ANDRA's scientific report "Dossier 2005" /AND 05/. Since then, the research programme has been further developed with additional activities in the MHM-URL to provide more comprehensive and realistic models of the repository behaviour for both the operation and the post-closure periods considering especially radionulide migration and the related characteristic transport properties of excavation damaged zones, determining the hydric transient taking into account the gas production within the repository /DEL 09/, /LEB 10/.

**Tab. 1.1** Main experiments conducted in the MHM-URL /AND 00/, /AND 05/, /DEL 07/

| Experiments | Purpose |
|---|---|
| SUP | Scientific survey of shaft sinking (geological survey, monitoring of geotechnical behaviour, sampling) |
| SUG | Scientific survey of the excavation of all the drifts (geological survey, monitoring of geotechnical behaviour, sampling) |
| REP | Monitoring of the hydromechanical response of the clay rock to the sinking of the main access shaft of the underground laboratory |
| GIS | *In situ* geomechanical characterisation: *in situ* stress, deformability of the clay rock in the short and medium term |
| KEY | Feasibility study of Excavation Disturbed Zone (EDZ) cut-off |
| PEP | *In situ* measurements of permeability and pore pressure in the Callovo-Oxfordian formation |
| PAC | Water samplings in the Callovo-Oxfordian formation for chemical and isotopic analyses and *in situ* measurement of certain non-conservative parameters |
| DIR | Characterisation of diffusion and chemical retention of the Callovo-Oxfordian formation by tracing tests |
| TER | Monitoring of the response of the clay rock to the thermal loading in terms of hydraulic, mechanical and chemical disturbances |

GRS has contributed to ANDRA's programme with laboratory tests, *in situ* measurements and numerical modelling in the frame of the following projects.

**MODEX-REP** was a European project for development and validation of constitutive models describing the coupled hydro-mechanical processes in the COX clay rock during sinking of the main shaft of the MHM-URL from 2000 to 2005 /MOD 06/, /SU 07/. GRS contributed to the project with laboratory investigations on the hydro-mechanical behaviour of the COX clay rock, including determination of the fundamental properties, such as short-term and long-term mechanical behaviour and permeability /ZHA 02/,

/ZHA 04a/. The results are presented as part of the database in the “Dossier 2005” delivered to the French government in 2005 /AND 05/.

From July 2001 to December 2003, GRS conducted a pre-project (**BURE-PRE**) for the preparation of the envisaged collaboration with ANDRA /ZHA 04b/, /ZHA 04c/. In this project, special lab testing methods were developed for the characterization of the THM behaviour of the COX claystone. In order to gather experience with the finite element computing code CODE-BRIGHT developed by UPC /UPC 04/, numerical modelling exercises were also performed for the analysis of coupled THM processes in the clay rock and in backfill.

From October 2003 to December 2005, a mock-up heating experiment called **HE-D** was jointly performed by ANDRA and GRS at the MT-URL /WIL 03/, /KUL 07/, /ZHA 07a/. The Opalinus clay was heated up to 100 °C by a heater of 300 mm diameter and 6 m length installed in a horizontal borehole. Responses of the surrounding rock to heating were observed by monitoring the evolution of temperature, pore-water pressure, gas migration and permeability using mini-packer-systems developed by GRS, while the rock deformation was measured by the other partners. The THM properties of the Opalinus clay from the HE-D test field were investigated at GRS’s laboratory. The very complex THM processes observed during the heating experiment were numerically simulated and analysed by GRS and the other modelling teams as well. The results were reported in /KUL 07/, /ZHA 05/, /ZHA 06/, /ZHA 07a/, /ZHA 09a/.

After the preparation phase within the pre-project (**BURE-PRE**) /ZHA 04b/, the main project (**BURE-HAUPT**) was launched in July 2005 under contract 02E10045 with BMWi /BUE 05/. Its tasks were defined as follows:

- Laboratory investigations on the THM behaviour of the COX claystone including
  - a) short- and long-term deformation,
  - b) swelling and shrinkage,
  - c) permeability changes induced by damage and reconsolidation, and
  - d) thermal effects.
- Contribution to the TER heating experiment performed in the MHM-URL /WIL 07/ with special GRS mini-packer-systems for measurements of pore-water pressure and temperature before, during and after heating.

- Validation of constitutive models implemented in the finite element (FEM) code CODE-BRIGHT by modelling the following *in situ* experiments

  a) **REP** experiment for monitoring hydro-mechanical responses of the COX clay rock to the excavation of the main shaft of the MHM-URL /MOD 06/, /SU 07/, and

  b) **TER** experiment for characterizing the thermal properties of the COX clay rock and evaluating the thermal impact on the hydro-mechanical processes during heating / cooling cycles in a horizontal borehole /WIL 07/.

In addition to the characterization of the clay rock, crushed claystone from the drift excavation in the MHM-URL was preliminarily investigated as an alternative backfill material instead of highly expansive bentonite which is being investigated as backfill/buffer material in repositories in crystalline rocks.

One year later after starting the **BURE-HAUPT** project, GRS participated in the European project called **TIMODAZ** /TIM 06/ started in October 2006 and terminated in September 2010. The main purpose of this project was to investigate the thermal impact on the damaged zone around underground repository rooms in clay host rocks. Totally, 14 participating organisations representing 8 European countries (BE, FR, CH, DE, NL, ES, CZ, UK) were involved in the project. The plastic Boom clay, the argillaceous Opalinus and Callovo-Oxfordian clay rocks, which are being considered as potential host formations for repositories, were investigated in the TIMODAZ programme by conducting

- Laboratory experiments for determination of the thermo-hydro-mechanical-chemical (THMC) behaviour, particularly the fracturing and sealing behaviour of the clay rocks under relevant repository conditions;
- *In situ* heating experiments in the URLs at Mont-Terri in Switzerland, HADES in Belgium, and Josef UEF in Czech for characterization of coupled THMC processes in the rock mass;
- Benchmark modelling of the specific laboratory and *in situ* experiments for validation and improvement of the predictability of the constitutive models and computer codes used for the long-term THM processes in clay host rocks;
- Assessment of the significance of the thermally-impacted EDZ for the Performance and Safety Assessment (PA, SA) of repositories in clay formations.

GRS has contributed to the TIMODAZ programme with laboratory experiments and numerical modelling of the THM behaviour of the COX clay rock within 5 work packages:

WP2: Review of the state of the art of the understanding of the THMC behaviour for Boom, Opalinus and Callovo-Oxfordian clays /D02 07/

WP3.1: THM characterization of the studied clays /D05 10/

WP3.3: EDZ simulation tests on large hollow clay rock cylinders /D07 10/

WP5.1: Development and improvement of THM constitutive models /D10 10/

WP5.2: Benchmark modelling of lab and *in situ* experiments /D13 10/.

The work of GRS within TIMODAZ was co-funded under contract number 02E10045 by BMWi as an additional part of the ongoing BURE-HAUPT project and by the European Commission (EC) as part of the sixth Euratom research and training Framework Programme (FP6) on nuclear energy (2002-2006) under contract FP6-CT-036449.

In this final report, achievements and results of the combined BURE-HAUPT & TIMODAZ project are presented. In Chapter 2, experimental results including deformability, swelling capability, permeability, thermal effects, large-scale simulation tests on the COX claystone, and characterisation of the crushed claystone are illustrated and discussed. Chapter 3 focuses on the modelling work including description of applied constitutive models, determination of model parameters, numerical simulations of the laboratory and *in situ* experiments, and scoping prediction of coupled THM processes in a clay rock – bentonite buffer system around a HLW disposal borehole. Main results and conclusions from the laboratory experiments and the modelling exercises are finally summarized in Chapter 4.

# 2 Laboratory Experiments

In order to enhance the knowledge about the THM behaviour of argillaceous rocks as host medium for the disposal of HLW, comprehensive experiments were carried out on the COX clay rock at the MHM-URL in the framework of the BURE-HAUPT/TIMODAZ project. The laboratory programme focused on investigating the

- deformability of the clay rock, which is of particular importance for the stability of the repository construction during the operation phase and for the long-term integrity of the geological and engineered barriers after backfilling and closing of the repository;
- swelling capability of the clay rock, which will play a key role in the self-sealing process of the EDZ when water flows through;
- permeability changes induced by damage and re-compaction of the EDZ as the basic EDZ parameter evaluated in long-term performance and safety assessments of a repository;
- thermal impact on the hydro-mechanical behaviour and the integrity of the clay host rock;
- fracturing and self-sealing processes in the EDZ during excavation, ventilation, backfilling, water flow, heating and cooling simulated in the laboratory tests on large hollow COX claystone cylinders; and
- hydro-mechanical properties of crushed claystone as backfill / buffer material.

## 2.1 Basic characterization of the Callovo-Oxfordian argillaceous formation

The underground research laboratory MHM-URL has been constructed in the Callovo-Oxfordian argillaceous formation on the eastern boundary of the Paris Basin, comprising a sequence of nearly horizontal limestone layers, marls and argillaceous rocks deposited at the bottom of former oceans (Fig. 2.1) /AND 99/. The formation represents over-consolidated sediments of the Jurassic Age (about 150 million years old). The homogeneous rock mass of about 130 m located at depths between 420 m to 550 m is investigated in the MHM-URL. The URL consists of two shafts, a large number of drifts and boreholes at depths between 445 m and 490 m. In accordance with the mineral composition and common mechanical characteristics, the COX formation is divided into three rheological zones or layers, the upper (A'), the median (B'), and the lower (C') zone. Fig. 2.2 illustrates the distribution of mineral components in these zones /AND 99/, while the distribution of the geomechanical properties, such as water content (w), uniaxial compressive strength ($R_c$), and elastic modulus (E), is presented in fig. 2.3 and in tab. 2.1 /SU 07/.

**Tab. 2.1** Basic mechanical characteristics of the different geological zones of the Callovo-Oxfordian formation /AND 05/, /SU 07/

| Characteristic | Rheological zone | | | Overall |
|---|---|---|---|---|
| | Upper | Median | Lower | |
| Depth (m) | 420 – 455 | 455 – 515 | 515 – 550 | 420 – 550 |
| Initial total stresses | 12 – 16 MPa at -500 m | | | |
| Initial pore pressure | ~5 MPa at -500 m | | | |
| Bulk density (g/cm$^3$) | 2.42 | 2.42 | 2.46 | 2.40 – 2.45 |
| Water content (%) | 6.1 | 7.1 | 5.9 | 5.3 – 8.8 |
| Porosity (%) | 14.0 | 15.5 | 13.0 | 12.0 – 17.0 |
| Young's modulus (GPa) | 6.2 | 5.5 | 7.2 | 6.0 |
| Uniaxial compressive strength (MPa) | 30 | 21 | 21 | 24 |
| Uniaxial tensile strength (MPa) | | | | 2.6 |
| Hydraulic conductivity (m/s) | 10 – 13 to 10 – 14 | | | |

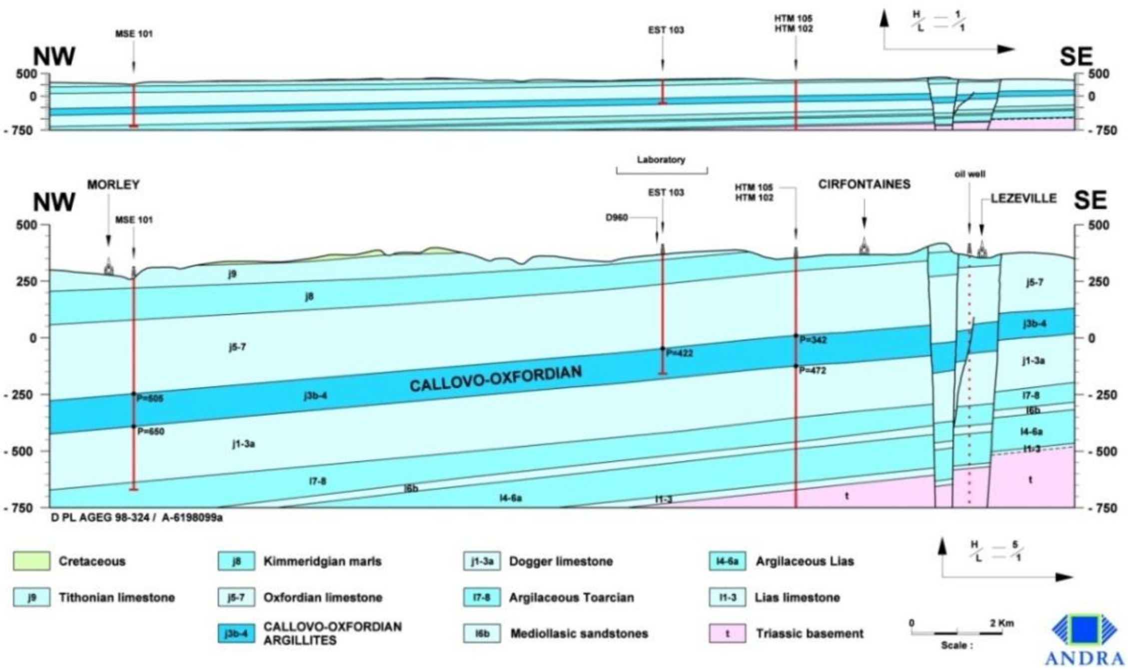


**Fig. 2.1** Geological cross section of the Meuse/Haute Marne site /AND 99/

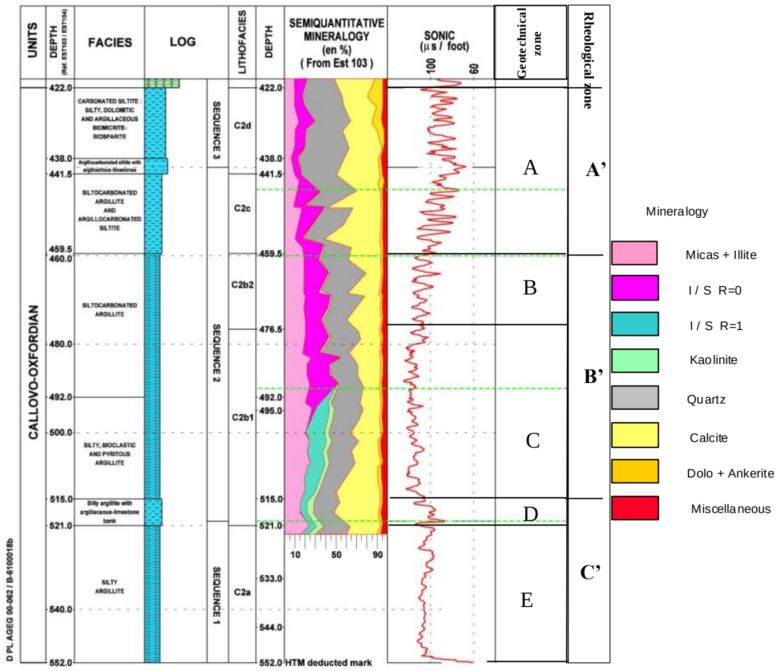


**Fig. 2.2** Mineralogy of the Callovo-Oxfordian argillaceous formation /AND 99/

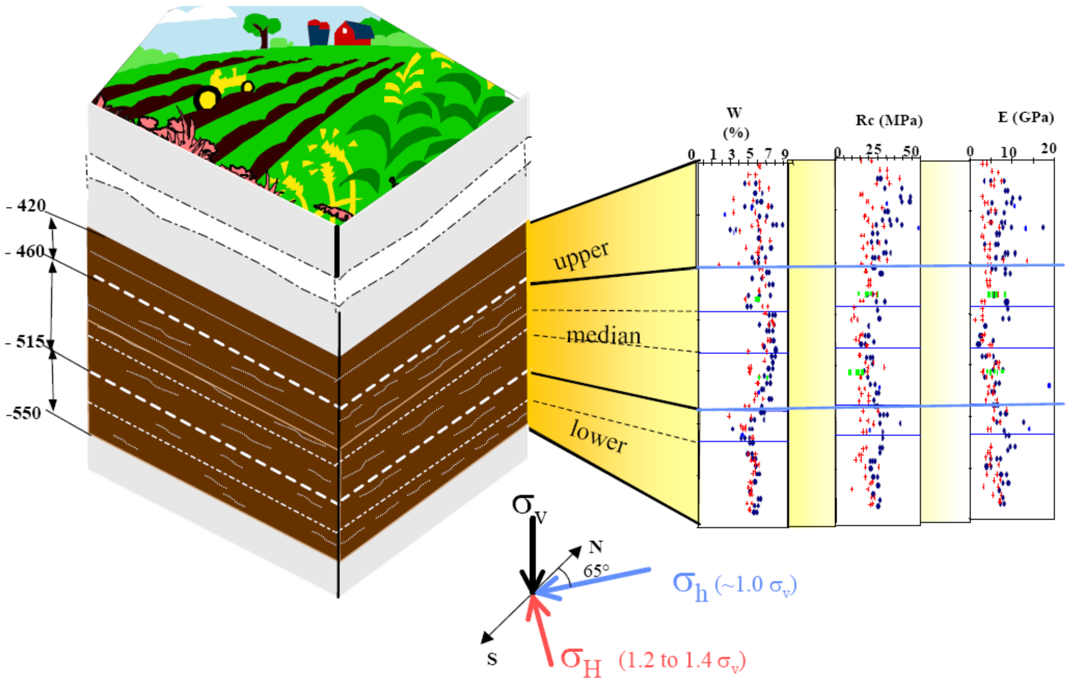


**Fig. 2.3** Geomechanical properties of the Callovo-Oxfordian argillaceous formation /SU 07/

On an average, the COX clay rock contains 25 – 55 % clay minerals, 20 – 38 % carbonates and 20 – 30 % quartz, 1 % feldspar, and small amounts of others /AND 05/. The three zones correspond to the three geological sedimentary sequences: two stiff zones (upper and lower) with higher carbonate contents surrounding a central less stiff zone (median) with more clay content. However, the transition from one zone to the other is progressive. The combined effect of the geological sedimentation, compaction and diagenesis has reduced the pore space to very low porosities of 12 – 17 %. The small pores lead to large resistance to fluid flow and correspondingly to very low hydraulic conductivities of $10^{-14}$ to $10^{-13}$ m/s. In the natural state, the clay rock is fully saturated with water and solutes (pore-water type: Na-Cl-$SO_4$) /MAZ 08/. The sedimentation has caused a preferential orientation of the clay foliage and consequently a stratification of the matrix structure. This however results in anisotropy of the rock properties, for instance, the anisotropy factor of the hydraulic conductivity parallel versus normal to the bedding plane ranges from 2 to 10 /AND 05/. The *in situ* stress state at the -490 m main level of the MHM-URL is also anisotropic, the vertical component $\sigma_v$ = 12.7 MPa, the minor horizontal component $\sigma_h$ = 12.4 MPa (oriented 065° ±10°), and the major horizontal component $\sigma_H$ = 14.8 MPa (oriented 155° ±10°).

## 2.2 Preparation and characterization of samples

For the envisaged tests, a large number of core samples of various sizes were extracted from the following boreholes drilled at different locations in the MHM-URL:

- **REP2206** drilled vertically from the floor of the -445 m niche to a depth of 467 m;
- **RPA27** drilled vertically along the axis of the main shaft from the -451.4 m level to a depth of 484.5 m;
- **PPA35** drilled from the wall of main shaft at the depth of 479.1 m and oriented to the direction of the horizontal major stress (~N150°);
- **TER1101** heater borehole drilled at the depth of 490.0 m and oriented to the direction of the horizontal major stress (~N150°);
- **SUG1103** drilled at the depth of 490.0 m and oriented to the direction of the horizontal major stress (~N150°);
- **PAC1011** drilled horizontally at the depth of 490.0 m;
- **PAC1012** drilled horizontally at the depth of 490.0 m;
- **DIR2002/3/4** drilled vertically from the floor of the -445 m niche;
- **DIR1002/4** drilled vertically from the -445 m main level.

Most of the core samples had a length of 320 mm and different diameters of 80 to 120 mm. In addition to the normally-sized cores, 8 large cores of 290 mm diameter and 0.6 – 1.0 m lengths were extracted from the diffusion test boreholes drilled vertically from the floor of the -445 m niche (DIR2002/3/4) and the -490 m main level downwards (DIR1002/4), respectively. The sampling positions cover the *in situ* experimental depths from 447 m to 500 m.

The drilled cores were confined in sealing cells, delivered by ANDRA to the GRS laboratory, and then stored there until testing in a climate-controlled room at 22 °C. From the normally-sized cores, cylindrical samples were carefully prepared by cutting and planishing the surface to the desired sizes. Fig. 2.4 shows a core sample confined in cell (a), unpacked (b), and prepared to a 120 mm diameter and 220 mm length (c). The large cores were wrapped in aluminium foil, covered by rubber jackets, and confined by pressing two-half parts of a plastic tube over the jackets using stretching bands to prevent damaging and de-saturation. From the big cores, large hollow cylinders were prepared to 280 mm outer diameter and 460 – 650 mm lengths with axially-centred boreholes. Fig. 2.5 shows pictures of the cores during storage and preparation. Generally, no macro-cracks were visually recognized on the sample surfaces and bedding planes are insignificant. Only a few cores were damaged during the preparation and could not be used for testing.


(a) confined in cell (b) unpacked (c) prepared

**Fig. 2.4** Normally-sized samples prepared from COX drill cores

(a) storage in confinement

(b) unpacked core

(c) borehole drilling

(d) planishing the end face

**Fig. 2.5** Large hollow cylinders prepared from big COX drill cores

The fundamental properties of the samples such as grain density, dry density, bulk density, porosity and water content were measured according to ISRM (International Society for Rock Mechanics) suggested testing methods /ISR 81/, /ZHA 07a/. The properties are defined as follows:

**Grain density**

$$\rho_s = \frac{M_s}{V_s} \tag{2.1}$$

$M_s$ = mass of solids, $V_s$ = volume of solids.

**Bulk density**

$$\rho_b = \frac{M}{V} = \frac{M_s + M_w}{V} \tag{2.2}$$

$M$ = mass of bulk sample, $V$ = volume of bulk sample,
$M_s$ = mass of solids, $M_w$ = mass of water.

**Dry density**

$$\rho_d = \frac{M_s}{V} \tag{2.3}$$

**Porosity**

$$\phi = \frac{V_v}{V}100 = \left(1 - \frac{\rho_d}{\rho_s}\right) \cdot 100 \ \ (\%) \tag{2.4}$$

$V_v$ = volume of voids.

**Water content**

$$w = \frac{M_w}{M_s}100 \ \ (\%) \tag{2.5}$$

**Degree of water saturation**

$$S_l = \frac{V_w}{V_v}100 \ \ (\%) \tag{2.6}$$

**Relationship between degree of saturation and the other physical characters**

$$S_l = \frac{w}{\rho_w} \frac{1}{\left( 1/\rho_d - 1/\rho_s \right)} = \frac{\rho_d w}{\rho_w \phi}100 \ \ (\%) \tag{2.7}$$

$\rho_w$ = density of pore water.

Before starting each test, the bulk density of the samples with natural water content was determined by measuring their volume and weight. The water content was measured on pieces remaining from sample preparation. They were dried in an oven at a temperature of 105 °C over 2 days. On basis of the measured bulk density and water content, the dry density was calculated. The grain density was measured on powder produced during sample preparation by use of pycnometer with helium gas. The porosity was calculated on basis of the measured grain and dry densities. The basic characteristics determined on the COX samples are summarized in tab. 2.2 together with the test plan. Due to the long storage periods of months to years and the preparation, they were more or less de-saturated.

**Tab. 2.2** Characteristics of drill cores used for the investigations at the GRS laboratory

| Borehole | Core ID | Diameter (mm) | Length (m) | Depth (m) | Grain density (g/cm$^3$) | Bulk density (g/cm$^3$) | Dry density (g/cm$^3$) | Porosity (%) | Water content (%) | Water saturation (%) | Testing |
|---|---|---|---|---|---|---|---|---|---|---|---|
| REP2206 normal to bedding ⊥ | EST21156 | 80 | 2.50 – 2.78 | 447.6 | 2.694 | 2.589 | 2.552 | 5.3 | 1.43 | 70.0 | creep/damage/sealing/ swelling/thermal |
| | EST21158 | 80 | 4.00 – 4.28 | 451.1 | 2.690 | 2.401 | 2.307 | 14.2 | 4.66 | 73.0 | creep |
| | EST21160 | 80 | 6.00 – 6.28 | 453.1 | 2.695 | 2.402 | 2.310 | 14.3 | 4.99 | 75.0 | creep/damage/sealing |
| | EST21162 | 80 | 8.00 – 8.28 | 455.1 | 2.708 | 2.399 | 2.286 | 15.6 | 4.94 | 72.0 | creep/swelling/thermal |
| | EST21164 | 80 | 10.00 – 10.28 | 457.1 | | 2.430 | 2.300 | 14.8 | 5.73 | 89.0 | creep/damage/sealing |
| | EST21166 | 80 | 12.41 – 12.45 | 459.1 | 2.707 | 2.530 | 2.430 | 10.2 | 4.12 | 98.0 | creep/damage/sealing |
| | EST21168 | 80 | 14.00 – 14.28 | 461.1 | 2.694 | 2.393 | 2.272 | 15.7 | 5.33 | 77.0 | creep/damage/sealing |
| | EST21171 | 80 | 16.95 – 17.23 | 463.1 | 2.681 | 2.363 | 2.243 | 16.3 | 5.34 | 73.0 | creep/damage/sealing |
| | EST21173 | 80 | 17.58 – 17.85 | 464.1 | 2.684 | 2.399 | 2.276 | 15.2 | 5.40 | 81.0 | creep/damage/sealing |
| | EST21177 | 80 | 20.00 – 20.28 | 467.1 | 2.694 | 2.393 | 2.272 | 15.7 | 5.33 | 77.0 | creep/damage/sealing |
| PPA35 parallel to bedding ‖ | EST19533 | 80 | 0.45 – 0.77 | 479.1 | 2.700 | 2.448 | 2.300 | 14.9 | 6.10 | 94.2 | permeability |
| | EST19534 | 80 | 0.77 – 1.09 | 479.2 | | 2.428 | | | | | permeability |
| | EST19535 | 80 | 1.09 – 1.41 | 479.3 | | 2.422 | | | | | permeability |
| | EST19538 | 80 | 2.00 – 2.31 | 479.4 | | 2.442 | | | | | permeability |
| | EST19541 | 80 | 3.40 – 3.72 | 479.5 | | 2.436 | | | | | permeability |
| | EST19557 | 80 | 12.34 – 12.66 | 479.6 | | 2.440 | | | | | permeability |
| PPA27 ⊥ | EST17290 | 80 | | | 2.707 | 2.387 | 2.246 | 17.0 | 6.24 | 83.0 | creep |
| | EST17282 | 80 | 20 – 20 | 471.0 | | 2.44 | 2.34 | 13.3 | 4.45 | 78.1 | thermal |
| | EST17313 | 80 | 29 – 30 | 480.9 | | 2.38 | 2.24 | 17.0 | 6.58 | 86.5 | thermal |
| | EST17322 | 80 | 30 – 33 | 484.6 | | 2.43 | 2.29 | 15.2 | 6.6 | 99.5 | thermal |

**Tab. 2.2 Characteristics of drill cores used for the investigations at the GRS laboratory** [continued]

| Borehole | Core ID | Diameter (mm) | Length (m) | Depth (m) | Grain density (g/cm$^3$) | Bulk density (g/cm$^3$) | Dry density (g/cm$^3$) | Porosity (%) | Water content (%) | Water saturation (%) | Testing |
|---|---|---|---|---|---|---|---|---|---|---|---|
| TER1101 | EST25321 | 122 | 1.54 – 1.74 | 491.2 | 2.687 | 2.417 | 2.286 | 15.2 | 5.70 | 86.0 | creep |
| ∥ | EST25324 | 122 | 3.08 – 3.28 | 491.3 | 2.700 | 2.428 | 2.296 | 14.9 | 5.73 | 88.0 | creep |
| | EST25335 | 122 | 6.26 – 6.56 | 491.5 | 2.709 | 2.426 | 2.285 | 15.7 | 6.18 | 90.0 | creep |
| | EST25339 | 122 | 7.28 – 7.60 | 491.7 | 2.705 | | | | 5.88 | | creep |
| | EST25344 | 122 | 8.51 – 8.81 | 491.9 | 2.709 | 2.421 | 2.277 | 16.0 | 6.33 | 93.0 | creep |
| SUG1103 | | | | | | | | | | | |
| ∥ | EST22101 | 80 | | 490.9 | 2.70 | 2.436 | 2.285 | 15.35 | 6.57 | 97.9 | swelling |
| PAC1011 | EST27334 | 80 | 2.50 – 2.81 | 490.0 | | 2.400 | | | | | triaxial compression |
| ∥ | EST27335 | 80 | 2.81 – 3.12 | 490.0 | | 2.450 | | | | | triaxial compression |
| | EST27338 | 80 | 3.12 – 3.82 | 490.0 | | 2.421 | | | | | triaxial compression |
| | EST27339 | 80 | 3.82 – 4.18 | 490.0 | | 2.448 | | | | | triaxial compression |
| PAC1012 | EST27382 | 80 | | 490.0 | | | | | | | thermal |
| ∥ | EST27390 | 80 | 3.25 – 3.35 | 490.0 | 2.70 | 2.437 | 2.286 | 15.34 | 6.60 | 98.3 | thermal |
| DIR1002⊥ | EST19454 | 290 | 1.66 – 1.96 | 498.0 | 2.70 | 2.45 | 2.34 | 13.3 | 5.43 | 95.2 | thermal |
| DIR1004⊥ | EST27319 | 290 | 8.45 – 9.03 | 501.3 | 2.70 | 2.43 | 2.28 | 15.7 | 6.8 | 98.0 | EDZ simulation |
| DIR2003⊥ | EST19387 | 290 | 6.14 – 7.22 | 460.0 | 2.70 | 2.41 | 2.28 | 15.4 | 5.5 | 82.0 | EDZ simulation |
| DIR2004⊥ | EST27315 | 290 | 13.94 – 14.53 | 461.5 | 2.70 | 2.45 | 2.29 | 15.0 | 6.8 | 100.0 | EDZ simulation |
| DIR2004⊥ | EST27312 | 290 | 15.81 – 16.63 | 463.0 | 2.70 | 2.41 | 2.26 | 15.8 | 6.2 | 89.0 | EDZ simulation |

## 2.3 Deformability

### 2.3.1 Short-term deformation

Sufficient knowledge of short-term deformation, damage, and strength of a clay host rock is required for the proper design of an underground repository. Important aspects of the short-term mechanical behaviour are the characteristic parameters relating stresses and strains in the elastic range, the stress levels at which yield, damage or fracturing occurs in the rock, and the post-failure behaviour of the fractured rock. The short-term deformation behaviour of the COX claystone was determined on samples of 78.5 mm diameter and ~150 mm length. They were extracted from a horizontal borehole PAC1011 parallel to the bedding plane (see tab. 2.2). The samples were slightly de-saturated due to coring and preparation.

#### 2.3.1.1 Testing method

Triaxial compression tests were carried out in a standard triaxial apparatus, which permits a maximum axial load of 1600 kN (~200 MPa) and a maximum lateral stress of 70 MPa /ZHA 02/. In order to minimize effect of the material alteration induced by coring and preparation, the samples were firstly reconsolidated at a temperature of 30 °C by isostatic loading up to the original lithostatic stress of $\sigma_m$ = 12 to 18 MPa at the sampling positions. This was done because pre-compacted samples are more representative for the initial state of the clay rock. Following that, the axial and lateral stresses were decreased to the desired levels. Keeping the lowered lateral stress constant ($\sigma_2 = \sigma_3$ = const), the deviatoric stress ($\Delta\sigma = \sigma_1 - \sigma_3$) was increased at an axial strain rate of $1 \cdot 10^{-6}$ $s^{-1}$ up to failure. During the tests, the axial strain ($\varepsilon_1$) was measured by a LVDT-transducer installed outside of the triaxial cell, while the volumetric strain ($\varepsilon_v$) was determined both directly from the volume change of the confining oil in the cell using a pressure/volume GDS-controller and indirectly by strain gauges attached on the sample surfaces at the sample mid-height. Radial strain ($\varepsilon_2 = \varepsilon_3$) was calculated from the $\varepsilon_1$– and $\varepsilon_v$–data obtained by the indirect measurement of oil volume in the cell rather than the direct measurement from the strain gauges because the data from the strain gauges were limited regarding the measuring locations and the measuring range of ~1 %.

#### 2.3.1.2 Isostatic compaction

Fig. 2.6 illustrates the volumetric strains measured on five samples by multiple isostatic loading / unloading cycles. At each sample, the isotropic loading led to a nearly linear compaction in volume. The volumetric strain recovered linearly again with decreasing the load. This observation indicates the domination of elastic closure and opening of the pores and micro-cracks in the samples over the testing range. From the slope of the $\sigma_m - \varepsilon_v$ – curve, Bulk modulus can be determined to a range of K = 8 to 20 GPa. The difference in elastic stiffness might be attributed to the different degrees of water saturation of the samples. The less saturated pores are more easily compacted because of lower stiffness.

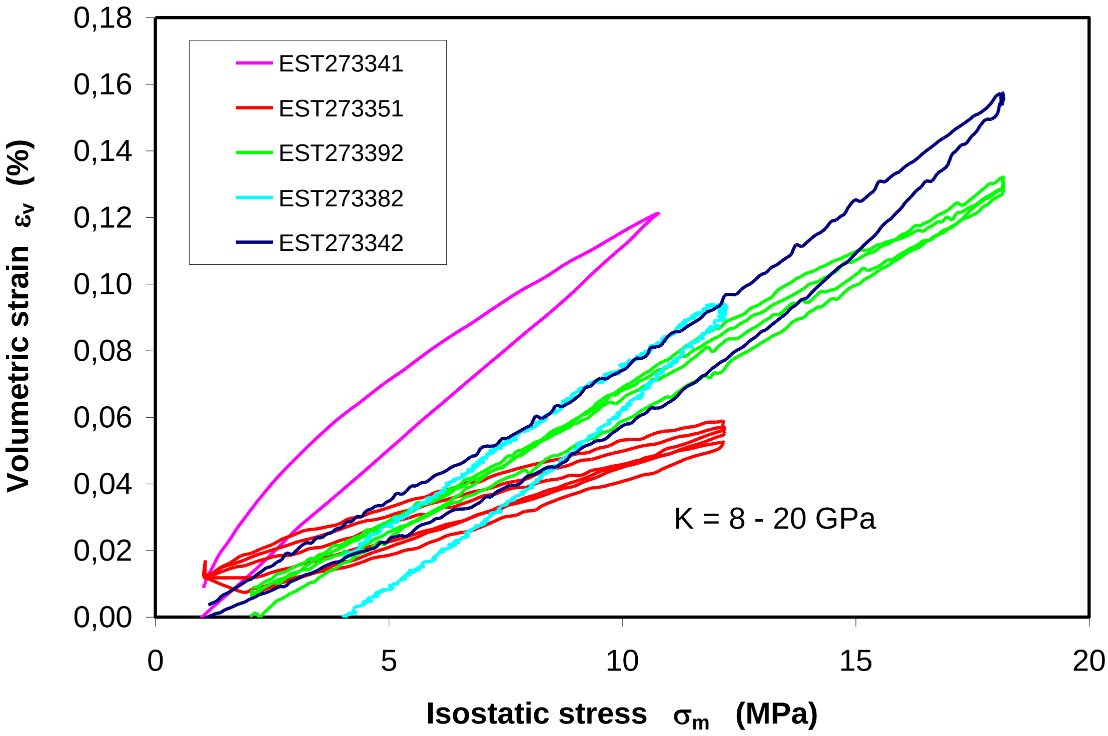


**Fig. 2.6** Isostatic compaction behaviour of the COX claystone

#### 2.3.1.3 Deviatoric compression and strength

Following the isostatic compaction, the deviatoric stress was increased up to failure. The deviatoric stress-strain curves obtained from a typical test are illustrated in fig. 2.7 showing the yield point ($\sigma_Y$), the onset of dilatancy ($\sigma_D$), the peak strength ($\sigma_F$), and the residual strength ($\sigma_R$), while the results obtained on the other samples at different lateral stresses of 1 to 7 MPa are summarized in fig. 2.8. The difference of the measured volumetric strains (see fig. 2.7) is because the $\varepsilon_{v\text{-oil volume}}$ was obtained directly from the balance calculation of the confining oil in the cell and thus is more representative for the sample volume change, while $\varepsilon_{v\text{-strain gauge}}$ was indirectly calculated by the local radial strain recorded with a strain gauge and thus not precise.

Generally, all the samples exhibited the typical elasto-plastic behaviour. The stress-strain curves start with linear axial compression, radial extension, and volumetric compaction until yield occurs at stress $\sigma_Y$ where a deviation from the linear elastic behaviour appears. Further deformation with the stress involves some irreversible plastic parts due to micro-fracturing. The opening of micro-fractures might be identified by a transition from the volumetric compaction to dilation at stress $\sigma_D$. When the fracturing continues up to the formation of macro-fractures and shear planes in the clay (a fractured sample shown in fig. 2.9), failure occurs at stress $\sigma_F$. The corresponding axial strain at the failure varies between 1 % and 2 %. From the peak point, the stress drops quickly down to the residual strength ($\sigma_R$), at which further plastic slip on the shear planes continues unstably to a range over 3 % – 6 %.

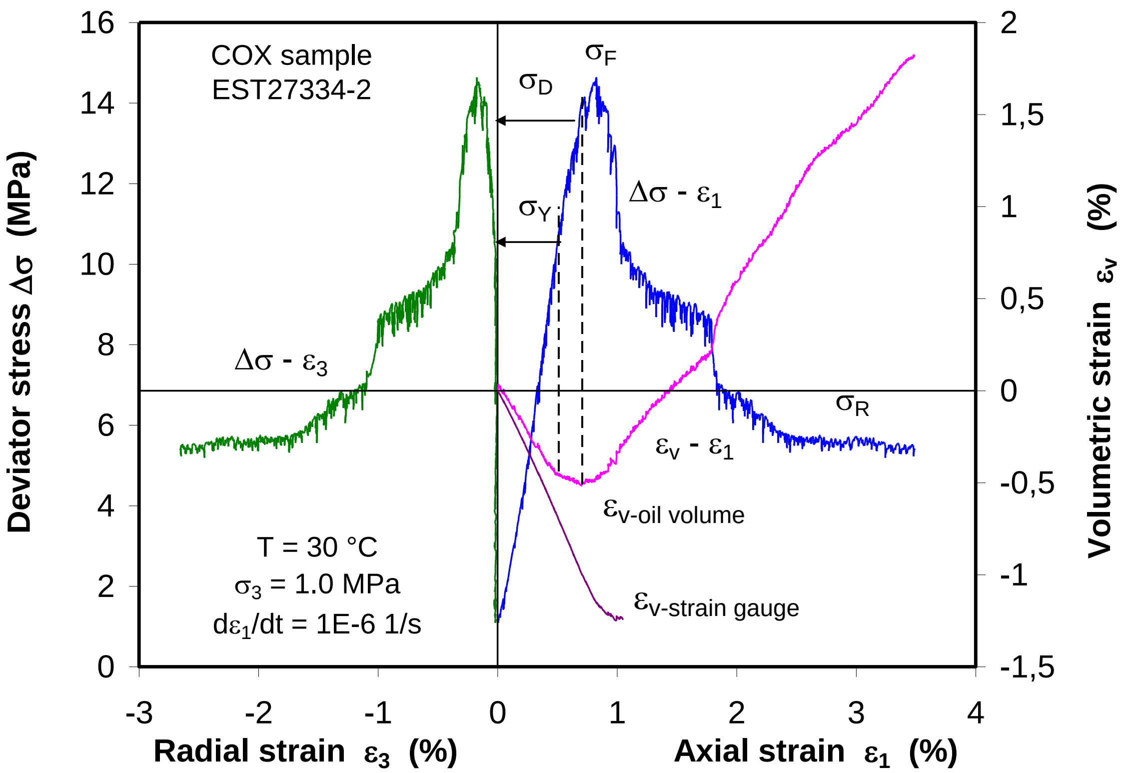


**Fig. 2.7** Stress-strain curves obtained from a typical triaxial test on a COX sample with identification of yield, dilatancy, peak, and residual strengths

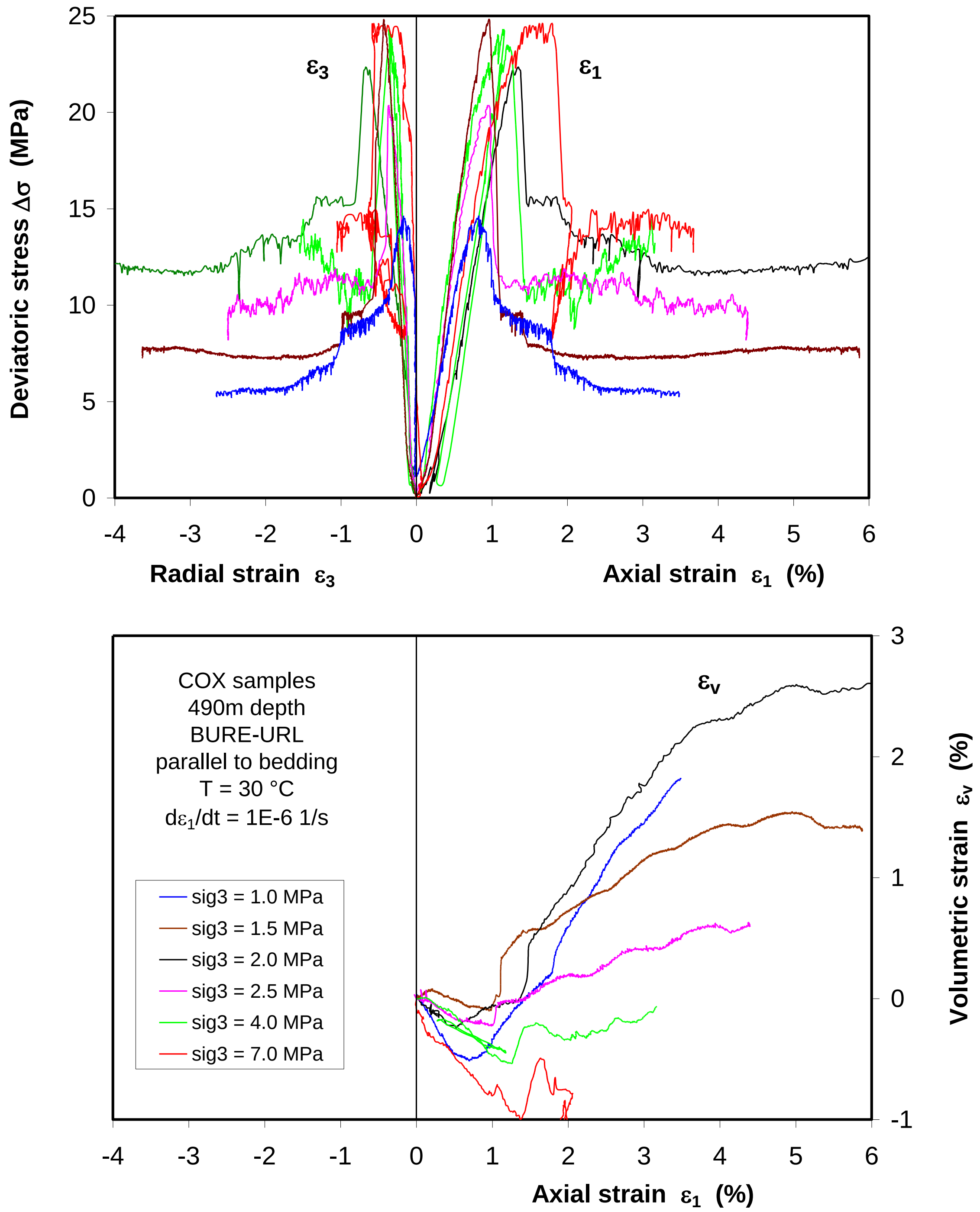


**Fig. 2.8** Stress-strain behaviour of the COX claystone at different confining stresses

The values of the yield, dilatancy, peak and residual strength obtained by loading the samples parallel to the bedding plane are depicted in fig. 2.9 as a function of the confining stress. It is obvious that the data of peak and dilatancy strength are quite close. The yield strength is about 30 % of the peak strength. The residual strength remains at 40 % to 50 % of the peak strength.

The dependency of the strengths on the confining stress can be approached by the Mohr-Coulomb criterion:

(a) $\tau = \sigma_n \cdot \tan\varphi + c$

or

(b) $\sigma_1 = 2 \cdot c \cdot \tan\left(45° + \frac{\varphi}{2}\right) + \sigma_3 \tan^2\left(45° + \frac{\varphi}{2}\right)$ (2.8)

where $\tau$ represents the shear stress at failure on the failure plane, $\sigma_n$ is the normal stress on the failure plane, $c$ is the cohesion and $\varphi$ is the angle of internal friction. The strength parameters of $c$ = 6.5 MPa and $\varphi$ = 24° are estimated from the peak / dilatancy strength envelope. From the picture of a fractured sample after testing, one can identify the angle of the shear plane to the axial load, ß ≈ 32°, i. e. ß ≈ 45° – $\varphi$/2. The yield boundary may be expressed by $\sigma_Y \approx 0.7 \cdot \sigma_F$. The residual strength seems to be independent of the confining stress or normal stress with $c$ = 5 MPa and $\varphi$ = 0°.

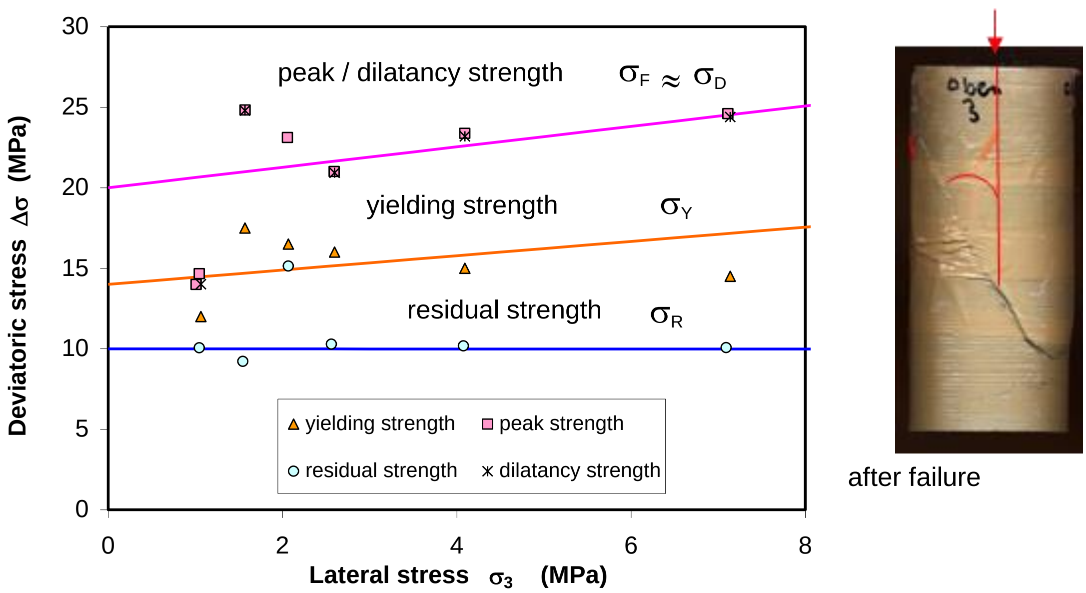


**Fig. 2.9** Determination of the dilantancy, peak, and residual strength

The peak strength and residual strength parallel to bedding ($\sigma_{F\parallel}$, $\sigma_{R\parallel}$) obtained in these tests are compared in fig. 2.10 with those previously obtained by loading the samples perpendicular to bedding ($\sigma_{F\perp}$, $\sigma_{R\perp}$) /ZHA 02/, /ZHA 04a/. The strengths perpendicular to bedding are higher than those parallel to bedding. The anisotropic ratios are $\sigma_{F\perp}$ /

$\sigma_{F\parallel}$ = 1.2 to 1.3 and $\sigma_{R\perp}$ / $\sigma_{R\parallel}$ = 1.1 to 1.8. Because the tested samples had been taken from the different locations and might have different mineralogical contents, particularly for clay and carbonate, the above drawn conclusion on the mechanical anisotropy needs to be confirmed by more systematic tests on samples from the same location.

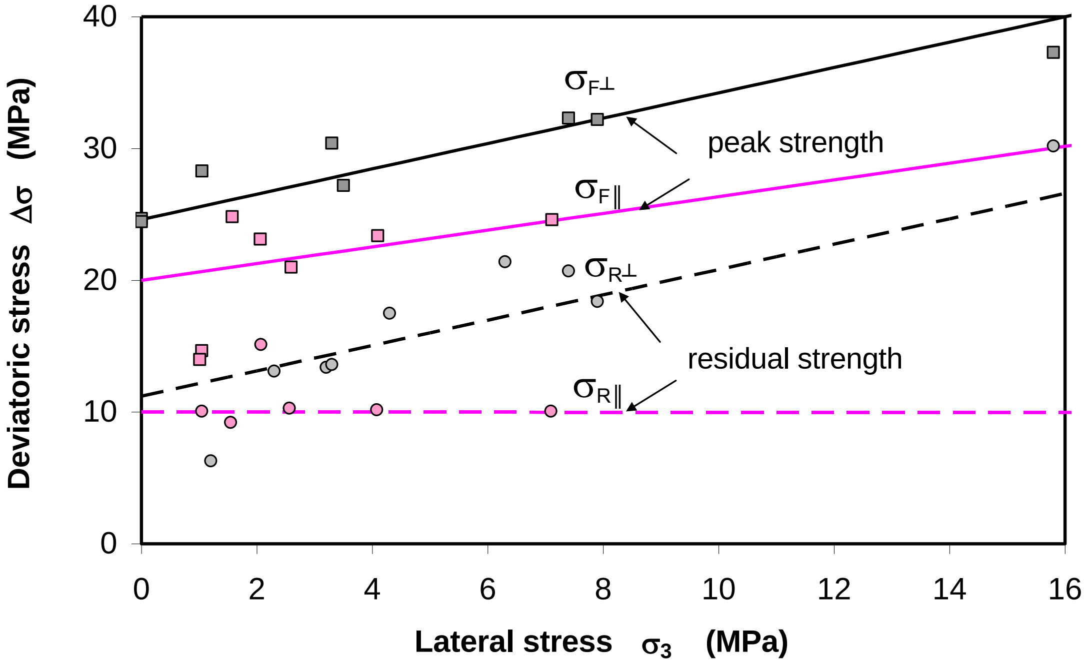


**Fig. 2.10** Comparison of the peak strength and residual strength parallel and perpendicular to bedding

### 2.3.1.4 Elastic parameters

The elastic parameters of Young's modulus E and Poisson's ratio $\nu$ were determined on a sample EST05634 (D/L = 78/102 mm) at a lateral stress of 3.4 MPa as function of deviatoric stress, whereby the ultrasonic wave velocity was recorded, too. A high loading rate of 0.4 MPa/s was applied to minimize time effects on the elastic deformation. Fig. 2.11 illustrates the stress-strain curves along the loading and the unloading paths. The E- and $\nu$-values were determined by short loading / unloading cycles at different stress levels in the linear elastic strain part below yield ($\sigma_D \approx$ 19 MPa). The E- and $\nu$-data are depicted in fig. 2.12 as a function of the applied deviatoric stress. Young's modulus increased from E ≈ 3200 MPa at $\Delta\sigma$ = 3.5 MPa to E ≈ 3800 MPa at $\Delta\sigma$ = 19 MPa. The increase of the elastic stiffness implies a consolidation process during which the pre-existing micro-fissures more oriented normal to the axial load tended to close. In contrast, Poisson's ratio did not change much over the test range with an average value of $\nu$ = 0.10. The increase in stiffness was also detected by the wave velocity as shown in fig. 2.13. The velocity increased with increasing the stress. The velocity increase rates during the isostatic loading are higher than those during the deviatoric loading. The consolidated state remained to some degree, indicated by the less decreased velocities along the unloading path.

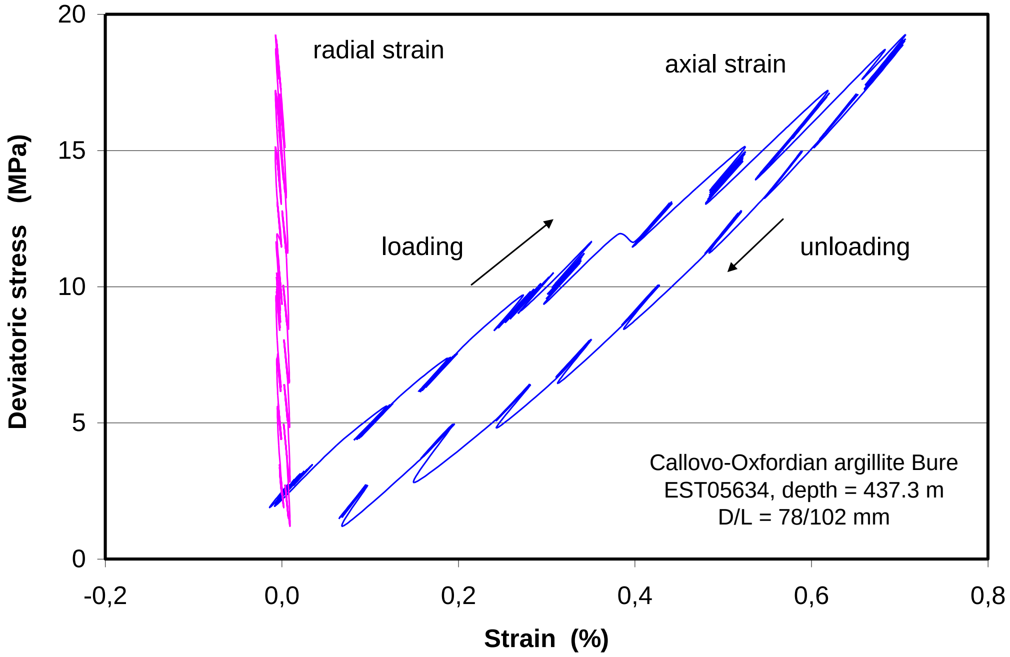


**Fig. 2.11** Determination of elastic parameters from the stress-strain curves

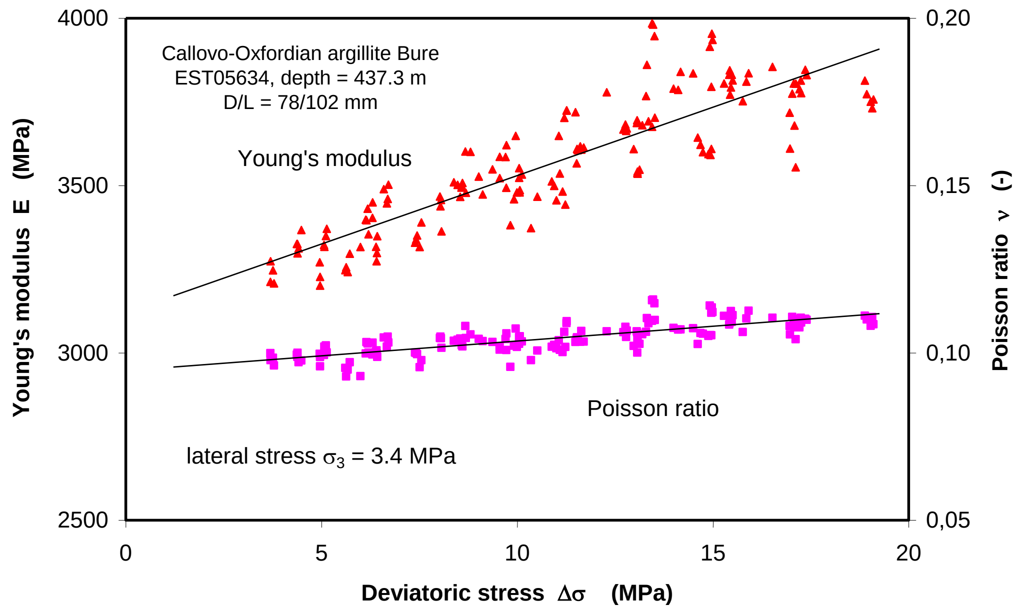


**Fig. 2.12** Dependence of the elastic parameters on applied deviatoric stress

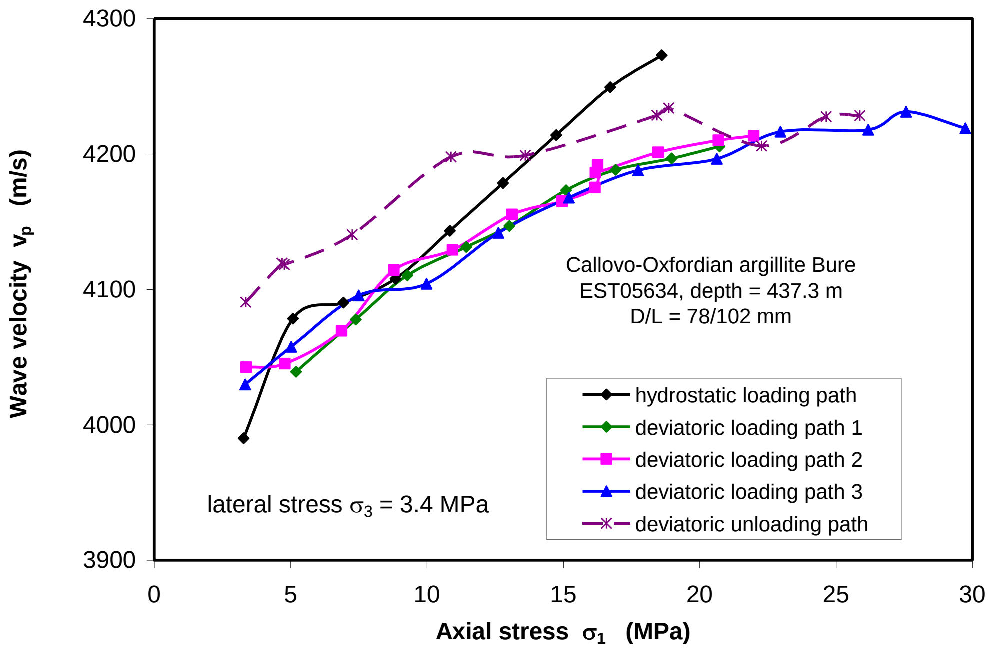


**Fig. 2.13** Measurements of ultrasonic wave velocity along different loading paths

### 2.3.2 Long-term deformation

The long-term deformability of the clay host rock is one of the most important factors governing the sealing of fractures in the EDZ and the compaction of pores in the buffer/backfill surrounding waste canisters in a repository. The sealing processes in the EDZ and in the Engineered Barrier System (EBS) must be predicted by performance and safety assessments of the repository. Knowledge of the time-dependent deformation behaviour of the host rock is needed in this respect.

#### 2.3.2.1 Earlier results

Within the previous projects (MODEX-REP, BURE-PRE, HE-D /ZHA 02/, /ZHA 04b/, /ZHA 07a/), the time-dependent behaviour of the COX and the OPA clay rocks was investigated in uniaxial creep tests by taking into account a number of influence factors such as load level, material anisotropy, scale effect, water content and temperature. The main observations are:

- Both claystone exhibit significant creep strains even under very low loads of less than 1 MPa, indicating negligible stress threshold for the onset of creep;
- Quasi-steady state creep appears after a transient phase over several months;

- The steady state creep rate seems to be linearly related to the applied stress;
- The creep behaviour parallel and perpendicular to the bedding plane are almost the same, suggesting a negligible anisotropy effect;
- High carbonate content and low water content slow down the creep;
- Creep of the saturated claystone is accelerated at elevated temperatures under undrained condition.

According to Mitchell /MIT 76/, /MIT 92/, the term "**creep**" is used to refer to time-dependent shear strains and/or volumetric strains that develop at a rate controlled by the viscous resistance of the soil structure. Mitchell suggests that creep results from continued slipping along contacts between clay particles accompanied by both bond breaking and new bond formation. According to the current state of knowledge /AND 03/, /AND 05/, different mechanisms may lie behind the creep, such as a) rebalancing of pore pressure because of the very low permeability; b) deformation of the mineral skeleton by sliding clay flakes; c) subcritical propagation of fissures and the possible creation of new fissures; d) stress-induced solution transfer (pressure solution) because the indurated clays contain a relatively high amount of carbonates. Moreover, recent observations reported in /ZHA 04a/, /ZHA 07a/, /ZHA 07b/ indicated that deformation of interparticle water-films adsorbed on the particle surfaces may play a key role for the creep in claystone. To our knowledge, it is still not clear which micro-processes really dominate the creep of argillaceous rocks.

In the frame of this project, the studies on the long-term deformation of the COX and OPA claystone have been continued not only in uniaxial but also in triaxial creep tests to consolidate the database and to improve the understanding of the creep mechanisms.

#### 2.3.2.2 Creep under uniaxial loads

Uniaxial creep tests were performed in five rigs. One rig allows five samples being simultaneously tested at the same load up to 500 kN at ambient temperature, while each of the other four rigs allows two samples tested in separate chambers at elevated temperatures between 20 to 200 °C. Details of the test rigs are given in /ZHA 02/, /ZHA 04b/. In order to avoid a loss of pore water during testing, the samples were sealed in rubber jackets and steel plates. Totally, 13 uniaxial creep tests were carried out in five groups, each consisting of two or five samples:

- Group I:EST21156⊥ and EST21158⊥ (D/L = 80/160 mm)
- Group II:EST21160⊥ and EST21162⊥ (D/L = 80/160 mm)
- Group III:EST17290⊥ and EST21166⊥ (D/L = 80/160 mm)
- Group IV:EST25335∥ and EST25344∥ (D/L = 122/220 mm)
- Group V:EST21171⊥, EST21173⊥, EST21177⊥, EST21168⊥, EST25321∥ (D/L = 80/160 mm)

The main characteristics of the samples are given in tab. 2.2. Because the samples drilled from boreholes REP2206 and PPA27 had been stored over a long period of 2.5 years before testing, their water loss was relatively significant and the remaining water saturation was in relatively low ranging between 70 % and 83 %. In contrast, the tests on the other samples from borehole TER1101 were started within a short period of time of a month after coring, so that the water loss was limited and the saturation degree was relatively high ranging between 86 % and 93 %. The axes of the samples from boreholes REP2206 and PPA27 were perpendicular to the bedding plane (⊥) while the others from borehole TER1101 were parallel to bedding (∥). The uniaxial creep tests were performed under multi-step loads between 1 and 13 MPa at ambient temperature of 23.0 ±0.5 °C in an air-conditioned room. Most of the tests lasted over an exceptionally long duration of 2 to 4.5 years with a creep phase duration of 4 to 18 months.

The axial strains measured on five COX samples from the same borehole REP2206 and one from PPA27 under uniaxial loads of 1, 2 and 5 MPa are plotted over the testing time of about 4 months in fig. 2.14a/b/c. Comparing them, one can find out that:

- The compressive strains increase gradually with time at all the applied stresses except for the sample EST21156 at 1 MPa (fig. 2.14a) which originated from the upper zone A' (fig. 2.2) with less clay and water contents but more carbonates;
- All the creep curves can be characterized by a transient phase with decreased strain rates during the first 2 – 3 months and a quasi-stationary phase with a relatively constant strain rate;

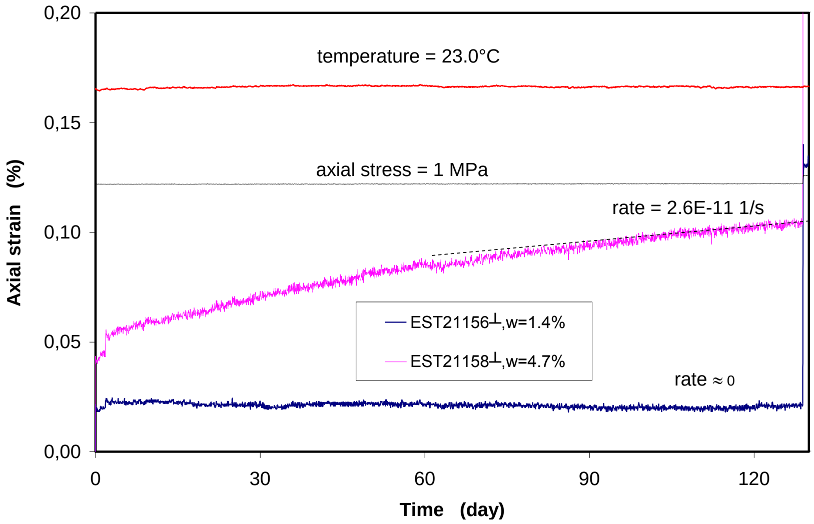


(a) under uniaxial load of 1 MPa

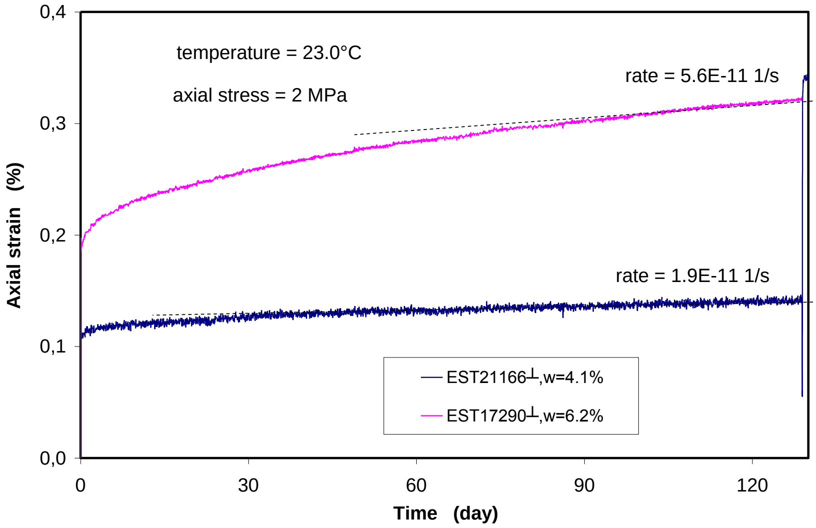


(b) under uniaxial load of 2 MPa

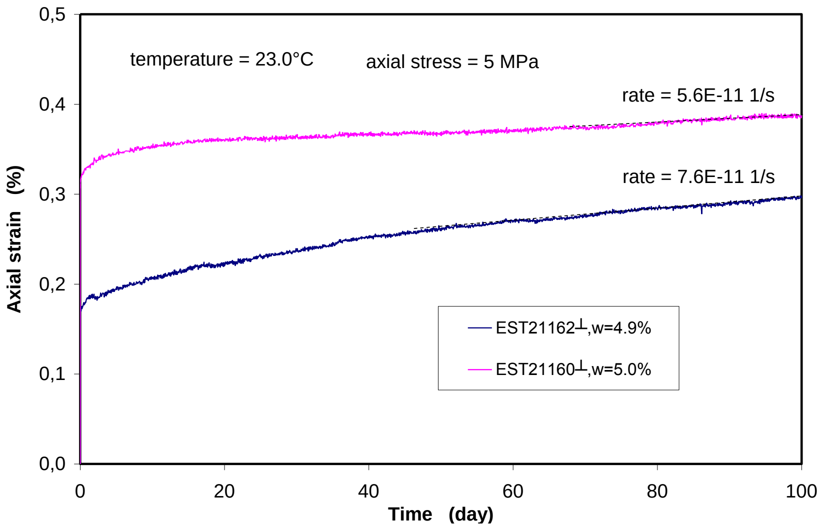


(c) under uniaxial load of 5 MPa

**Fig. 2.14** Creep curves of six COX samples under various uniaxial loads perpendicular to bedding

- The quasi-steady state creep rates determined over the last interval of ~1 month are in a range between $2 \cdot 10^{-11}$ $s^{-1}$ and $8 \cdot 10^{-11}$ $s^{-1}$, being higher at more water contents under the same load;

- The higher the applied load, the larger the total and viscous deformations.

Fig. 2.15 compares the multi-step creep curves obtained on two samples from borehole TER1101 with similar water contents of 6.2 % and 6.3 %, respectively. The samples were axially loaded parallel to the bedding at 3 MPa over 4 months, 6 MPa over 9 months, 9 MPa over 11 months, and 11 MPa over 12 months. The tests were disturbed two times by failure of the air-conditioner within the second and the fourth phase. Consequently, longer testing durations were needed to reach a steady state at each load step. The creep rates were determined from the quasi-linear parts of the strain-time curves. The creep curves show that a) the sample EST25344 with slightly higher water content deformed faster but unfortunately failed earlier at a lower stress of 9 MPa; b) true steady state creep seemed not to be reached during each load phase; and c) the quasi-steady state creep rates determined from the data of each last phase at 6, 9 and 11 MPa vary in a small range between $2 \cdot 10^{-11}$ $s^{-1}$ and $3 \cdot 10^{-11}$ $s^{-1}$, indicating little or almost no dependence on the applied stresses.

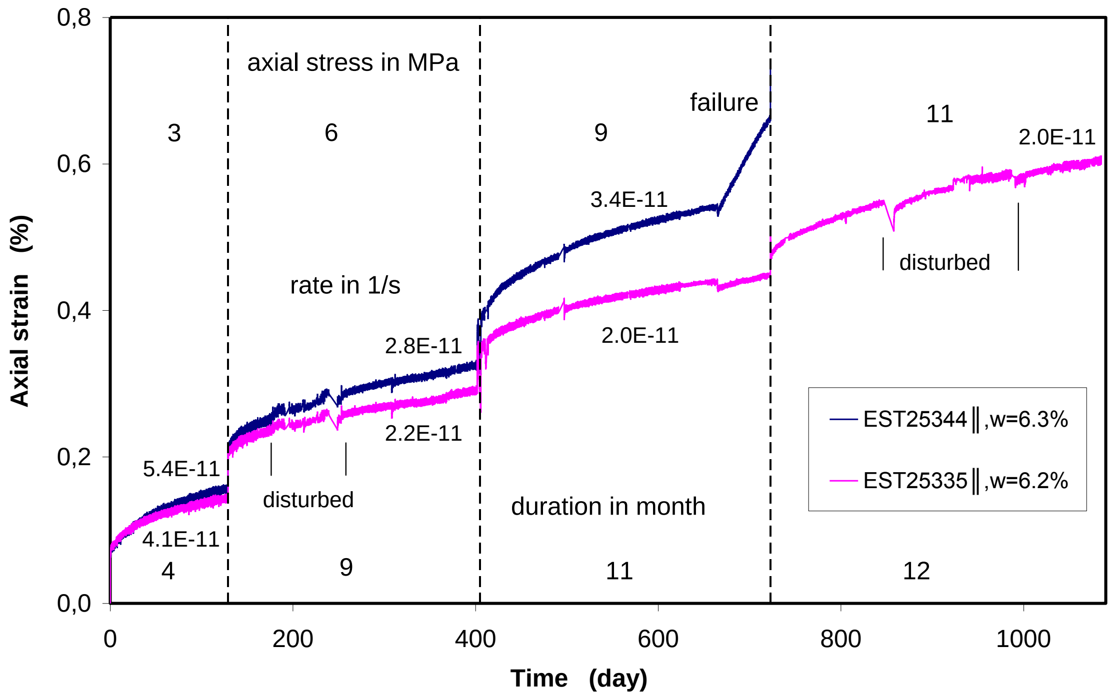


**Fig. 2.15** Creep curves of two COX samples under multi-step uniaxial loads parallel to bedding

Fig. 2.16 summarizes the creep curves obtained on five samples under the multi-step uniaxial loads applied upwards to 4, 7, 10, 13 MPa and downwards to 10 and 7 MPa. Each creep phase lasted over 4 to 17.5 months. Sample EST25321 from borehole TER1101 was axially loaded parallel to bedding while the others from borehole REP2206 were loaded perpendicular to bedding. The measurements indicate that the total strains in direction perpendicular to bedding are larger than those in parallel direction. But the strain evolution curves are relatively parallel, suggesting little anisotropy of the viscous deformation in the claystone. The distances between the creep curves perpendicular to bedding arise from the differences in the stiffness of the samples and thus the short-term deformation during each loading. As mentioned before, the tests were also disturbed by the failure of the air-conditioner in the test room.

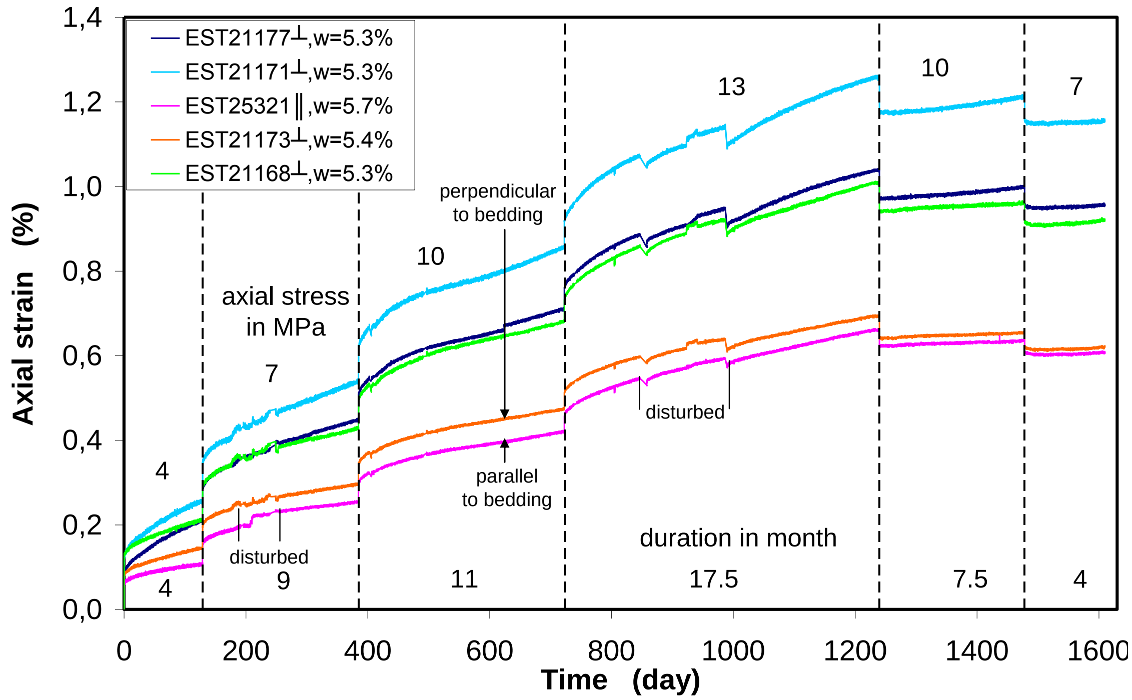


**Fig. 2.16** Creep curves of five COX claystone samples under multi-step uniaxial loads parallel and perpendicular to the bedding plane

It is interesting to compare the creep curves obtained at the same stress level but reached by different loading paths (loading / unloading). Fig. 2.17 shows the creep curves obtained at 10 MPa axial load reached by loading (a) and unloading (b), while the other creep curves at 7 MPa reached by loading (a) and unloading (b) are compared in fig. 2.18. The creep curves at the same stress but reached by different loading paths show different patterns.

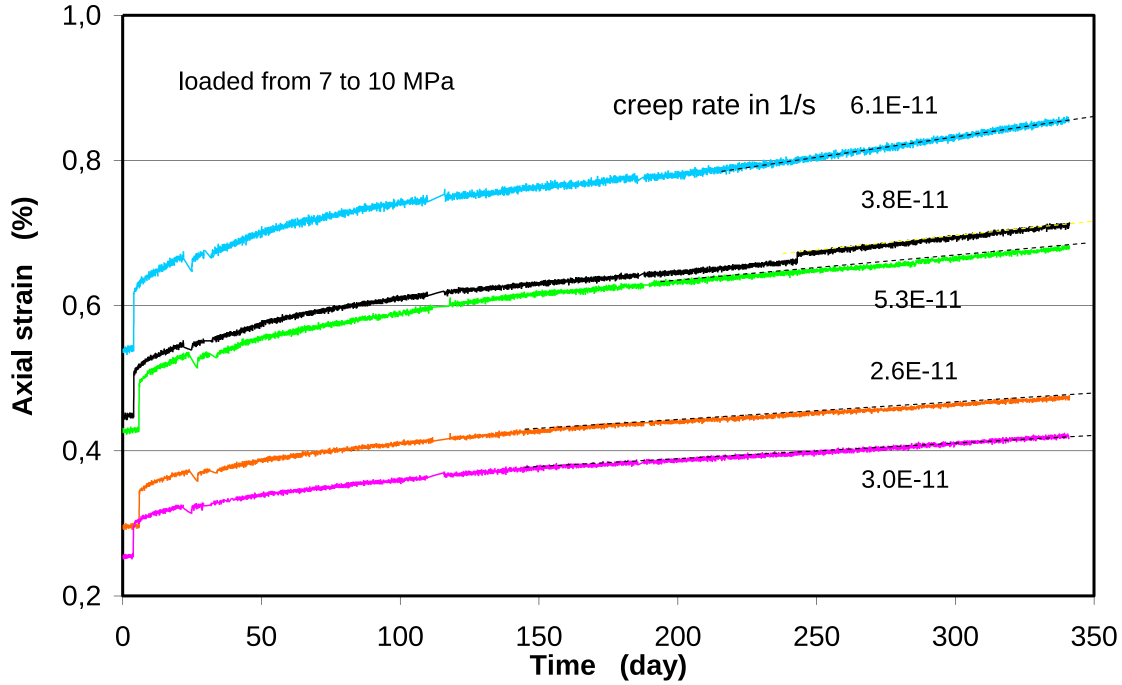


(a) loaded from 7 to 10 MPa

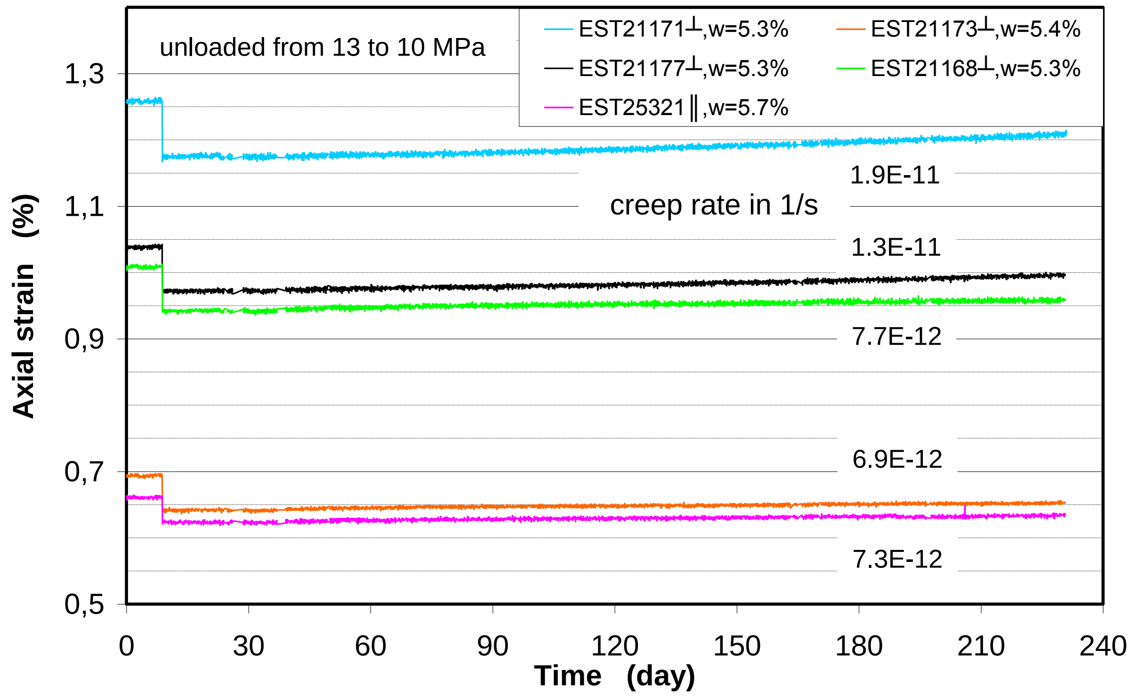


(b) unloaded from 13 to 10 MPa

**Fig. 2.17** Effects of loading paths on the creep behavior at uniaxial load of 10 MPa

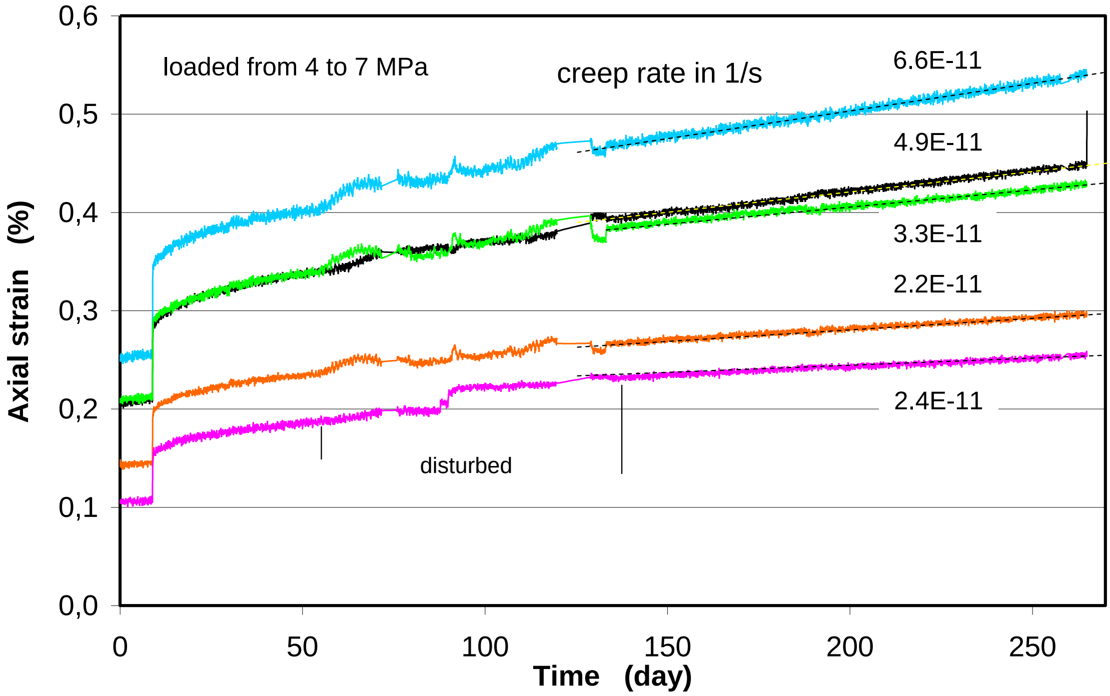


(a) loaded from 4 to 7 MPa

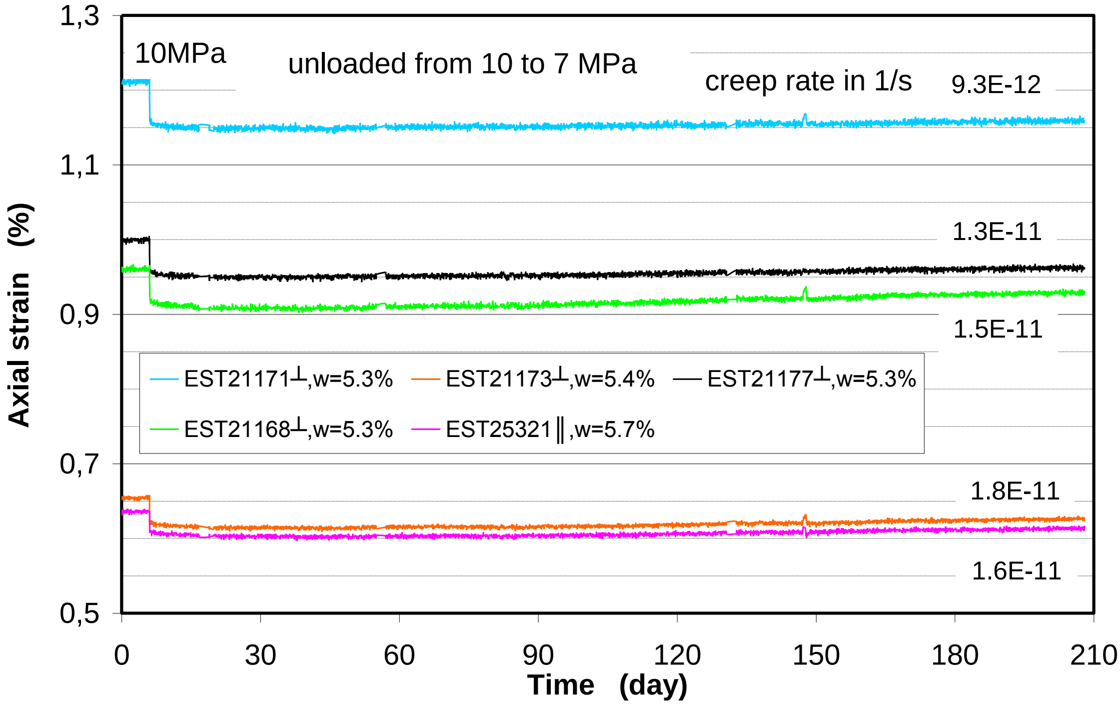


(b) unloaded from 10 to 7 MPa

**Fig. 2.18** Effects of loading and unloading on the creep behaviour at a uniaxial load of 7 MPa

The creep strain curve at an increased load is typically characterized with a transient phase with decreasing rates and a following stationary phase with a nearly constant rate. In contrast, the creep strain at lowered load evolves firstly backwards with negative rates and then returns with time to a positive constant rate, at which the creep is in steady state. At decreased load, the effect of strain hardening, usually occurring during stress rising, does not appear. The creep rates determined from the last parts of each creep curve are also remarked in fig. 2.17 and fig. 2.18. The strain rates of $3 \cdot 10^{-11}$ to $6 \cdot 10^{-11}$ $s^{-1}$ after loading are 2 to 5 times that of $7 \cdot 10^{-12}$ to $1 \cdot 10^{-11}$ $s^{-1}$ after unloading. Almost the same conclusion is true for the creep rates at 7 MPa after loading and unloading, but the rates are slightly lower. As mentioned above, the difference is mainly attributed to the effect of strain hardening by loading.

To highlight the influence of stress on the creep rate of the clay stone, the strain rates obtained at the end of each phase are depicted in fig. 2.19 versus the applied stresses. The relatively higher creep rates established at the lower stress of 4 MPa suggest that the creep within 4 months did not attain a steady state. The strain rates obtained at 7, 10 and 13 MPa reached by loading seem to be linearly correlated to the stress applied to the sample. But the flat slopes of the rate-stress curves imply a low significance of the stress effect on the creep rate. Similarly, the steady state creep rates obtained at 7 and 10 MPa reached by unloading are rather comparable to each other, indicating insignificant dependency of the creep rate on the applied stress. Additionally, the small distances between each creep rate-stress curves reflect comparable qualities of the samples and a good homogeneity of the rock.

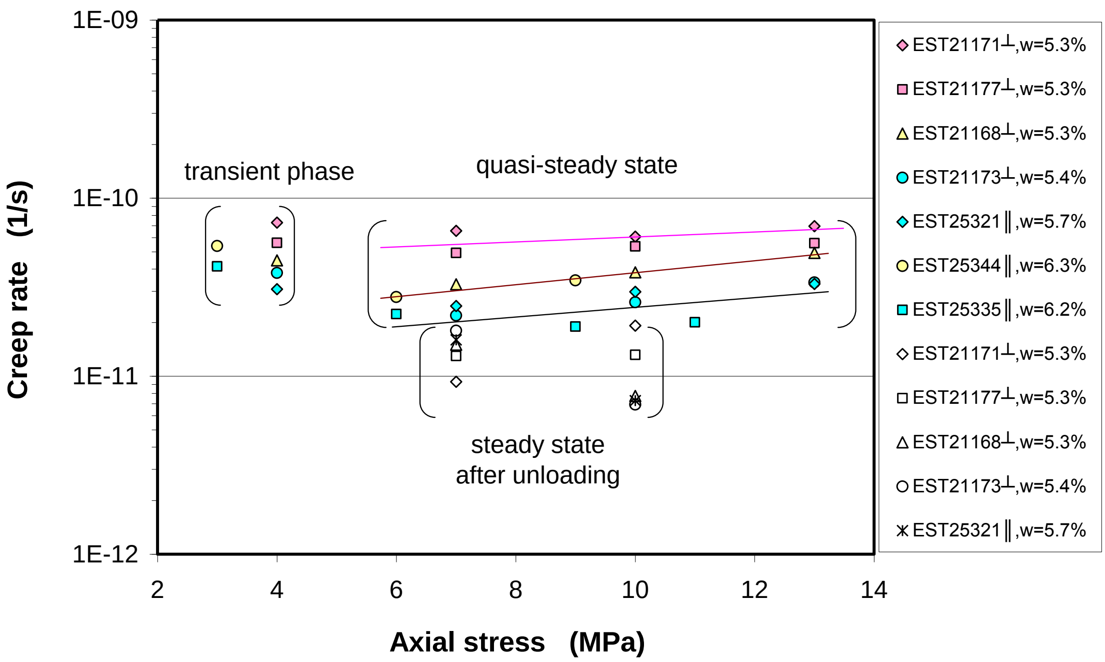


**Fig. 2.19** Dependency of the creep rate on the applied stress

### 2.3.2.3 Creep under triaxial load

In the above uniaxial creep tests, the applied uniaxial loads are more representative for the *in situ* stress states near drift walls. On the other hand, the quality of used samples is degraded after coring and preparation, possibly reflecting the rock state in the EDZ. In order to characterize the long-term deformation behaviour of the clay rock in the far-field, where the rock material remains intact and the magnitude of the deviatoric stress is relatively small, triaxial creep tests were carried out on a COX clay sample EST25335∥ (D/L=100/190mm) from borehole TER1101 and on an Opalinus clay sample BET-7∥ from the Mont Terri-URL. Fig. 2.20 shows a photo of the used triaxial creep rig and the schematic assembly of a triaxial creep test. The triaxial cell allows a maximum axial stress of 70 MPa and a lateral pressure of 50 MPa within an accuracy of ±0.05 MPa. The sample can be heated by means of a heater mounted outside around the cell up to a temperature of 150 °C within an accuracy of ±0.01 °C. While axial deformation is recorded by a LVDT deformation transducer installed inside the cell between the top and bottom of the sample, radial strain can be measured by a circumferential extensometer mounted around the sample outside the jacket. Strain gauges are attached on the surface at the sample mid-height. The sample is inserted in a rubber jacket and located between two load pistons, in which piezo-electric wave transducers are introduced for measuring ultrasonic wave velocities during the test.

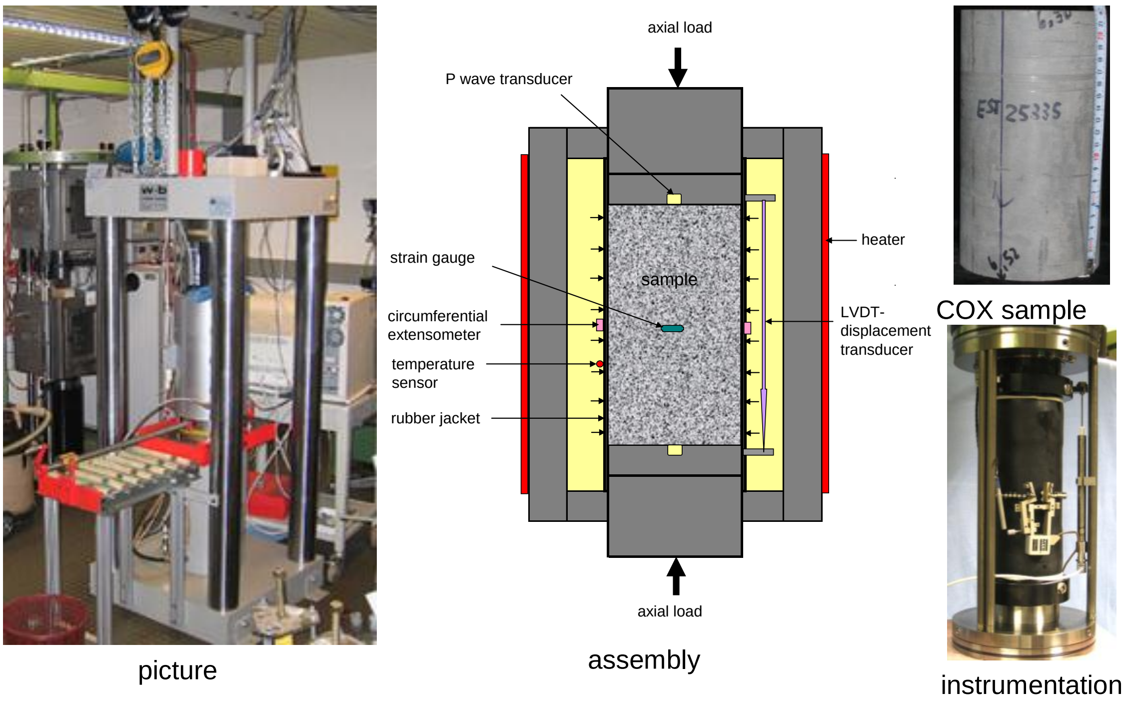


**Fig. 2.20** Schematic assembly of the triaxial creep test on a claystone sample

In order to achieve the original rock state, the samples were pre-consolidated under high isostatic stresses up to 40 MPa. Following that, different stress states were adjusted by decreasing the axial and lateral stresses to the desired levels. In the tests, the *in situ* stress states in the COX formation at the main level (-490 m) of the MHM-URL were taken into account by applying a constant axial stress of $\sigma_1$ = 15 MPa and various lateral stresses of $\sigma_3$ = 12, 9, 6, 3 MPa.

**Test 1**

Fig. 2.21 illustrates the results of the first test on the COX sample EST25335‖ with an initial porosity of 15.7 % and a water content of 6.2 % (calculated degree of water saturation $S_l$ = 90 %). The application of an isostatic load of $\sigma_1 = \sigma_2 = \sigma_3$ = 40 MPa over two weeks led to a compaction in all directions of $\varepsilon_1$ = 0.26 % and $\varepsilon_3$ = 0.42 %. The large radial strain perpendicular to the bedding is 1.6 times of the axial strain parallel to the bedding, i. e., the anisotropy ratio amounts to $\varepsilon_\perp/\varepsilon_{//}$ ($\varepsilon_3/\varepsilon_1$) = 1.6. This value only reflects the anisotropy of the disturbed sample but not necessarily that of the natural clay rock. Based on the data, the volumetric strain is calculated by $\varepsilon_v = \varepsilon_1 + 2\varepsilon_3$ = 1.1 % and the remaining porosity is $\phi$ = 14.6 %. Taking into account the dry density of $\rho_d$ = 2.45 g/cm$^3$ and the pore-water density of $\rho_w$ = 1.0 g/cm$^3$, the degree of water saturation after the consolidation is determined to $S_l$ = 104 % according to eq. (2.7). This value suggests full saturation of the consolidated sample. The compaction of the pre-existing micro-fissures was also detected by a significant increase of the elastic wave velocity from $v_p$ ≈ 1000 to $v_p$ ≈ 3300 m/s.

Following the consolidation, the stresses were lowered down to $\sigma_1$ = 15 MPa and $\sigma_3$ = 12 MPa, similar to the anisotropic stress state of the original COX formation at a depth of ~ 500 m. Corresponding to the unloading, a rapid dilation in radial direction perpendicular to the bedding was clearly recorded both by the circumferential extensometer and the strain gauge, while the axial compressive strain was very small. Beyond this elastic deformation, the radial dilation continued with time during a time period of 4 months, whereas no significant axial strain could be detected by the LVDT displacement transducer with an accuracy of ±0.01 of full scale. From the data, an average radial dilation rate of $d\varepsilon_3/dt = -7\cdot10^{-11}$ s$^{-1}$ can be determined.

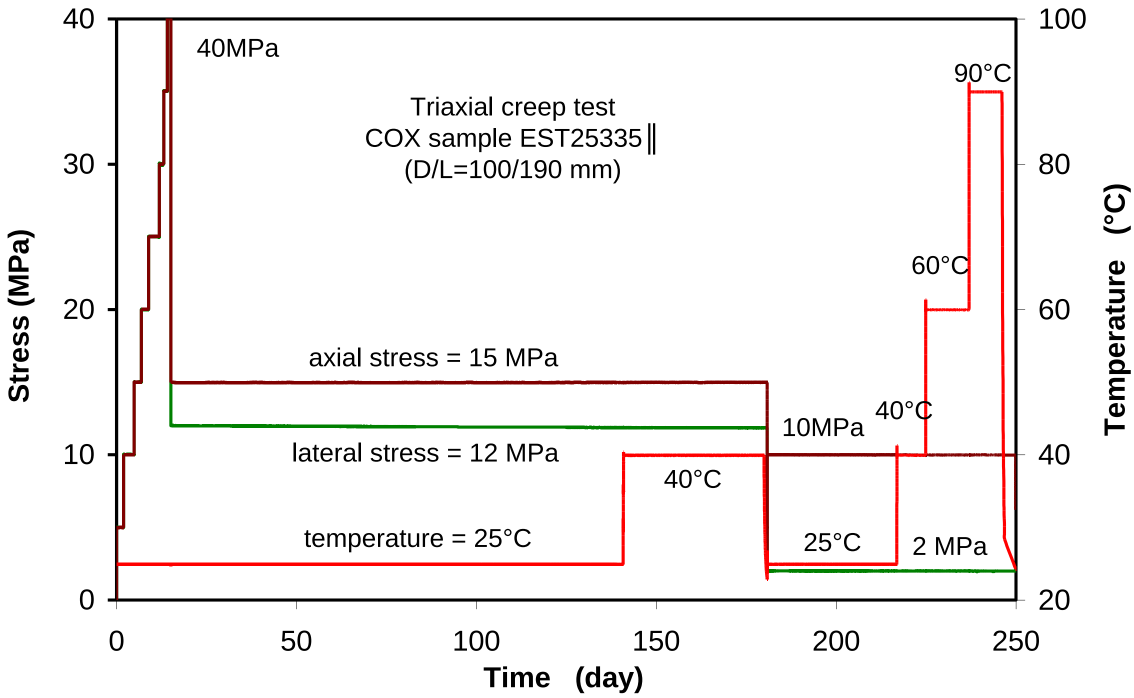


(a) applied stresses and temperature

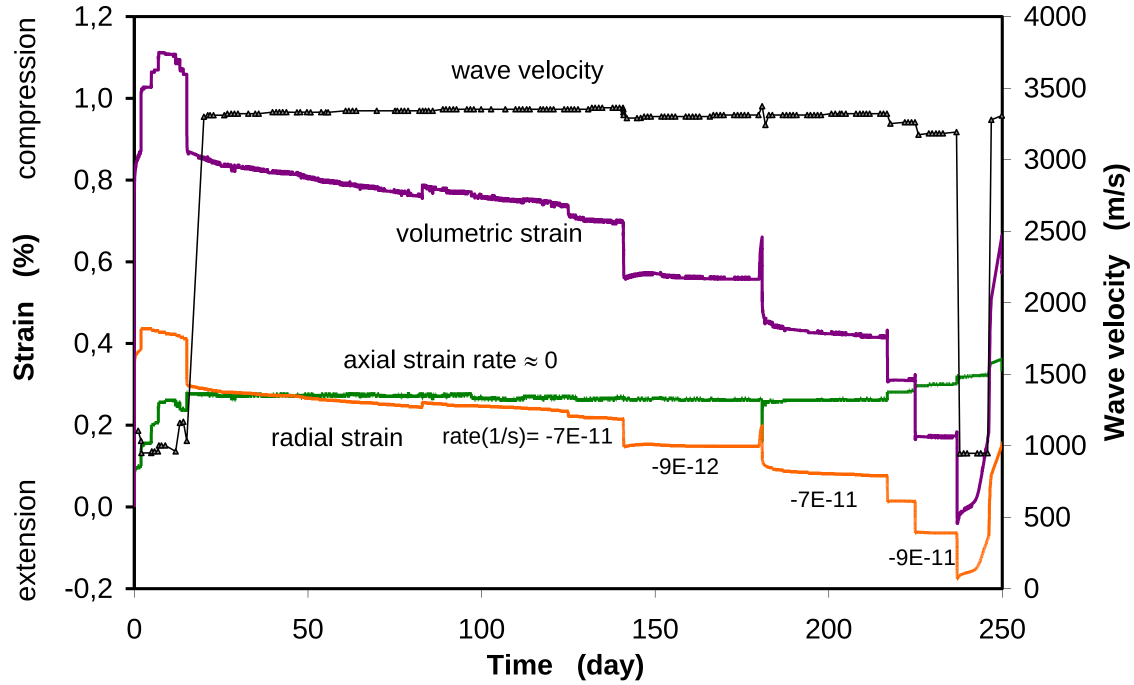


(b) measurements of strains and wave velocity

**Fig. 2.21** Results of a triaxial creep test on a COX sample under different deviatoric stresses and temperatures

Keeping the stress state unchanged, the sample was heated to 40 °C. The heating caused expansion in radial direction, but not in axial direction. At the elevated temperature, the radial dilation seemed to be slowed down while no significant changes in axial strain could be recorded. At that time, it was believed that the displacement transducer might fail. To check that, the sample was unloaded to $\sigma_1$ = 10 MPa and $\sigma_3$ = 2 MPa and cooled down to 25 °C. This resulted in an impulse of the axial strain, confirming the ordinary operation of the displacement transducer. Over a month under these conditions, however, no significant axial strain was observed, while the radial dilation continued with time.

Subsequently, the sample was heated again step by step to 40, 60 and 90 °C. At a deviatoric stress of $\sigma_1 - \sigma_3$ = 10 – 2 MPa, each heating resulted not only a radial expansion but also an axial compression. At 90 °C, the pore-water probably evaporated, indicated by a rapid reduction of the wave velocity from 3300 to 1000 m/s. The evaporation might generate high vapour pressures exceeding the confining pressure on the rubber jacket at the pistons, letting the vapour passing through. The consequence of the water release was the compaction under the confining stress. This is clearly indicated by the gradual compression in radial direction. The last cooling phase accelerated the compaction mainly due to thermal contraction of the pore-water and solid particles.

**Test 2**

In the second test on OPA sample BET-7‖ (D/L=100/200 mm), a more precise LVDT displacement transducer with an accuracy of ±0.001 of full scale was used. The axis of the sample was parallel to the bedding. It was characterized by a dry density of $\rho_d$ = 2.45 g/cm$^3$, a porosity of $\phi$ = 14.0 %, a water content of w = 5.7 %, and a saturation degree of $S_l$ = 100 %. Fig. 2.22 illustrates the results.

Before the creep test, the saturated sample was also pre-consolidated under an isostatic stress of 40 MPa over 10 days, causing a compaction in all directions of $\varepsilon_1$ = 0.09 % parallel and $\varepsilon_3$ = 0.34 % perpendicular to the bedding. The porosity reduction is $\Delta\phi$ = 0.77 %. From the above given data, one can conclude that the remaining pores after the compaction were fully saturated. Subsequently, creep test followed by stepwise decreasing the stresses to $\sigma_1$ = 14.9 MPa and $\sigma_3$ = 12, 9, 6 MPa over 1.5, 2, and 4 months, respectively. During the test, the temperature was controlled at 24.94 ±0.01 °C. From the measured axial and radial strains and the calculated volumetric strain versus time in fig. 2.22, it can be identify that: a) each reduction of the radial stress led to a rapid elastic deformation with radial dilation, axial compression, and volume expansion due to the relatively larger magnitude of radial dilation; and b) under each constant deviatoric stress, the axial compression continued with time while the radial dilation slowed down and then remained more or less constant, leading to volumetric compaction with time.

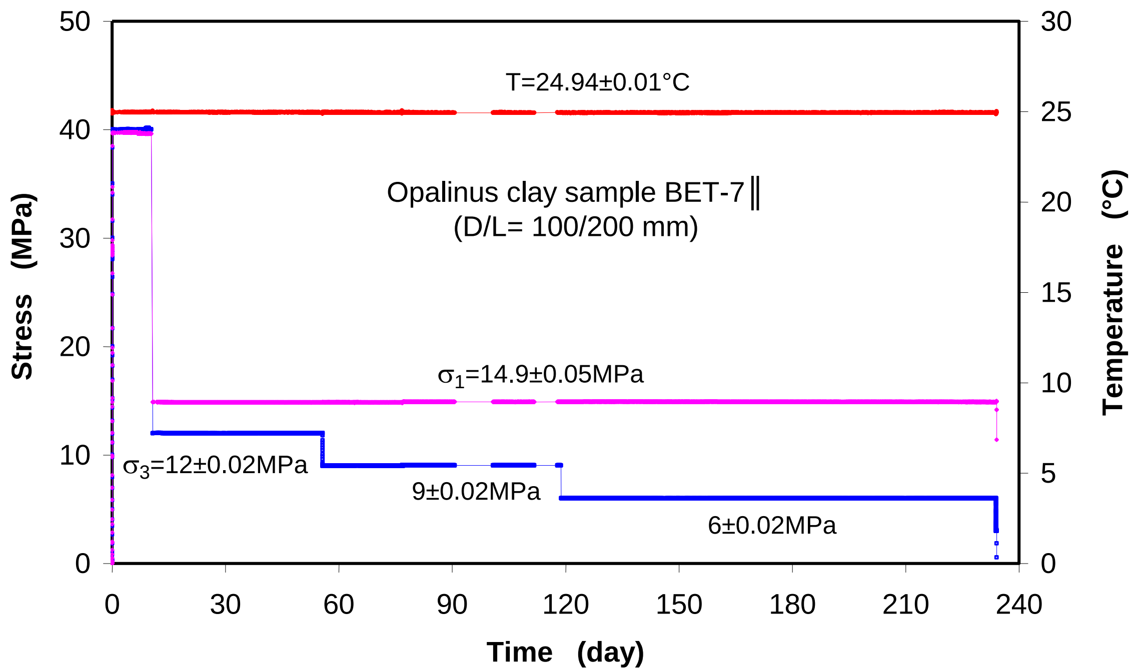


(a) applied stresses and temperature

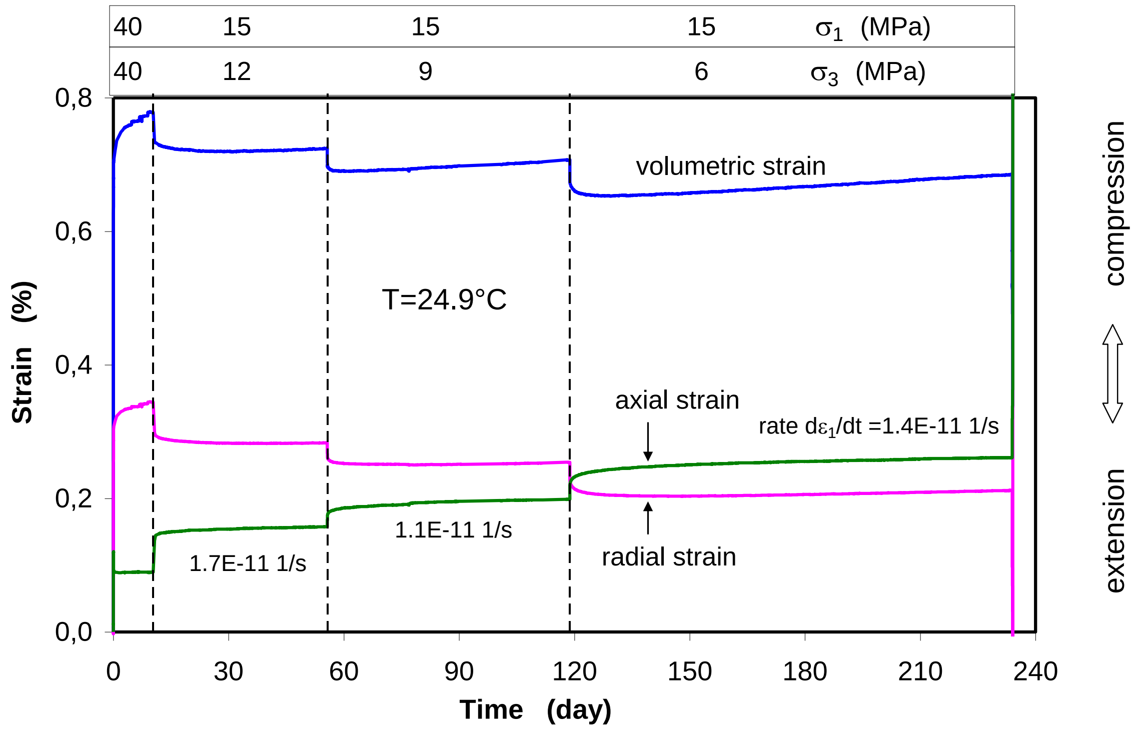


(b) responses of strains

**Fig. 2.22** Results of a triaxial creep test on Opalinus clay at constant axial stress and reduced radial stresses

The axial strain rates determined at each stress level are plotted in fig. 2.23 versus time together with the axial strain. After a transient phase with decreasing rates, a stationary creep state seemed to be reached with a nearly constant rate. The steady state creep rates are nearly the same between $1.1 \cdot 10^{-11}$ and $1.7 \cdot 10^{-11}$ $s^{-1}$ for the applied stresses. This finding agrees with the conclusion from the uniaxial creep tests, i. e. the dependency of the creep rate on the stress is insignificant.

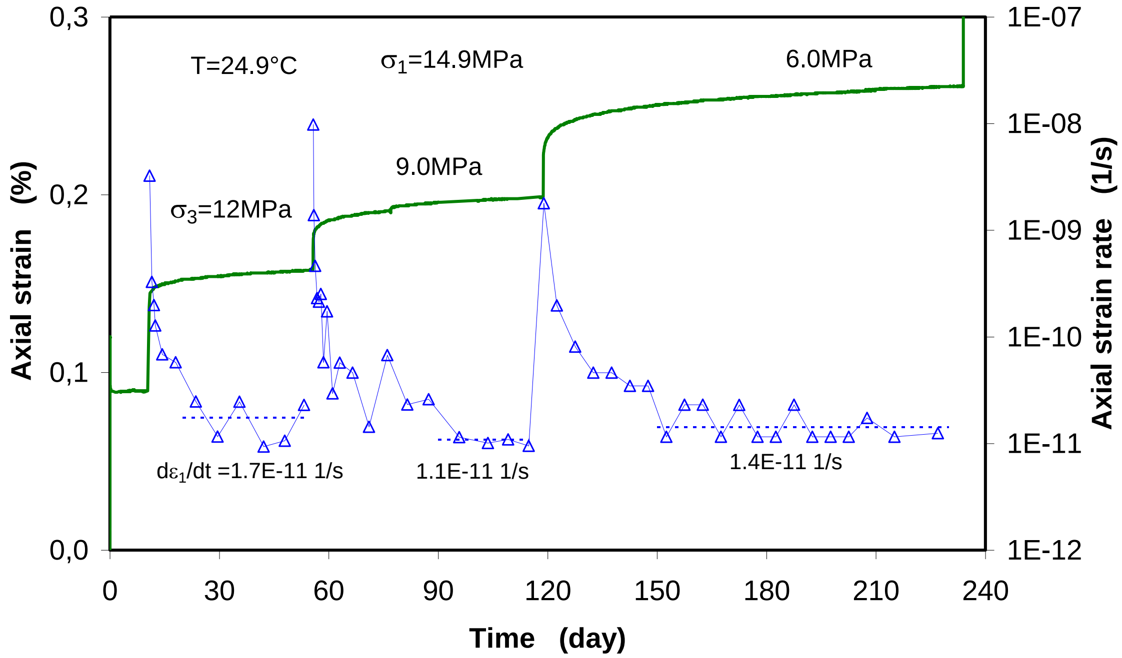


**Fig. 2.23** Evolution of axial creep strains and rates for the Opalinus clay sample at constant axial stress and reduced radial stresses

For comparison, the result of another triaxial creep test made by BGR /SCH 09/ on an Opalinus clay sample is represented here in fig. 2.24. The sample was loaded at increased axial stress to $\sigma_1$ = 25, 27, 29 and 31 MPa at constant lateral stress of $\sigma_3$ = 12 MPa. Even though this loading path is different from that applied in the GRS test mentioned above (fig. 2.23), both provided the same pattern of the creep curves. Moreover, the creep rates determined on both samples in the range of deviatoric stress between 3 and 15 MPa are very close to each other in a narrow range of $1.1 \cdot 10^{-11}$ to $1.7 \cdot 10^{-11}$ $s^{-1}$ (see fig. 2.25).

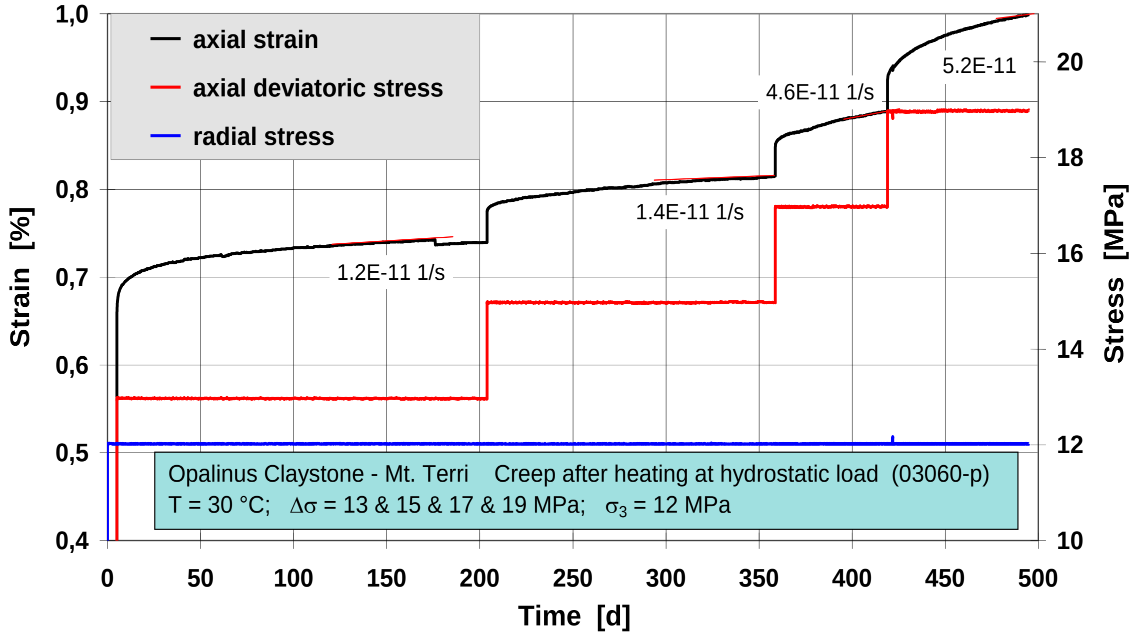


**Fig. 2.24** Results of a triaxial creep on another Opalinus clay sample at constant radial stress and elevated axial stresses (slightly modified after /SCH 09/)

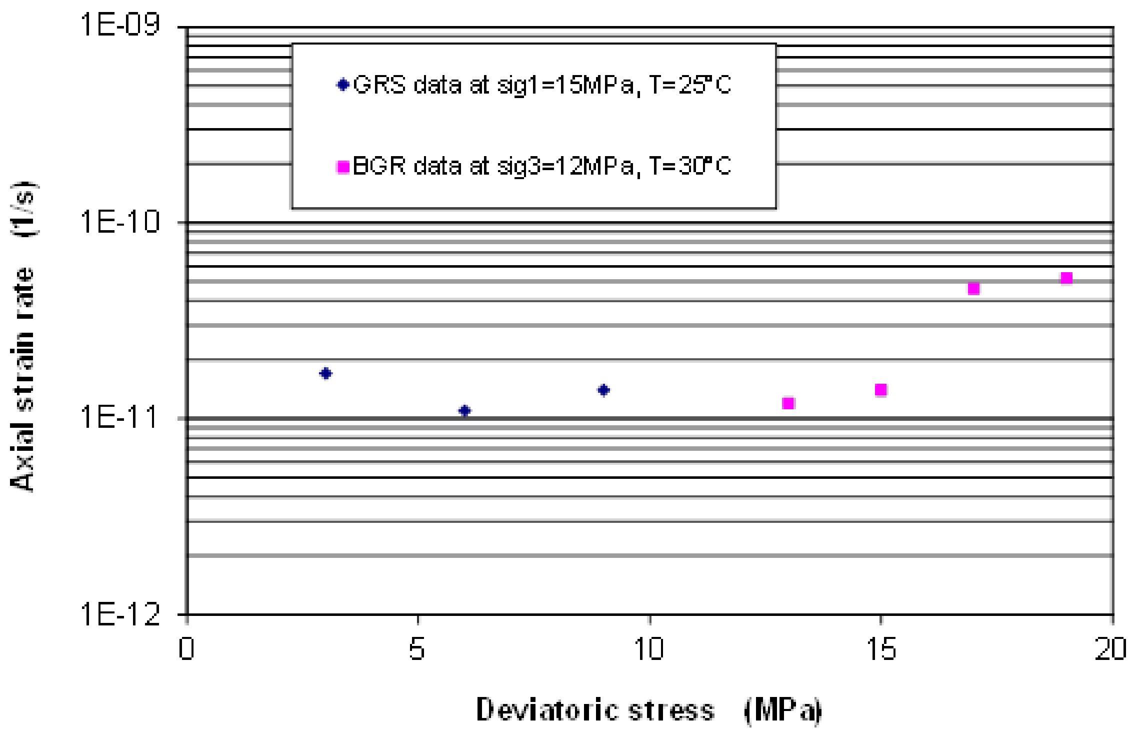


**Fig. 2.25** Creep rate as a function of applied deviatoric stress for the Opalinus clay

At the high stresses of 17 and 19 MPa, the strain rates determined are relatively higher. This might be attributed to possible initiation of damage. The strain rate data from the triaxial creep tests on the OPA claystone also suggest an insignificant dependency of the creep rate on the deviatoric stress, confirming the conclusion from the uniaxial creep tests on the COX claystone (see fig. 2.19). This finding is different from the previous observations during relatively short test durations /AND 05/, /ZHA 02/, /ZHA 04b/, /ZHA 07a/. Because of its importance for the long-term stability of a repository in the clay formation, this conclusion has to be confirmed in the future by more precise tests.

### 2.3.3 Conclusions on deformability

The major findings from the short- and long-term deformation tests on the COX and OPA claystone under uniaxial and triaxial load conditions are summarized as follows:

- The pre-consolidation of clay samples before testing is a necessary precondition to make testing more representative for the natural clay rock and thus to gather more transferable test results for the rock.
- The **short-term deformation** of the consolidated COX claystone is typically characterized by elasto-plastic behaviour. The elastic stiffness and the wave velocity observed increase with applied deviatoric stress until yielding, indicating the compaction of the pre-existing micro-cracks in the samples. Further increasing the deviatoric stress results in re-opening / creation, propagation and coalescence of micro-cracks forming shear fractures. The peak strength increases with the lateral confining stress and can be reasonably approached by the Mohr-Coulomb criteria. The parameters determined for the peak strength parallel to bedding plane are the cohesion of 6.5 MPa, the internal friction angle of 24°, and the major principle strain of 1 – 2 %. By comparing with the previous data, the strength perpendicular to bedding is relatively higher than that parallel to bedding with a mean anisotropic ratio of 1.25. Whereas the elasto-plastic yield occurs at ~70 % of the peak strength, the dilatancy onset detected by volumetric strain is closer to the failure point. After failure, a certain residual bearing capacity still remains in the fractured claystone.
- The **long-term deformability** of the claystone was investigated under uniaxial and triaxial creep tests over long durations of months to several years. The test results suggest a significant time dependency of the deformation:
- The claystone deform continuously with time even at low deviatoric stresses of 1 – 2 MPa, indicating negligible threshold for the onset of creep.
- The creep behaviour is dependent upon the loading path, i. e. raising or lowering the load in uniaxial tests. After elevating the load to a desired level, the claystone

deforms gradually with time at decreasing rates and then a (quasi-) stationary creep phase follows with a nearly constant rate. In contrast, after lowering the load to a desired level, the creep strain evolves first with negative but increased rates until a constant positive rate is reached. The duration of the transient creep at lowered load is relatively shorter than that at increased load, depending on the magnitude of load increments.

- The quasi-steady state creep rates determined the COX claystone at elevated uniaxial loads of 1 to 13 MPa range from $2 \cdot 10^{-11}$ to $7 \cdot 10^{-11}$ $s^{-1}$, whereas the steady state creep rates observed at lowered stresses lie between $7 \cdot 10^{-12}$ and $1 \cdot 10^{-11}$ $s^{-1}$. The creep rates determined on the OPA claystone in the deviatoric stress range of 3 to 15 MPa are very close to each other in a narrow range of $1.1 \cdot 10^{-11}$ to $1.7 \cdot 10^{-11}$ $s^{-1}$. All the data suggest no or insignificant dependence of creep on the applied stress in the test range from 1 to 15 MPa.
- The creep rate is less or independent of the loading directions parallel or perpendicular to bedding plane, i. e., insignificant anisotropy effect on creep.
- The higher carbonate content and / or the lower water content, the slower the creep.

## 2.4 Swelling capability

During the operation phase of a repository, the ventilation of the underground openings will lead to de- and re-saturation of the surrounding rock, depending on the changing humidity of the ventilating air. De- and re-saturation may result in shrinking and swelling and even fracturing of the clay rock. After closing the repository, the previously desaturated clay rock will be gradually re-saturated again by taking up water from the saturated far-field, accompanied by swelling of clay minerals into fracture voids. The swelling capability of natural clays depends on the mineral components, particularly clay content, the density or porosity, the intensity of cementation, the water uptake, and confining conditions etc. Within the framework of this project, the swelling capabilities of both COX and OPA claystone with different clay contents were examined by drying and wetting samples with measurements of water adsorption, free swelling strain in unconstrained and confined conditions, and swelling pressure under axially-fixed and laterally-unconstrained conditions.

### 2.4.1 Water retention

First of all, the relationship between suction and water content, usually called water retention curve, was established for the COX and OPA claystone, as it controls the de- and re-saturation and the swelling behaviour. Samples were extracted from the TER heater borehole at the main level (-490 m) and from the DIR borehole in the niche at -445 m depth in the MHM-URL, respectively. While the COX-TER samples have a clay content of ~40 %, the COX-DIR samples have a lower clay content of ~12 %. The OPA samples taken from the ventilation test field (VE) in the MT-URL have a clay content of ~65 %.

#### 2.4.1.1 Testing method

The determination of the water retention curve was performed on unconfined samples of 40 – 80 grams using the vapour equilibrium technique. The samples were placed in desiccators at different relative humidity values adjusted by means of differently saturated salt solutions. The tests were carried out at a constant temperature of 22 °C and different humidity values in a range of 22 % to 100 %. The corresponding suctions lies between 0.0 and 206 MPa. The relative humidity in each desiccator was continuously recorded by transistor psychrometer sensors, while the water content of each sample was measured outside at different periods of time. The suction is related to the relative humidity by Kelvin's law /FRE 93/:

$$s = -\frac{RT}{v_{wo}\omega_v} \ln\left(\frac{p_v}{p_{vo}}\right) = -\frac{RT}{v_{wo}\omega_v} \ln(RH) \qquad (2.9)$$

where $s$ = soil suction (kPa)

$R$ = universal gas constant (= 8.31432 J/mol K)

$T$ = absolute temperature (K)

$v_{wo}$ = specific volume of water or the inverse of density of water (= $1/\rho_w$, $m^3/kg$)

$\rho_w$ = density of water (= 998 $kg/m^3$ at 20 °C)

$\omega_v$ = molecular mass of water vapour (= 18.016 kg/kmol)

$p_v$ = partial pressure of pore-water vapour (kPa)

$p_{vo}$ = saturation pressure of water vapour over a flat surface of pure water at the same temperature (kPa)

$RH$ = relative humidity (= $\frac{p_v}{p_{vo}} \cdot 100\%$).

Based on the data of the water content $w$, dry density $\rho_d$ and porosity $\phi$, the degree of water saturation of the samples can be calculated according to eq. (2.7). The relation of suction to the effective water saturation can be expressed by the Van Genuchten model

$$S = \frac{S_l - S_{lr}}{S_{ls} - S_{lr}} = \left[1 + \left(\frac{s}{P}\right)^{1/(1-\beta)}\right]^{-\beta} \qquad (2.10)$$

where $S_l$, $S_{lr}$, $S_{ls}$, and $S$ are the actual, residual, maximum and effective saturation of liquid, respectively, $s = P_g - P_l$ is the suction, $P$ is a material parameter, and $\beta$ controls the shape of the water retention curve.

#### 2.4.1.2 Results

Fig. 2.26 shows the evolution of water content measured on COX-DIR and TER samples at different suctions between 5 and 206 MPa. The data at zero suction or 100 % relative humidity are plotted in fig. 2.27. In the first phase, changes of the water content of the original samples were measured with time. The samples were either wetted or dried, depending on the initial water content and the applied suction. After reaching equilibrium in each desiccator over about one month, the second phase followed by wetting the samples at a higher level of the relative humidity, except for those two samples previously wetted at suction of 5 MPa and then dried at suction of 206 MPa. The time needed to reach equilibrium was shorter due to the small change in suction.

Fig. 2.27 compares the water uptake of the COX and OPA claystone with different clay contents. It is interesting to see that in the wet environment at null suction, the claystone can take up large amounts of water of up to w = 14 % for the COX-TER with a clay content of c = 40 %, of w = 11 % for the COX-DIR with c = 12 %, and w = 18 % for the OPA with c = 65 % over 8 months during which equilibrium was not achieved. The higher the clay content, the more water is taken up. The water uptake is significantly higher than that of 6 % – 8 % in the natural confined state. This finding suggests that if not all, at least the pore water in the natural clays is bound on particle surfaces. Only the adsorbed water can be set free if high external loads and/or high temperatures are applied, for instance in case of extraction of pore water from claystone by squeezing the samples under high pressures or evaporation of pore-water by heating and drying.

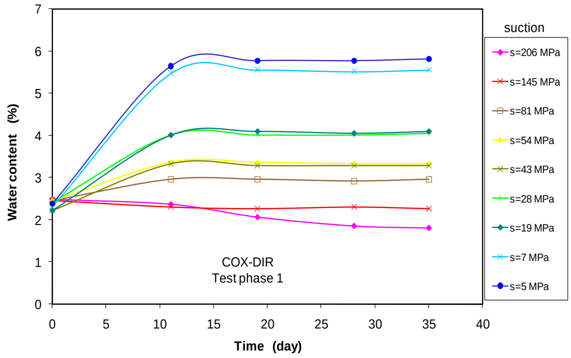


phase 1

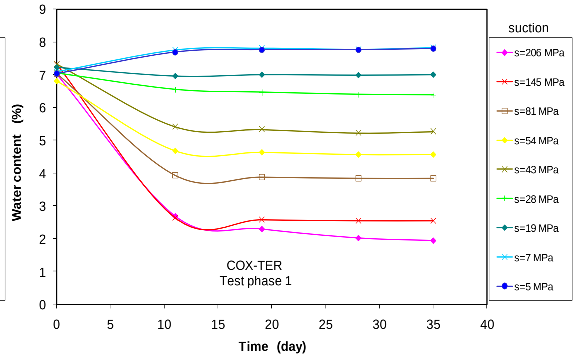


phase 1

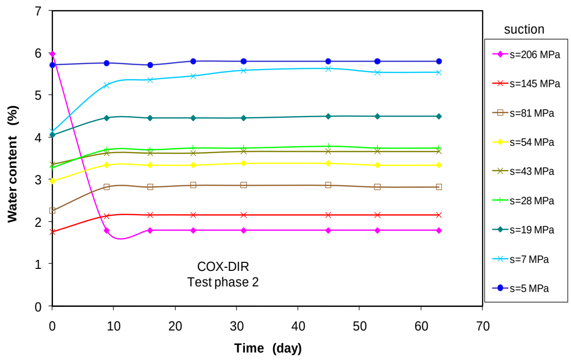


phase 2
COX-DIR samples
with clay content of ~12%

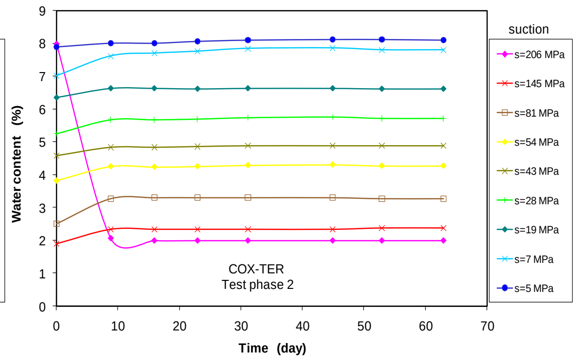


phase 2
COX-TER samples
with clay content of ~40%

**Fig. 2.26** Evolution of water content measured on COX samples with different clay contents at various suctions

Fig. 2.27 compares the water uptake of the COX and OPA claystone with different clay contents. It is interesting to see that in the wet environment at null suction, the claystone can take up large amounts of water of up to w = 14 % for the COX-TER with a clay content of c = 40 %, of w = 11 % for the COX-DIR with c = 12 %, and w = 18 % for the OPA with c = 65 % over 8 months during which equilibrium was not achieved. The higher the clay content, the more water is taken up. The water uptake is significantly higher than that of 6 % – 8 % in the natural confined state. This finding suggests that if not all, at least the pore water in the natural clays is bound on particle surfaces. Only the adsorbed water can be set free if high external loads and/or high temperatures are applied, for instance in case of extraction of pore water from claystone by squeezing the samples under high pressures or evaporation of pore-water by heating and drying.

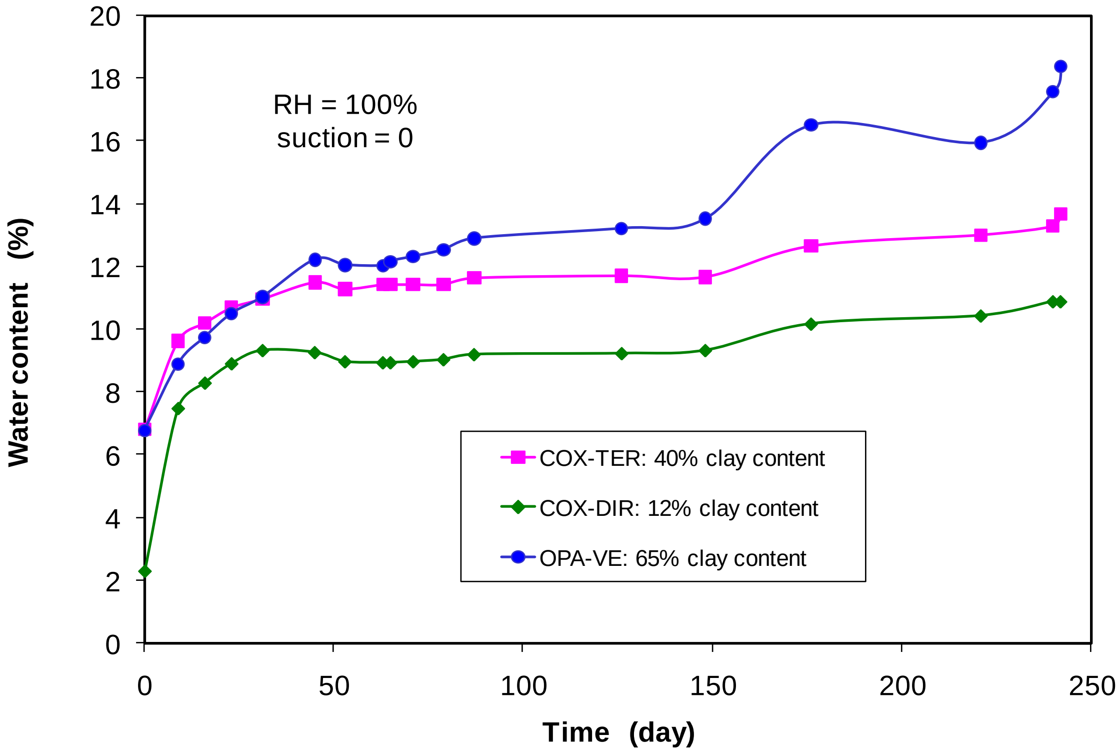


**Fig. 2.27** Evolution of water content measured on COX and OPA samples with different clay contents at zero suction

The equilibrium water contents reached at different suctions are summarized for the clay rocks in fig. 2.28. The degree of water saturation is calculated from the data according to eq. (2.7) and illustrated in fig. 2.29 as function of suction. Because of the negligible differences between the retention curves measured along the wetting and the drying paths, an average relationship between suction and the degree of saturation is established for each clay rock type. The parameters of the van Genuchten model (Eq. (2.10)) are summarized in tab. 2.3. The water retention curves of the studied claystone are close to each other. This indicates a minor dependency on the clay content.

**Tab. 2.3** Parameters of the water retention curves for the COX and OPA claystone

| Parameter | COX-DIR | COX-TER | OPA-VE |
|---|---:|---:|---:|
| Clay content (%) | ~12.0 | ~40.0 | ~65.0 |
| Porosity (%) | 13.0 | 15.2 | 15.0 |
| $P_o$ (MPa) | 28 | 50 | 23 |
| *ß* (-) | 0.37 | 0.5 | 0.4 |

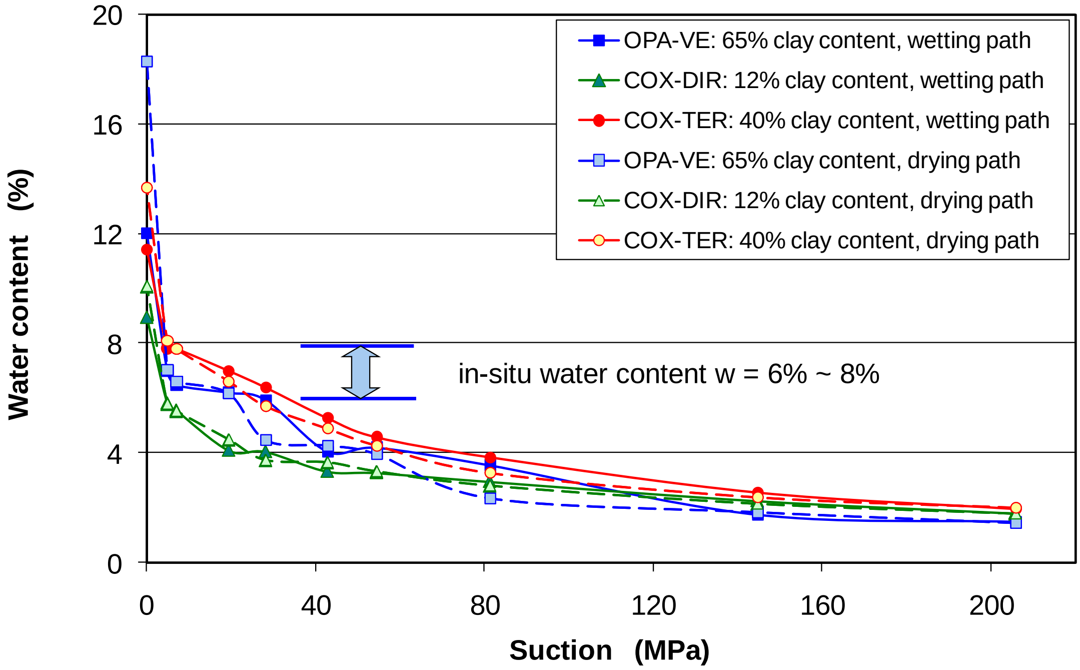


**Fig. 2.28** Equilibrium water contents of the COX and OPA claystone as a function of suction

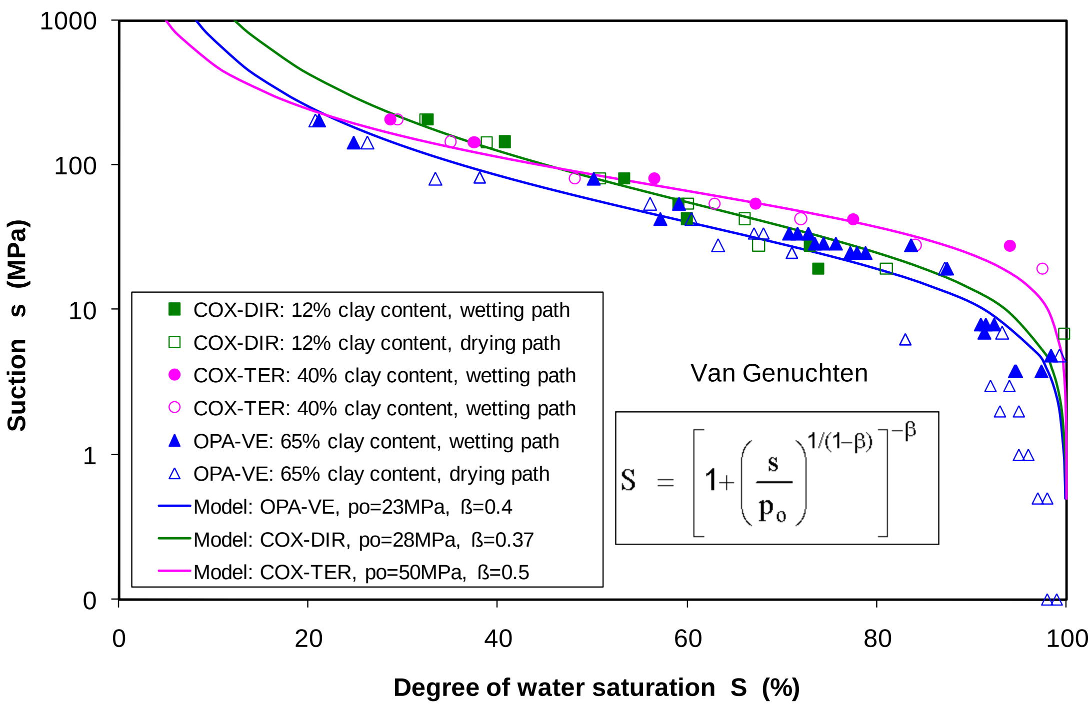


**Fig. 2.29** Suction-water saturation curves of the COX and OPA claystone

### 2.4.2 Swelling strain

Corresponding to the change in water content, the distance or pore space between solid particles changes too, resulting in macroscopic swelling or shrinking strains. The moisture effects on the deformation of the COX claystone were examined by wetting or drying unconstrained samples at various humidity conditions, during which the deformation and water content changes were recorded.

#### 2.4.2.1 Due to wetting with vapour

Fig. 2.30 illustrates the evolution of strains measured on COX-DIR and COX-TER samples at a low humidity of 23 % (suction s = 206 MPa) for two months and 100 % humidity (s = 0) for eight months, respectively. At the high suction applied externally, the adsorbed water evaporated and moved out the pores, indicated by the reduction of the water content. The release of the pore water as stress-supporting element resulted in a collapse of the pore structure and thus a macroscopic shrinkage. After reaching equilibrium during drying at RH = 23 %, the remaining water contents in both samples are nearly the same with 1.7 % and shrinkage is limited to $\varepsilon_v$ = 0.3 %. During the following wetting phase with water vapour at zero suction around the sample surface, the high suction potential of s = 206 MPa in the inner pores which had been induced by the previous drying drew water molecules into the pores. This increased the water content and hence the thickness of the water-films. As mentioned before, the COX claystone can take up great amounts of water of about 9 – 13 %, much more than that of 6 – 8 % in the natural and saturated state. The increase of the water content yielded a large volume expansion of up to 7 – 8 % for both samples. An even higher water uptake and volume expansion could be expected if the wetting would have continued until reaching equilibrium. Additionally, the swelling of the sedimentary claystone is anisotropic due to the bedding planes. A larger swelling strain occurred at the COX-DIR sample in axial direction and at COX-TER in radial direction perpendicular to the bedding plane. The anisotropic swelling was so strong that fracturing took place along the bedding planes in the COX-TER sample.

Regardless of the swelling anisotropy, the volumetric strains are calculated and plotted in fig. 2.31 as a function of the water content for the COX samples together with that of another OPA sample. It is evident that at a given water content in the unsaturated region, the volume increase attained by wetting is larger than that obtained by drying. After re-saturation, the claystone are still able to take up more water. The accompanying volume expansion is linearly proportional to the increase of the water content. If wetting continued, more expansion of the claystone could be expected.

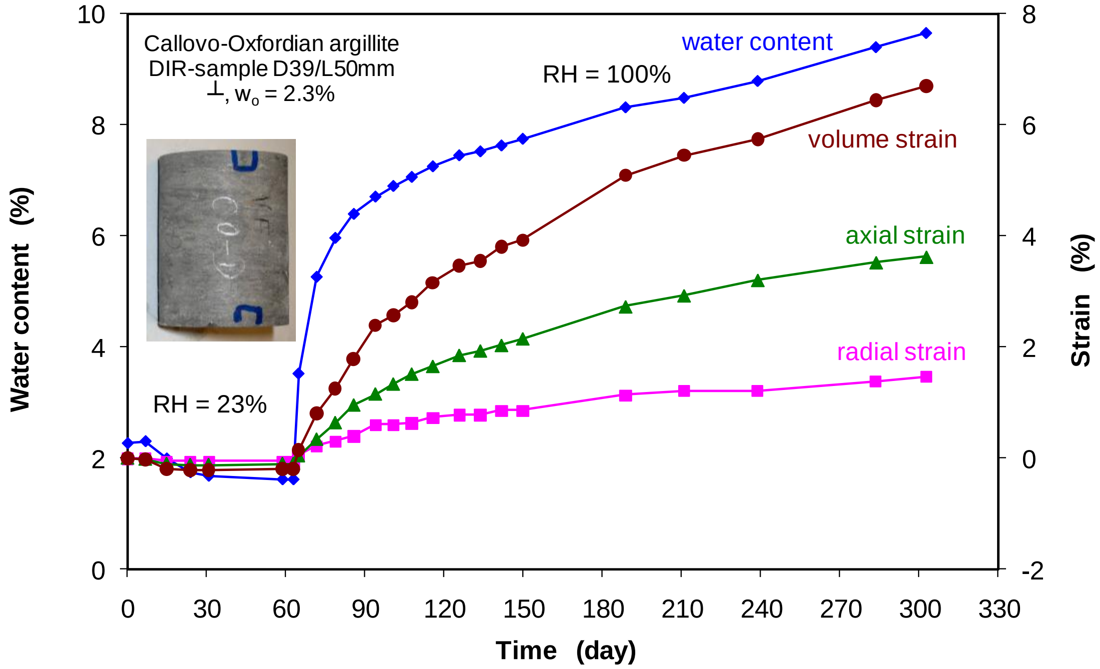


(a) COX-DIR sample with clay content of ~12 %

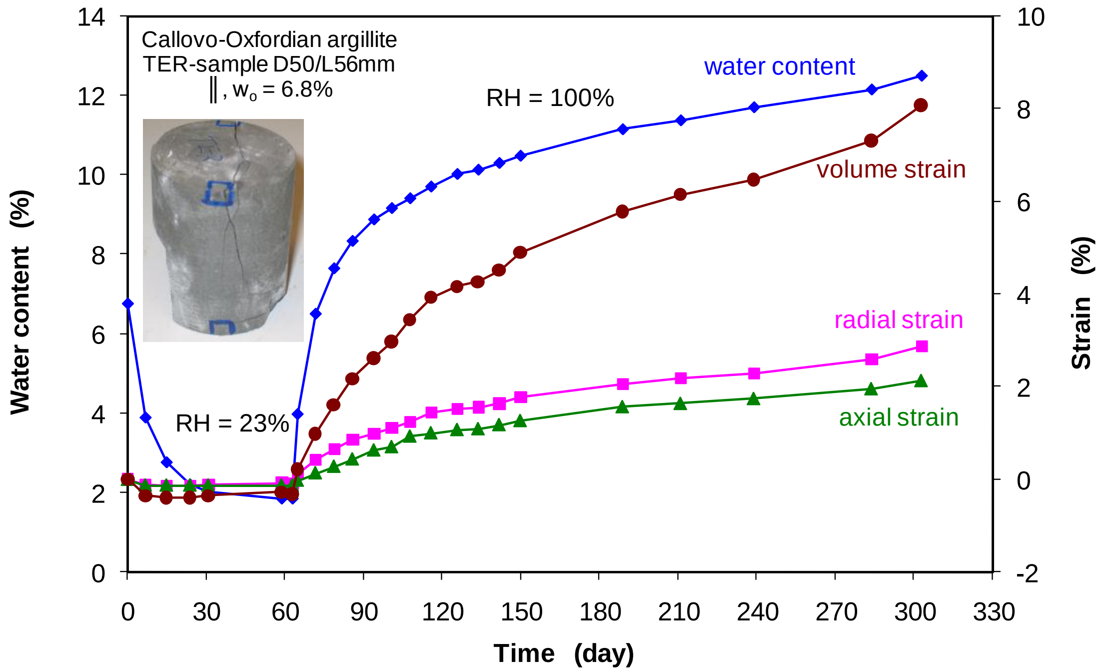


(b) COX-TER sample with clay content of ~40 %

**Fig. 2.30** Free swelling strains measured on COX samples at different humidity values

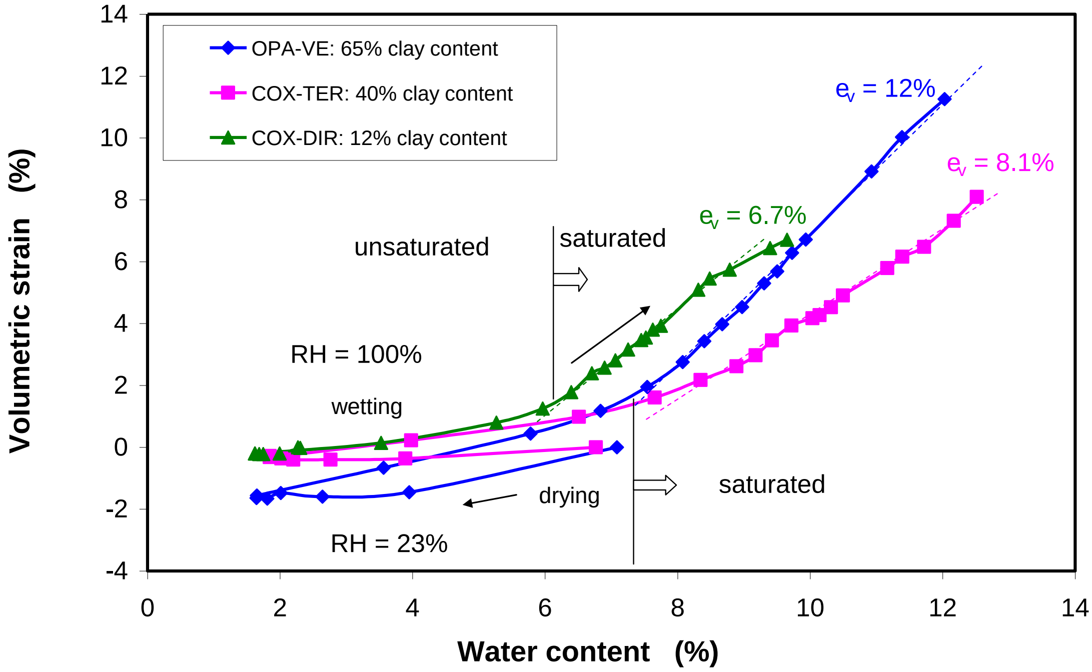


**Fig. 2.31** Volumetric strain as a function of water content during wetting and drying

### 2.4.2.2 Due to wetting with synthetic pore water

On another COX sample of 50 mm diameter and 10 mm thickness, axial swelling was measured in an oedometer cell by introducing synthetic pore water into the top and bottom at atmospheric pressure. The swelling curve is depicted in fig. 2.32. As the sample came into contacted with the water, a rapid expansion took place and then gradually increased with time over 4 months to 7 %. The swelling curve obtained during wetting with liquid water is quite similar to that observed during wetting with vapour (fig. 2.30).

The high swelling capability of the claystone was also confirmed by other tests under high confining stresses. Fig. 2.33 shows a triaxial swelling test on a COX sample EST21164 (D/L = 50/100 mm) under the original *in situ* lithostatic stress state at the sampling location of $\sigma_1$ = 15 MPa and $\sigma_2 = \sigma_3$ = 12 MPa. The *in situ* water pressure of $p_w$ = 4.5 MPa was applied by injecting synthetic pore water to both ends of the sample. The strain curves show that a continuous expansion rather than compression occurred in axial direction even though the sample was subjected to the high effective compressive stress of $\sigma_1 - p_w$ = 11.5 MPa in this direction. The gradual expansion suggests that the swelling potential (pressure) stored in the claystone is larger than the difference between the externally applied total stress and the water pressure. By subsequently elevating the temperature, the thickness of the adsorbed water-films reduces due to the thermally-induced desorption and evaporation of the water. In the drained condition applied during the test, the thermally-mobilized pore water was expelled from the sample under the confining stresses, causing compaction of the pores.

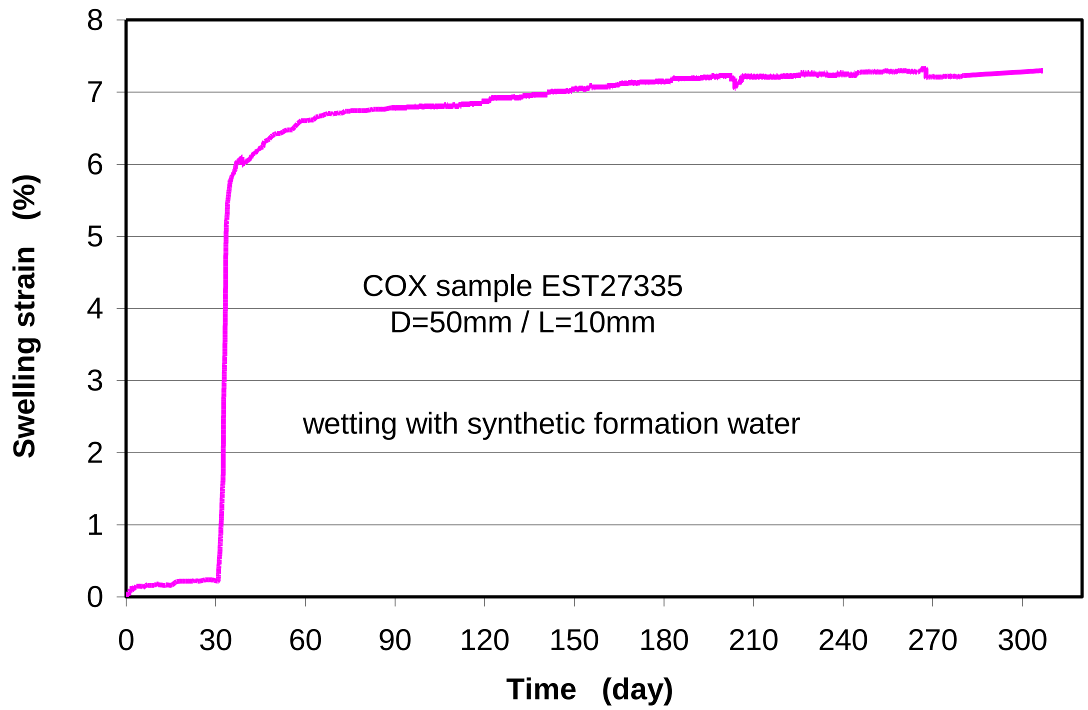


**Fig. 2.32** Axial free swelling strain measured on a COX sample with synthetic formation water

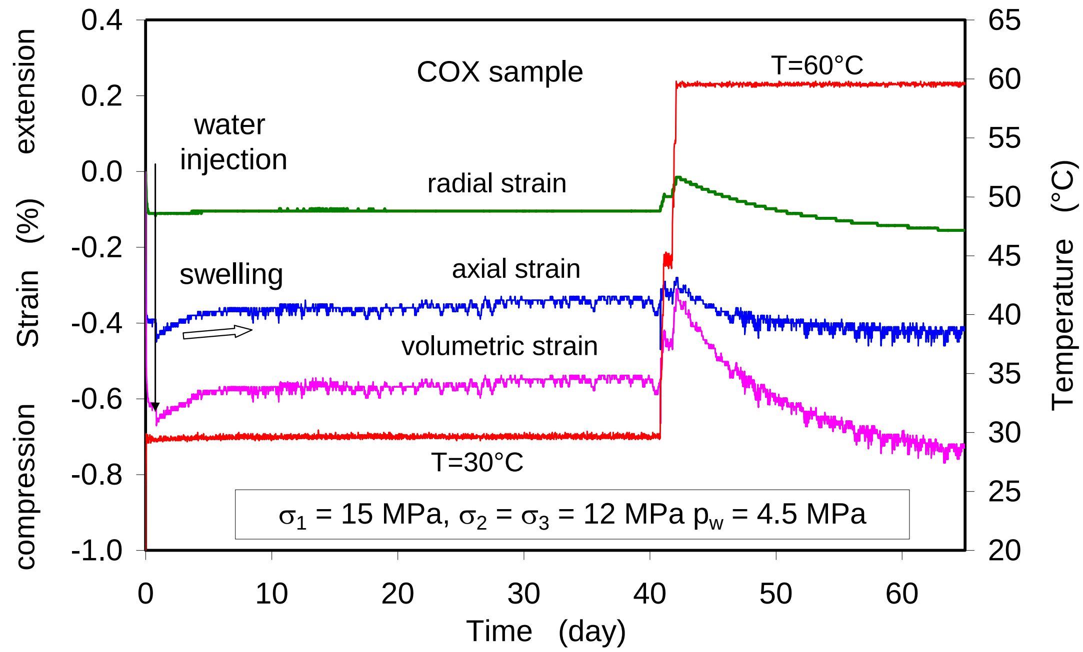


**Fig. 2.33** Swelling strains of a COX sample under high triaxial confining stress

### 2.4.3 Swelling pressure

Physico-chemical interactions of water with clay minerals cause adsorption of water on the internal and external surfaces of clay particles, forming electrostatic double-layers. In the narrow spaces between clay particles in compacted clays the double-layers are overlapping. This generates local swelling pressures in interparticle water-films when the volume of the clay is maintained constant by enclosing it in a rigid permeable box. This means also that the adsorbed water-films in the clay are carrying stress. If the clay is uncemented and behaves as perfect colloid, i. e. there are no direct bonds between solid particles, the total external stress and even the lithostatic stress is carried by the adsorbed water films. In this case, the swelling pressure $\overline{\Pi}_D$ is equivalent to the conventional isostatic effective stress $\sigma_{eff}$. According to /HOR 96/ and /ROD 99/, the total stress $\sigma$ in the clay-water-system can be expressed by

$$\sigma = \sigma_{eff} + (p_w - p_o) = \overline{\Pi}_D + (p_w - p_o) = \overline{\Pi}_D - p_c \qquad (2.11)$$

where $p_o$ represents the reference atmospheric pressure, $(p_w - p_o)$ the gauge pressure in the absence of osmotic effects, and $p_c = p_o - p_w$ the matric suction.

This so-called dense colloid model and the associated stress concept have been validated by measuring swelling pressures of the natural COX and OPA claystone with clay contents of more than 40 %. The major test results and theoretical analysis of stress in saturated clay are published in /ZHA 10b/. More details of the swelling pressure tests on COX and OPA samples are given below.

#### 2.4.3.1 Due to wetting with synthetic water in volume-constraint conditions

As usual, the conventional testing method was applied to measure the swelling pressure of a COX claystone sample in a swelling cell under volume-constraint conditions. Fig. 2.34 shows the schematic setup of the swelling cell in which a disk sample of 10 mm thickness and 50 mm diameter was inserted. The constrained sample was wetted from the top and the bottom first with water vapour at controlled humidity and then with synthetic pore water.

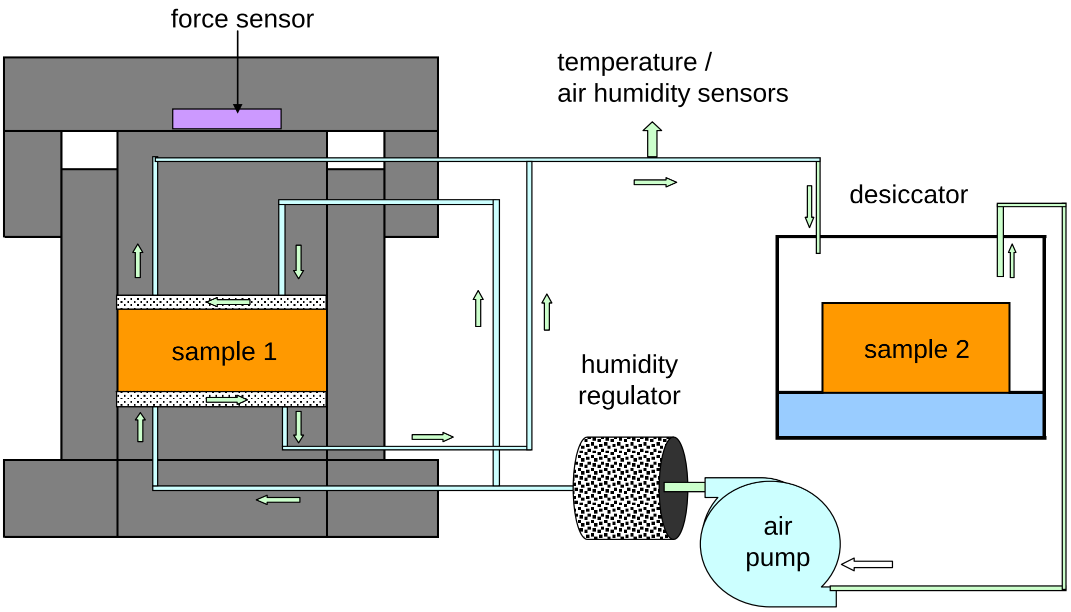


**Fig. 2.34** Schematic setup of a swelling cell for measurement of the swelling pressure of claystone with water vapour

Fig. 2.35 illustrates the evolution of swelling pressure measured on a partly-saturated COX sample with a clay content of ~40 %. The sample was pre-loaded to 0.5 MPa axially and then fixed. The first wetting was performed by circulating wetted air at a relative humidity of 90 with the axial stress rising up to ~1 MPa. The following wetting was performed by introducing synthetic pore water into the sample ends at atmospheric pressure. It gave a quick rise of the swelling pressure up to 2.5 MPa and then a gradual increase to 3.3 MPa over a time period of 4 months. Similar swelling pressure tests made by others on the same claystone provided lower values below 2 MPa /THU 99/, /LEB 00/. Obviously, these values are not comparable with the theoretical expectation, i. e. the swelling pressure should be close to the overburden stress of ~12 MPa at the sampling depth of 490 m. One reason for the measured low values of swelling pressure might be that the clay minerals close to the entering water expanded so highly that the local pore spaces were rapidly closed, making more water entering into the constraint samples more difficult or even impossible. Thus, the swelling pressure in the samples could not develop homogenously.

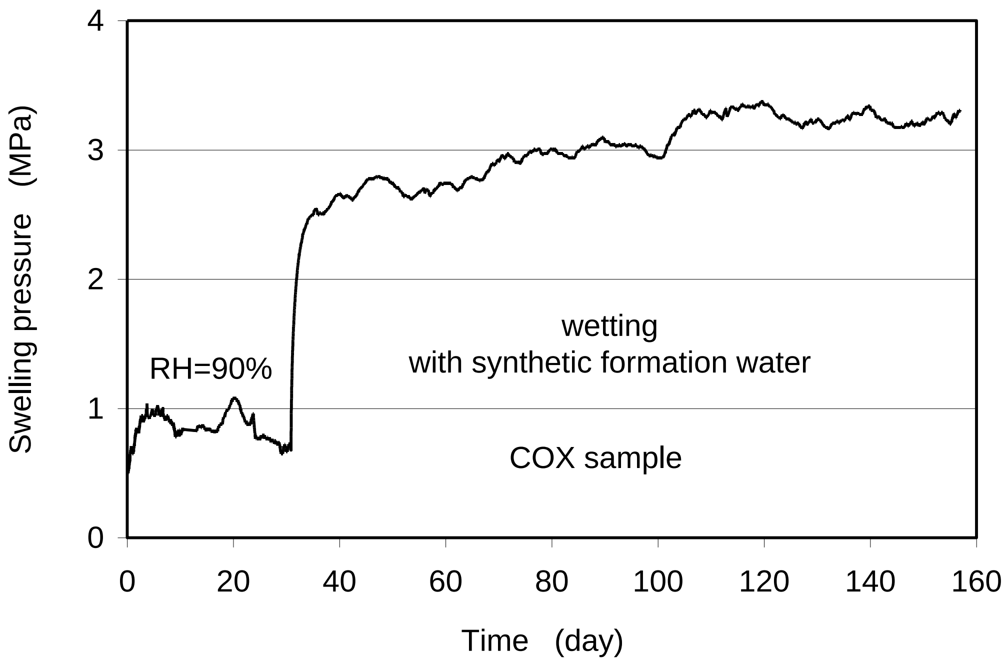


**Fig. 2.35** Swelling pressure measured on a COX sample in a cell with wetted air and synthetic water

#### 2.4.3.2 Due to wetting with water vapour in axially-fixed and laterally-unconstrained conditions

In order to minimize effects of rapid closure of the entry pores during wetting and to achieve a homogeneous distribution of the entering water within a sample, a new test method has been developed by the authors /ZHA 04b/, /ZHA 04c/, /ZHA 07b/ for the determination of the swelling pressure of hard claystone. Fig. 2.36 illustrates the principle of the so-called uniaxial swelling test. A clay sample is axially fixed and laterally unconstraint in a cell. It is believed that water vapour molecules can easily access and move deeply into the narrow pore spaces, so that re-hydration of the clay sample may be better achieved by circulating wetted air around the peripheral surface at controlled relative humidity or suction. Variation of the air humidity leads to changes in the water content and thus in the thickness of interparticle water-films, which determines the swelling pressure. A sufficiently high stiffness of hard claystone makes it possible to maintain its stability without any radial confinement. While the build-up of the swelling pressure in the sample is measured in axial direction by the reaction of the rigid piston, it is also possible to monitor the swelling strain in radial direction. The second sample is wetted through the same air circulating system outside the cell and serves to measure changes in the water content.

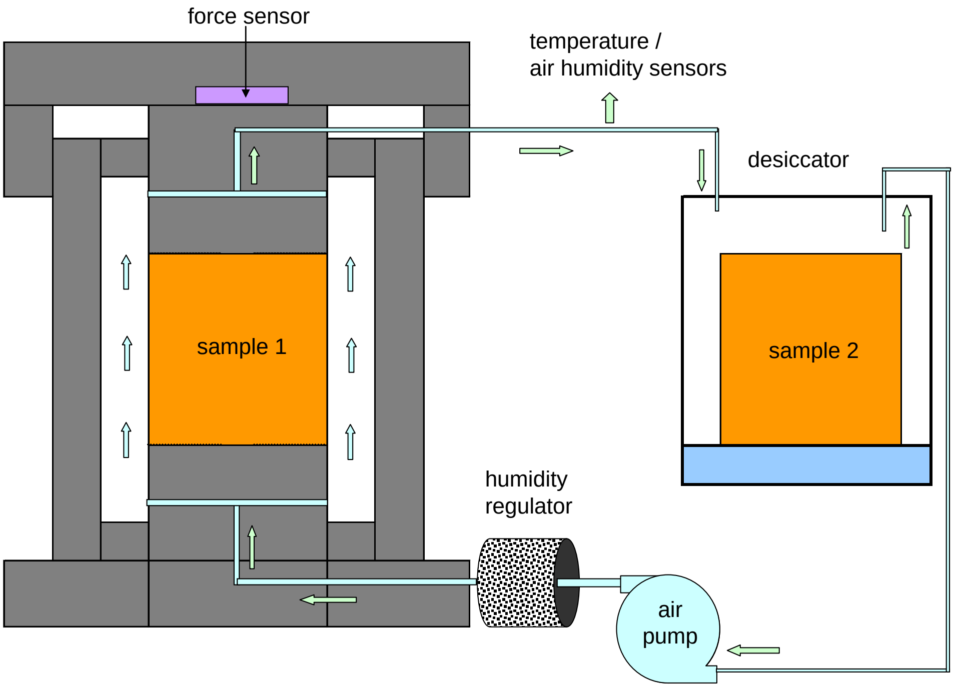


**Fig. 2.36** Principle of a uniaxial swelling test on claystone by wetting with water vapour

fig. 2.37 presents the results of the swelling pressure measurements on two COX samples with a clay content of ~40 %. The initial water contents were measured w = 7.3 % and 8.3 % at 105 °C over 48 hours. The samples were prepared to a size of 40 mm diameter and 50 mm length. They were axially pre-loaded to 2 MPa and then the axial strain was fixed. The data show that the circulating air of 80 % humidity caused a quick drop of the axial stress tending to zero due to the de-saturation. The subsequent increase in humidity led to the axial stress rapidly rising. At 95 % humidity, the reacting stress in axial direction against the rigid steel pistons reached a maximum of 10 – 10.5 MPa. In a previous test, wetting another COX sample with water vapour at 100 % humidity led to higher swelling pressures of 11 to 12 MPa /ZHA 04b/, /ZHA 04c/. These maximum values of swelling pressure are almost equal to the overburden stress of 12 MPa prevailing at the sampling position. This test result clearly confirms the theoretical stress concept for uncemented clay (Eq.(2.11)), $\sigma = \sigma_{eff} = \overline{\Pi}_D$ at $p_w = p_o$ or $p_c = 0$. This suggests also that the saturated claystone can be considered as a compacted colloid without direct bonds between solid grains. Because the studied claystone does not contain significant quantities of expansive clay minerals such as smectite of 13 – 23 % in the COX clay rock /TOU 07/, it seems possible that the swelling forces are developed between the external surfaces of closely-packed platy clay minerals such as illite

(3 – 20 %) by mechanisms which are similar to those operating during interlayer swelling /HOR 96/. The observed phenomenon of stress relief by drying and stress rising by wetting reflects that adsorbed interparticle water-films in the over-consolidated claystone support the externally-applied loads and even the lithostatic stress. Additionally, the build-up of swelling pressure in the fixed axial direction without any lateral confinement may suggest that the pressure acting in the water-films between clay platelets is probably not a scalar quantity and should be represented by a second-rank tensor /HOR 96/, /ROD 99/.

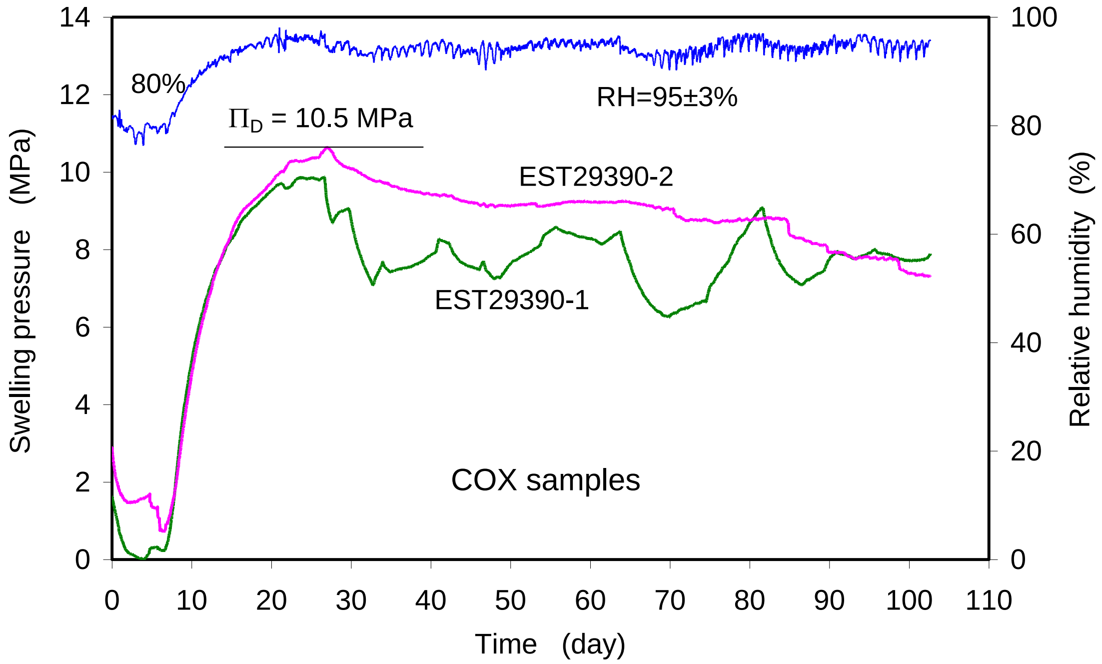


**Fig. 2.37** Evolution of uniaxial swelling pressures measured on COX samples as function of the humidity of the surrounding air

The similar stress response to moisture change was also observed on an OPA sample with a higher clay content of ~65 % (see fig. 2.38). The maximum swelling pressure of 5.5 MPa recorded is very close to the major lithostatic stress of 6 – 7 MPa at the sampling position in the MT-URL /BOS 03/. The so-called dense clay-colloid model with the associated stress concept mentioned above is also confirmed by the Opalinus claystone. But this model seems to be unsuitable for natural clay rocks with low clay contents. This is shown by the low swelling pressure recorded on the COX sample with a small clay component of ~12 % (see fig. 2.38). One the other hand, the pressure decrease during wetting may be due to the reduction of the stiffness.

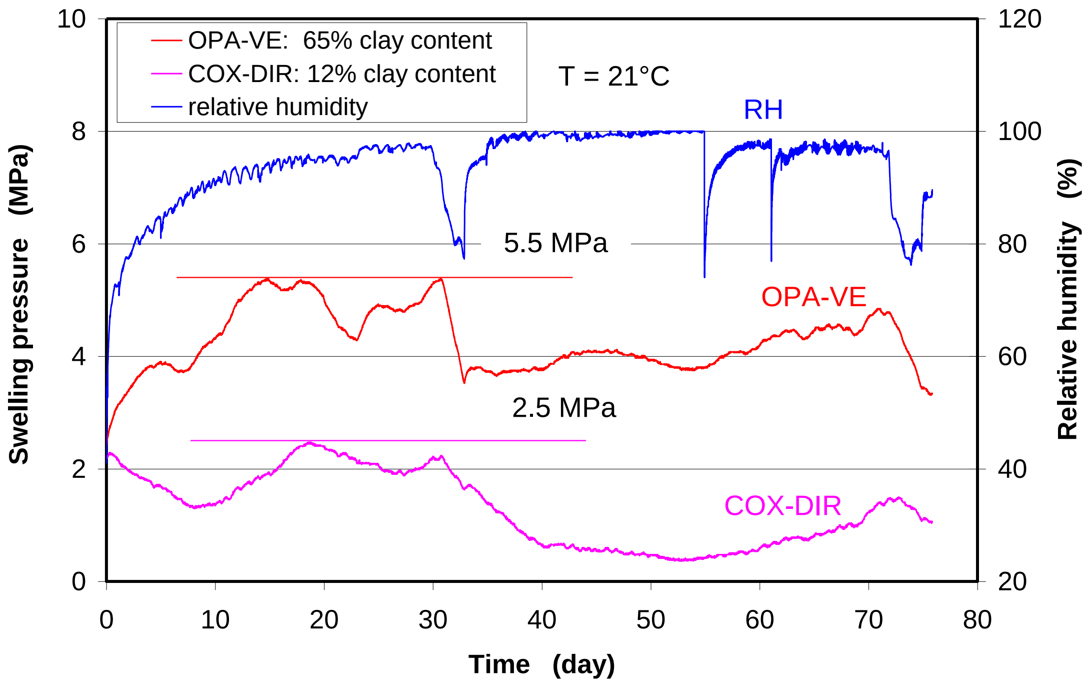


**Fig. 2.38** Evolution of uniaxial swelling pressures with humidity changes obtained on OPA sample with ~65 % clay content and COX sample with ~12 % clay content

### 2.4.4 Conclusions on the swelling behaviour

From the measurements of water adsorption / desorption, swelling strain and pressure on the COX and OPA claystone at different suction- and load-controlled conditions, the following conclusions can be drawn:

- The studied claystone exhibit high adsorption potentials, under which a great amount of water can be taken up from the humid environment to water contents of 10 – 18 % in unconstrained conditions, about two to three times that in the naturally-confined and saturated rock mass. The higher the clay content, the higher is the water adsorption potential.

- The water uptake enlarges the distance or pore space between solid particles, resulting in swelling. The claystone in unconstrained and humid conditions can expand largely up to 8 – 12 %. Because of the sedimentary structure, the swelling strain is more significant in direction perpendicular to bedding plane and even fractures appear along the weak plane. The higher the clay content, the larger the swelling strain.

- The adsorbed water-films in the claystone are capable of bearing externally applied loads and even carrying the lithostatic stress, as indicated by the measured swelling pressures up to 10 – 12 MPa on COX samples with a clay content of ~40 % from the depth of 490 m and 5.5 MPa on OPA samples with a clay content of ~65 % from the depth of 230 m, respectively. This conclusion is also supported by the swelling strain observed on a COX sample at the stress state at the MHM-URL with high confining stresses of 12 – 15 MPa and pore pressure of 4.5 MPa.
- Conversely, a dry condition causes evaporation of pore water and release of the stress-supporting elements, leading to collapse of the pore structure. The macroscopic shrinkage increases with decreasing moisture, but is limited to 0.3 % at COX to 1.7 % at OPA claystone in a dry condition of 23 % air humidity. A more clay content results in a larger shrinkage.
- The saturated claystone with clay contents of more than 40 % seemed to behave as compacted colloid without direct bonds between solid particles. Consequently, the swelling pressure acting in interparticle water-films is equal to the effective stress (total external stress minus free pore water pressure). This so-called dense clay-colloid model may be helpful to improve the understanding and modelling of strongly-coupled hydro-mechanical processes in natural clay rocks and engineered clay barriers, such as water and gas transport, rheological deformation, self-sealing and healing of fractures, etc.

## 2.5 Permeability

Excavation of an underground repository produces a damaged zone with fractures around the openings. The permeability of the damaged zone may increase so significantly that the barrier function of the host rock against radionuclide migration will be affected. After backfilling and closing of the repository in an argillaceous formation, however, a self-sealing process of the fractures can be expected due to the combined impact of viscous rock deformation, backfill support, and the swelling of clay minerals in the clay rock and the clay-based backfill during the long lasting post-closure period of time. The sealing process is determined by the deformability and swelling capacity of the host rock and the backfill as well as by the boundary conditions (rock deformation rate, availability of water, temperature etc.). The damage and sealing of clay rocks was investigated in the frame of EC projects such as SELFRAC /DAV 03/ and NFPRO /ZHA 08a/, /ZHA 08b/, /ZHA 08c/. However, very limited data are available, particularly for the permeability behaviour related to damage and re-compaction. In order to enhance the knowledge about this issue, a series of combined damage and re-compaction experiments was performed by gas flow tests on COX samples under various confining stresses. The major results are published in /ZHA 08b/, /ZHA 09b/.

### 2.5.1 Permeability of undisturbed claystone

First of all, the permeability of the intact clay rock was determined on core samples from the borehole PPA35 drilled horizontally from the wall of the main shaft at a depth of ~480 m and oriented towards the direction of the horizontal major stress (~N150°). Totally, 12 hollow cylindrical samples were prepared to a size of 80 mm diameter and 150 mm length with a thin central hole of 5 mm diameter for permeability measurements. The basic properties of the samples were determined on a core (Tab. 2.2): porosity $\phi$ = 14.9 %, water content $w$ = 6.1 % and degree of water saturation $S_l$ = 94.2 %. Fig. 2.39 shows the principle of the permeability tests on the hollow cylinders. The samples were inserted into rubber jackets of 100 mm diameter. The central hole and the annular gap between sample and jacket were filled with fine-grained quartz sand. The hole was linked to the inlet line while the gap was connected to the outlet via the porous disc at the bottom. A testing apparatus with an oil pressure vessel was used, which allows simultaneous measurements of permeability on four samples at injection pressures of up to 10 MPa under a confining stress of up to 25 MPa. In case of the tests reported here, the samples were confined at constant hydrostatic stress of 2.2 MPa. Nitrogen gas was introduced into the central hole at a pressure of 1.6 MPa. Before injection, the gas was wetted through a water bath in order to avoid artificial drying. The outflow was measured at the outlet by means of partially water-filled burettes. Based on the measurements, the gas permeability in radial direction of the hollow cylinder can be calculated according to Darcy's law for compressive media:

$$\mathrm{k_g} = \frac{\mathrm{q_g} \cdot \mu_g \cdot \mathrm{p_0}}{\pi \cdot L \cdot (\mathrm{p_1^2} - \mathrm{p_0^2})} \ln \frac{r_1}{r_2} \qquad (2.12)$$

where $\mathrm{k_g}$ = the effective gas permeability ($m^2$),

$\mathrm{q_g}$ = the flow rate of the gas ($m^3/s$),

$\mu_g$ = the gas dynamic viscosity (Pa·s),

$L$ = the length of the sample (m),

$\mathrm{p_o}$ = the atmospheric pressure (Pa),

$p_1$ = the gas injection pressure (Pa),

$r_1$ = the inner radius (m), and

$r_2$ = the outer radius (m).

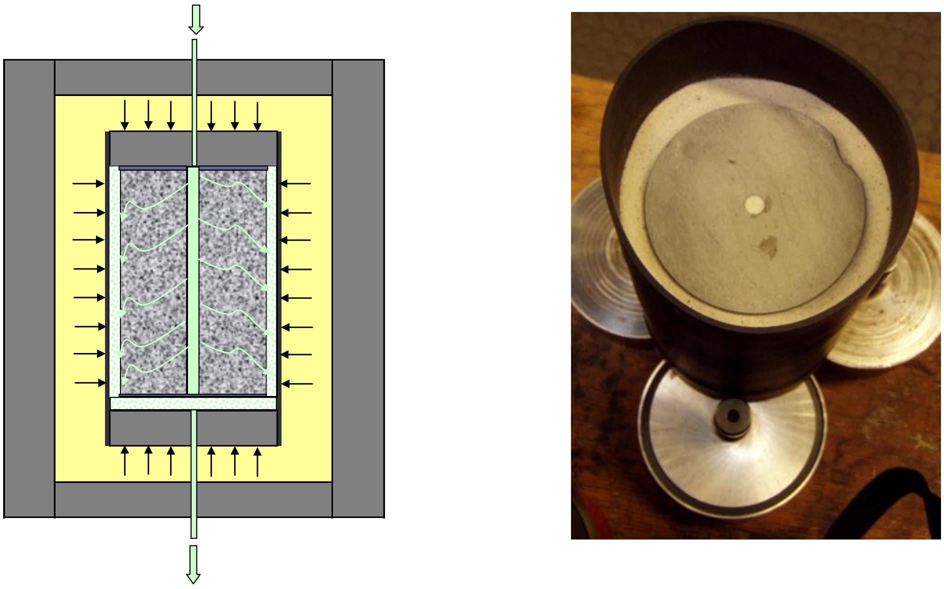

**Fig. 2.39** Principle of a permeability measurement on a hollow cylindrical sample

Fig. 2.40 summarizes the evolution of the measured permeability data for all the samples. The permeability values varied more or less during the first 10 to 20 days and then maintained relatively constant over time periods of 10 to 40 days. Most of the samples showed a very low permeability of $10^{-21}$ to $10^{-20}$ $m^2$, except for two samples showing relatively high values of $10^{-18}$ to $10^{-17}$ $m^2$. These two samples might be strongly damaged by the preparation. The data obtained during the last periods are depicted in fig. 2.41 as function of the distance to the shaft wall. As mentioned before, except for the two damaged samples, the permeability data obtained on the other less disturbed samples from the different locations are quite close to each other. It is, however, questionable if one can conclude from the measurements on the small sized samples that the shaft excavation did not produce damage and hydraulic pathway in the surrounding rock, in which fractures are often generated by excavation.

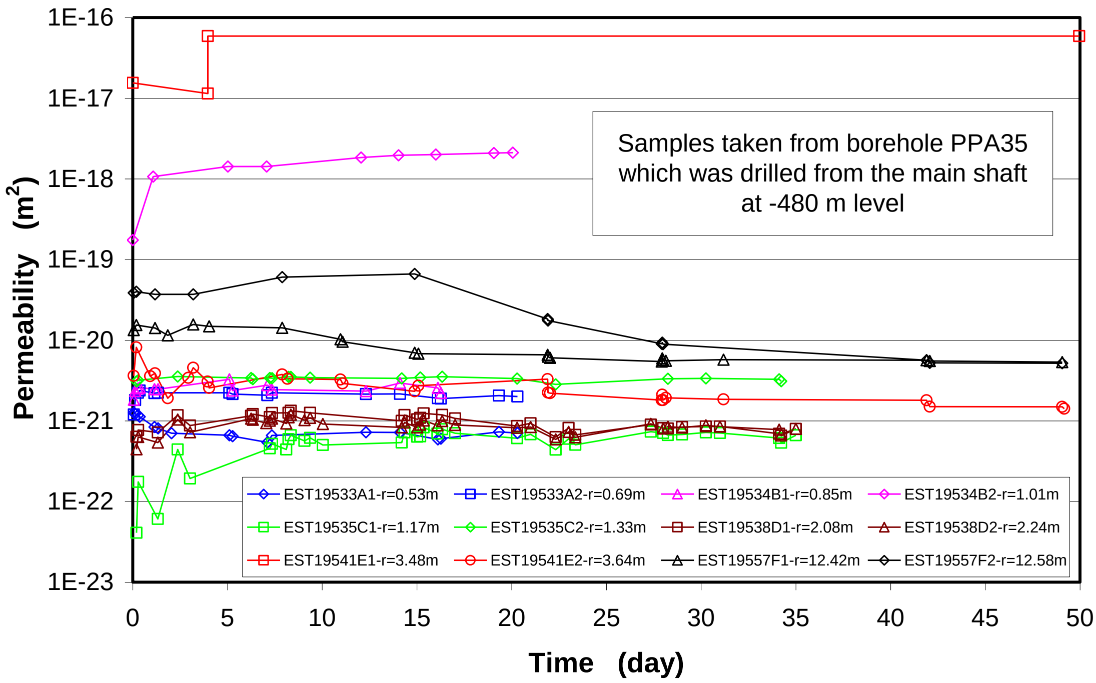


**Fig. 2.40** Results of gas permeability measurements on COX samples

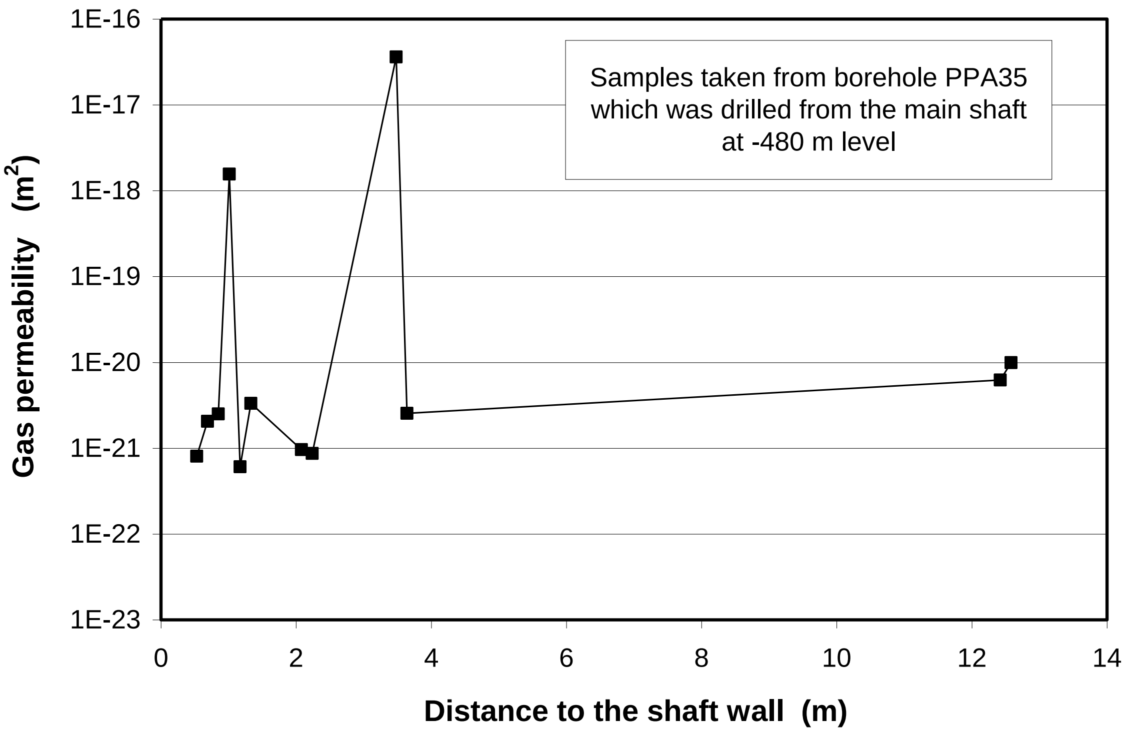


**Fig. 2.41** Gas permeability of the COX claystone as a function of the distance to the shaft wall

### 2.5.2 Permeability changes due to damage

Permeability changes induced by damage and re-compaction were investigated on COX samples from borehole REP2206 drilled vertically from the floor of the -445 m niche to a depth of 467 m. The characteristics of the samples are given in tab. 2.2. In order to generate fractures which intersect both sample end faces, the 79mm-diameter samples were prepared to a length of 80 – 115 mm. Thus, the length / diameter ratio of 1.0 to 1.5 was smaller than the standard ratio of 2 usually applied in strength tests.

The tests were carried out on seven samples in a triaxial apparatus with measurements of deformation and gas permeability under various stress conditions. Fig. 2.42 illustrates schematically the assembly of a sample in a triaxial cell. The sample was isolated in a jacket and porous discs at its top and bottom. The annular gap between sample and jacket was sealed with silicon to avoid any leakage. Considering the possible development of an excavation damaged zone around underground openings, a test procedure consisting of damage and re-compaction was applied to each sample at an ambient temperature of 25 °C. Each sample was first loaded to an isotropic stress in a range of 2 to 10 MPa and then, keeping the radial stress constant, the axial stress was increased either at stress rates of $1\cdot10^{-5}$ to $1\cdot10^{-4}$ MPa/s or comparable strain rates of $2\cdot10^{-8}$ to $8\cdot10^{-8}$ $s^{-1}$ to failure. Thereafter, the samples were re-compacted again to examine permeability changes at various mechanical loads. During the tests, the axial strain was measured by a LVDT-transducer installed outside of the cell. The volumetric strain was determined both directly from the volume change of the confining oil in the cell by using a pressure/volume GDS-controller and indirectly by strain gauges attached to the sample surface at its mid height. Permeability changes induced by the mechanical loading were measured along the sample axis by injecting dry nitrogen gas to the bottom at constant pressure of p = 1 MPa and recording the outflow at the opposite side. The gas outflow was continuously recorded by using a burette. During steady state gas flow, the permeability along the sample axis is determined according to Darcy's law for compressive media:

$$k_g = \frac{2 \cdot q_g \cdot \mu_g \cdot p_0 \cdot L}{A \cdot (p_1^2 - p_0^2)} \tag{2.13}$$

where L is the length (m) and A is the cross section of the sample ($m^2$). The meanings of the other symbols are given in eq. (2.12).

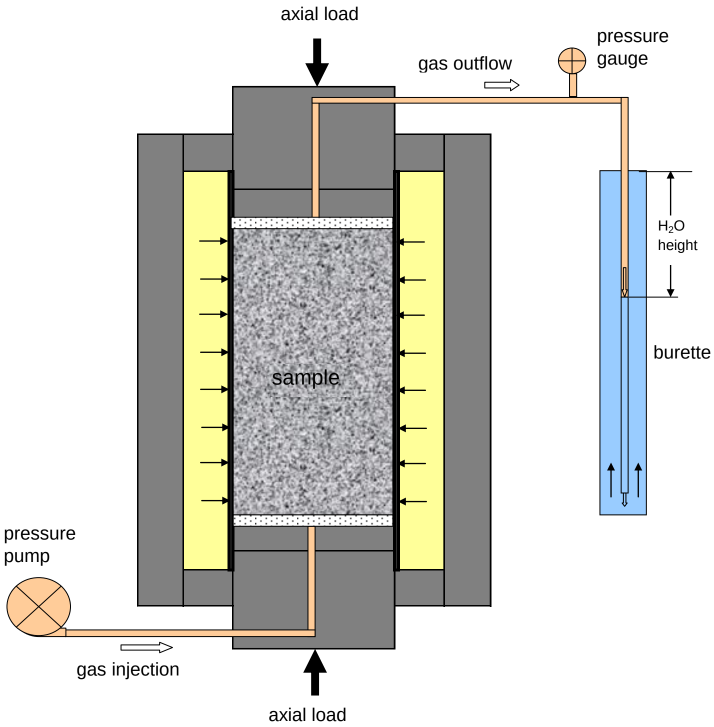


**Fig. 2.42** Schematic of the triaxial compression tests with permeability measurement

A typical example of the combined damaging – sealing tests is illustrated in fig. 2.43 in terms of the applied axial / radial stresses, measured axial strain and gas permeability over time. Fig. 2.44 presents typical deformation and permeability responses to deviatoric loading applied to two samples at a radial confining stress of $\sigma_2 = \sigma_3 = 4$ MPa and 8 MPa, respectively. Both samples showed a similar stress-strain behaviour. The deviatoric stressing led to a linear elastic compression until yielding. The pre-existing cracks created by coring and preparation were closed thus decreasing the permeability to some degree due to elastic compression. Following yielding, the volumetric strain turned to increase. Dilatancy onset and yielding stress seemed to be consistent. As the deviatoric stress increased, dilatancy developed progressively due to micro-fracture opening and growth resulting in an increase in permeability. But beyond the dilatant point, the increase rate is insignificant up to the point of the so-called percolation threshold. At this point, the permeability increase was accelerated, indicating coalescence of the micro-fractures and creation of macro-fractures. Further loading over this point caused a rapid propagation and connection of the fractures. Consequently, the permeability of sample EST21156 jumped up from $2 \cdot 10^{-22}$ m$^2$ to $1 \cdot 10^{-18}$ m$^2$. On sample EST21160, however, no significant change in permeability was observed just before failure. At failure, the shear fracturing developed very quickly, resulting in large axial strains of ~17 % and ~8 %, respectively. The strongly fractured sample EST21156 was then re-stabilized by increasing the radial stress to 10 MPa. The radial compression reduced the permeability from $1{\cdot}10^{-18}$ $m^2$ to $3{\cdot}10^{-19}$ $m^2$. The subsequent stress relaxation did not result in a significant permeability change. On another sample EST21160 at a higher confining stress of 8 MPa, the permeability increase during the post-failure phase was not very significant.

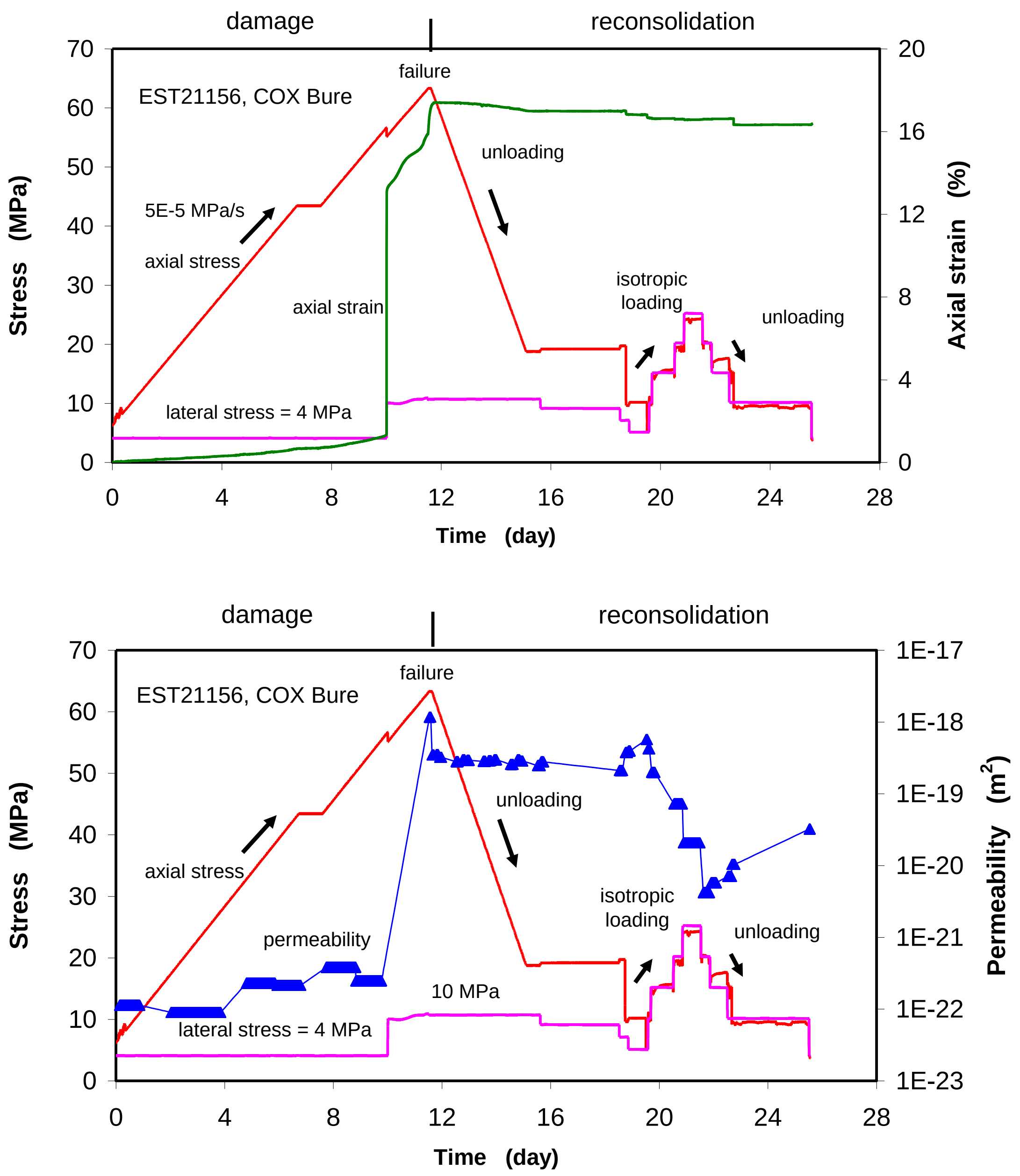


**Fig. 2.43** Measurement of stress/strain/permeability during a combined damaging-sealing test on a COX sample

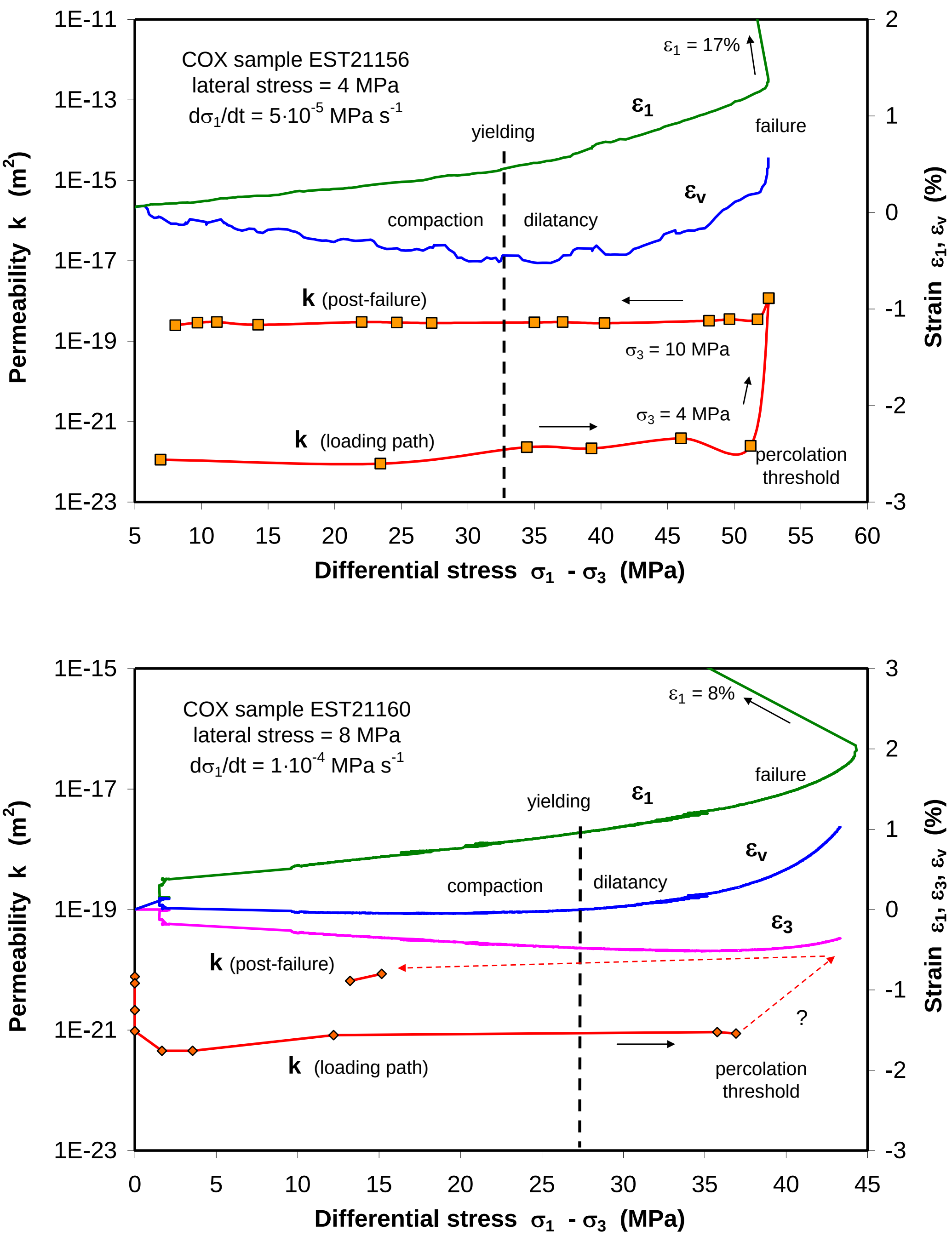


**Fig. 2.44** Responses of deformation and permeability to deviatoric loading

The results of permeability measurements on the other samples which were also loaded over failure are summarized in fig. 2.45. The samples showed very low initial permeability values ranging between $10^{-22}$ and $10^{-21}$ $m^2$. The permeability changes due to deviatoric loading are insignificant below the percolation threshold. Due to the different initial states of the samples, the influence of radial stress on the magnitude of axial permeability could not be identified. Beyond the percolation threshold, the permeability increases quickly. Because the created fractures differ from one sample to another (fig. 2.47), the maximum permeability at failure ranges from $10^{-21}$ to $10^{-18}$ $m^2$, which is up to four orders of magnitude higher than below the percolation threshold. At a high radial stress of 10 MPa, no clear increase in permeability was observed even though the failure strength was exceeded.

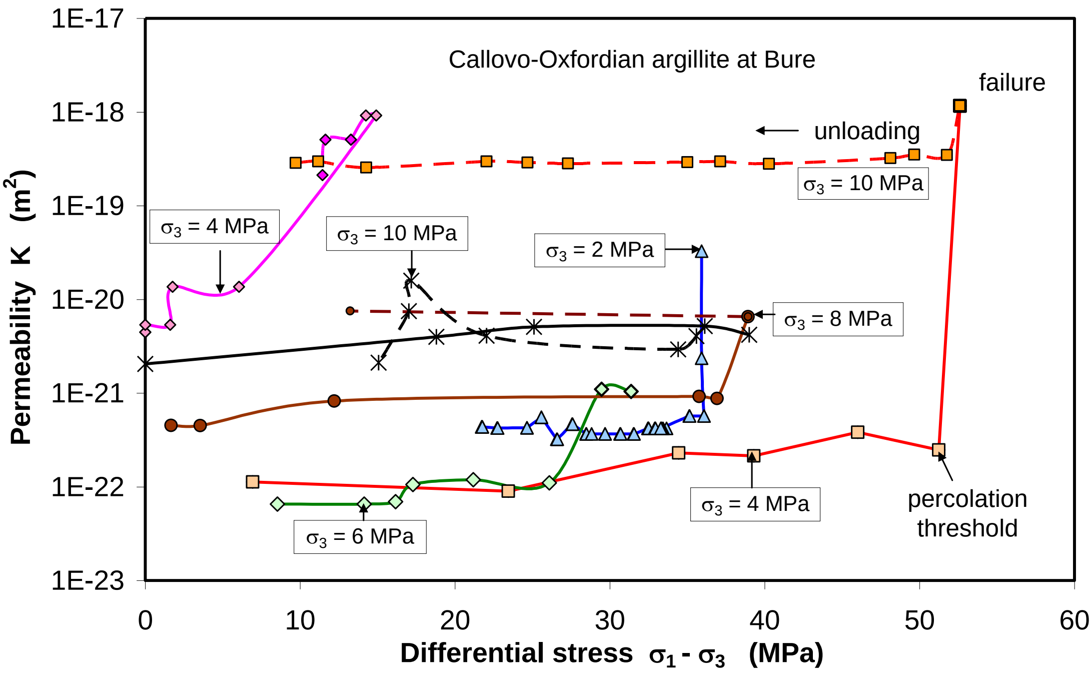


**Fig. 2.45** Permeability measured on COX samples as a function of deviatoric stress at different lateral confining stresses

The damage-induced permeability is very dependent on geometry, connectivity and orientation of the fractures. Fig. 2.47 shows pictures of the damaged samples after testing. Mapping of the true opening width of the fractures under loaded conditions was not possible. Multiple shear macro-fractures were developed obliquely to the direction of axial stress and gas injection at angles of 30° – 50° which intersected both sample end faces. Two major families of cracks were observed which intersected at angles of 50° – 70°. At a low radial stress of 2 to 4 MPa, more cracks were created than at a high radial stress of 6 to 10 MPa. The stress-rate controlled loading caused a sudden shear failure. The axial strain reached just after the peak strength varies between 14 % and 22 %, which is larger than that of 8 % to 10 % observed at strain-rate controlled loading. Generally, the laboratory observation that the damage intensity and the resulting permeability decrease under confining stress agrees with the in situ situation that the intensity and the interconnectivity of individual fractures in the EDZ decreases from the opening walls with low confining stresses into the rock mass with higher confining stresses. However, a most important question whether the test data obtained on small-scale samples are transferable to the large-scale in situ EDZ remains still to be answered.

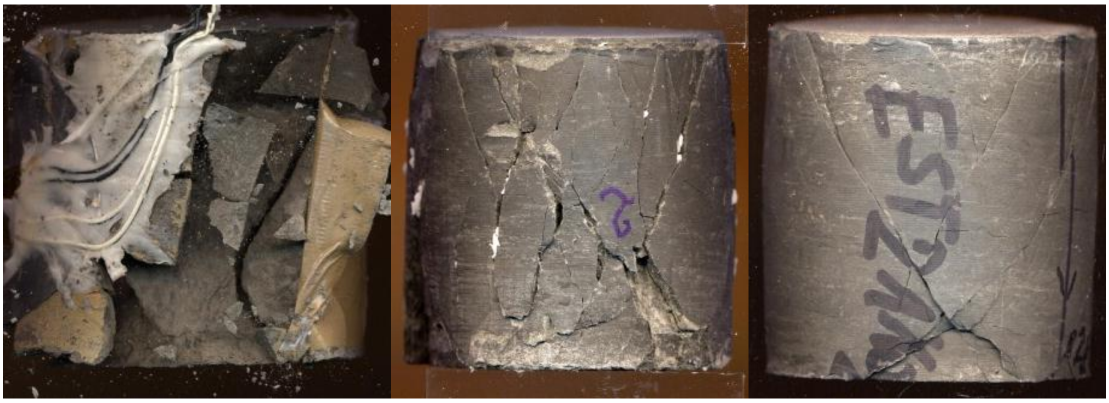

| | | |
|---|---|---|
| EST22173 | EST21166 | EST21156 |
| $\sigma_3$=2MPa, $\sigma_1$=50MPa | $\sigma_3$=2MPa, $\sigma_1$=38MPa | $\sigma_3$=4MPa, $\sigma_1$=57MPa |
| $\varepsilon_1 \approx 10\%$, $8 \cdot 10^{-8}\,s^{-1}$ | $\varepsilon_1 \approx 22\%$, $5 \cdot 10^{-5}$MPa/s | $\varepsilon_1 \approx 17\%$, $1 \cdot 10^{-5}$MPa/s |

| | | |
|---|---|---|
| EST21162 | EST21160 | EST21168 |
| $\sigma_3$=6MPa, $\sigma_1$=36MPa | $\sigma_3$=8MPa, $\sigma_1$=55MPa | $\sigma_3$=10MPa, $\sigma_1$=51MPa |
| $\varepsilon_1 \approx 14\%$, $1 \cdot 10^{-4}$MPa/s | $\varepsilon_1 \approx 8\%$, $3 \cdot 10^{-8}\,s^{-1}$ | $\varepsilon_1 \approx 8\%$, $4 \cdot 10^{-8}\,s^{-1}$ |

**Fig. 2.46 Photographs of macro-fractures in COX samples after failure**

It is also interesting to note that the percolation threshold of the samples is far beyond the dilatancy onset stress, but close to the failure strength. The dilatancy onset $\sigma_D$ detected from the volumetric strain data varies widely from 70 % to 98 % of the failure strength $\sigma_F$. Similar results were obtained on OPA samples by volumetric strain measurements /NAU 07/. Moreover, lower dilatancy onset stresses were detected by measurements of shear and longitudinal wave velocities in a range from 60 % to 80 % of the failure strength /POP 07/. The ratio $R_D = \sigma_D / \sigma_F$ is relatively constant. The dilatancy point is a criterion to identify whether the clay rock deforms with generation and propagation of micro- and macro-fractures or not. If the fractures are interconnected, a pathway for fluid flow is built up. The corresponding percolation threshold stress $\sigma_P$ which was detected by the permeability measurement is 90 % to 100 % of the failure strength.

Assuming the ratios of dilatancy and percolation threshold to failure strength as constant and taking the lower limit values of $R_D = \sigma_D / \sigma_F = 0.7$ and $R_P = \sigma_P / \sigma_F = 0.9$, a modified damage concept may be preliminarily established for the studied COX claystone. An average failure boundary has been determined on the database but with a relatively large scatter /AND 05/, as expressed by the Hoek-Brown model:

$$\sigma_{1-F} = \sigma_3 + (m \cdot \sigma_c \cdot \sigma_3 + s\sigma_c^2)^{1/2} \qquad (2.14)$$

where the uniaxial compression strength $\sigma_c$ = 25 MPa, the parameter $m$ = 2.5, and $s$ = 1 were estimated by /ZHA 02/, /ZHA 04a/. The data scatter is mostly caused by the different sample quality and the variation in mineral content (particularly clay and carbonates) and pore-water content.

The dilatancy and percolation boundaries may be approached by

$$\sigma_{1-D} = R_D \cdot \sigma_{1-F} = 0.7 \cdot \left[\sigma_3 + (m \cdot \sigma_c \cdot \sigma_3 + s\sigma_c^2)^{1/2}\right] \qquad (2.15$$

$$\sigma_{1-P} = R_P \cdot \sigma_{1-F} = 0.9 \cdot \left[\sigma_3 + (m \cdot \sigma_c \cdot \sigma_3 + s\sigma_c^2)^{1/2}\right] \qquad (2.16)$$

These preliminary boundaries for the studied COX rock are illustrated in fig. 2.48 showing limited data of the dilatancy and percolation thresholds. Stress induced damage and associated effects can be identified in this stress diagram. Below the dilatancy boundary, loading leads to compaction and closure of pre-existing micro-cracks. Between the dilatancy and the percolation boundary, loading gives rise to the generation and propagation of local micro-fractures, which are not completely interconnected yet. Thus, the permeability increase is still insignificant. Above the percolation boundary, loading enhances the propagation and connectivity of micro-fractures thus forming macro-fractures. Macro-fracture growth leads to a drastic increase in permeability to a maximum value at failure. In the post-failure phase after stress relaxation, the fractures may extend further, but geometry changes probably just cause a minor increase in permeability. It has to be pointed out that further experiments are needed to provide high quality data for precise determination of the damage evolution and the ctritical boundaries. Additionally, other relevant influencing factors have to be taken into account for an improvement of the damage criteria, such as material anisotropy, long-term deformation, de- / re-hydration, temperature, and scale-effect.

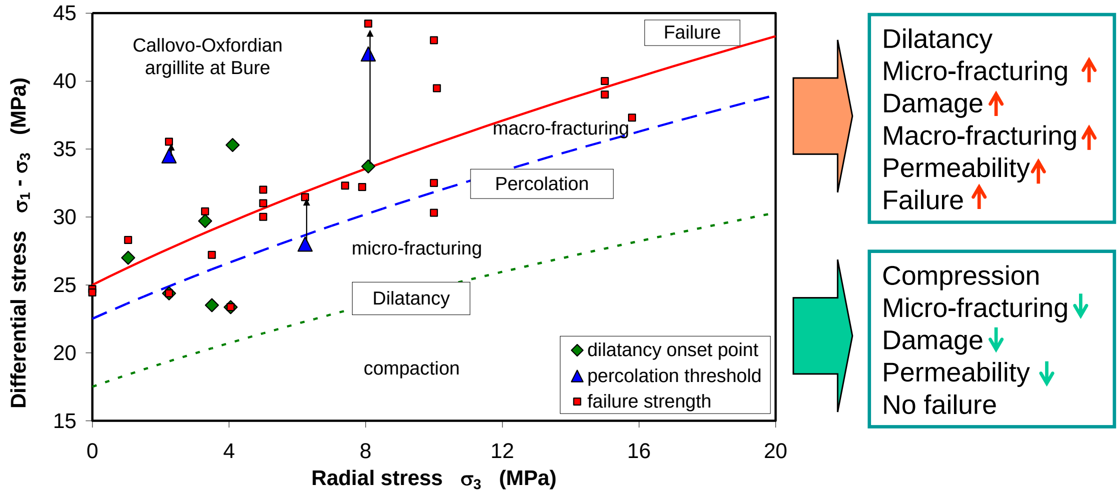


**Fig. 2.47** Preliminary dilatancy, percolation, and failure boundaries for the COX clay rock

### 2.5.3 Permeability changes by re-compaction

The COX samples with shear fractures (fig. 2.47) were re-compacted by application of different loading paths: a) isotropic loading by simultaneously increasing axial and radial stress $\sigma_1 = \sigma_2 = \sigma_3$, or b) deviatoric loading by increasing $\sigma_1$ at $\sigma_2 = \sigma_3$ = constant, or c) at $\sigma_1/\sigma_3$-ratio = constant. In fact, all the loading paths generate normal and shear components on the fracture surfaces. The normal stress is the main factor governing the fracture aperture and permeability. Fig. 2.48 summarizes the permeability values obtained on all the pre-fractured samples as a function of the normal stress $\sigma_n$, which is calculated according to

$$\sigma_n = \frac{\sigma_1 + \sigma_3}{2} + \frac{\sigma_1 - \sigma_3}{2} \cos 2\beta \qquad (2.17)$$

where $\beta$ representing the angle of inclination of the axial stress to the fracture plane.

In the log $(k)$ – $\sigma_n$ – diagram, the relation of permeability and normal load seems to be linear. Because of the different features of the fractures (apertures, roughness, density, connectivity), the permeability magnitude and the decrease rate varies from sample to sample. The measured data are scattered in a band between $k_g = 5\cdot10^{-16}\cdot\exp(-0.4\sigma_n)$ and $k_g = 1\cdot10^{-18}\cdot\exp(-0.4\sigma_n)$.

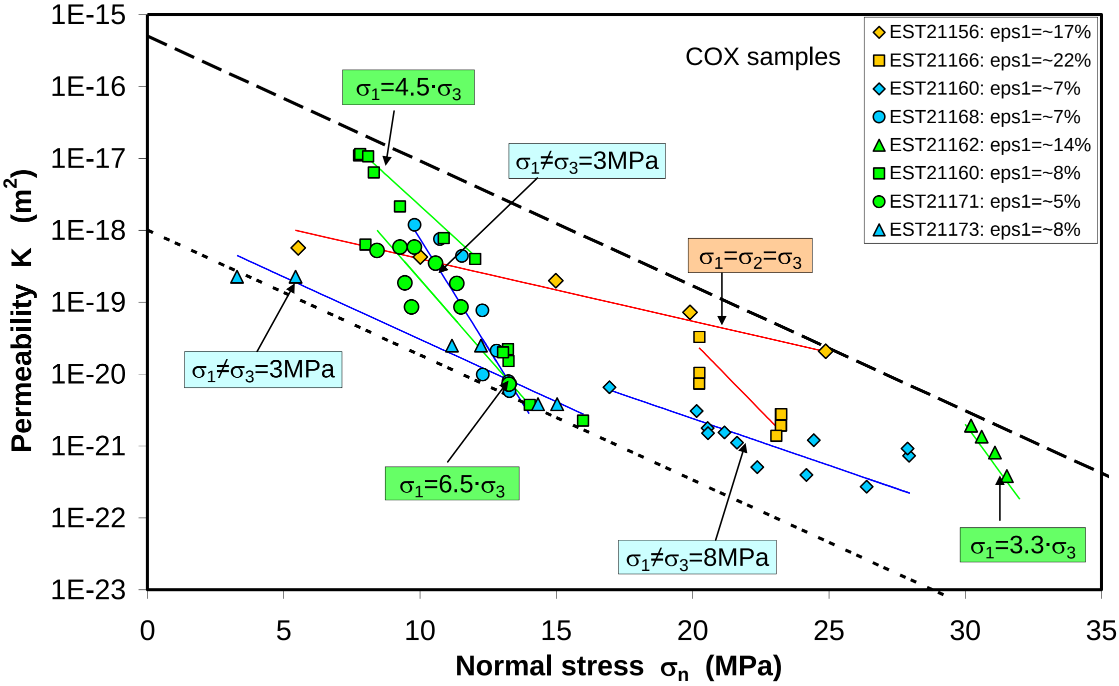


**Fig. 2.48** Permeability changes of fractured samples due to re-compaction along various loading paths

### 2.5.4 Conclusions on the permeability changes

Gas permeability of the undisturbed COX claystone and its changes induced by damage and re-compaction were determined under various load conditions. The following conclusions can be drawn:

- **Intact state**: Very low gas permeabilities of $10^{-22}$ – $10^{-20}$ m$^2$ were determined on the COX samples extracted from different distances of 0.5 – 13.0 m to the wall of the main shaft. They were more or less disturbed and de-saturated before testing. In case of full water-saturation, the effective gas permeability will be lower and the clay rock practically impermeable for gas when the gas entry pressure is below the sum of the capillary pressure and the swelling pressure acting in adsorbed water-films between particles.

- **Damage**: The permeability increases dramatically by several orders of magnitude up to $10^{-18} – 10^{-17}$ m$^2$ when a stress criterion (percolation threshold) is exceeded, at which micro-cracks are growing sufficiently to be interconnected, forming macro-fractures and preferential pathways. The increased permeability depends on the minor confining stress dominating the fracture aperture. At high confining stresses over ~6 MPa, no significant permeability changes take place. Shear fracturing after failure does not change the permeability very much due to the limited variation of the fracture geometry.

- **Re-compaction**: The high permeability of the damaged clay rock decreases significantly when increasing the confining stresses applied along the different loading paths, isotropic loading $\sigma_1 = \sigma_2 = \sigma_3$, deviatoric loading at $\sigma_2 = \sigma_3$ = const. or $\sigma_1/\sigma_3$-ratio = const.. In fact, all the loading paths generate normal stress on the fracture surfaces, which dominates the fracture aperture and permeability. At confining stresses over 15 MPa (corresponding to a depth of ~500 m), the permeability of compacted clay rock shows very low values of $10^{-19} – 10^{-20}$ m$^2$ which is close to the intact state.

- Because of the limited test data, some degrees of uncertainty still remain for some conclusions derived above. In order to build strong confidence in the understanding and prediction of the damaging and sealing processes in the EDZ around repositories in clay formations, these issues have being treated in the ongoing project THM-TON /THM 07/. Preliminary results were presented at the 4th international clay meeting in Nantes, March 2010 /ZHA 10b/.

## 2.6 Thermal effects

In order to characterize the THM behaviour and to enhance the knowledge about thermal effects on argillaceous rocks, various thermal tests were conducted on COX samples under well controlled conditions. These included heating the samples up to 90 °C – 150 °C to investigate thermal expansion and contraction, pore-water pressure changes, temperature influence on shrinkage and swelling, and thermal impact on strength. The applied temperatures are significantly beyond the upper limit of 90 °C considered as maximum temperature in clay formations hosting HLW repositories /AND 05/, /NAG 02/. In earlier projects, some thermal tests were performed on both COX and OPA claystone. The main results are reported in /ZHA 05/, /ZHA 07a/, /ZHA 07c/, /ZHA 08c/. The most recent tests are presented in the following.

### 2.6.1 Testing methods

Thermal tests were carried out on COX samples of 50 mm diameter and 100 mm length in a triaxial apparatus, which allows a maximum axial and radial load of 50 MPa, a maximum temperature of 200 °C, and a maximum fluid pressure of 16 MPa at top and bottom of the sample. Fig. 2.49 shows schematically the assembly of the testing apparatus and the applicable THM conditions. Axial deformation is recorded by a LVDT deformation transducer mounted inside the cell between the upper and lower loading platen, while a circumferential extensometer is mounted around the sample outside the jacket at its mid-height to determine lateral deformation. Heating is accomplished using an electrical heater positioned near the bottom of the cell. Fluid is allowed to be injected into the stressed sample through both upper and lower sintered porous discs. The fluid pressure is usually generated by gas pressure in a pressure vessel containing the fluid. Fluid outflow can be measured by means of a burette or flow rate gauges. It is to be pointed out that for very compacted clays, the water back-pressure recorded at the top and bottom must not be equal to the pore-water pressure inside the sample. Regarding the pore-water pressure in compacted clays one should distinguish between the pressure of free pore-water ($p_w$) and the pressure prevailing in interparticle water-films ($p_{fm}$) which consists of the free pore-water pressure ($p_w$) and the disjoining pressure in water-films ($\Pi_D$). Only in case of existing pathways connecting the inner free pore-water and the external water reservoirs, the back-pressure is equal to the free pore-water pressure.

In order to examine specific aspects of the THM behaviour of the claystone, such as thermal expansion/contraction, pore-water pressure changes, temperature influence on deformation/damage/strength, shrinkage and swelling, various combinations of testing procedures were designed and applied to each sample. Test results are presented and interpreted below with respect to each individual aspect.

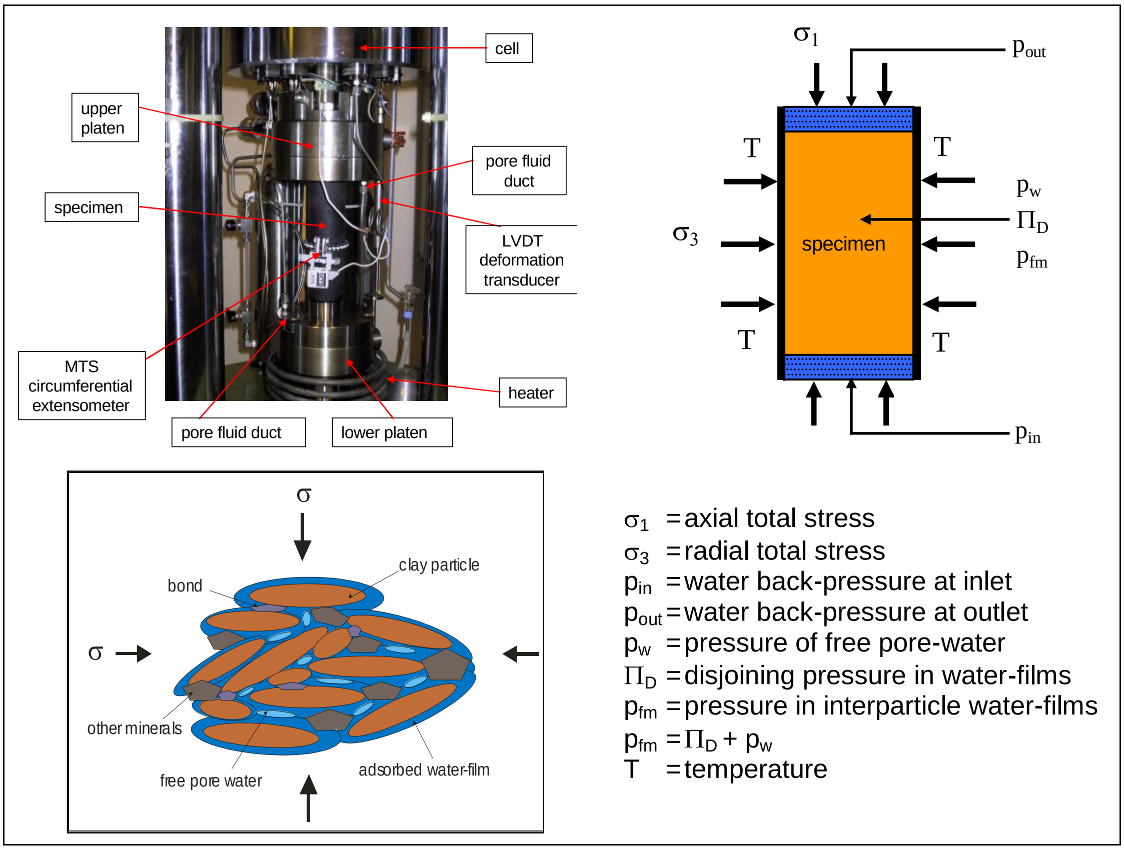


**Fig. 2.49** Triaxial testing apparatus and applicable conditions for coupled THM experiments on claystone

### 2.6.2 Thermally-induced pore-water pressure

In conventional tests, the pore-water pressure of porous samples is usually measured by back-pressure at the end faces, as shown in fig. 2.49. In fact, this test method assumes that the free pore water in the sample and the water in the external reservoirs are interconnected. This assumption is true for conventional porous media such as sand, soils, sandstone, etc., but may be not for highly-consolidated clays without or minor amounts of free pore water. Thus the water back-pressure may not really be representative for the inner pore-water pressure in the compact clay samples.

The first test examining pore pressure changes by thermal loading was carried out on COX sample EST21156 (D/L = 50/100 mm). It was initially unsaturated with a saturation degree of 58 %. In order to achieve a fully saturated state, a re-saturation phase was performed by injecting the synthetic pore water into the end faces of the sample at pressure of 0.5 MPa under confining stress of 1 MPa over 48 days. An increase in the confining pressure to 15 MPa followed over 21 days to compress the remaining unsaturated pores. At that moment, it was assumed that a full saturation had been achieved, and a heating phase was started after switching off the inlet and outlet valves. fig. 2.50a illustrates the evolution of applied confining stress and temperature as well as the resulted water back-pressures at the top and bottom, while the corresponding deformations are shown in fig. 2.50b. At a confining stress of 15 MPa, the temperature in the cell was elevated from 30 to 60 °C at a rate of 2 °C/h (step 1). This generated high impulses of the back-pressures to 4.3 MPa at top and 7 MPa at bottom, respectively. Keeping the elevated temperature, the pressures dissipated then gradually down to 2.2 and 1.7 MPa within 2 days. The second heating up to 90 °C (step 2) caused higher pressure rising to 6.5 MPa at top and 11.7 MPa at bottom. After the peaks and at the increased temperature, the pressures dropped quickly down to nearly zero. The water pressure changes were simultaneous with sudden expansion by heating and gradual contraction at each elevated temperature. The following shutoff tests were performed by increasing the pressure at top to 5 MPa and then switching off for several days (step 3, 4). As unexpected, the pressure increase did not generate any response of the water pressure at the opposite side. This may indicate that the sample was still unsaturated or/and there was no build-up of any hydraulic pathways between the opposite water reservoirs. Independent of the changes in the water back-pressure, the consolidation continued.

Another test was carried out on a more saturated COX sample EST19454 (D/L = 50/100 mm) with a saturation degree of 95.2 %. The sample axis was nearly parallel to the bedding plane. In order to achieve full saturation, the synthetic pore water was firstly sprayed upon the sample surface. After sealing the sample in jacket, the test was started with water injection into both end faces at pressure of 1 MPa under confining stress of 1.5 MPa over 7 days. Fig. 2.51 shows the test process in terms of the applied temperature and stress, the resulted water back-pressures and deformations. During the re-saturation phase, swelling took place to a large volume increase of 4 %. At this point, a full saturation seemed to be reached.

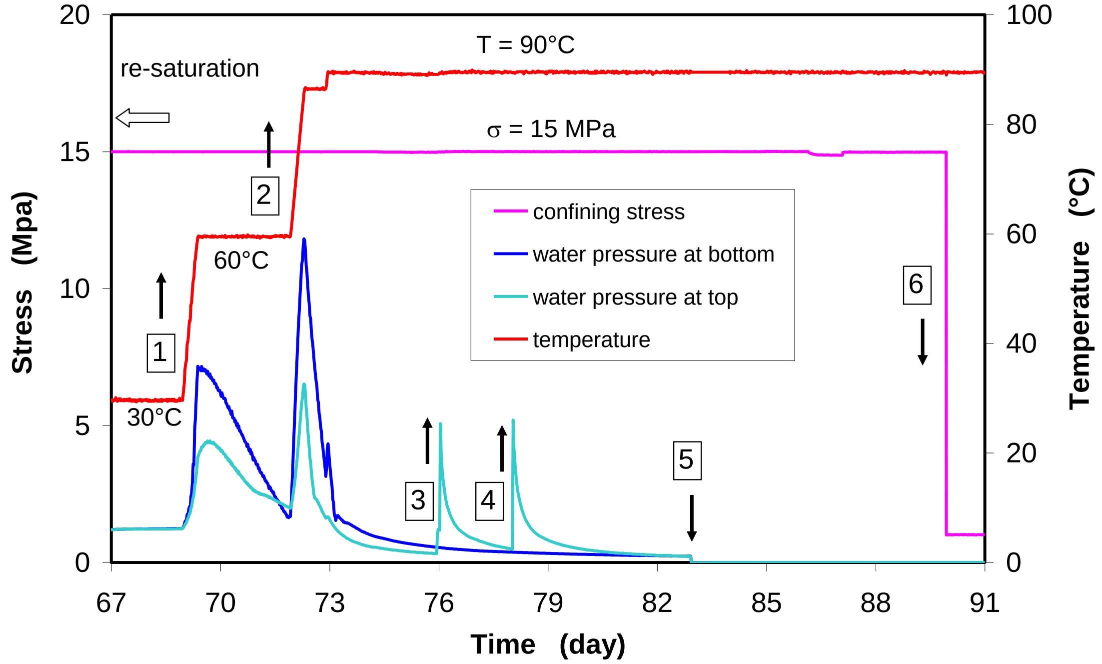


(a) applied temperature, confining stress, and response of water-back-pressures

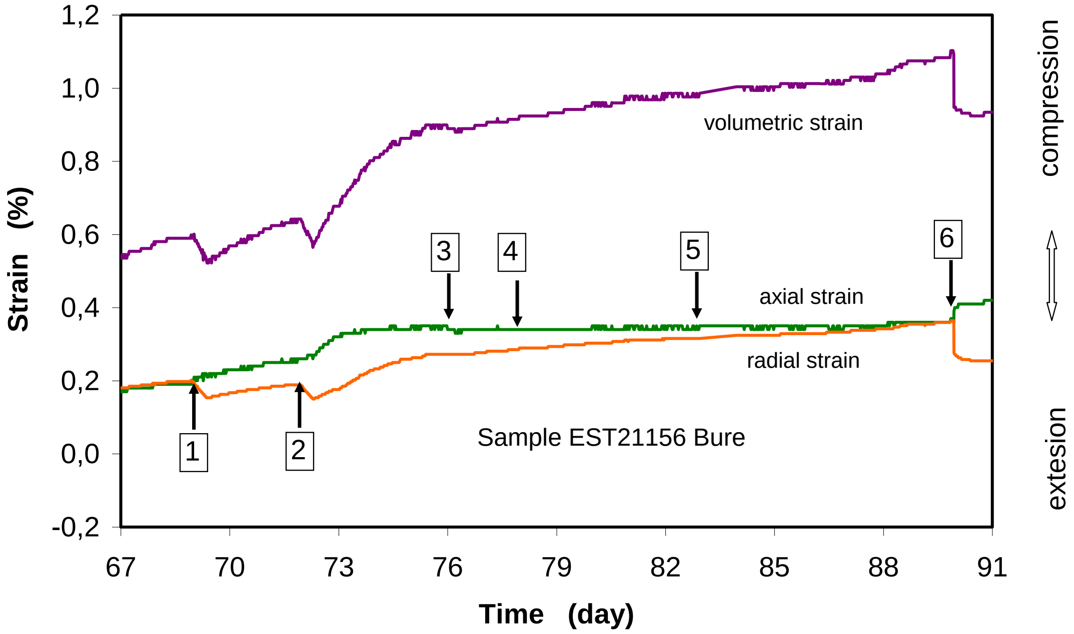


(b) response of axial, radial and volumetric strain

**Fig. 2.50** Evolution of thermally-induced pore-water pressure observed at the ends of an unsaturated COX sample

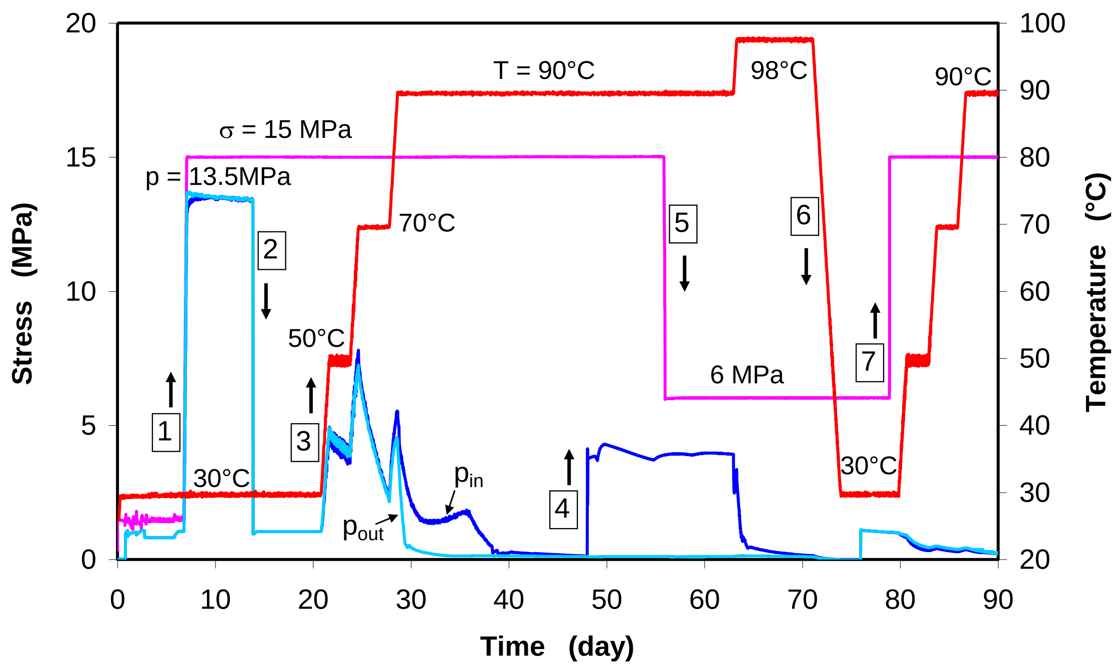


(a) applied temperature, confining stress, and response of water-back-pressures

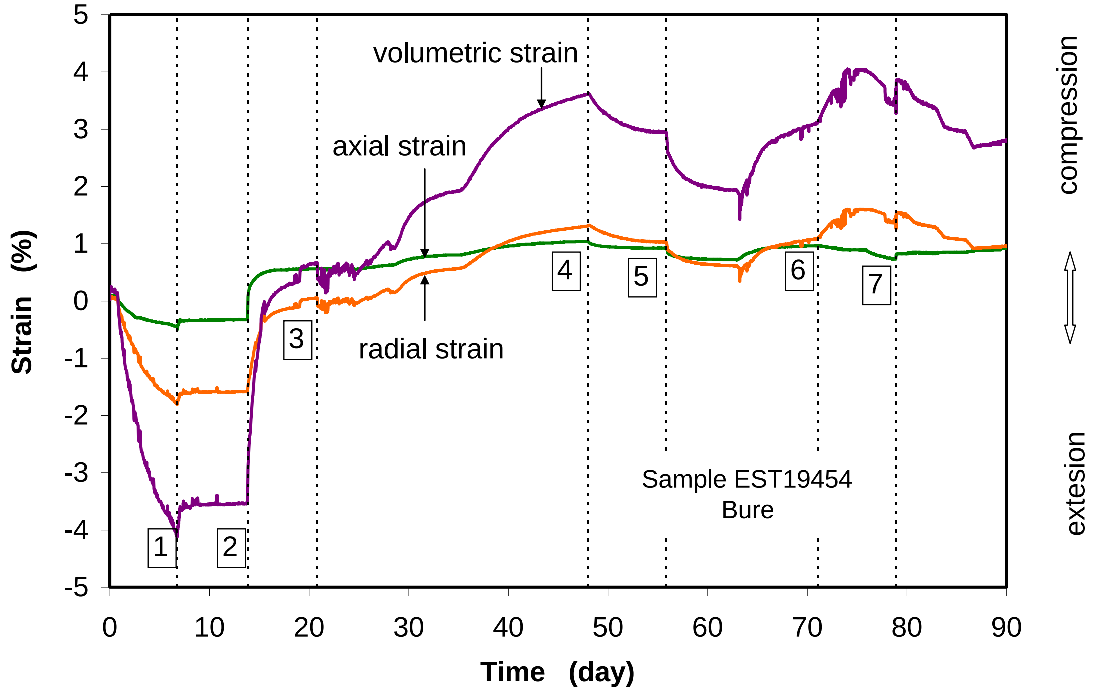


(b) response of axial, radial and volumetric strain

**Fig. 2.51** Evolution of thermally-induced pore-water pressure observed at the ends of a nearly saturated COX sample

On the “saturated" sample and in undrained conditions, response of pore-water pressure to mechanical loading was examined by increasing the confining stress to 15 MPa (step 1). The compression led to an increase of the back-pressures at the top and bottom to the same value of 13.5 MPa remaining constant, indicating the existence of hydraulic interconnection between both end sides. From the data, the Skempton's coefficient was derived to be B = 92.6 %. From this value of less than 100 % it is difficult to distinguish whether the sample or the water reservoirs or both was not fully saturated. Following the test of pore pressure increase by loading, another test was carried out to examine response of deformation to pore pressure drop down to 1 MPa (step 2). This increased the effective stress and thus led to a large compaction recovering the previous expansion. After switching off the inlet and outlet valves, the sample was heated by elevating temperature from 30 to 50, 70 and 90 °C at a rate of 0.6 °C/h, keeping for days to a month each (step 3). The temperature increase caused the back-pressure rising. The maximum water pressure was reached at 7.8 MPa at both end sides by heating from 50 to 70 °C. At each increased temperature the water pressure dissipated with time. This indicates that the pore water moved out of the "saturated" sample in any way, else the pressure peak reached by each heating must maintain. Accompanying the pore-water pressure decrease, a gradual consolidation took place and reached at a volume reduction of 3.5 % over one month. To ensure a full saturation of the sample, the inlet pressure was increased to 4 MPa again (step 4) and then the confining stress was lowered down to 6 MPa (step 5). These led to a volume expansion of ~2 %. After switching off the inlet, the temperature was increased from 90 to 98 °C. As unexpected, this heating phase led the water pressure dropping down rather than rising up. This might be caused by some leakage of thermally-induced water vapour with high pressures through the "undrained" system. The subsequent cooling phase to 30 °C (step 6) produced an extraction, reloading to 15 MPa resulted in a small compaction, and reheating to 50, 70 and 90 °C again (step 7) generated expansion. However, no significant changes in the water back-pressures were observed.

The magnitude of the pore-water pressure increase due to a temperature rise is dependent on the confining stress and can be evaluated by the "pore pressure temperature parameter" F /HOR 96/:

$$F = \frac{\Delta p_w}{\sigma \; \Delta T} \tag{2.18}$$

where $\Delta T$ is the increment in temperature, $\Delta p_w$ is the increment in pore pressure, and $\sigma$ is the mean effective stress. Fig. 2.52 illustrates the measurements of water back-pressure as function of applied temperature for three COX samples and an OPA sample under the confining stress of 15 MPa. The $p_w$-T-curves are relatively linear, i. e. the slope of $A_p = \Delta p_w / \Delta T$ is constant. Assuming the water back-pressure at the sample ends being the same as he inner pore pressure and taking the applied external stress as the “effective” stress (strictly not correct, because the true pore pressure is unknown, so that the effective stress cannot be determined), the parameter F can be roughly estimated by $A_p / \sigma$. The F-values obtained range from 0.01 to 0.025 °C$^{-1}$ for the COX claystone, averaged at F = 0.017 °C$^{-1}$. For the OPA sample the mean F-value is 0.011 °C$^{-1}$. They are close to a common value of 0.017 °C$^{-1}$ for many saturated clay soils /HOR 96/.

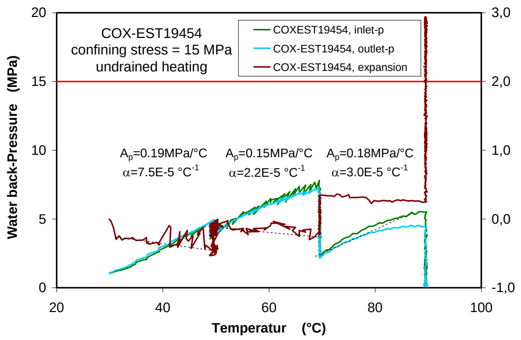


COX sample EST19454

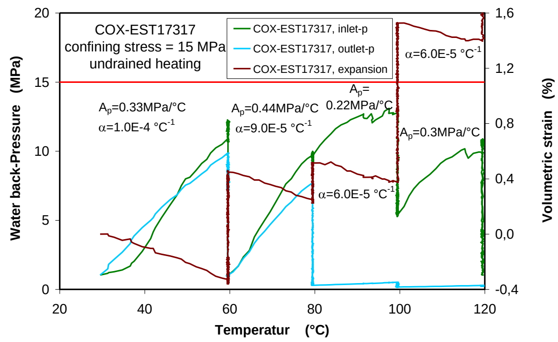


COX sample EST21156

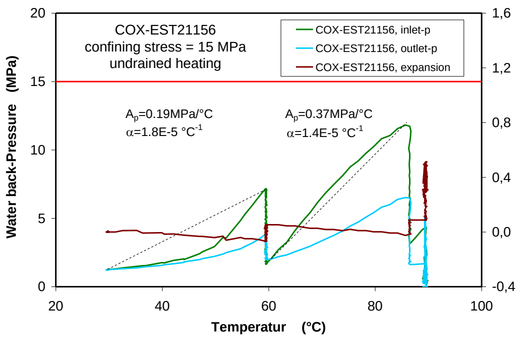


OPA sample HED6-14

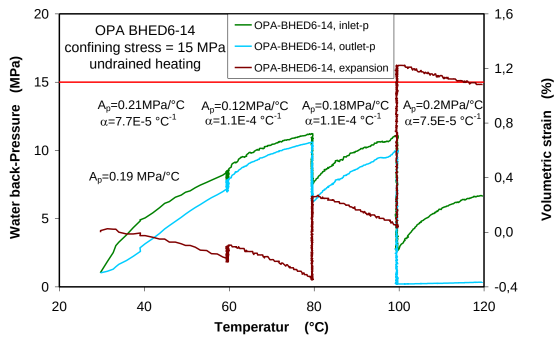


COX sample EST17317

**Fig. 2.52** Thermally-induced increase in pore-water pressure and volume expansion

Additionally, the volumetric thermal expansion coefficient can also be determined from the slope of the $\varepsilon_V$-T-curve, $\alpha = \Delta\varepsilon_V / \Delta T$. For the COX claystone, the coefficient $\alpha$ varies in a range from $1.5 \cdot 10^{-5}$ to $7.5 \cdot 10^{-5}$ °C$^{-1}$, yielding a mean value $\alpha = 4.5 \cdot 10^{-5}$ °C$^{-1}$.

It is to be pointed out that the values of the pore pressure parameter F and the thermal expansion coefficient $\alpha$ were obtained on more or less desaturated samples. For the fully-saturated clay rocks, the F- and $\alpha$-values must be higher because the thermal expansion of pore water is about two orders of magnitude stronger than solid grains.

### 2.6.3 Thermal expansion and contraction

Usually, the thermal expansion is measured by heating samples under hydrostatic confining stresses and in undrained conditions. Taking into account the deviatoric stress states in the host rock around disposal cells, three COX samples were heated at constant radial stress of 3 MPa and axial stress of 15 MPa in drained and undrained conditions, whereby the induced deformation in axial and radial directions were recorded. The drained condition was imposed by exposing the sample end faces to porous discs which were interconnected to atmosphere, whereas the undrained condition was assumed by sealing the sample in a rubber jacket and steel plates. Fig. 2.53 presents the test results.

Two drained samples EST17313 and EST17322 were heated by increasing the temperature from 27 to 150 °C at a rate of 2.9 °C/h (fig. 2.53a/b). Both samples showed the similar thermal deformation behaviour. Heating led to a gradual expansion in radial direction at a rate of $\alpha_3 \approx -3.9 \cdot 10^{-5}$ °C$^{-1}$ and a continuous contraction in axial direction at a rate of $\alpha_1 \approx 3.2 \cdot 10^{-5}$ °C$^{-1}$ up to the water boiling point of 100 °C. Beyond this point, the radial strain changed to contraction with increasing temperature at rates of $\alpha_3 \approx 3.9 \cdot 10^{-5}$ °C$^{-1}$, while the axial compression continued at higher rate of $\alpha_1 \approx 15.0 \cdot 10^{-5}$ °C$^{-1}$. The higher axial compression might be due to the higher load in this direction. Due to the heating in drained and loaded conditions, the pore water evaporated and escaped in a total amount of w ≈ 6.6 % from the sample, causing a volume compaction of ~2.3 %.

Another undrained sample EST17282 was heated stepwise from 27 to 60, 85, 104, 128 and 150 °C at a low rate of 1.0 °C/h by keeping each step for several days (fig. 2.53c). Under the undrained conditions and the deviatoric stress, the temperature increase led to radial expansion with an average rate of $\alpha_3 = -2.0 \cdot 10^{-5}$ °C$^{-1}$ and axial compression with a rate of $\alpha_1 = 2.7 \cdot 10^{-5}$ °C$^{-1}$ for the range between 28 and 150 °C. But within each heating phase at elevated temperatures, gradual compression in all directions occurred. This might be caused by the collapse of the pores occupied by air and by porewater release of ~1.0 % on the other hand, which was detected after testing.

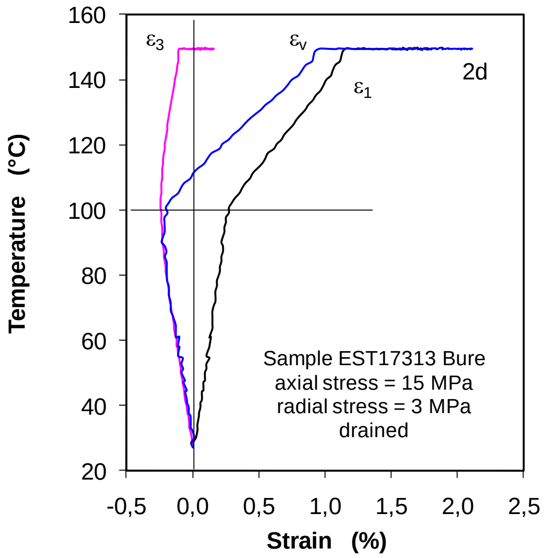


(a) drained test EST17313

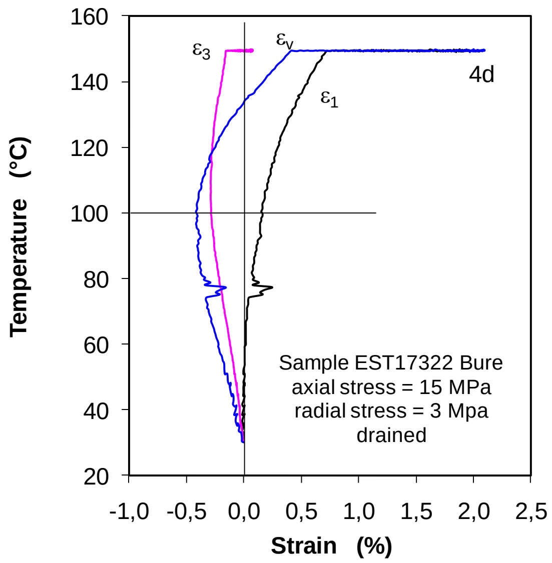


(b) drained test EST17322

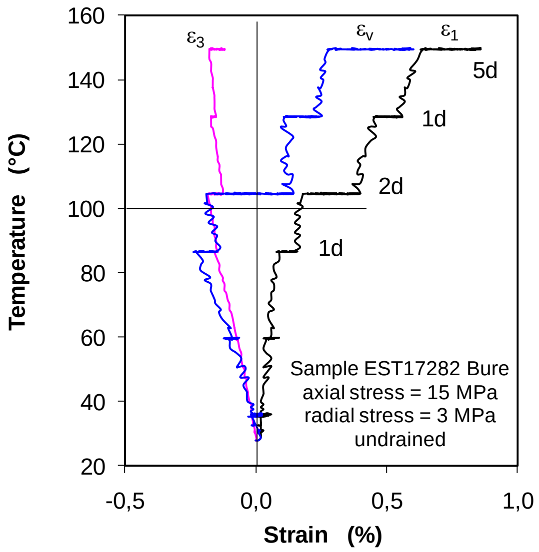


(c) undrained test EST17282

**Fig. 2.53** Thermal strains of COX samples obtained by heating at a deviatoric stress and in drained or undrained conditions

### 2.6.4 Swelling capability of pre-heated claystone

The clay rock around HLW disposal cells will be heated up to the designed maximum temperature of 90 °C and dried. This may result in shrinkage and fractures in the surrounding rock. Another concern is whether the heated clay rock is still capable of swelling when wetted again to seal the fractures. This issue was studied by drying and wetting COX samples of 40 mm diameter and 50 mm length. During the tests, the following parameters were measured:

- de-saturation and free shrinkage by heating,
- re-saturation and free swelling by wetting with water vapour, and
- swelling pressure under axially-fixed and laterally-unconstraint conditions.

First, the samples were heated in oven up to 100 °C and 120 °C beyond the maximum temperature of 90 °C designed for the HLW disposal in clay formations. During the heating phase, changes in water content and shrinkage were measured on the samples as function of applied temperature. The results are shown in fig. 2.54. Heating induced evaporation of the pore water out of the porous claystone, resulting in collapse of the pore structure and thus volume shrinkage, but no macro-fractures were visually observed in the heat-dried samples. All the samples showed the same evolution of water loss with temperature. However, the resulted shrinkage differs largely from one sample to another between 0.3 % and 1.0 % after heating at 100 °C and 120 °C.

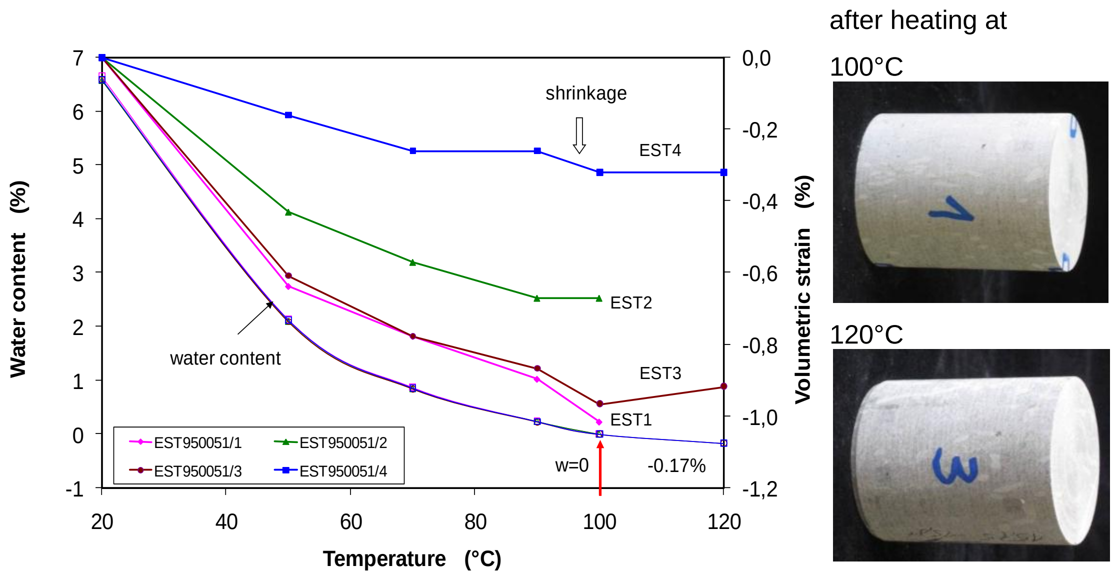


**Fig. 2.54** De-saturation and induced shrinkage of COX samples during heating

Secondly, the swelling capacity of the heated samples was examined by measuring swelling strain and pressure during wetting with water vapour. While the swelling deformation was measured on two samples in unconstraint conditions, the swelling pressure was determined on the other two samples as stress reaction against the rigid piston in axial direction. The test principle for the swelling pressure measurement is shown in fig. 2.36. The results of free swelling strain and swelling pressure are summarized in fig. 2.55 and fig. 2.56 respectively. Major observations are:

- Wetting gave rise in the amount of water uptake up to 10 % over 7 months, resulting in large free expansion up to 12 % and even fractures along the bedding planes. The results are comparable with those obtained on other non-heated samples (cf. fig. 2.30).

- Significant swelling pressures of 4 to 5 MPa were determined on the COX samples pre-heated to 100 and 120 °C. The values are lower than those of 10 to 12 MPa obtained on the non-heated samples (cf. fig. 2.37).

Generally, the COX claystone, even though exposed to high temperatures up to 100 to 120 °C and highly dried, still exhibits a significant swelling potential.

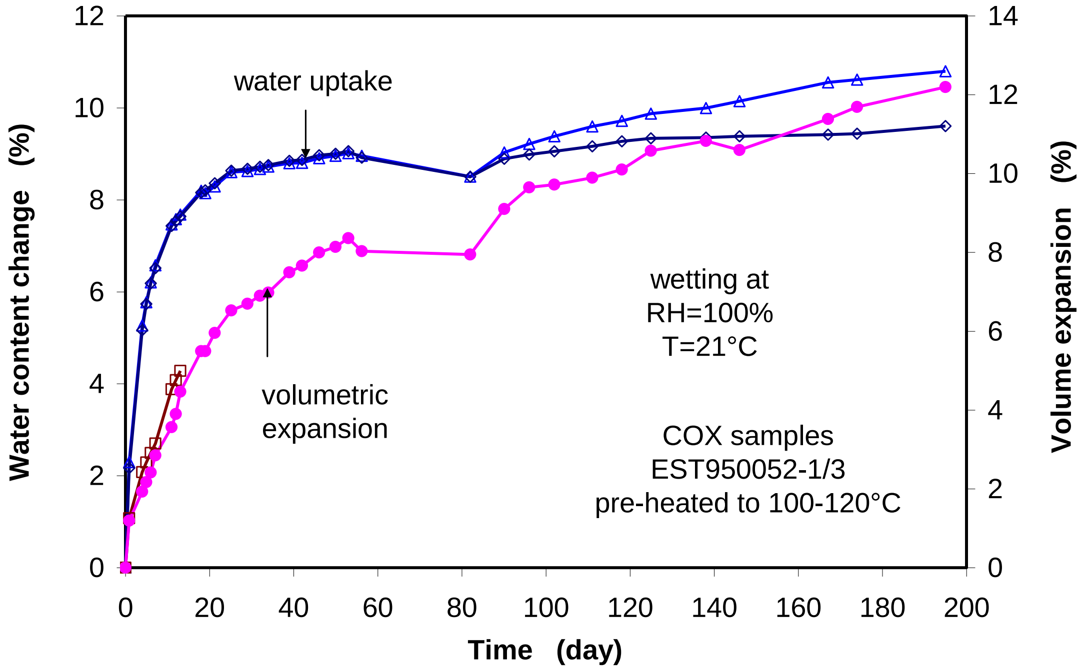


**Fig. 2.55** Evolution of water uptake and free volume expansion of pre-heated COX samples during wetting with water vapour

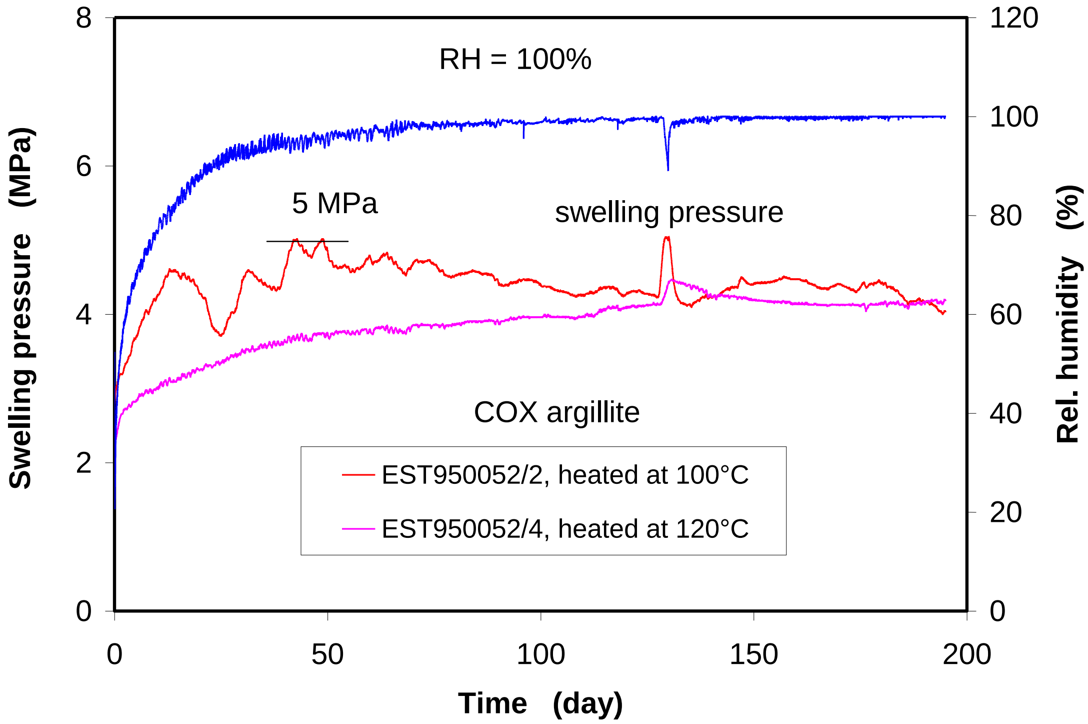


**Fig. 2.56** Evolution of axial swelling pressure of pre-heated COX samples during wetting with water vapour

### 2.6.5 Deformation and strength at elevated temperatures

The samples previously loaded under hydrostatic stress of 15 MPa and heated up to 90 °C to 150 °C were used again for determination of deformation and strength at re-elevated temperatures of 90 °C and 150 °C. The tests were carried out in drained or undrained conditions and at radial confining stresses of 0 to 3 MPa. Fig. 2.57 summarizes the stress-strain-curves obtained on four samples, showing the typical linear elastic and non-linear plastic deformation with hardening but without dilatancy until failure. From the linear parts of the curves, the elastic parameters are determined and given in tab. 2.4. The Young's modulus E varies in a large scatter between 1.2 to 11.0 GPa while the Poisson's ratio $\lambda$ = 0.03 – 0.17. The data yield an average value of E = 5.7 GPa and $\lambda$ = 0.1.

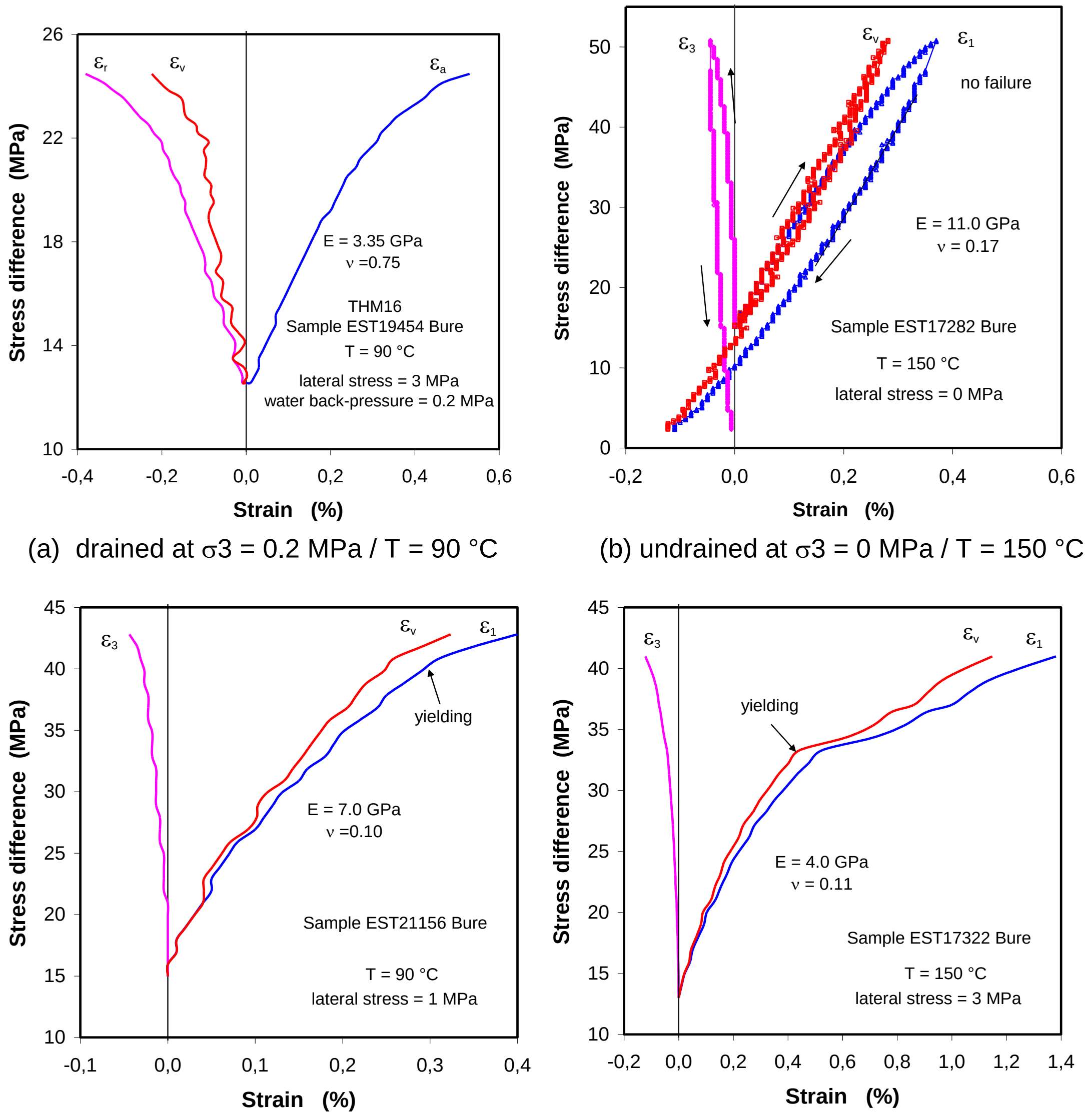


(a) drained at σ3 = 0.2 MPa / T = 90 °C

(b) undrained at σ3 = 0 MPa / T = 150 °C

(c) undrained at σ3 = 1 MPa / T = 90 °C

(d) undrained at σ3 = 3 MPa / T = 150 °C

**Fig. 2.57** Stress-strain behaviour of COX claystone at elevated temperatures

**Tab. 2.4** Elastic parameters and strength of COX samples at elevated temperatures

| Sample | T (°C) | $\sigma_3$ (MPa) | $\sigma_1$ (MPa) | E (GPa) | λ (-) | $\sigma_F$ (MPa) |
|---|---|---|---|---|---|---|
| EST17313 | 30 | 3 | 3 → 9 | 1.2 | 0.10 | |
| | 30 | 3 | 9 → 15 | 17.0 | 0.04 | |
| EST17322 | 30 | 3 | 3 → 15 | 2.1 | 0.03 | |
| | 150 | 3 | 9 → 36 | 4.0 | 0.11 | 45.0 |
| EST21156 | 90 | 1 | 15 → 41 | 7.0 | 0.10 | 44.0 |
| EST21164 | 150 | 3 | 15 → 50 | 11.0 | 0.17 | |
| | 150 | 0 | 15 → 50 | 11.0 | 0.12 | 51.0 |
| EST19454 | 90 | 3 | 15 → 27 | 3.4 | 0.75 | 27.5 |

The data of strength $\sigma_F$ at failure are compared in fig. 2.58 with those previously obtained on COX samples at ambient and elevated temperatures. The new data points are significantly above the averaged deviatoric – mean stress – failure boundary. The higher strength might be contributed by the consolidation during the previous heating and drying processes under loads. The other data (ANDRA-data) obtained at elevated temperatures between 40 and 100 °C /D02 07/ indicate slightly lower strength than that at ambient temperature. The thermal impact on the strength is actually dependent on the hydraulic conditions, i. e. water content, drained, undrained, etc. This issue has being currently investigated in another research programme THM-TON /THM 07/.

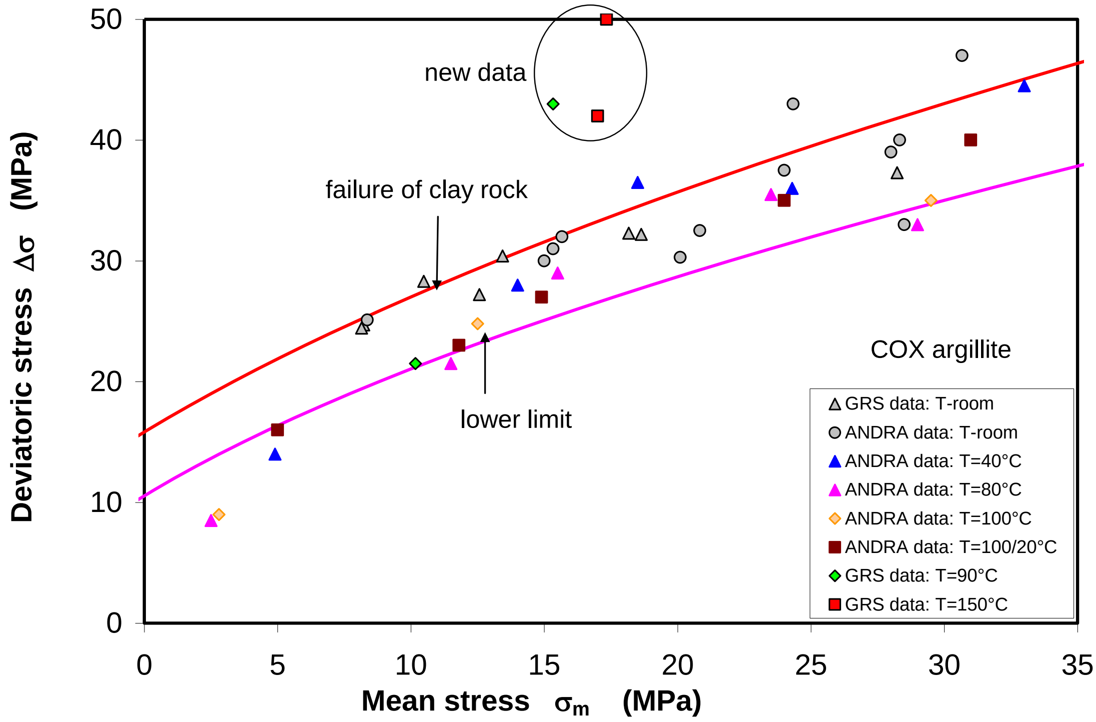


**Fig. 2.58** Strength of COX argillite as function of confining stress and temperature

### 2.6.6 Conclusions on the thermal effects

The thermal impact on the COX claystone was experimentally studied in various respects of thermal expansion and contraction, changes in pore pressure, alteration of swelling capacity, variations in stiffness and strength. The maximum temperatures of 100 to 150 °C applied to the samples are higher than the upper limit of 90 °C designed for the clay host rock around repositories. The following significant thermal effects are observed:

- The thermal expansion of the claystone depends on both the water saturation and the hydro-mechanical boundary conditions. In saturated and undrained conditions, the thermal expansion is predominantly controlled by the pore water because of its much higher expansion coefficient compared to that of the solid grains. In unsaturated and/or drained conditions, heating causes mobilisation and expulsion of the pore water from the rock, giving rise to pore collapse and thus consolidation. The thermally-induced consolidation enhances the stiffness and strength of the clay rock. No thermal fracturing was observed by heating the nearly-saturated samples even at a deviatoric stress of $\sigma_1$ = 15 MPa and $\sigma_3$ = 3 MPa.

- Heating increases the pore-water pressure in the saturated claystone. The maximum pore pressure up to 12 MPa was recorded by heating the nearly-saturated samples up to 90 °C, but still lower than the externally applied confining stress of 15 MPa. At elevated temperatures, the pore pressure decreases with time. The same phenomenon is also observed in the clay rock mass during the TER and HE-D heating experiments performed in the MHM- and MT-URLs. This is attributed to the dissipation of the thermally-mobilized pore water outward seepage in drained conditions.

- Heating to 100 – 120 °C dries up the claystone leading to a maximum shrinkage of ~1 % without appearance of visual fractures even in unconfined conditions.

- The claystone, even though previously exposed to high temperatures to 100 – 120 °C, still exhibits a remarkable swelling potential with free expansion up to 12 % and swelling pressure up to 5 MPa during wetting.

Generally, no negative thermal impact on the integrity of the clay rock was found.

### 2.7 Simulation tests on large hollow cylinders

In order to investigate responses of the clay host rock around HLW boreholes to the excavation, ventilation, backfilling, water flow, heating and cooling, a series of simulation tests was also carried out on large hollow cylinders of the COX claystone under relevant *in situ* conditions. A number of advantages can be expected from such large-scale experiments, as for instance:

- The possibility to simulate variations of the *in situ* boundary conditions during the whole test procedure (simulating excavation, ventilation, backfilling, water flow, heating/cooling, etc.);
- Monitoring responses of the testing material inside and outside the large hollow cylinder to defined THM loading;
- Bridging the gap between test results obtained on small-scale samples and field observations because large samples are more representative for the *in situ* rock mass;
- Supporting the understanding and interpretation of observations of large and full-scale *in situ* experiments where the boundary conditions are usually not well known;
- Serving to validate constitutive models by comparing modelling results with the measurement results obtained from testing under well-controlled conditions.

In the frame of this project, two types of simulation tests were carried out on large hollow cylinders of the COX claystone: a ventilation test and an EDZ-simulation test. The tests were conducted in the MTS big triaxial apparatus at GRS's laboratory. This apparatus allows THM coupling experiments on cylindrical samples of 280 mm diameter and 450 – 700 mm lengths. The testing system permits a maximum load of 50 MPa lateral stress and 75 MPa axial stress, a maximum temperature of 150 °C, and a maximum fluid pressure of 16 MPa. Various parameters, such as axial / radial stresses, axial / radial strains, borehole convergence, temperature, pore pressure, fluid flow and others, can be controlled and/or monitored with various instruments installed outside and inside the sample. Details about this testing apparatus are given in /ZHA 07a/. Results of the EDZ-simulation tests served as database for the benchmark modelling within the TIMODAZ work package WP5.2 /D13 10/.

### 2.7.1 Ventilation tests

#### 2.7.1.1 Samples and testing method

In order to examine ventilation effects on deformation and damage of clay rock surrounding boreholes and drifts, three large hollow cylinders of the COX claystone were tested. The cores of 290 mm diameter and 0.7 – 1.0 m length were drilled vertically from a borehole of the DI diffusion experiment in the niche at -445 m depth. After drilling they were stored without any confinement in an above ground storage hall over about one year. Consequently the samples were strongly de-saturated down to water contents of 1.3 % to 1.7 %. From the cores three hollow cylinders of 280 mm outer diameter, 55 mm inner central borehole diameter and 580 – 650 mm length were prepared. The central boreholes were perpendicular to the bedding plane. Macroscopically, all the samples were very compact and relatively homogeneous (fig. 2.59). The basic properties are given in tab. 2.5.

**Tab. 2.5** Basic characteristics of large COX hollow cylinders used in ventilation tests

| Test No. | Sample | Size D/d/L [mm] | Grain density [g/cm$^3$] | Bulk density [g/cm$^3$] | Dry density [g/cm$^3$] | Porosity [%] | Water content [%] |
|---|---|---|---|---|---|---|---|
| VE1 | DIR2002-K1 at -445 m | 280/55/580 | 2.69 | 2.39 | 2.36 | 12.3 | 1.3 |
| VE2 | DIR2002-K2 at -445 m | 280/55/650 | 2.69 | 2.33 | 2.30 | 14.5 | 1.6 |
| VE3 | DIR2003-K5 at -445 m | 280/55/610 | 2.69 | 2.38 | 2.33 | 13.0 | 1.7 |

Fig. 2.59 illustrates schematically the assembly of the ventilation test system and a photo of a large COX hollow cylinder (D/d/L = 280/55/610 mm). The sample was sealed with an outer rubber jacket, while the central borehole was equipped with a dilatometer. The rock stresses could be applied to the hollow cylinder by increasing the external axial and radial stresses. Borehole ventilation was simulated by pumping air through the central hole under controlled humidity. Axial and radial strains were measured by a LVDT deformation transducer mounted to the lower piston outside the cell with accuracy better than 0.1 % and by a circumferential extensometer installed outside the jacket around the sample with accuracy better than 0.2 %, respectively. As one of the most important measuring parameters, convergence of the central borehole could be monitored with a dilatometer at four positions in different horizontal directions of 0°/45°/90°/135°, as shown in fig. 2.60. The measuring range of the dilatometer lies between 50 and 57 mm with a resolution of 0.001 mm.

Outside of the triaxial cell, two small COX samples (D/L = 50/100 mm) taken from the central borehole of the large sample and two OPA samples (D/L = 68/100 mm) taken from the Opalinus clay in the VE test field at the Mont Terri URL /WIE 08/ were placed in a chamber which enabled the measuring of the water content changes during the ventilation in a by-pass. The small samples were unconstraint and sealed in rubber jackets, but the top face of each sample was exposed to the airflow. Two balances were used to record changes in the water content of a COX and an OPA sample. Response of axial deformation to moisture change was monitored by means of a LVDT deformation transducer mounted on the top face of the samples. Fig. 2.61 shows a photo of the small samples in the test chamber.

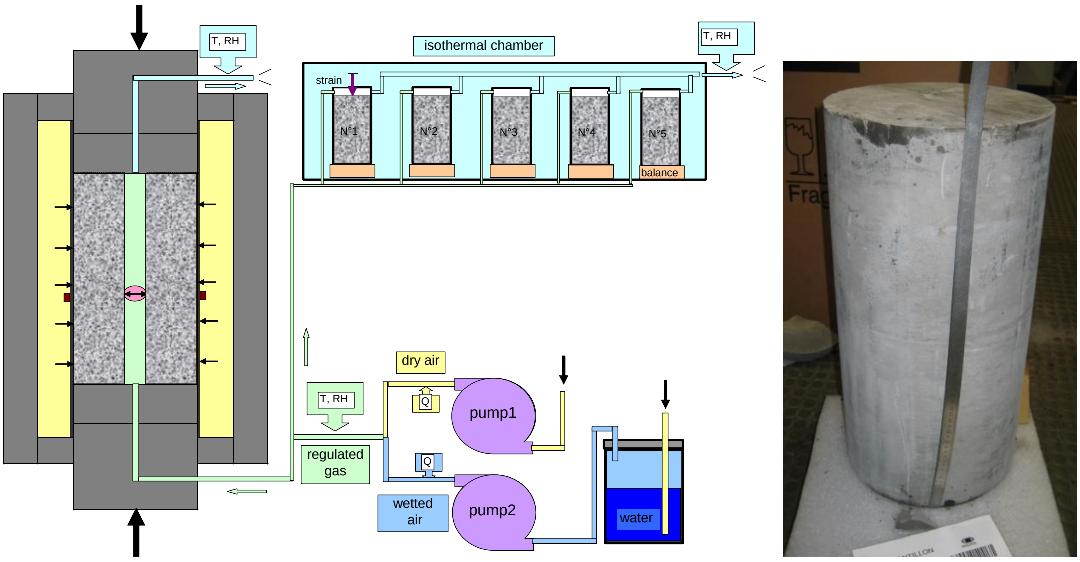


**Fig. 2.59** Assembly of a ventilation test on a large COX hollow cylinder under confining stresses and a photo of the sample (right)

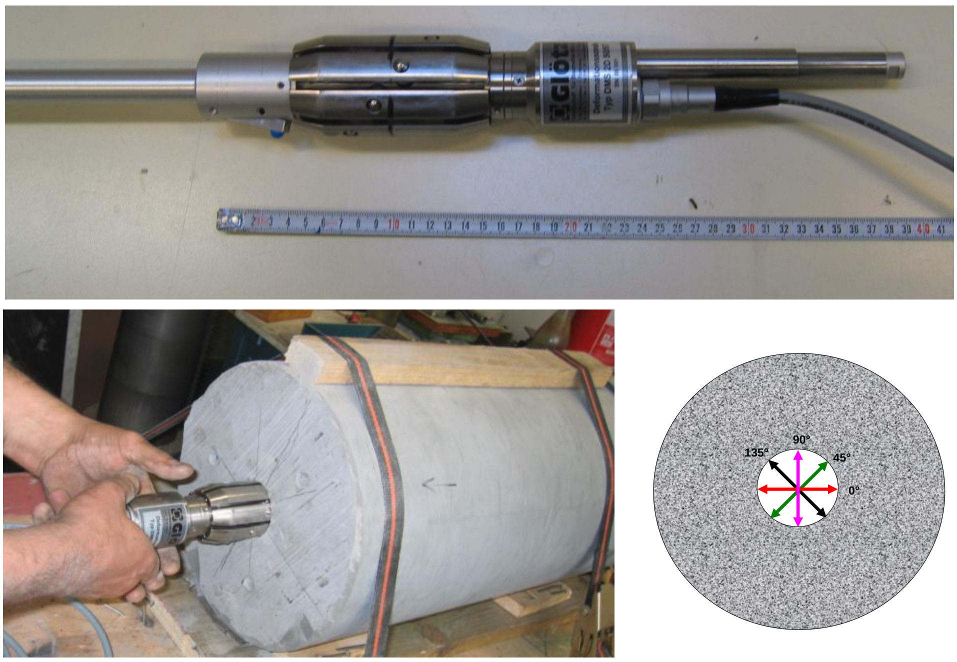


**Fig. 2.60** Installation of a dilatometer for measuring borehole convergence

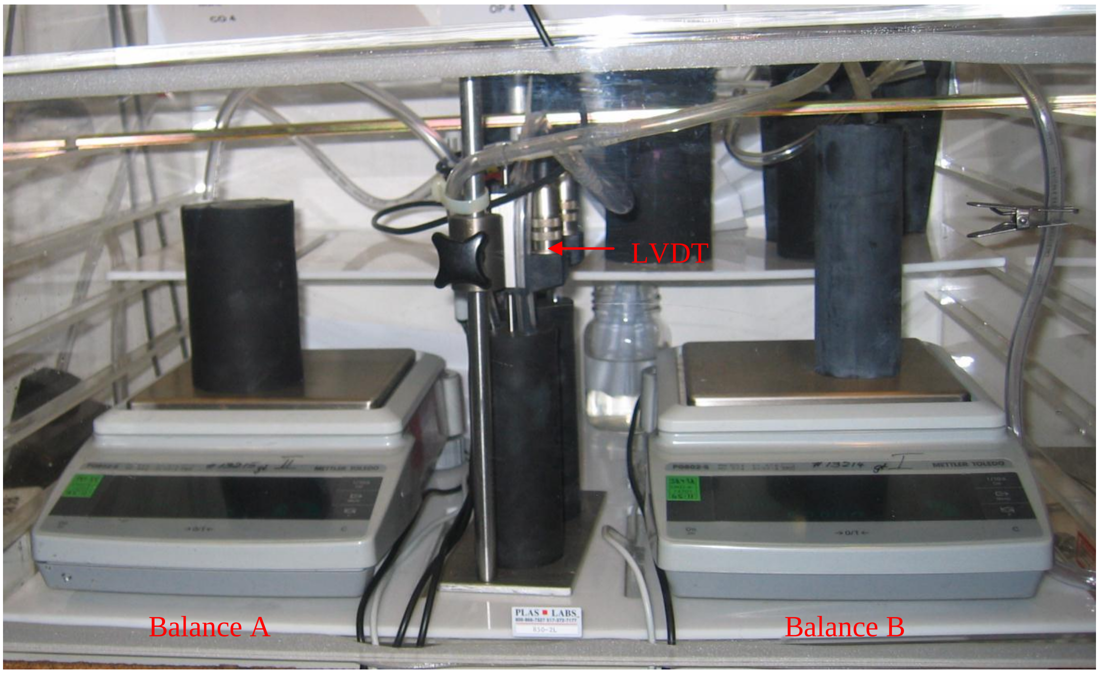


**Fig. 2.61** Measurements of water content change and axial deformation on small-sized samples during ventilation through the top faces

The above mentioned parameters are evaluated according to the following definitions:

**Axial stress**

$$\sigma_a = \frac{F}{A_{ring}} = \frac{4 \cdot F}{\pi(D^2 - d^2)} \tag{2.19}$$

where $F$ = axial force,

$A_{ring}$ = cross section of the hollow cylinder,

$D$ = outer diameter of the sample,

$d$ = diameter of the central borehole.

Outer radial stress on the outer surface $\sigma_R$ = applied oil pressure in the triaxial cell.

Inner radial stress on the borehole wall $\sigma_r$ = 0.

**Axial strain**

$$\varepsilon_a = \frac{\Delta L}{L_o} = \frac{L_o - L}{L_o} \tag{2.20}$$

where $L$ = length of the sample,

$L_o$ = initial length of the sample.

**Outer radial strain**

$$\varepsilon_R = \frac{\Delta D}{D_o} = \frac{D_o - D}{D_o} \tag{2.21}$$

where $D$ = outer diameter of the sample,

$D_o$ = initial outer diameter.

**Inner radial strain or borehole convergence**

$$\varepsilon_r = \frac{\Delta d}{d_o} = \frac{d_o - d}{d_o} = 1 - \sqrt{\frac{V_b / L}{V_{bo} / L_o}} \tag{2.22}$$

where $d$ = average diameter of the borehole,

$d_o$ = initial diameter of the borehole,

$V_b$ = volume of the borehole, which is determined by measuring the oil volume in the packer,

$V_{bo}$ = initial borehole volume.

**Volumetric strain**

$$\varepsilon_v = \frac{\Delta V}{V_o} = \frac{V_o - V}{V_o} = 1 - \frac{L}{L_o} \frac{(D^2 - d^2)}{(D_o^2 - d_o^2)} \tag{2.23}$$

with the borehole diameter $d = \sqrt{4V_b / \pi L}$ .

### 2.7.1.2 Results

Three tests were conducted under different quasi-isostatic confining stresses and at a temperature of 25 °C. The results are illustrated in fig. 2.62 to fig. 2.64 for sample DIR2002-K1, -K2 and DIR2003-K5 in terms of the applied axial / radial confining stresses, the resulting axial / radial / volumetric strains, and the borehole convergence, respectively.

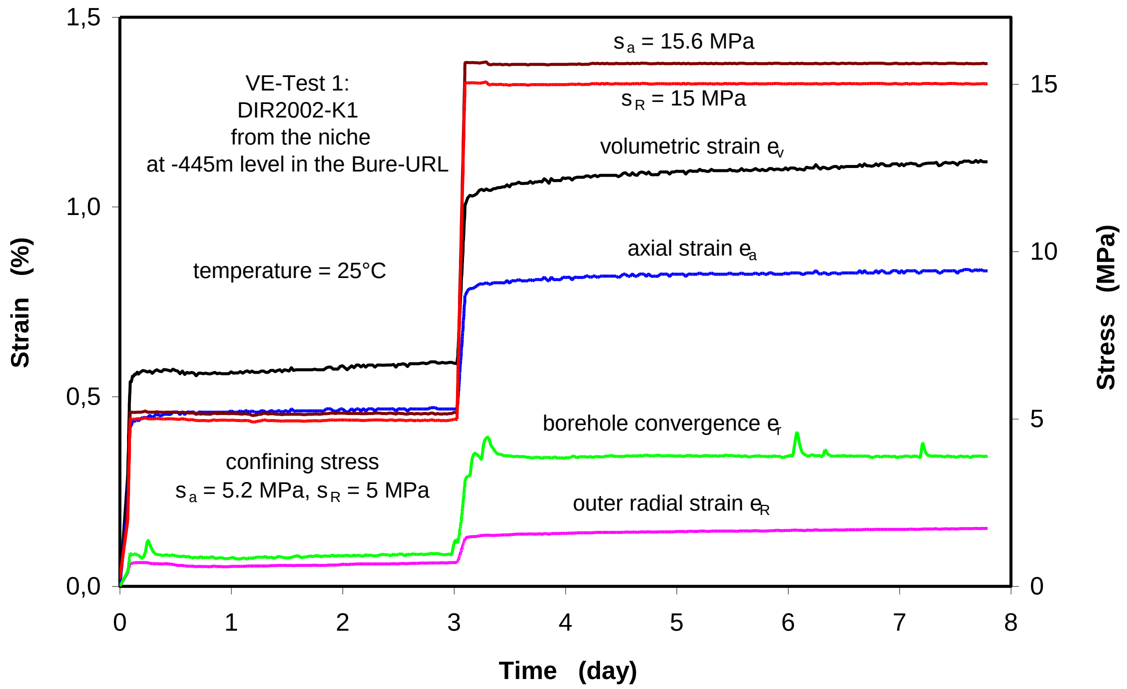


**Fig. 2.62** Deformation of a large hollow cylinder DIR2002-K1 under external loads

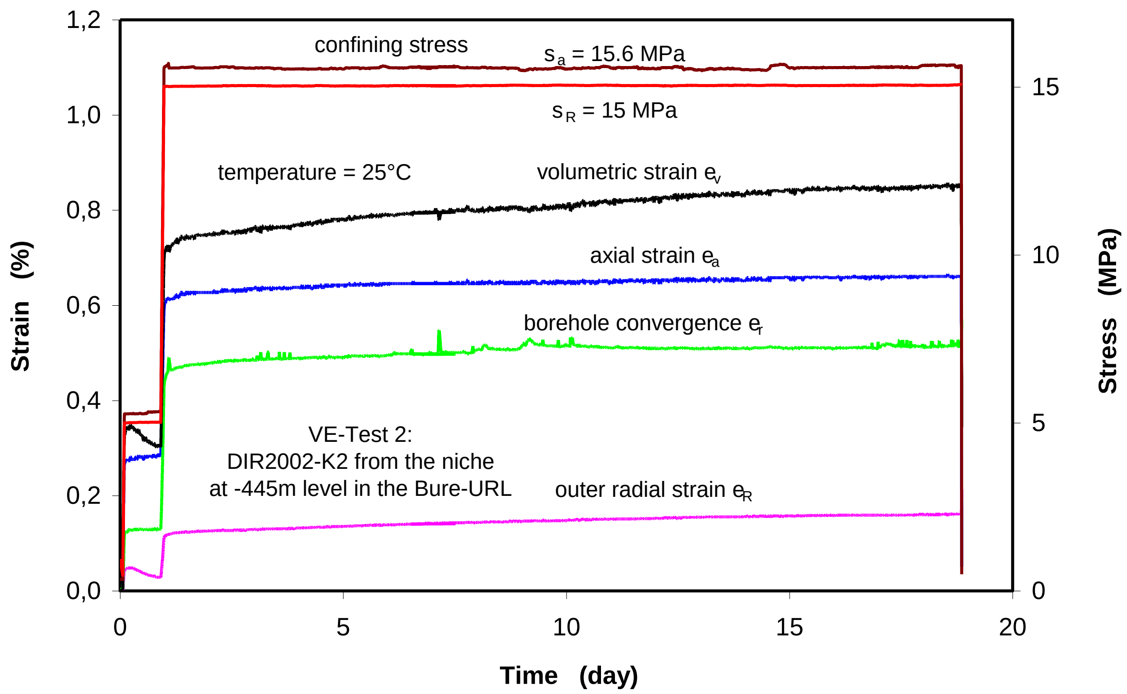


**Fig. 2.63** Deformation of a large hollow cylinder DIR2002-K2 under external loads

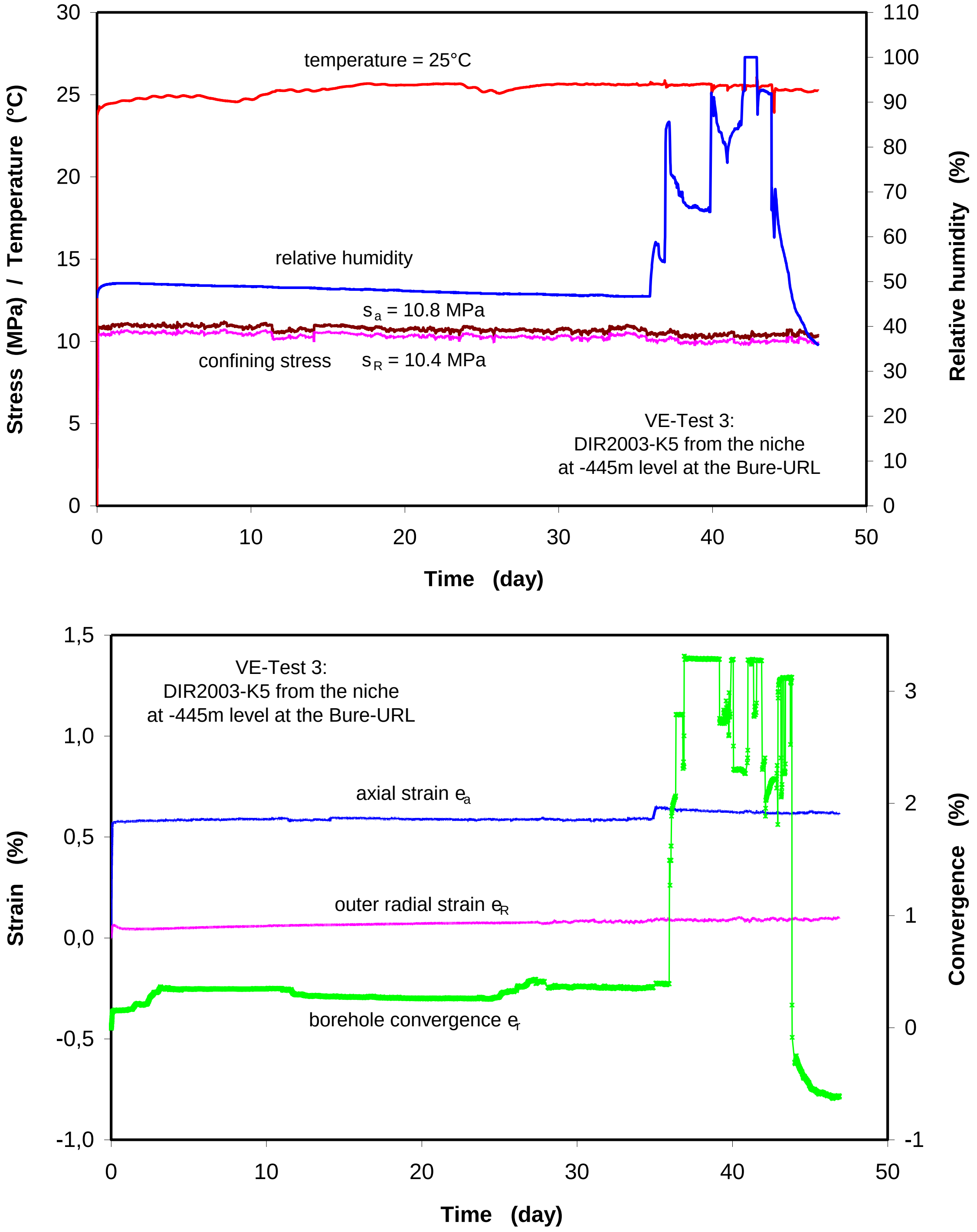


**Fig. 2.64** Deformation response of the hollow cylinder claystone DIR2002-K5 to external stressing and borehole ventilation

Both hollow cylinders DIR2002-K1/-K2 were loaded in two steps to the same confining stresses of $\sigma_a$ = 5.2 MPa / $\sigma_R$ = 5.0 MPa and 15.6 / 15.0 MPa, respectively. The stresses were kept constant for different time periods between 1 and 18 days. The measured data show that each loading led to a sudden deformation and the deformation continued with time. At $\sigma_a$ = 15.6 MPa / $\sigma_R$ = 15.0 MPa, the axial and radial strains of both cylinders reached values of $\varepsilon_a$ = 0.6 % – 0.8 % and $\varepsilon_R$ = 0.12 % – 0.13 %, respectively. The corresponding borehole convergences reached values of $\varepsilon_r$ = 0.35 % – 0.45 %. The calculated volumetric strains lie between 0.75 % and 1.05 %. The significant volume compaction might be caused by collapse of de-saturated pores under the applied confining stresses. Unfortunately, both tests were interrupted due to the failures of power supply, so that the planned ventilation could not be realised.

On the other sample DIR2003-K5, the ventilation test was carried out under isostatic confining stress of $\sigma_a$ = 10.8 MPa / $\sigma_R$ = 10.4 MPa. Fig. 2.64 shows the results. During the first phase of 37 days, the inlet and outlet of the borehole were closed. The relatively dry sample took up moisture from the relatively wet air remaining in the borehole, leading to a slight reduction of the air humidity from 49.3 % to 46.7 %. The outer radial and axial strains and the borehole convergence did not change significantly within this period. In the second phase, ventilation was conducted by pumping wetted air into the borehole for 10 days. The relative humidity in the borehole was increased step by step from 47 % to 100 %. The rapid increase of the humidity resulted in a large borehole convergence of 0.4 % to 3.3 % whereas the axial and radial strains remained unchanged. This was obviously attributed to the swelling of the claystone near the borehole wall. Because the gap between the borehole wall and the dilatometer is relatively narrow, the moisture in the wetted air might partly condense on the borehole wall causing flakes falling from the borehole wall as shown in fig. 2.65. During the ventilation phase, the inlet and the outlet of the borehole were closed again several times to observe changes of the air humidity in the borehole. A significant equilibrium process between the wet air and the dry sample took place indicated by the decease of the air humidity in the borehole. As the humidity was reduced down to 35 %, the borehole diverged from 3.3 % to -0.6 %. This indicates shrinkage of the claystone. During the ventilation, no changes in axial and radial strains were observed.

Ventilation effects were also observed on small samples in another testing system (fig. 2.61). Over the top faces of small COX and OPA samples that were sealed in jackets, air flowed with various humidities at 27 °C. The COX samples with an initial water content of ~1.5 % were much drier than the OPA samples with a water content of ~6.4 %. During the ventilation, changes in water content and axial deformation were measured. The data are depicted in fig. 2.66a and fig. 2.66b, respectively. The water content change defined here is related to the initial sample weight. During the first month of ventilation at an applied humidity of 80 ± 6 %, the dry sample COX5 took up water to

0.5 % while the wet sample OPA5 loss pore water down to 0.9 %. In a good correlation with the de-saturation, axial shrinkage of 0.6 % was observed on another wet sample OPA4 while no significant deformation was recorded on the dry sample COX4. A further increase of the air humidity to 92 ± 3 % provided more water for the re-saturation of the dry samples. Over another 4 months, the water content of the dry sample COX5 increased to 1.2 % and then remained in equilibrium, while the sample OPA5 which was partly de-saturated during the previous phase took up water, too. At high humidity, both claystone expanded to an axial strain of 0.28 % at the COX4 and 0.85 % at the OPA4 sample, respectively. The fluctuation of the water content and the deformation is in a good correlation with the variation of humidity.

**Fig. 2.65** Flakes generated by water condensation falling from borehole wall during ventilation

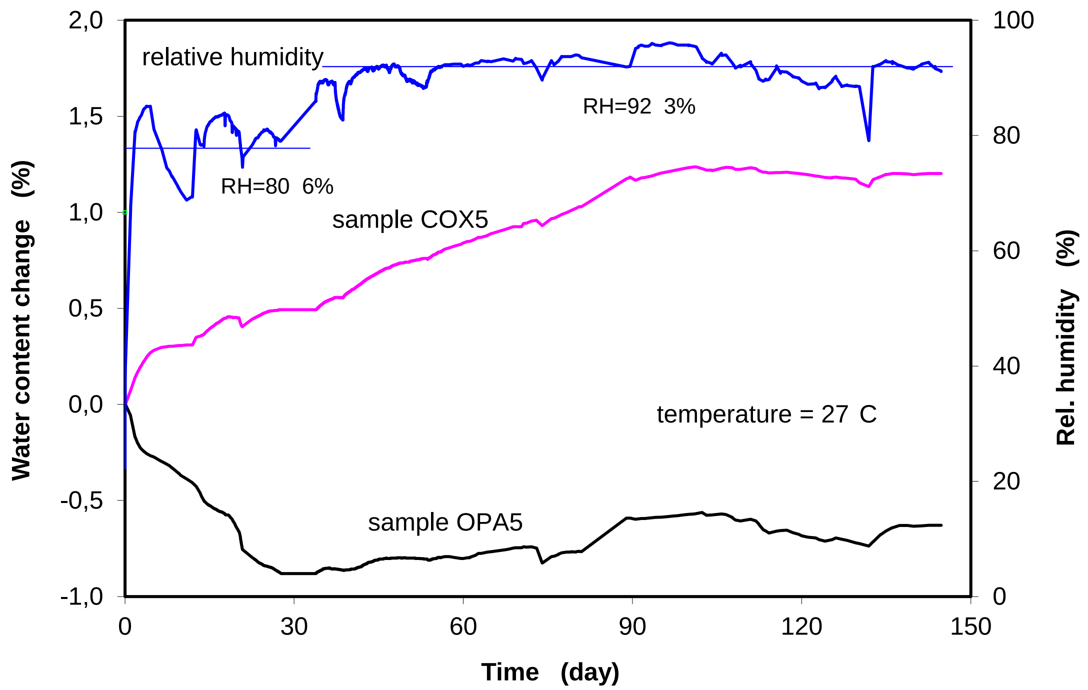


**Fig. 2.66** Water content changes of COX and OPA samples during ventilation

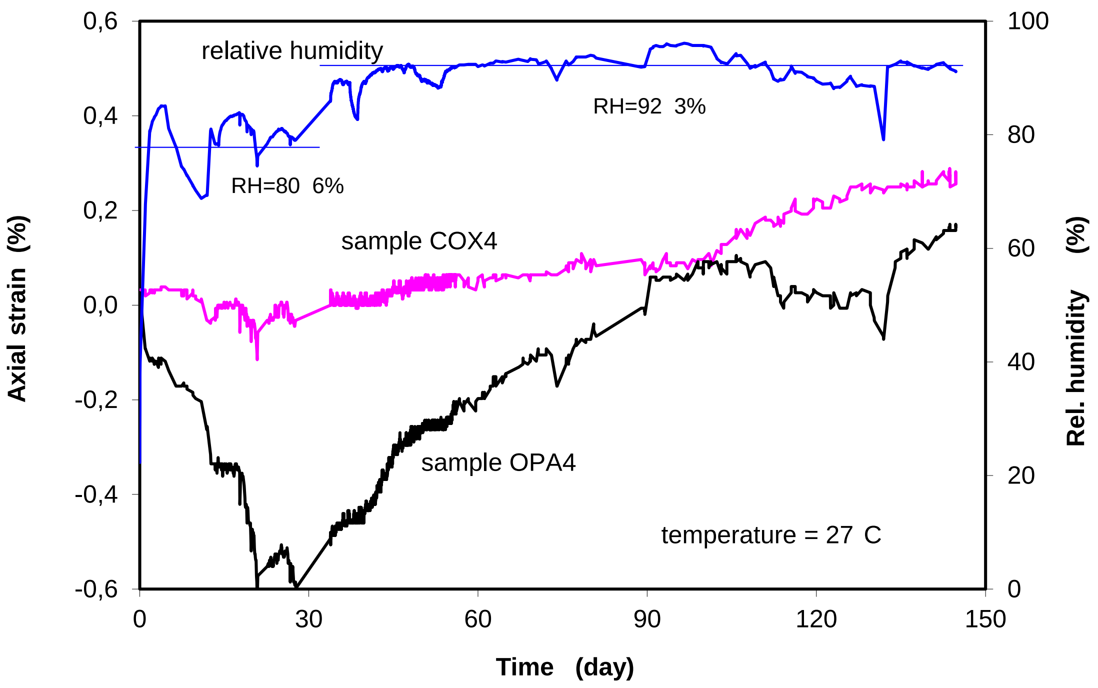


**Fig. 2.67** Deformation response of COX and OPA samples to ventilation

### 2.7.2 EDZ-simulation tests

Within work package WP3.3 of the TIMODAZ-project (Annex B work programme /TIM 06/), a series of EDZ-simulation tests (or benchmark tests (BMT)) was carried out on four large hollow cylinders of the COX argillite to investigate fracturing and sealing processes around HLW disposal boreholes taking place during excavation, backfilling, heating and cooling phases (Deliverable D07 /D07 10/). The test results served to validate the constitutive models by performing benchmark modelling in the framework of the TIMODAZ work package WP5.2 (Deliverable D13 /D13 10/).

#### 2.7.2.1 Samples and testing method

Four big cores of 290 mm diameter and 0.6 – 1.0 m length were extracted from vertical boreholes at depths between 460 m and 501 m in the rheological zone B' of the COX formation. The axes of the cores were nearly perpendicular to the bedding planes. For the BMT tests, four large hollow cylinders of 280 mm outer diameter, 100 mm inner diameter and length of 460 – 525 mm were carefully prepared by plane of the surfaces in a lathe and drilling the central borehole axially. Fig. 2.68 shows the photos of the prepared hollow cylinders before testing.

Due to the long storage periods of months to years, even though the cores were carefully confined, de-saturation took place to different degrees. Before testing, a re-saturation phase with water vapour was performed over several months. Fig. 2.69 illustrates the evolution of water uptake of two cores. While core DIR2004-EST27315 was confined over 8 months, the other one DIR2003-K4 was exposed to room air over 3 years and thus strongly dried. The highly dried core took up water more quickly and reached a water content of 5.5 % over 9 months, but was still not fully re-saturated. In contrast to that, another core DIR2004-EST27315 with a higher initial water content seemed to be fully re-saturated after 5 months. Because the samples were more or less disturbed by preparation and re-saturation, some visible cracks appeared on the surfaces and were mostly oriented parallel to the horizontal bedding planes. Their basic characteristics are summarized in tab. 2.6.

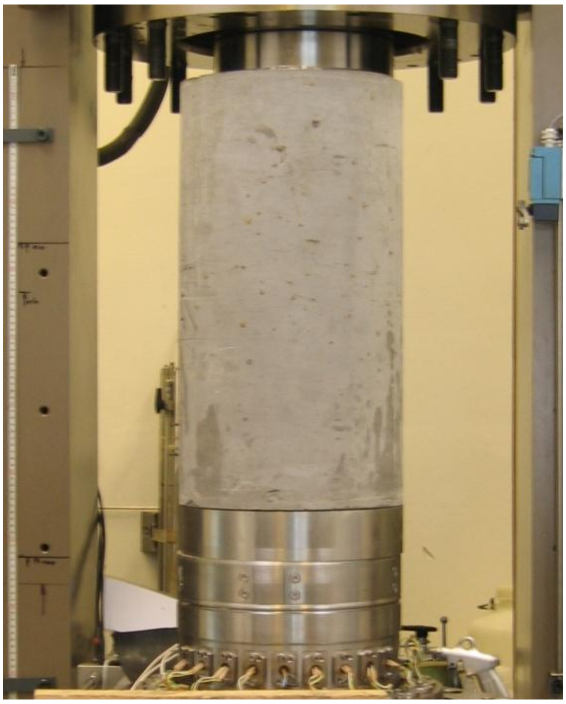

BMT1: DIR2003-EST19387
D280/d100/L525mm


BMT2 : DIR1004-EST27319
D280/d100/L520mm


BMT3: DIR2004-EST27315
D280/d100/L520mm


BMT4 : DIR2004-EST27312
D280/d100/L460mm

**Fig. 2.68** Large hollow cylinders prepared for the investigation of fracturing and sealing of the COX argillite

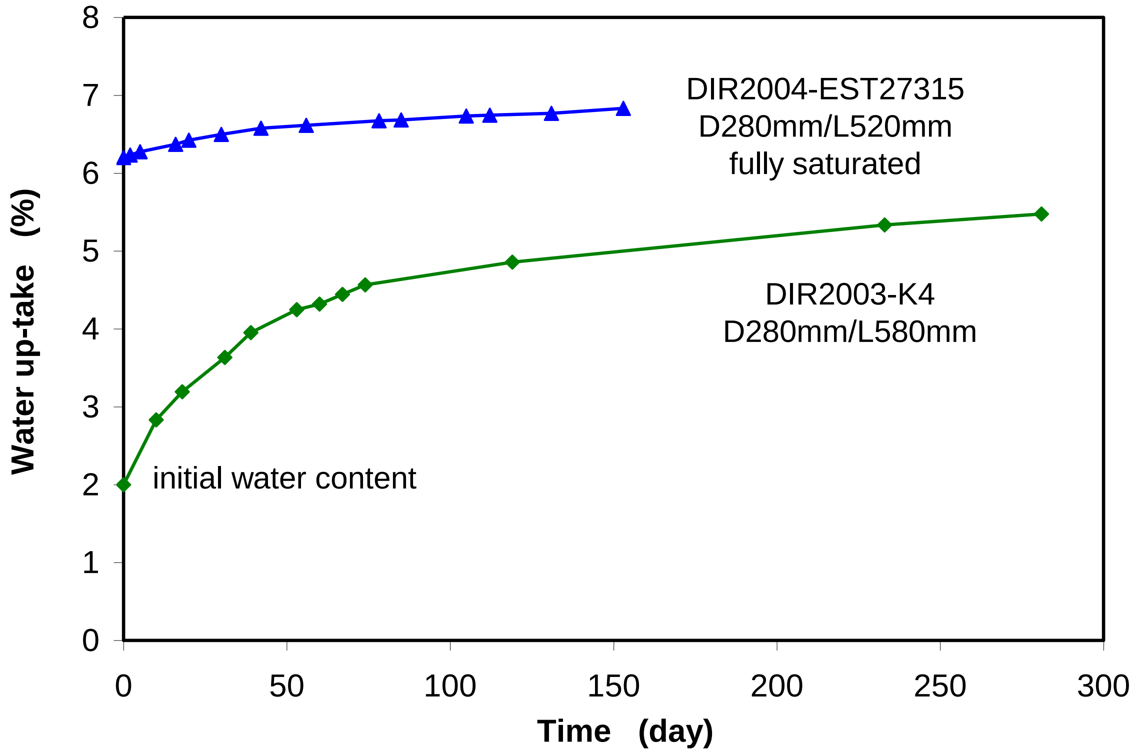


**Fig. 2.69** Water re-saturation of large COX samples with water vapour

**Tab. 2.6** Basic characteristics of the large COX hollow cylinders used in the EDZ-simulation tests

| Test No. | Sample | Size D/d/L (mm) | Grain density ($g/cm^3$) | Bulk density ($g/cm^3$) | Dry density ($g/cm^3$) | Porosity (%) | Water content (%) | Degree of saturation (%) | Initial suction (MPa) |
|---|---|---|---|---|---|---|---|---|---|
| BMT1 | DIR2003-EST19387 (-460m) | D280 d100 L525 | 2.70 | 2.41 | 2.28 | 15.4 | 5.5 | 82.0 | 23.0 |
| BMT2 | DIR1004-EST27319 (-501m) | D280 d100 L520 | 2.70 | 2.43 | 2.28 | 15.7 | 6.8 | 98.0 | 5.0 |
| BMT3 | DIR2004-EST27315 (-461m) | D280 d100 L520 | 2.70 | 2.45 | 2.29 | 15.0 | 6.8 | 100.0 | 0.0 |
| BMT4 | DIR2004-EST27312 (-463m) | D280 d100 L460 | 2.70 | 2.41 | 2.26 | 15.8 | 6.2 | 89.0 | 10.0 |

Originally, a reference BMT test was planned and designed. Fig. 2.70 shows the test layout and a photo of an installed large hollow cylinder. An inflation packer is installed in the central borehole for simulating the backfill support. The packer allows a maximal pressure of 15 MPa and is controlled by a precise syringe pump with oil supply. The external stress around the borehole is applied by regulating the outer axial load and lateral pressure in the cell. Thermal loading due to the heat release of HLW is simulated by means of an outer heater mounted around the outer surface of the cell. During the test, the outer radial strain is recorded by a circumferential extensometer at the sample mid-height, while axial strain is measured by a LVDT deformation transducer mounted to the lower piston outside the cell. Additionally, borehole convergence or divergence is monitored by measuring changes of the oil volume in the central packer. The temperature is recorded by two PT100 sensors in the borehole and on the outer surface of the sample, respectively. Permeability changes of the hollow cylinder are monitored in axial direction by injecting nitrogen gas or synthetic formation water to the bottom at constant pressure and by measuring the outflow at the top.

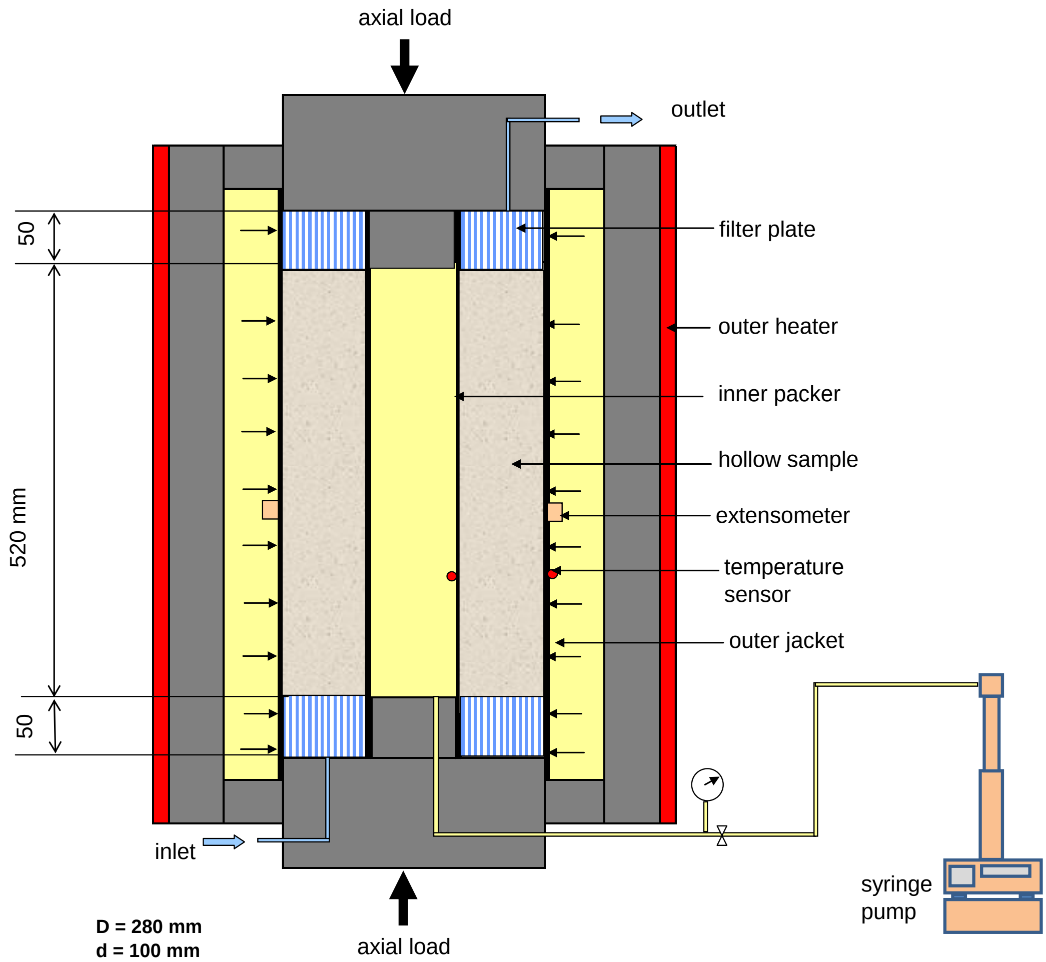


**Fig. 2.70** Layout of EDZ simulation tests on a large hollow cylinder of COX claystone

The measurements of stress and strains are evaluated according to eq. (2.19) to (2.23), while the permeability to gas and synthetic water is calculated after Darcy's law:

**Gas permeability**

$$K_g = 2\mu_g \frac{p_a \cdot Q_g}{(p_{in}^2 - p_a^2)} \cdot \frac{L}{A_{ring}} \tag{2.24}$$

where $K_g$ = gas permeability ($m^2$),

$Q_g$ = flow rate of the gas ($m^3/s$),

$\mu_g$ = dynamic viscosity of the gas (Pa·s),

$L$ = length of the sample (m),

$A_{ring}$ = the section of the hollow sample ($m^2$),

$p_a$ = atmospheric pressure (Pa),

$p_{in}$ = injection pressure (Pa).

**Water permeability**

$$K_w = \frac{Q_w \cdot \mu_w \cdot L}{A_{ring} \cdot \Delta p} \tag{2.25}$$

where $K_w$ = water permeability ($m^2$),

$Q_w$ = flow rate of the water ($m^3/s$),

$\mu_w$ = dynamic viscosity of water (Pa·s),

$\Delta p$ = pressure difference (Pa).

The *in situ* conditions of the TER heating experiment conducted in the MHM-URL (see section 3.4) were taken into account in the BMT test design. The main purpose of the TER experiment was to determine the thermal properties and to observe THM processes in the COX clay rock. The surrounding rock was heated by means of an electric heater from an ambient temperature of 22 °C to 90 °C and then cooled down. Responses of rock temperature, pore-water pressure, and deformation were monitored at different locations in the near-field. An anisotropic stress state dominates in the rock with a major horizontal component of $\sigma_H$ = 16 MPa, a minor horizontal component of $\sigma_h$ = 12 MPa and a vertical component of $\sigma_v$ = 12 MPa. The axis of the TER heater borehole was oriented parallel to the direction of the major horizontal stress. The pore water pressure in the rock is estimated to 4.5 MPa.

Before testing, a general test procedure was agreed:

1. Determination of the initial state of the hollow cylinder

2. Pre-consolidation of the sample at increased compressive load to approach the original rock state

3. Borehole excavation by reduction of the inner pressure in the borehole

4. EDZ intensification by increasing external stress to generate sufficient fractures for to enable subsequent investigations on the sealing of the fractures

5. Re-compaction of the fractured sample by increasing the inner borehole pressure to investigate the effect of the backfill pressure on the sealing of the fractures

6. Injection of synthetic water to simulate the flow of formation water towards the EDZ

7. Heating the sample to the upper limit of 90 °C in order to investigate the thermal impact on the sealing of the EDZ

8. Cooling down to ambient temperature

9. Unloading, dismantling and inspection of the sample.

Obviously, conducting such a very complex experiment is a great challenge for the experimenter. Because of unexpected technical difficulties, the spent efforts exceeded the original plans with only one test significantly. In reality, three additional tests were conducted after stepwise improvements of the test design and techniques.

#### 2.7.2.2 Results

**BMT test 1**

The first test was carried out on sample DIR2003-EST19387. Fig. 2.71a illustrates the evolution of applied temperature, axial and radial confining stress, and back-pressure in the borehole, while the responses of axial strain, outer radial strain, and gas permeability are presented in fig. 2.71b. The test started with the application of the initial conditions of T = 26 °C and $\sigma_a = \sigma_R = \sigma_r$ = 1 MPa for the first day.

1. A reconsolidation phase was conducted by quasi-isotropic loading at a rate of 6 MPa/h up to an axial stress of $\sigma_a$ = 17 MPa and an outer radial stress and inner borehole pressure of $\sigma_R = \sigma_r$ = 15 MPa. This load caused a compression to an axial strain of $\varepsilon_a$ = 0.8 % and an outer radial strain of $\varepsilon_R$ = 0.2 %. The relatively large axial strain was mainly generated by closure of the pre-existing cracks oriented along

the horizontal bedding planes. At the end of the consolidation, the gas permeability parallel to the borehole was determined to $K_g = 2 \cdot 10^{-21}$ $m^2$ at an injection pressure of 1.5 MPa.

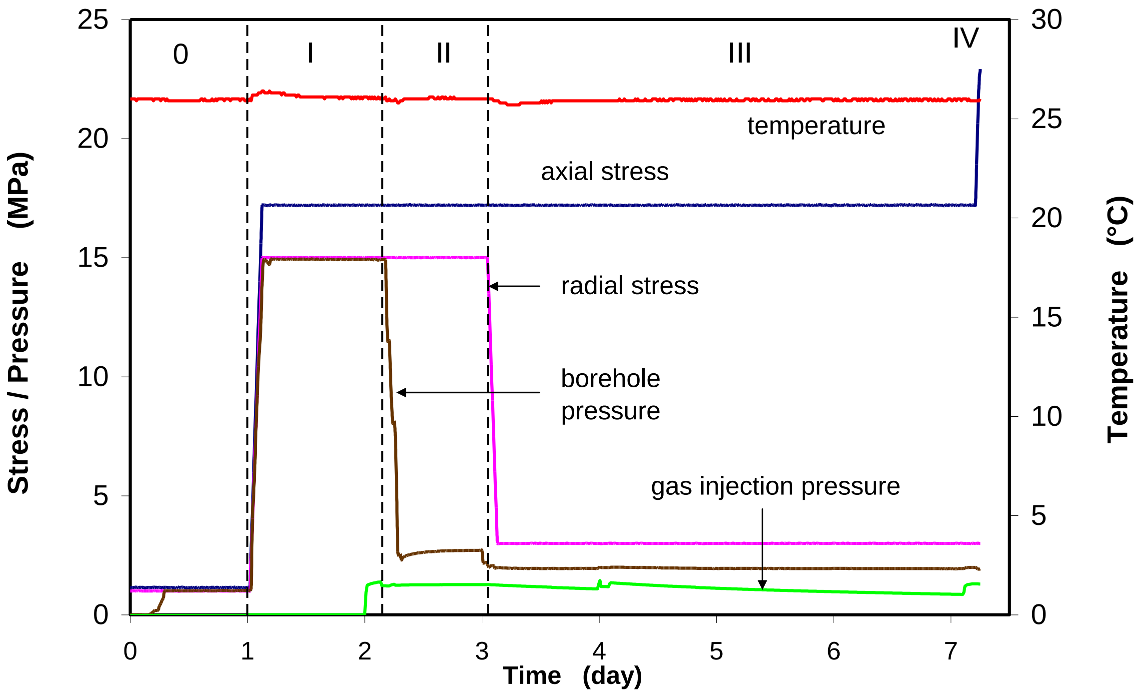


(a) boundary conditions of temperature, external stresses and borehole pressure

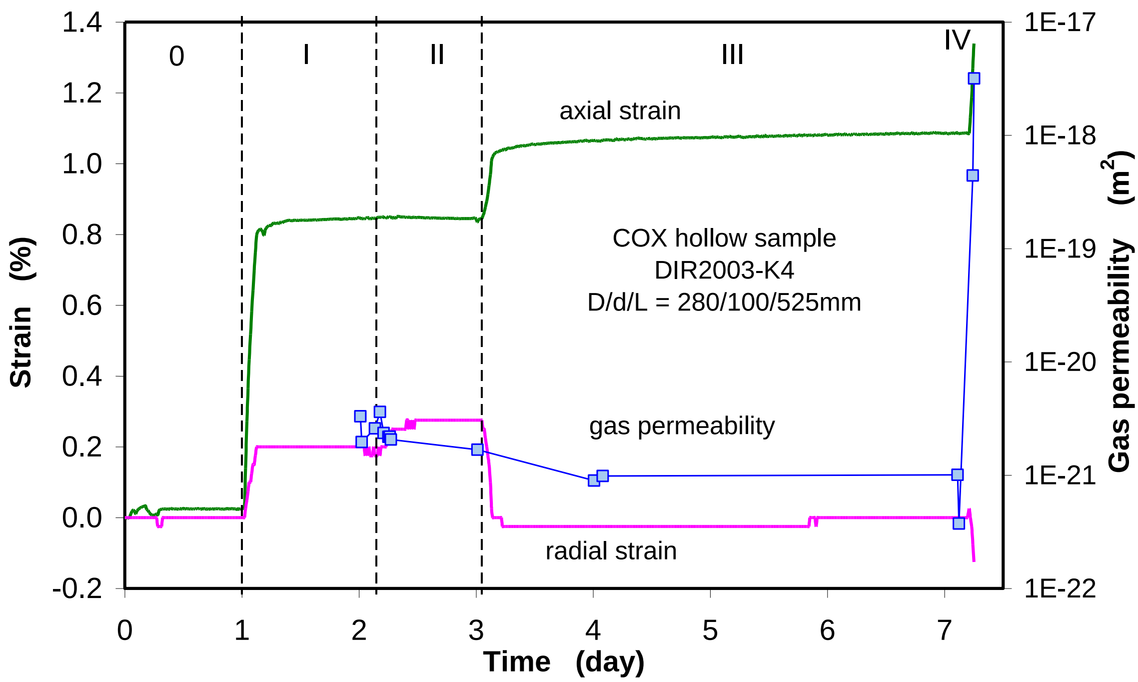


(b) responses of strains and gas permeability to mechanical loading

**Fig. 2.71** Results of the BMT test 1 on a large COX hollow cylinder

2. Subsequently, borehole excavation was simulated by decreasing the borehole pressure down to 2.6 MPa. This resulted in a convergent deformation towards the borehole, while the axial strain remained nearly constant. However, the reduction of the borehole pressure obviously did not generate pathways through the hollow cylinder, because no increase in permeability could be detected.

3. In order to intensify the deformation to damage, the deviatoric load was increased by reducing the radial stress to 3 MPa at the constant axial stress of 17 MPa. This resulted in a significant radial extension of $\Delta\varepsilon_R \approx 0.3$ %. But again, no increase of the permeability could be observed. A significant permeability increase was firstly recorded by additionally increasing the axial load to failure at 23 MPa. Just before failure, the permeability jumped up from 1·10-21 $m^2$ to 3·10-18 $m^2$.

**BMT test 2**

The second test was performed on sample DIR1004-EST27319 and because of a test interruption evaluated in two parts. The test results are shown in fig. 2.72 and fig. 2.73, respectively. The test started at T = 26 °C and $\sigma_a = \sigma_R = \sigma_r = 1$ MPa.

1. The hollow cylinder was firstly reconsolidated by rising the isotropic stress from $\sigma_a = \sigma_R = \sigma_r = 1$ MPa to 15 MPa at a temperature of 26 °C. This resulted in an axial compression of $\varepsilon_a = 0.55$ %, but a negligible radial strain. The anisotropic deformation of the argillite was due to the existence of bedding planes perpendicular to the sample axis.

2. At a constant confining stress of $\sigma_a = \sigma_R = 15$ MPa, the borehole excavation was simulated by decreasing the borehole pressure down to 1.8 MPa. This caused an axial compression of $\Delta\varepsilon_a \approx 0.1$ % and a radial strain of $\Delta\varepsilon_a \approx 0.05$ % towards the borehole. At the end of the unloading phase, the gas flow was first measured at a pressure of 1.5 MPa, from which the permeability was determined to $3 \cdot 10^{-19}$ $m^2$.

3. Following that, the backfill impact was approached by increasing the borehole pressure step by step to 6, 8, 10, 12 and 15 MPa for several days in each step. The backfill pressure compressed the existing cracks in the sample and reduced the permeability down to $10^{-21}$ $m^2$.

4. To create macro-fractures, various deviatoric stresses were applied to the hollow cylinder. First, the axial stress was increase to 20 MPa at a radial stress of 15 MPa. This caused an axial compression of $\Delta\varepsilon_a = 0.12$ %, a radial extension of $\Delta\varepsilon_R$

= -0.03 % and a slight increase in permeability. Secondly, the borehole pressure was reduced down to 1.5 MPa, causing radial strain towards the hole but no increase in permeability. Finally, the external axial and radial stresses were significantly increased, causing large axial / radial strains up to fractures and hence permeability increase. At $\sigma_R$ = 25 MPa and $\sigma_a$ = 24 MPa, the permeability started to rise and reached a maximum value of $10^{-16}$ $m^2$ at $\sigma_R$ = 28 and $\sigma_a$ = 25 MPa. Unfortunately, the test was interrupted due to the damage of the rubber jacket.

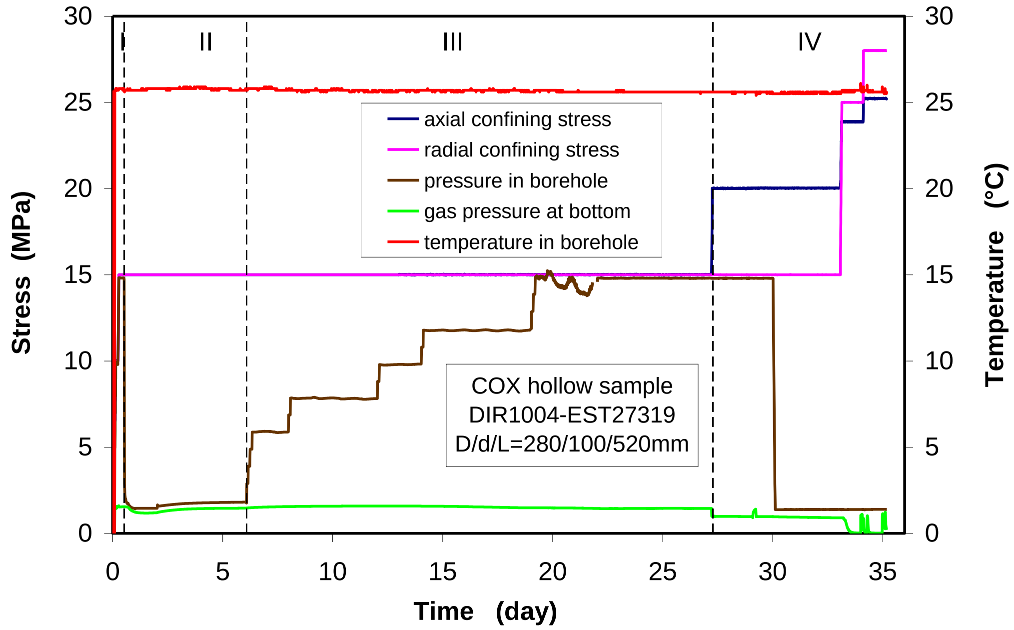


(a) boundary conditions of temperature, external stresses and borehole pressure

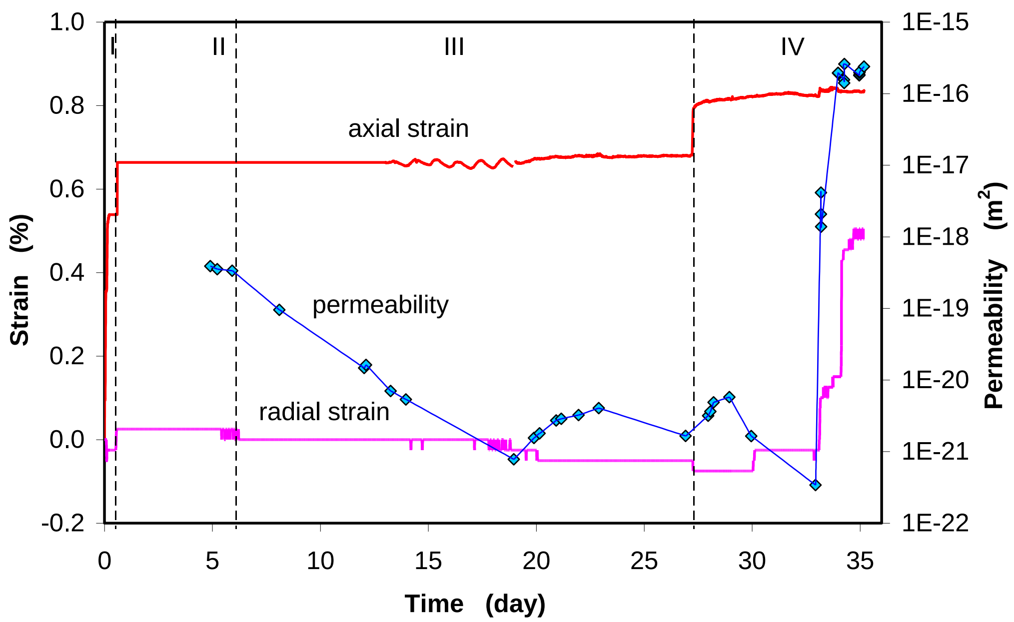


(b) responses of strains and gas permeability to mechanical loading

**Fig. 2.72** First part of BMT2 test results obtained on a large COX hollow cylinder

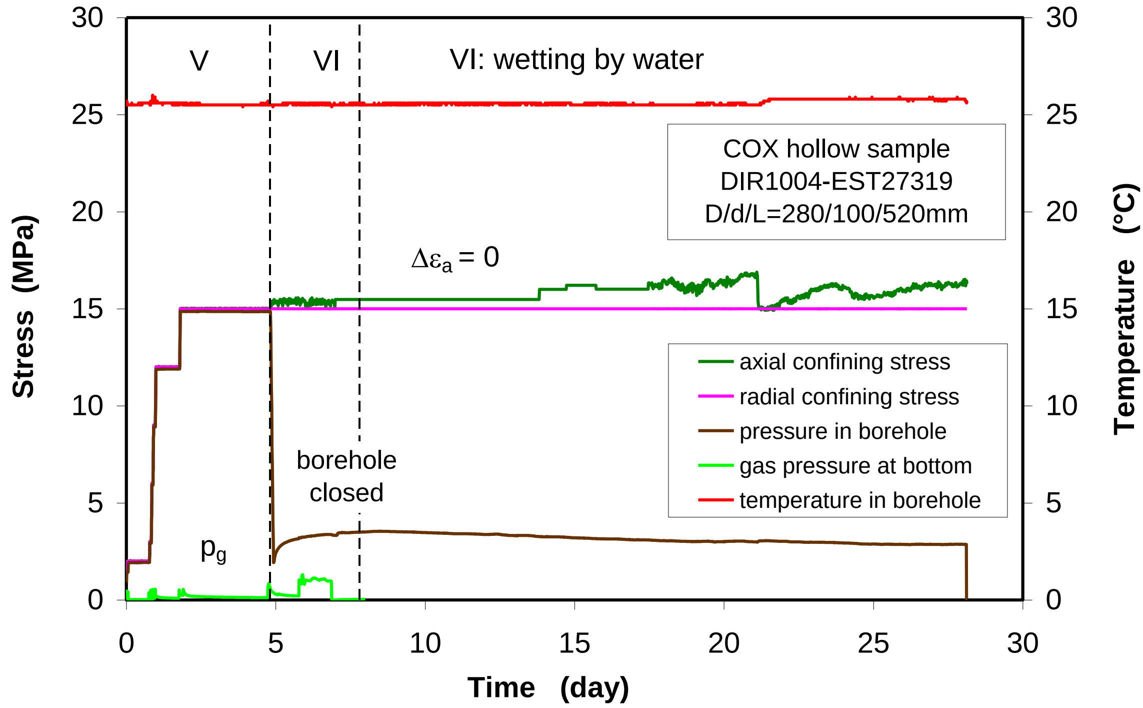


(a) boundary conditions of temperature, external stresses and back-pressure

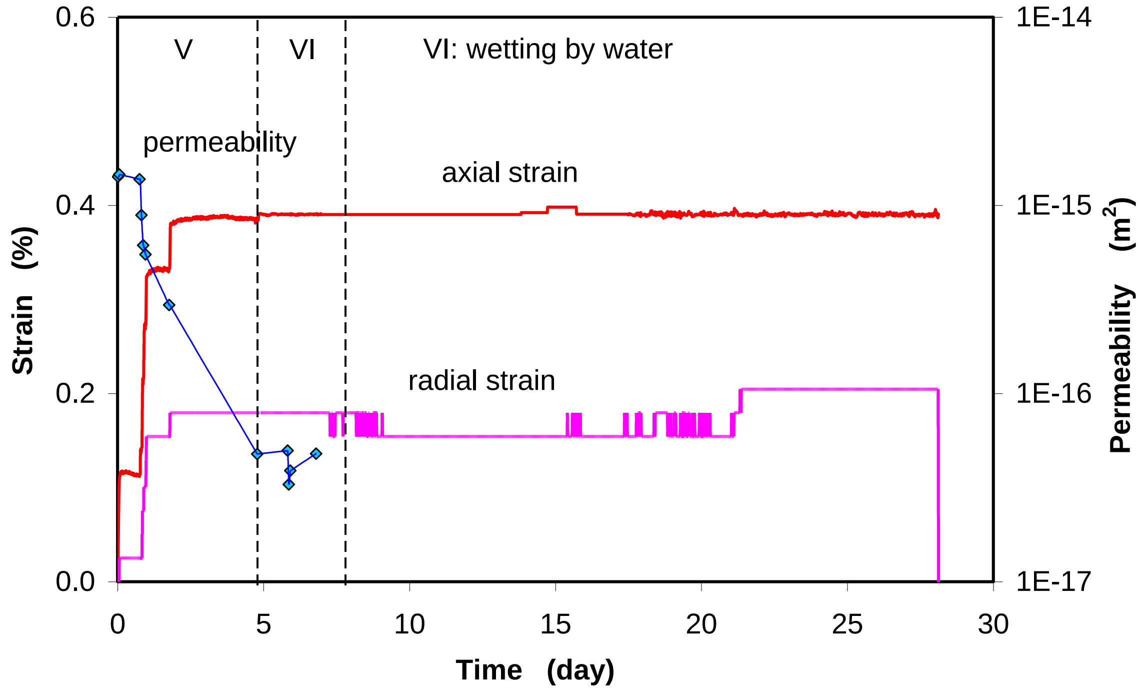


(b) responses of strains and gas permeability to mechanical loading

**Fig. 2.73** Second part of BMT2 test results obtained on a large COX hollow cylinder

5. Using a new jacket, the test was continued with re-compaction by increasing the isotropic stress up to 15 MPa again (fig. 2.73a). This caused a pronounced decease of the permeability from $1 \cdot 10^{-15}$ m$^2$ to $4 \cdot 10^{-17}$ m$^2$.

6. The following reduction of the borehole pressure down to 2.3 MPa did not produce any increase in permeability. In order to simulate a water flow towards the EDZ, synthetic formation water was introduced into the fractured cylinder at both ends at atmospheric pressure. At fixed axial strain, the axial stress varied slightly. This might be induced by swelling of clay minerals. Unfortunately, an interruption of the power supply terminated the test.

**BMT test 3**

The third test was performed on sample DIR1004-EST27315. Because of technical problems, the test results could not be evaluated.

**BMT test 4**

Based on the experiences from the above tests and the pre-experimental calculations, the originally designed test layout was slightly improved in the fourth test on sample DIR1004-EST27312. Fig. 2.74 shows the modified test layout and photos of the sample before testing. The pre-operational modelling indicates that local densification may have taken place at the ends of the sample due to the possible effect of the friction resistance of the load pistons, forming a barrier against fluid flow into the EDZ around the borehole. In order to avoid such local sealing effect, several small half-holes of 5 mm diameter were drilled from the top and the bottom to a depth of 60 mm along the borehole wall. The channels allowed a fluid supply directly into the middle region near the borehole wall. In addition to the measurement of the outer radial strain at the middle, another circumferential extensometer was installed at the lower position of ¼ sample length. A syringe pump was connected with the inlet tube at the top to inject synthetic formation water into the sample. While the injection pressure and flux could be automatically controlled and recorded by the pump, the water outflow was measured at the bottom using a burette at atmospheric pressure.

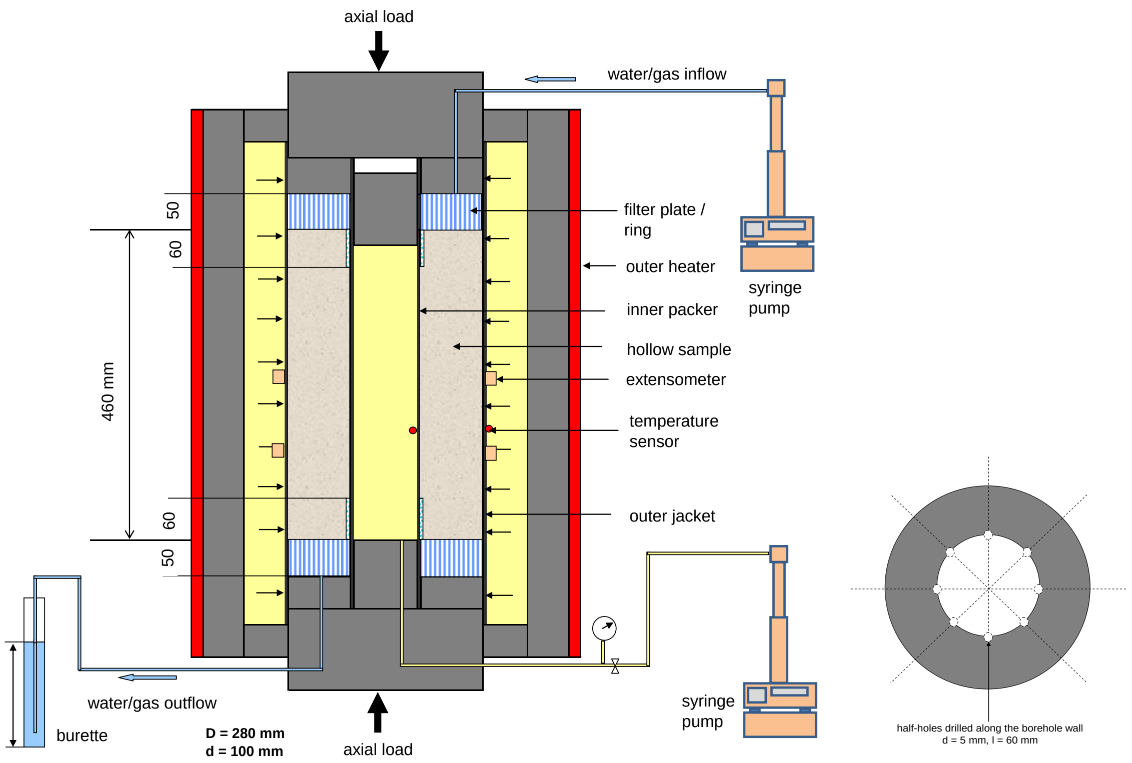


**Fig. 2.74** Modified test layout of the BMT test 4 on a large COX hollow cylinder

Fig. 2.75a illustrates the test procedure performed in six phases with respective boundary conditions, i. e. recovery of the initial state, borehole excavation, damage intensification, water injection, heating and cooling phases. Responses of deformation, gas permeability and water inflow / outflow are depicted in fig. 2.75b/c/d. The test results are described as follows:

1. **Initial state**: The test started from an initial isostatic stress of $\sigma$ = 1.0 MPa, a gas inlet pressure $p_g$ = 0.5 MPa, an outlet pressure $p_o$ = atmospheric, and a temperature T = 29 °C. The big hollow cylinder was reconsolidated by increasing the outer radial stress and the borehole pressure up to $\sigma_R = \sigma_r$ = 15 MPa at fixed axial strain ($\Delta\varepsilon_a$ = 0). This stress state is comparable to the lithostatic stress at the 490m main level of the MHM URL. The initial state of the sample was determined with a porosity of $\phi_o$ = 15.8 %, a degree of water saturation of 89 % (corresponding to suction *s* = 10 MPa), and an effective gas permeability of $5 \cdot 10^{-21}$ $m^2$ (fig. 2.75c). Since dry nitrogen gas had been injected into the sample over 5 days before the initial point, the sample might have become more unsaturated. But unfortunately, it was impossible to monitor changes of the water content during the test.

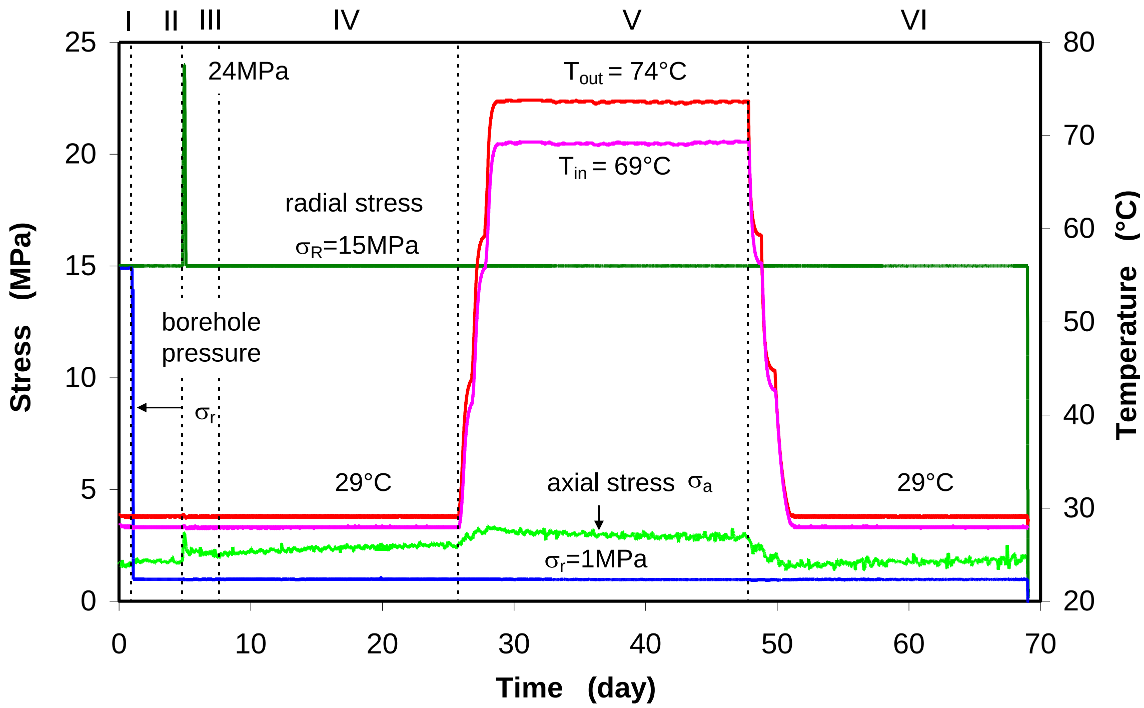



(a) boundary conditions of temperature, external stresses and borehole pressure

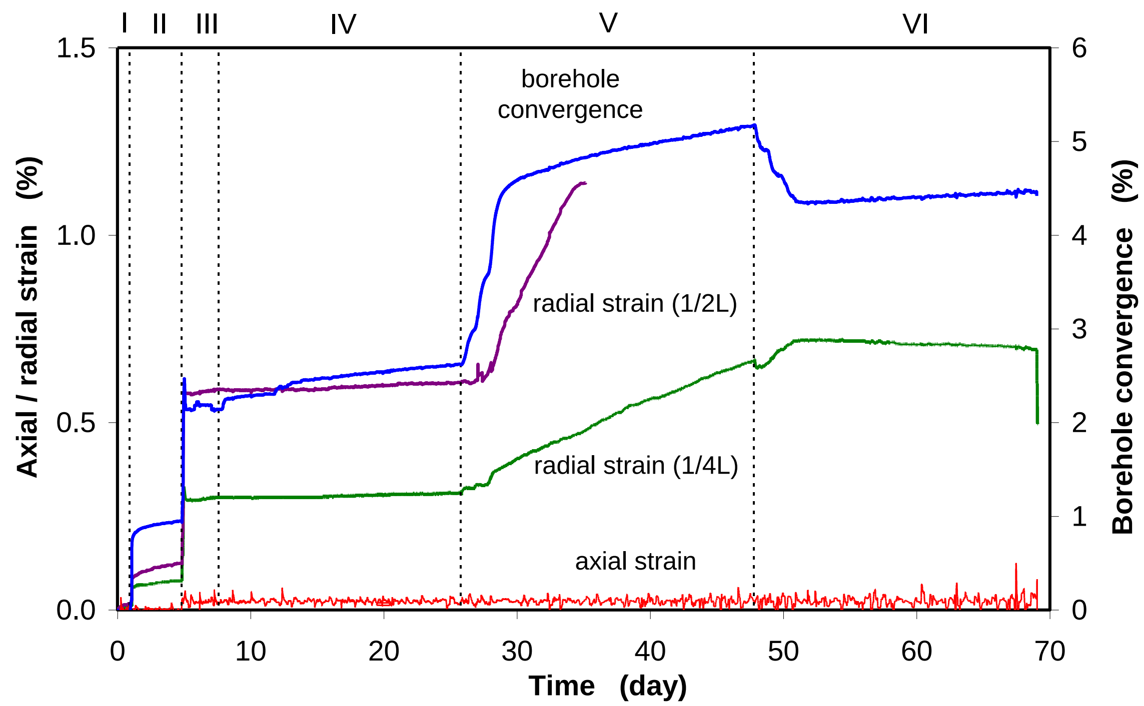



(b) responses of strains and borehole convergence to mechanical and thermal loading

**Fig. 2.75** Results of BMT test 4 simulating excavation, backfill support, water flow, heating and cooling on a large COX hollow cylinder

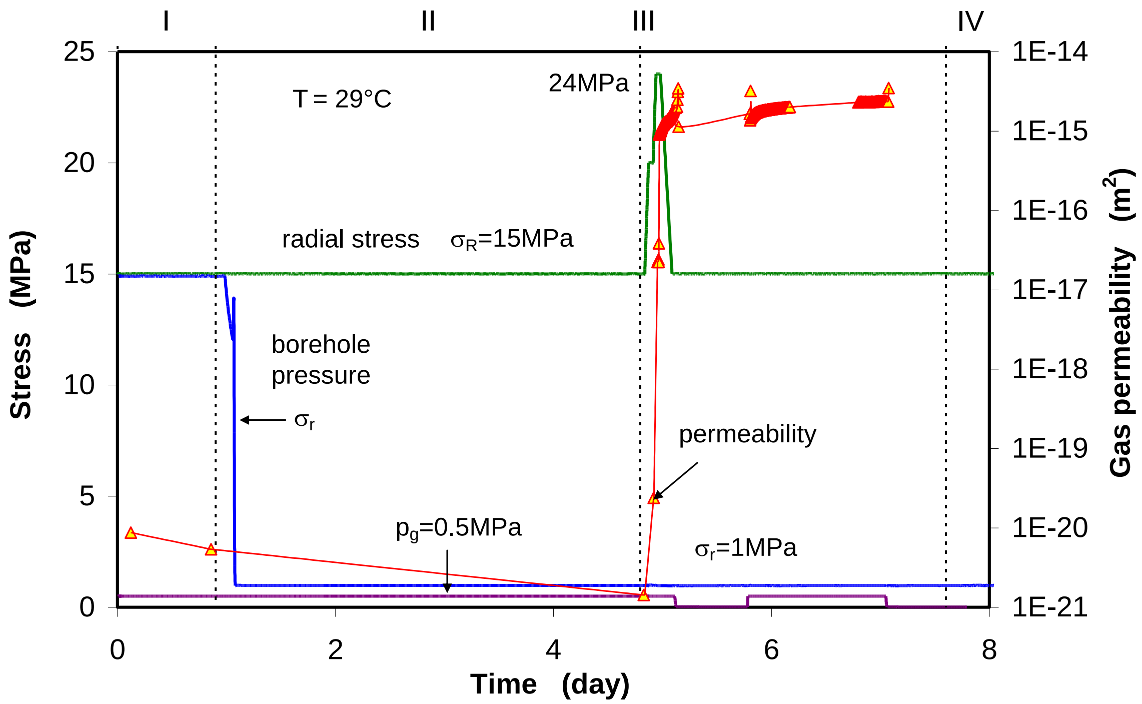


(c) changes in gas permeability due to mechanical loading

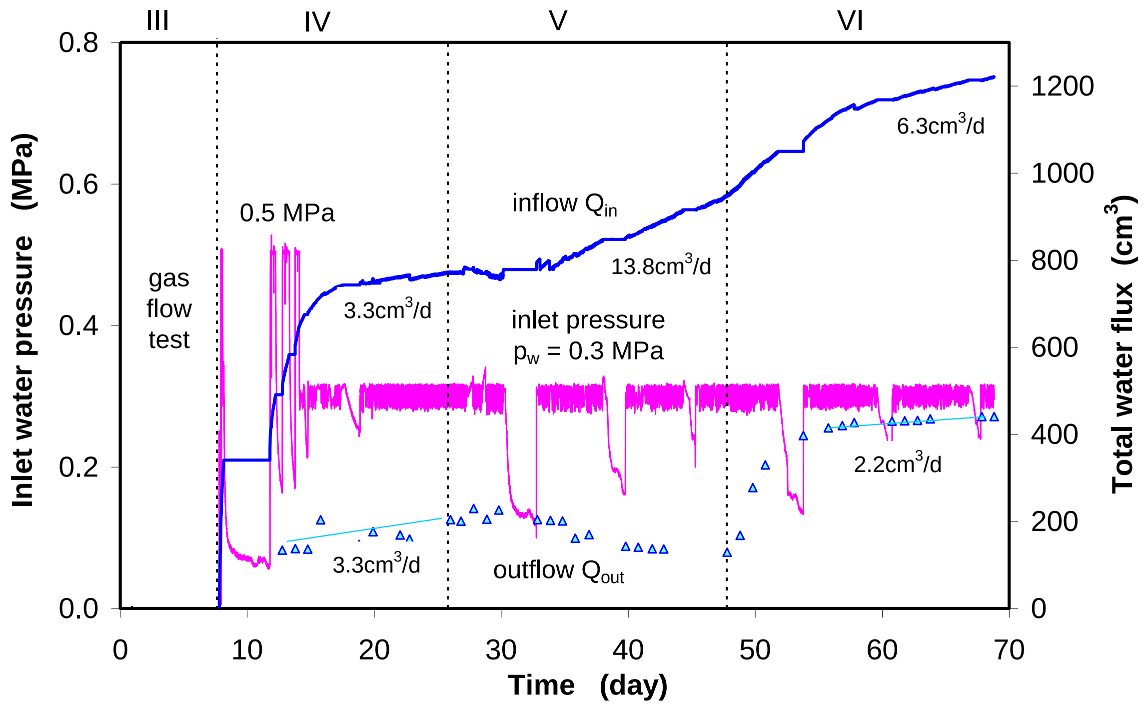


(d) water entering flux during the heating / cooling cycle

**Fig. 2.75** Results of BMT test 4 simulating excavation, backfill support, water flow, heating and cooling on a large COX hollow cylinder [Continued]

2. **Borehole excavation**: From the re-consolidated state, the borehole excavation was simulated by reducing the borehole pressure down to $\sigma_r$ = 1.0 MPa. Fig. 2.75b shows that the excavation resulted in a convergence of the borehole to $\varepsilon_r$ = 0.95 %

and the outer wall of the cylinder was displaced inwardly to a compressive strain of $\varepsilon_{R-1/2L}$ = 0.12 % at the middle and $\varepsilon_{R-1/4L}$ = 0.08 % at the position of ¼ length of the sample. The zone near the borehole should be damaged according to the *in situ* observations (TER experiment). However, no increase in gas permeability (fig. 2.75c) was recorded, suggesting that no pathway through the middle region of $\Delta L$ = 340 mm was created by the borehole excavation.

3. **EDZ-intensification**: In order to determine the critical condition for generating a flow pathway around the borehole, the external stress was further increased. As the stress $\sigma_R$ was over 20 MPa, the gas permeability started to rise and reached a value of $10^{-15}$ $m^2$ at $\sigma_R$ = 24 MPa. This permeability value is six orders of magnitude higher than it was before. With increasing the load, the outer surface of the cylinder moved largely inwards with $\varepsilon_{R-1/2L}$ = 0.6 % and $\varepsilon_{R-1/4L}$ = 0.3 %. With that the borehole became more narrow with $\varepsilon_r$ = 2.4 %. Immediately after gas break through, the external radial stress was reduced again down to 15 MPa for another 2 days, during which the deformation and the gas flow remained nearly constant.

4. **Water injection**: In order to simulate formation water flow towards the EDZ, synthetic pore water was introduced into the top of the fractured sample. The applied absolute injection pressure, the water inflow and the outflow are illustrated in fig. 2.75d. The first injection began at a pressure of 0.5 MPa and the water entered the sample quickly with $Q_{in}$ = 340 $cm^3$ within 8 hours. After closing the inlet, the water pressure in the inlet reservoir dropped down to atmospheric pressure (~0.1 MPa). After 4 days, the procedure of injection and closing was repeated several times within the next 3 days, during which the amount of injected water reached an amount of $Q_{in}$ = 675 $cm^3$ and a water outflow of $Q_{out}$ = 135 $cm^3$. The difference of $\Delta Q = Q_{in} - Q_{out}$ = 540 $cm^3$ between the inflow and the outflow was stored in the sample (mostlikely in the fracure space). Following that, the injection pressure was lowered to 0.3 MPa. Correspondingly, the water inflow slowed gradually and reached a quasi-steady state after several days. The recorded outflow rate is nearly the same as the inflow rate of 3.3 $cm^3$/d. From the data and the water viscosity of $8.5 \cdot 10^{-4}$ Pa·s at T = 29 °C, a water permeability of $2.0 \cdot 10^{-18}$ $m^{-2}$ can be estimated for the fractured cylinder. This value is three orders of magnitude lower than that measured with gas before in the interval III. The reduction of the intrinsic permeability by the flowing water is obviously caused by the clay swelling into the interstices. During the period of water injection, the axial stress at fixed strain ($\Delta\varepsilon_a$ = 0) increased progressively from 2.1 to 2.5 MPa (fig. 2.75a), while the borehole diame-

ter reduced from $\varepsilon_r$ = 2.2 % to 2.6 % over 17 days (fig. 2.75b). The movement of the outer sample surface towards the borehole was insignificant during the water injection phase.

5. **Heating** was performed by increasing the boundary temperature day by day from $T_{out}$ = 29 to 45, 60 and 74 °C. The last step continued for 19 days. Because the testing system was not thermally isolated in axial direction, a steady heat loss caused a temperature gradient between the outer and the inner boundary of the hollow cylinder of $\Delta T$ = 2 to 5 °C with increasing temperature. Fig. 2.75b shows that the heating accelerated the deformation towards the borehole. The compressive strain of $\varepsilon_{R-1/2L}$ at the middle was faster than $\varepsilon_{R-1/4L}$ at the lower position. Whereas the strain $\varepsilon_{R-1/4L}$ increased continuously, the measurement of $\varepsilon_{R-1/2L}$ unfortunately failed after reaching a value of 1.14 %. The borehole diameter decreased by elevating the temperature and then the convergence continued up to $\varepsilon_r$ = 5.2 % over the heating phase. The water flow slightly turned backwards at the beginning of heating (fig. 2.75d). After that, the water flowed inwards again and reached a high rate of 13.8 $cm^3$/d during the last 10 days. The increased inflow was caused by the decreased water viscosity of $4.4 \cdot 10^{-4}$ Pa·s at 74 °C. The intrinsic permeability of the fractured sample was not significantly influenced by heating. The measurement of outflow showed a backflow of the water into the sample. The reason is not yet clear. Additionally, switching off the inlet flow resulted each time in a drop of the inlet pressure.

6. **A cooling** phase followed by reducing the temperature stepwise down to 60, 45 and 29 °C in 3 days and the last step continued for 18 days. The cooling down led to an enlargement of the borehole of $\Delta\varepsilon_r$ = -0.8 % whereas the outer surface at ¼L position expanded transiently and then turned back to compression. This might be due to thermal contraction of the material. At the lowered temperature, the borehole convergence continued slowly while the outer surface remained almost constant. The borehole convergence rate (slope of the curve) is lower than that during the heating phase, but nearly the same as that before heating. As shown in fig. 2.75d, the cooling down caused higher water inflow and outflow in a short time and then the inflow and outflow slowed gradually down with different rates. While the inflow rate was determined to 6.3 $cm^3$/d within the last 10 days, a lower outflow rate of 2.2 $cm^3$/d was measured. Based on the data, the permeability can be roughly estimated between $1.2 \cdot 10^{-18}$ and $3.5 \cdot 10^{-18}$ $m^{-2}$, a value which is comparable with that obtained before heating. Generally speaking, the thermal impact on the hy-

draulic conductivity of the fractured argillite is controlled by the variation of the water viscosity. This means also that the thermal effect on the development of fractures in the argillite under certain confinements is insignificant.

7. **Dismantling and post-testing**: Fig. 2.76 shows pictures of the dismantled sample after testing. Multiple macro-fractures were generated and interconnected vertically and horizontally. In the upper region the fracturing was more intensive, probably due to the reduction of the stiffness and strength of the argillite by the increasing water content.


outer surface | vertical section | inner surface

**Fig. 2.76** Dismantled sample after EDZ-simulation test BMT 4

The water content of the tested sample was measured on pieces taken from different locations. The distribution of the water content along the sample is illustrated in fig. 2.77. The water content reached a maximum of more than 9.3 % at the top where water was injected and reduced linearly down along the sample to 6.2 % at the bottom. This value is the same as the initial water content. Above the position of L = 150 mm, the water content was higher than that of 6.8 % of the originally saturated argillite. This result indicates that the natural argillite has also a certain adsorption potential for taking up more water. The water adsorption potential was examined on a large piece of 2.67 kg from the tested sample. Fig. 2.78 shows the amount of water uptake by the material immersed into synthetic formation water. It is obvious that the water content increased rapidly in the first two days and reached a maximum of ~13 % after 6 days. This value is much higher than the water content in the naturally saturated state (~6.8 %), confirming the high adsorption potential of the clay rock.

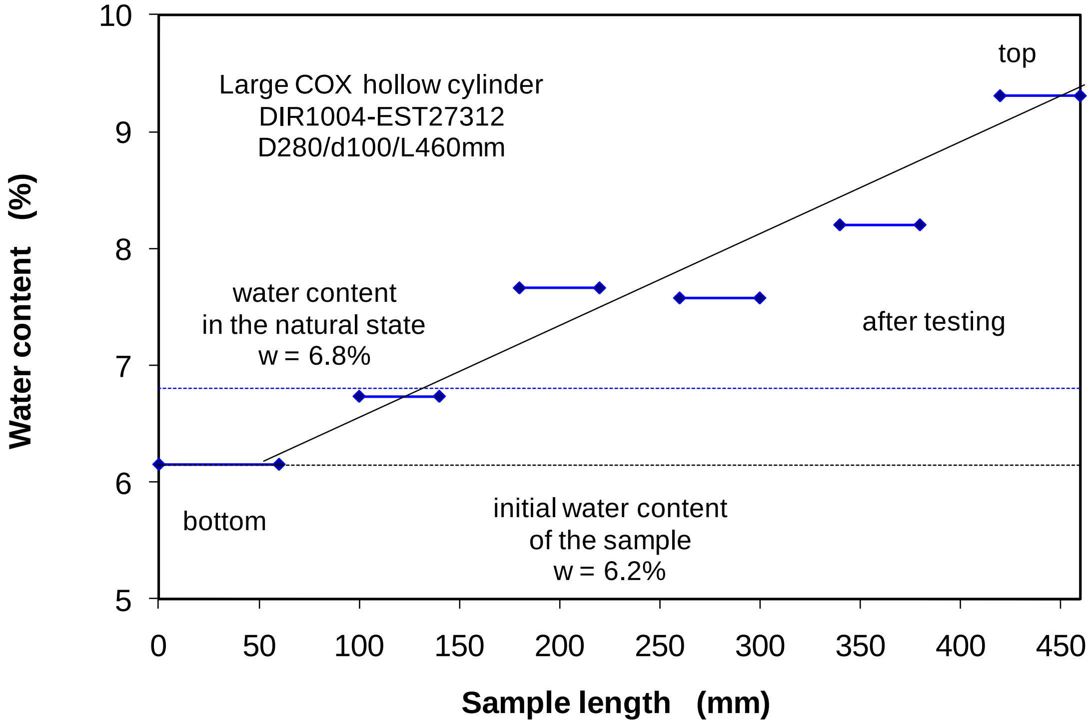


**Fig. 2.77** Distribution of the water content determined on the tested sample

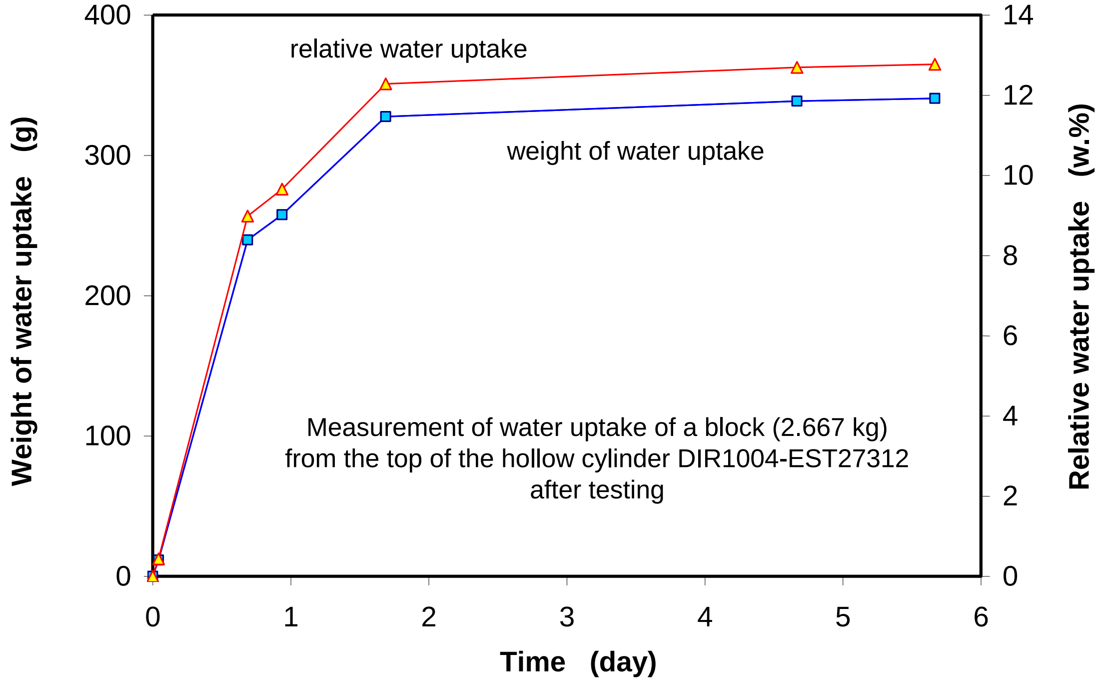


**Fig. 2.78** Measurement of water uptake on a large COX block immersed into synthetic pore water

Additionally, the outer diameter of the deformed cylinder was measured along the sample length, as shown in fig. 2.79. The higher wetted upper area expanded over the initial diameter due to the swelling of clay minerals, while the middle region was more compressed towards the borehole. The deformation in the lower region was insignificant. The measuring system was re-calibrated after testing.

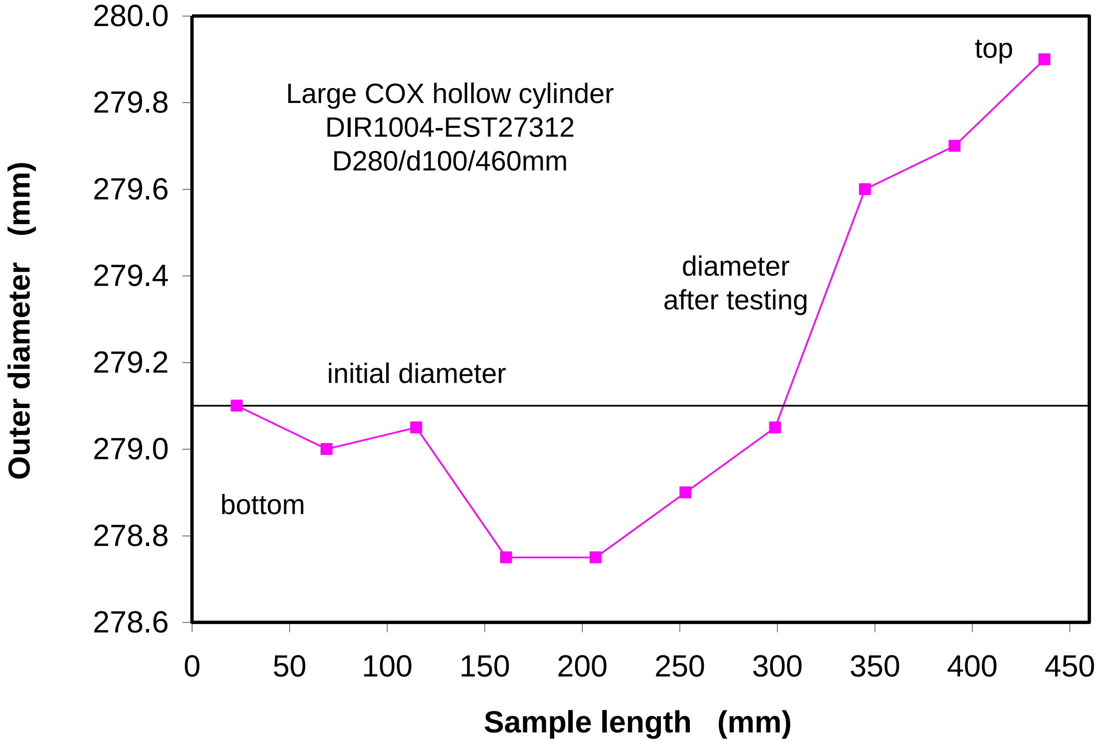


**Fig. 2.79** Outer diameter profile along the deformed cylinder

Fig. 2.80 and fig. 2.81 show the results of the volume measurement of the central borehole against the packer inflation pressure and temperature changes, respectively. The calibration curves are taken into account in the above evaluation of the borehole convergence.

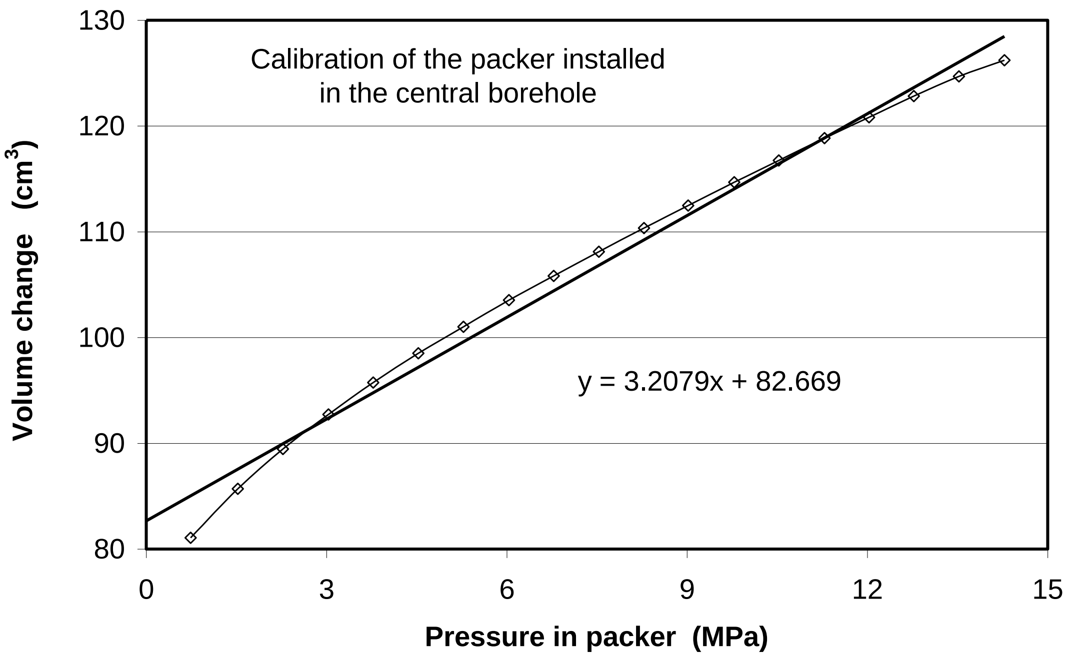


**Fig. 2.80** Measurement of the packer volume change versus the inflation pressure

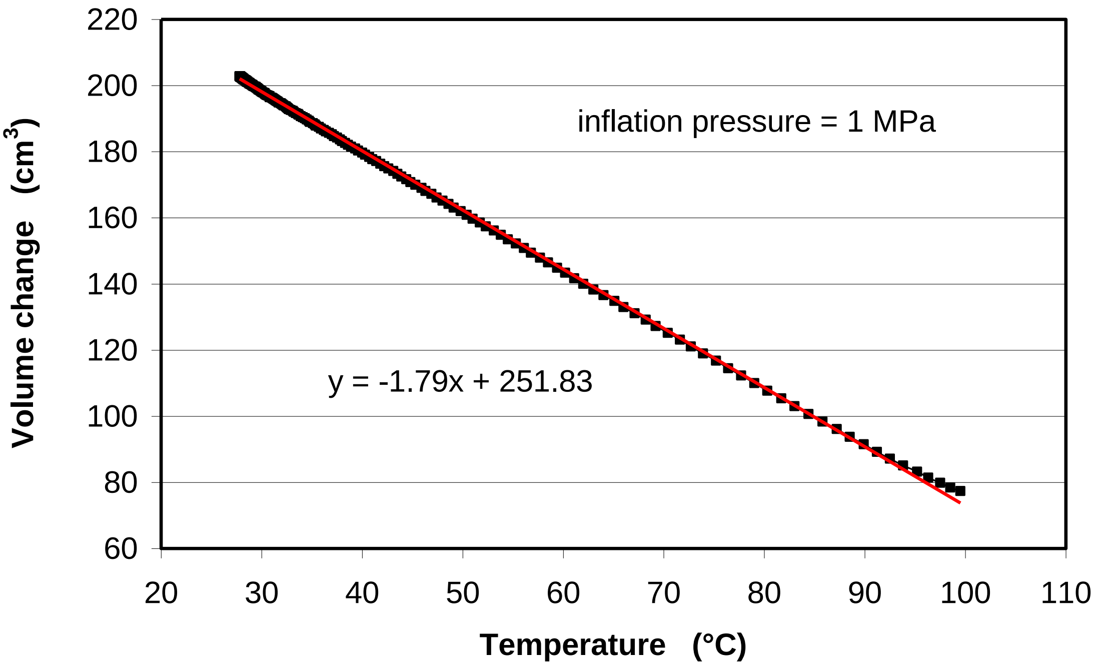


**Fig. 2.81** Measurement of the packer volume change versus temperature

### 2.7.3 Conclusions on the EDZ development around boreholes

For the validation of the constitutive models and computer codes used for analysing THM processes in the excavation damaged zone in argillaceous rock, a number of laboratory simulation tests was performed on large COX argillite cylinders with axially-drilled central boreholes (D = 280 mm, d = 55/100 mm, L = 460 – 650 mm) in the framework of the TIMODAZ project /D07 10/. In the tests, the relevant conditions around HLW boreholes such as excavation, ventilation, backfilling, heating and cooling, were simulated and the deformation of the borehole as well as the permeability parallel to the borehole were monitored. The main results are summarized below:

1. Simulation of the **borehole excavation** by reducing the inner borehole pressure from 15 MPa down to 1 MPa resulted in borehole convergence but without any increase in permeability along the cylinder axis. This indicates that there was no build-up of pathway through the samples. Increasing the external confining stress beyond 20 to 24 MPa (corresponding to the stress at a depth of 800 to 1000 m) led to a drastic increase in gas permeability from $10^{-21}$ $m^2$ to $10^{-14}$ $m^2$. This is attributed to the growth and interconnection of fractures through the claystone samples as observed after testing.

2. **Ventilation** of relatively dry air through the borehole caused de-saturation and shrinkage of the claystone and thus borehole divergence, and in contrast, ventilation wet air induced swelling of the claystone and then borehole convergence.

3. The **backfill impact** simulated by increasing the borehole pressure from 1 to 15 MPa led to a strong reduction of the gas permeability along fractures by more than three orders of magnitude from $10^{-17}$ to $10^{-21}$ $m^2$, depending on the initial characteristics of the excavation-induced fractures in the argillite.

4. The **water transport** through the fractures in the claystone produced swelling of clay minerals into the interstices and thus led to sealing of the fractures, whereby the intrinsic permeability decreased drastically. The permeability obtained by water flowtests was about $2 \cdot 10^{-18}$ $m^{-2}$, being more than three orders of magnitude lower than that determined by gas flow tests done before.

5. **Heating** a damaged hollow cylinder from 29 °C to 74 °C accelerated the borehole convergence and the water inflow. The thermal impact on the water conductivity of fractured claystone is governed by the change of the water viscosity, while the intrinsic permeability is less affected by heating.

6. **Cooling** down slowed the deformation and the water transport through the fractured argillite. The permeability estimated after cooling varied from $1.0 \cdot 10^{-18}$ $m^2$ to $3.5 \cdot 10^{-18}$ $m^2$, nearly the same as that before heating.

7. The **post-test investigation** on a sample showed a significant increase of the water content of up to 9.3 % at the inlet and to 6.2 % at the outlet. Most parts of the sample were “over saturated”, i. e. the water content was higher than that of ~7 % in the natural and saturated state. The increase in water content led to an expansion of the claystone into the fracture space, thereby sealing the fractures under confined conditions.

8. A remaining task is to examine the transferability of the laboratory conclusions to the damaged zone *in situ.*

## 2.8 Characterization of crushed claystone as backfill material

The disposal concepts developed by many countries for repositories in clay formations are based on the principle of a multi-barrier system, which comprises the natural geological barriers and the engineered barriers (EBS). After having been filled with radioactive waste, the disposal rooms, drifts, and shafts must be backfilled and sealed with suitable materials to re-establish the integrity of the isolating rock zone surrounding the repository and thus to prevent a release of radionuclides from that rock zone. The properties of each EBS component are to be specified with regard to the various barrier functions of, for instance, buffer surrounding waste containers, seals in disposal boreholes, backfill in drifts, plugs in drifts and shafts. Crushed claystone produced during excavation of the repository is a favourable alternative as backfill/sealing material, because of many advantages such as

a) chemical-mineralogical compatibility with the host rock,

b) availability,

c) low material and transport costs in comparison to the use of expensive bentonite,

d) shortfall of the recycling of excavated tailings and thus no occupancy of the ground surface, and

e) little effort for environmental conservation of the repository site.

Within the framework of ANDRA’s ongoing research programme /AND 06/, the suitability of crushed COX claystone as a potential backfill/sealing material has being investigated. GRS has contributed to this programme with laboratory tests on crushed claystone produced during the excavation of drifts in the MHM-URL. The GRS investigations focused on characterizing the hydro-mechanical properties of the crushed claystone such as:

- grain size distribution;
- water adsorption / retention capacity;
- compaction behaviour;
- permeability in relation with porosity;
- swelling potential.

### 2.8.1 Sample preparation

The crushed COX claystone was obtained from the stockpile at the surface of the MHM-URL. For the tests, raw material with coarser grains was firstly broken by a jaw crusher to a maximum grain size of 10 mm and 16 mm, respectively. After drying at 105 °C over 48 hours, the water content was measured in a range of 6.4 % to 7.4 %. The grain size distribution was determined on the dried aggregate. Fig. 2.82 summarizes the measured curves for all samples. While the grain sizes of the samples with a maximum diameter $d_{max}$ = 16 mm are relatively comparable, the others with $d_{max}$ = 10 mm vary in a relatively large scatter. An average grain size distribution was selected as reference material in the tests. The maximum grain size of 10 mm allows standard compaction tests in oedometer cells of 100 mm diameter and 200 mm length (the ratio of the cell diameter to the maximum grain size should be at least equal to 10).

### 2.8.2 Water retention

After backfilling and closing a repository, the initially unsaturated backfill material will take up water due to the suction gradient between the saturated rock and the unsaturated backfill from the moist air in the pores and from formation water intruding into the backfill. The re-saturation process is mainly controlled by the relationship between water content and suction (usually called water retention curve) of the backfill material. The re-saturation of the backfill in turn governs the swelling of the aggregate particles, leading to closing of the pores and building up resistance against deformation and damage propagation in the rock, particularly after a possible failure of the drift lining.

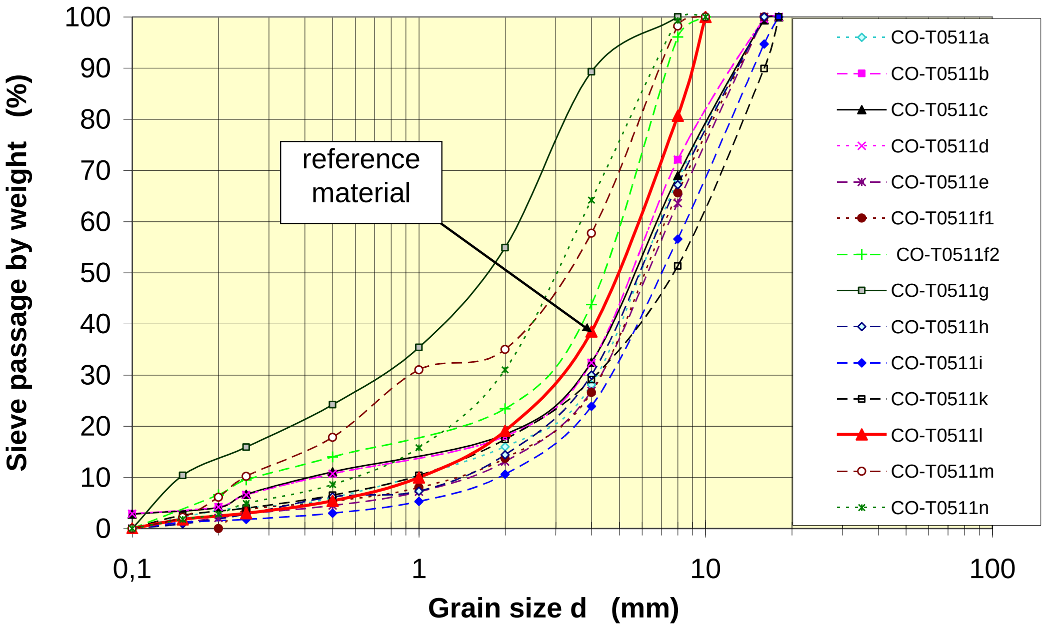


**Fig. 2.82** Grain size distribution of crushed COX claystone

The water retention curve of the crushed COX claystone was determined on loose samples. The vapour equilibrium technique was applied (for details see section 2.4.1). The tests were performed in desiccators at different relative humidity values of 12 % to 100 %, the corresponding suctions between 0 and 287 MPa. The water content of each sample was measured over several months. Fig. 2.83 shows the samples and humidity sensors placed in the desiccators.

**Fig. 2.83** Measurement of the water retention curve of crushed COX claystone in desiccators

The water contents measured at different suctions from 0 to 287 MPa are illustrated in fig. 2.84 over the time. The samples with an initial water content of 6.4 % were de-saturated at suctions higher than 17 MPa, below which they were re-saturated. The de- and re-saturation processes reached equilibrium after one month, except for the sample at zero suction. At this low suction, the water content increased continuously to w = 19 % over 6 months. An equilibrium, however, was not achieved in this period of time. This indicates again the high water adsorption potential of the claystone as mentioned in section 2.4.1 above.

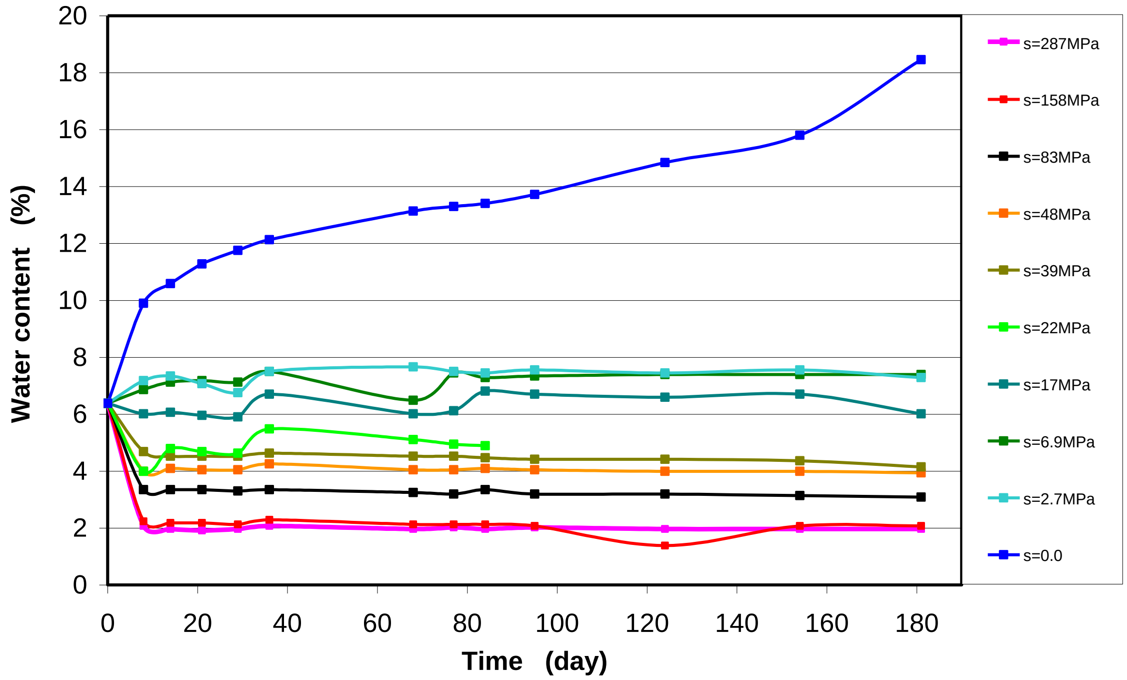


**Fig. 2.84** Water content measured on crushed COX claystone at various suctions

The high capability of water uptake is also reflected with compacted samples of the crushed claystone as shown in fig. 2.85. The samples were pre-compacted to high dry densities of 1.8, 1.9 and 2.0 g/cm$^3$ and then the water content was monitored at two low suction levels of s = 0 and 2.7 MPa. At s = 2.7 MPa, the water content increased to the maximum of 7.6 % – 7.8 %, while the water content at zero suction increased steadily up to 9 % – 10 % over 3 months. The re-saturation of the compacted claystone seems to be less dependent on the density.

The relationship of the water content to the applied suction is illustrated in fig. 2.86. It is again clearly to be seen that the water uptake at zero suction leads to a water content significantly higher than the original natural water content of 6.4 % – 7.4 %. This finding means in practice that the crushed claystone backfill material will take up and store large amounts of water from the wet air in its pores. In consequence, the backfill will become more dense and its barrier function more effective due to the swelling of the clay aggregate and its compression induced by convergence of the surrounding rock.

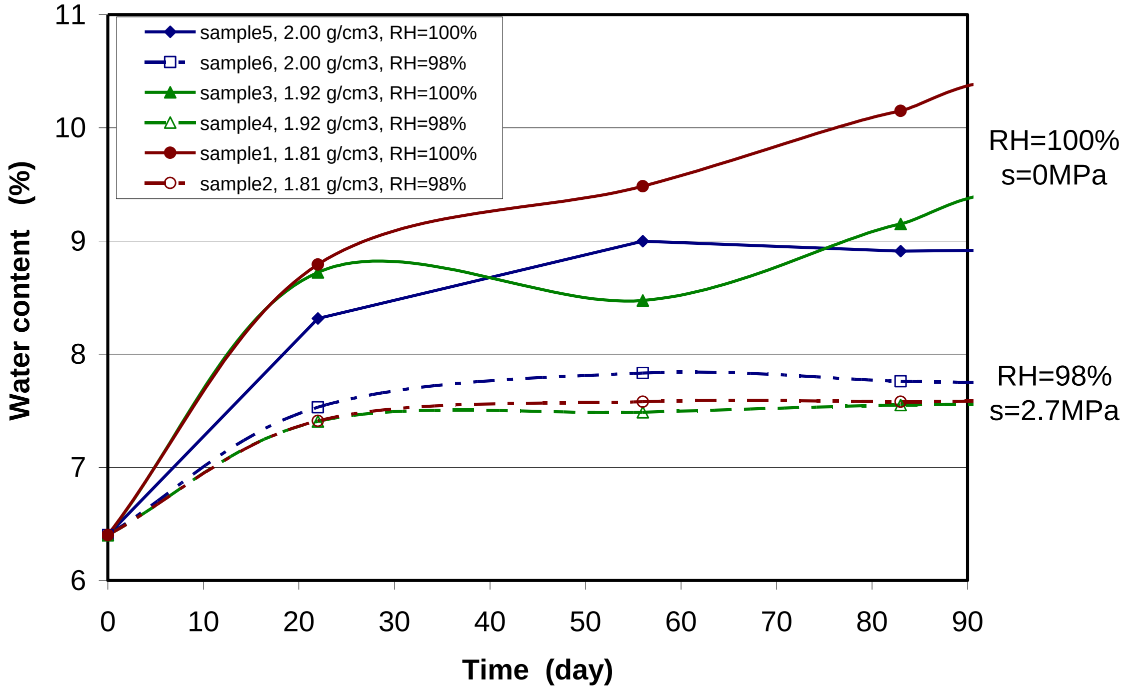


**Fig. 2.85** Water uptake of compacted COX aggregate in a humid environment

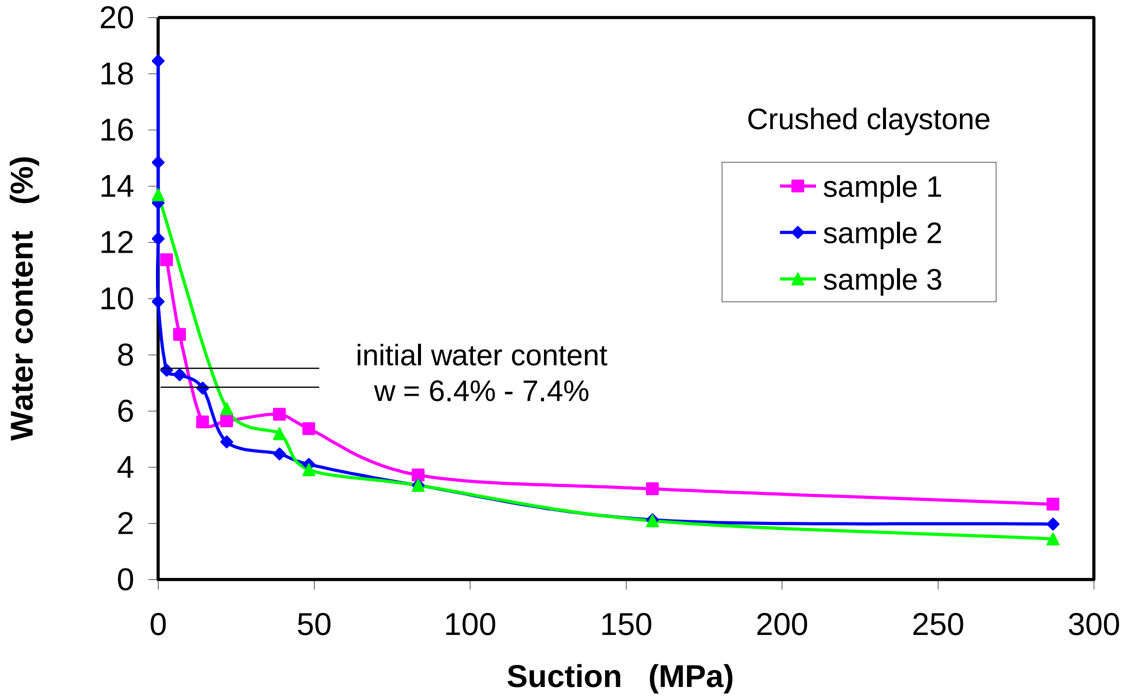


**Fig. 2.86** Water retention curve of the crushed COX claystone

### 2.8.3 Compaction

Crushed claystone can be emplaced loosely or compacted into disposal boreholes and drifts, depending on the EBS requirements defined for the different applications. After emplacement, the backfill will be compacted continuously by the viscous deformation of the surrounding. For evaluation of the interactions between the backfill and the surrounding rock, the compaction behaviour of the backfill is necessarily to be known.

First of all, the initial density of the backfill, achievable with available compaction techniques, was determined by proctor testing on samples with various water contents. Each sample with a mass of ~2 kg was filled in a proctor vessel of 100 mm diameter in three layers and compacted by 25 times falling of a 2.5 kg weight from a height of 300 mm. Then, the dry density of the compacted sample was determined. Fig. 2.87 shows the applied proctor apparatus and two compacted samples with different water contents. The wet sample with a water content of w = 9.4 % was more easily compacted to a higher density of $\rho_d$ = 1.62 g/cm$^3$ than the dry sample with a water content of w = 3.6 %, for which a lower density of $\rho_d$ = 1.28 g/cm$^3$ was reached only.

| | | |
|---|---|---|
|  | <br>grain size <10 mm<br>water content = 9.4 %<br>dry density = 1.62 g/cm$^3$ | <br>grain size <10 mm<br>water content = 3.6 %<br>dry density = 1.28 g/cm$^3$ |

**Fig. 2.87** Samples of crushed COX claystone after proctor compaction

Fig. 2.88 summarizes the dry densities reached for the crushed claystone with two grain size distributions of d < 16 mm and d < 10 mm. The samples were prepared to different water contents within a range from 2 % to 12 %. After treatment as backfill material the crushed claystone will be more or less de-saturated to water contents of less than 7 % – 8 % of the water content of the natural rock. The test data suggest that a dry density of ~1.5 g/cm$^3$ can be reached for the de-saturated crushed claystone (say w = 3 % – 7 %). If the material is more dried, the achievable density will be lower because of the high friction resistance between the material particles during compression. In order to keep the repository as dry as possible, addition of water to the backfill shall be avoided even though a relatively high initial density could be achieved thereby.

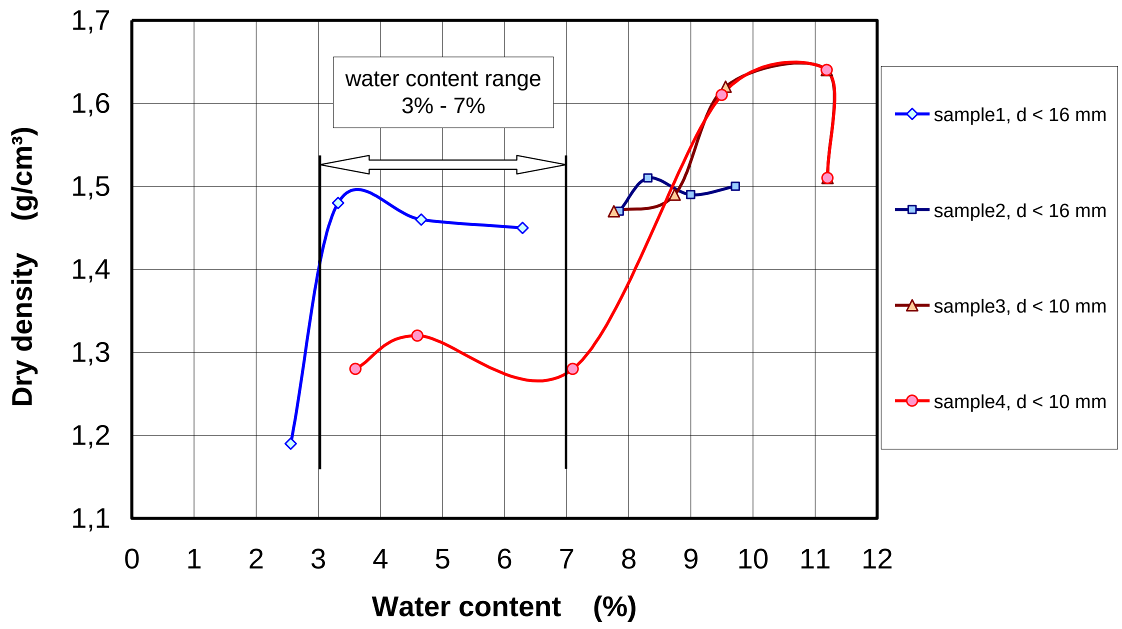


**Fig. 2.88** Densities of crushed claystone after proctor compaction

The compaction tests were carried out on the reference material with the maximum grain size of 10 mm in an oedometer cell of 100 mm diameter (fig. 2.89). The de-saturated crushed claystone with a water content of ~4.2 % was filled in the cell in three layers of 40 mm each to a total height of 120 mm. After each filling, the material was stamped by hand. An average dry density of 1.5 g/cm$^3$ or porosity of 45 % was achieved. The compaction was conducted at three strain rates of $1.5 \cdot 10^{-5}$, $1.5 \cdot 10^{-6}$ and $1.5 \cdot 10^{-7}$ s$^{-1}$ to examine the influence of the loading rate on the backfill deformation. During the compaction, the axial stress was recorded by the load sensor installed on the top loading piston. The axial strain was measured by the LVDT-displacement transducer. The gas or water flow was monitored at the outlet at a constant injection pressure for the determination of permeability of the sample.

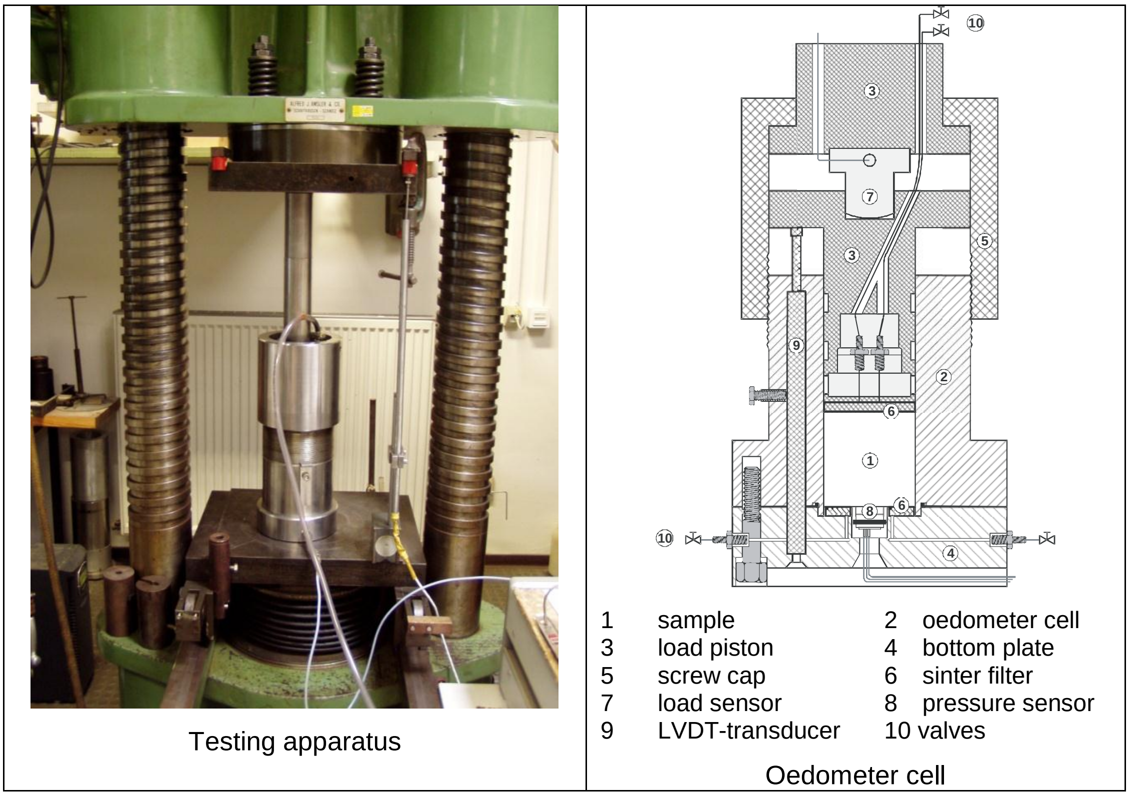


**Fig. 2.89** Oedometer test apparatus used for compaction and permeability tests

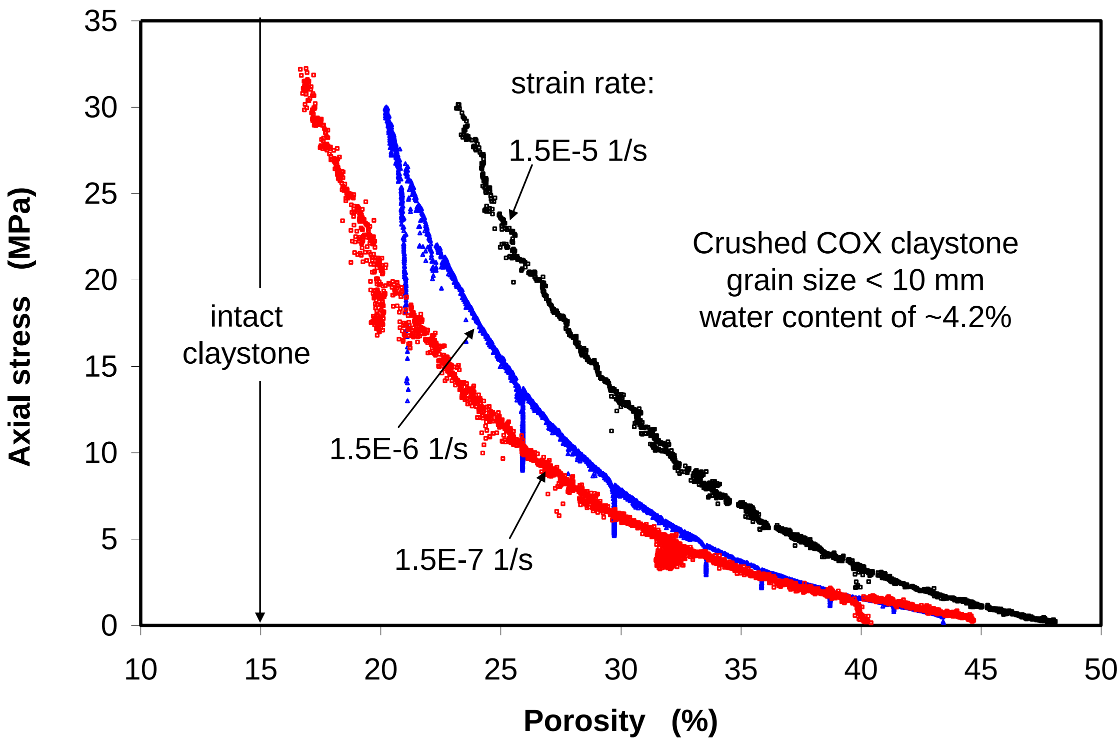


**Fig. 2.90** Compaction behavior of crushed COX claystone at various loading rates

Fig. 2.90 illustrates the compaction behaviour of the crushed claystone. It shows that the backfill resistance recorded by the axial stress gauge increases non-linearly with decreasing porosity and compaction rate. Each compaction curve approaches the porosity of ~15 % of the intact claystone at very high loads asymptotically. If the test result is extrapolated to the much lower convergence rates of the drifts in a repository, for instance lower than $10^{-10}$ $s^{-1}$ as observed in the MHM-URL /ARM 10/, the backfill support effect will be low, particularly during the early compaction phase at high porosity.

A number of stress relaxation phases was performed at the sample loaded at a strain rate of $1.5 \cdot 10^{-6}$ $s^{-1}$, by fixing the axial strain $\Delta\varepsilon_1 = 0$ at different porosities. The evolution of the axial stress and of the porosity is depicted in fig. 2.91. It can be seen that the stress previously applied to the backfill decreases gradually at fixed porosity. This indicates the time dependency of the compaction behaviour. The stress relaxation is faster at a low porosity. Similarly, the stress increase during re-compaction at a low porosity is faster, too. This suggests a higher stiffness and support effect of the backfill at low porosities.

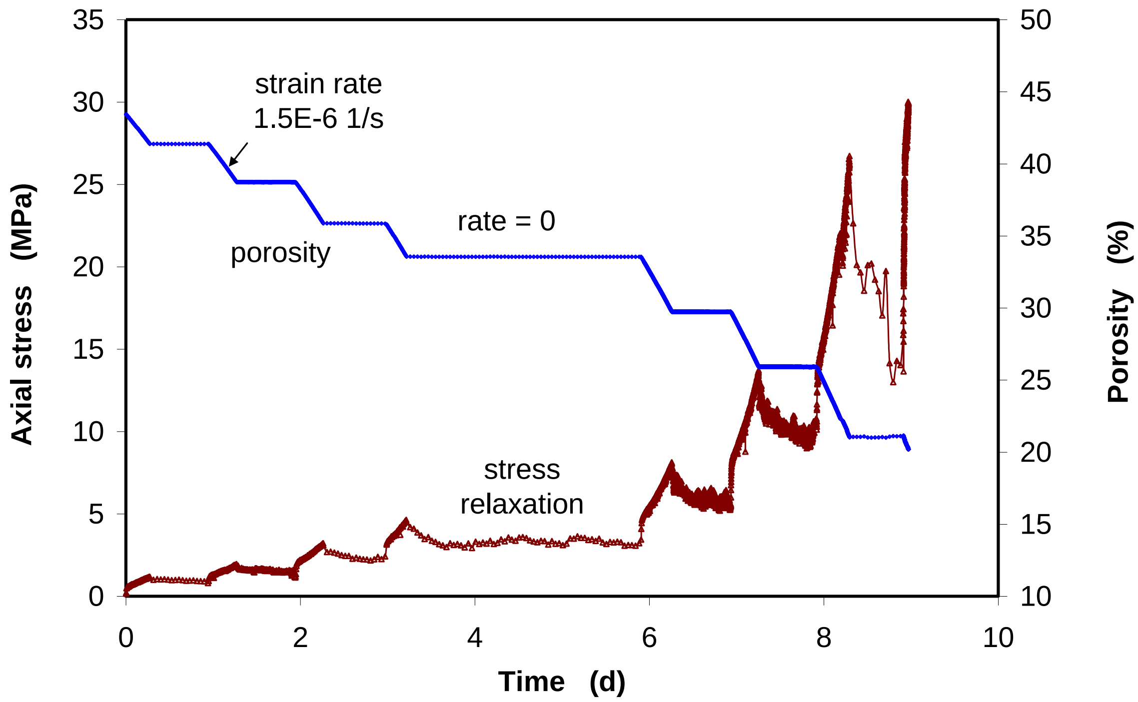


**Fig. 2.91** Stress relaxation of crushed COX claystone at various porosities

If a crushed claystone backfill of low initial porosity is selected to hinder the development of an EDZ, the porosity-stress relationship obtained above is helpful for the determination of the required energy or load needed during the manufacturing of backfill bricks. Fig. 2.92 shows photos of crushed claystone samples compacted under application of a high load of about 30 MPa. Because of the friction effect between the samples and the cell inner wall, low porosities can be identified at the top of the compacted samples contacting the driving piston.

$d\varepsilon/dt = 1.5 \cdot 10^{-5}\ s^{-1}$
$\sigma_{max}$ = 30 MPa
$\phi$ = 24 %

$d\varepsilon/dt = 1.5 \cdot 10^{-6}\ s^{-1}$
$\sigma_{max}$ = 30 MPa
$\phi$ = 22 %

$d\varepsilon/dt = 1.5 \cdot 10^{-7}\ s^{-1}$
$\sigma_{max}$ = 32 MPa
$\phi$ = 18 %

**Fig. 2.92** Photos of highly-compacted samples of crushed COX claystone

### 2.8.4 Permeability

To assess the hydraulic conductivity and the barrier function of the backfill against water migration during the various stages of compaction, permeability tests were carried out by pressing synthetic formation water through compacted samples in an oedometer cell. Fig. 2.93 shows the test set up used for the measurement of water permeability. The permeability was determined from steady state flow data obtained for a constant injection pressure of 1.0 bar.

Fig. 2.94 summarizes the permeability data obtained on three compacted samples with grains of d < 10 mm and one sample with d < 16 mm as a function of porosity. In the $log(k)$-$\phi$ diagram, the permeability decreases linearly with reduction of the porosity. The data can be approached by the exponential function: $k = 10^{-22} exp(-0.3\varphi)$. For sure, this relationship cannot be extrapolated to the intact clay rock. At a low porosity of 16 %, which was achieved at the compacted sample with a grain size of d < 16 mm, a low permeability of $1 \cdot 10^{-18}$ $m^2$ was determined. But this value is still about two orders of magnitude higher than that of $10^{-20}$ $m^2$ of the intact claystone with a similar porosity of 15 %. This might be explained by the pore structure of the short-term artificiallycompacted claystone which is different from that of the long-term naturally-consolidated rock matrix. Obviously, more precise data are needed to validate the preliminarily established relationship of permeability with porosity for the crushed claystone.

**Fig. 2.93** Test set up used for permeability measurements on crushed compacted claystone

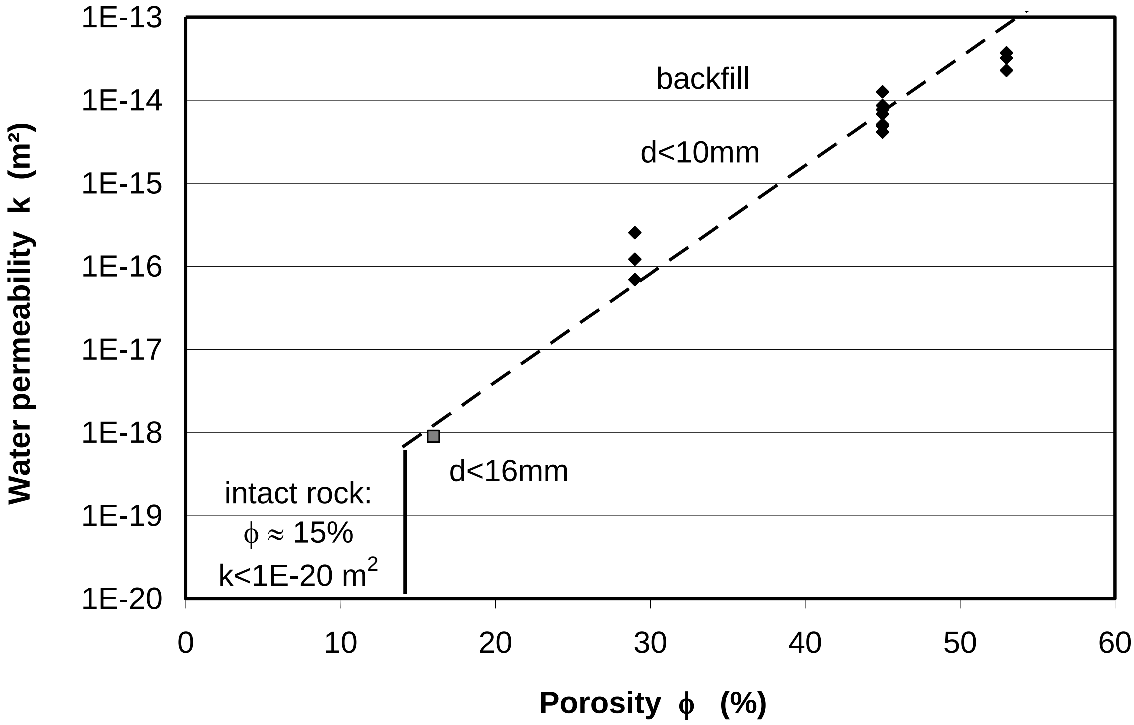


**Fig. 2.94** Permeability of crushed COX claystone as function of porosity

### 2.8.5 Swelling

The particles of the crushed COX claystone exhibit, as already explained above, a high capacity for water adsorption accompanied by distinct swelling properties (see the swelling tests reported in section 2.4). However, the swelling potential of the clay aggregate is mainly determined by its density after compaction. A certain swelling potential of the backfill material confined in boreholes and drifts is desired to enhance the closing of the pores in the backfill which leads to the to build up of backfill pressure which in turn supports the mechanical stability of the rock-backfill-system. The swelling potential of the crushed COX claystone was examined under different conditions.

Fig. 2.95 shows the evolution of swelling pressure recorded on a compacted sample during wetting with water vapour at 100 % relative humidity. The unsaturated sample was previously compacted in an oedometer cell to a porosity of 25 % at a compaction stress of 15 MPa. Afterwards, the sample was unloaded down to 0.2 MPa. After fixing the axial and volumetric strain at $\Delta\varepsilon_1 = 0$ / $\Delta\varepsilon_v = 0$, the sample was wetted by circulating water vapour over 20 days. During the re-saturation, the reacting stress or swelling pressure against the fixed piston increased gradually up to 1 MPa. The subsequent drying at 12 % humidity led to a rapid reduction of the swelling pressure.

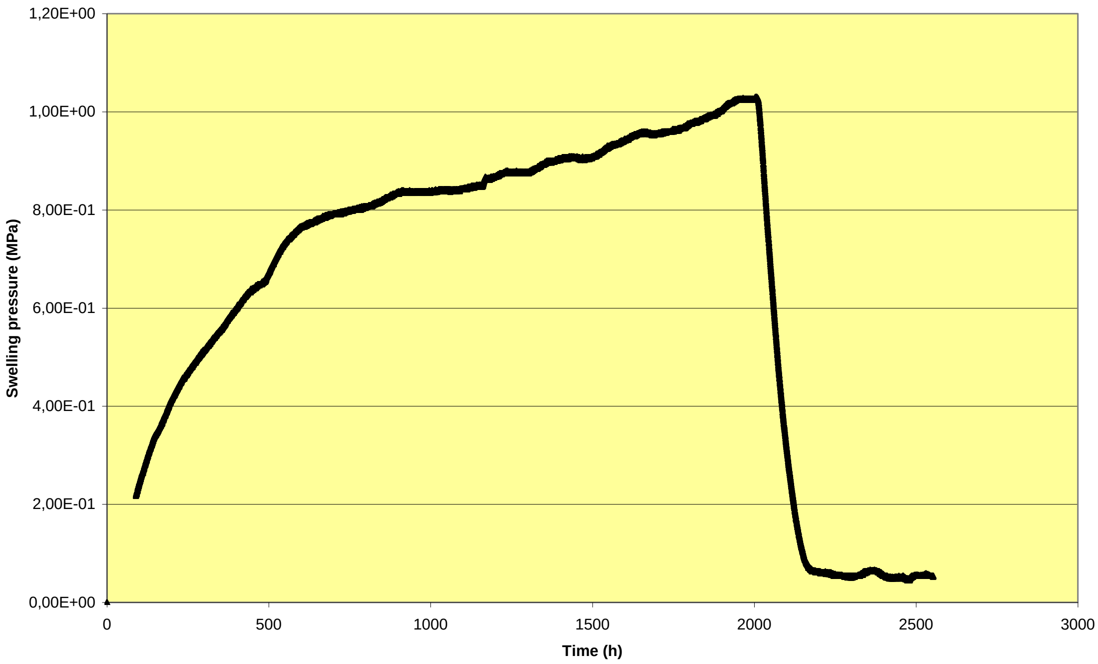


**Fig. 2.95** Swelling pressure of compacted COX claystone during wetting with water vapour

In further tests, two samples were firstly re-saturated with synthetic water and then compacted in oedometer cells to porosities of $\phi$ = 30 % at an axial load of $\sigma_1$ = 5 MPa and a porosity of $\phi$ = 19 % at an axial load of $\sigma_1$ = 15 MPa, respectively. After unloading to $\sigma_1$ = zero at $\phi$ = 30 % and $\sigma_1$ = 1.4 MPa at $\phi$ = 19 %, the axial strain was fixed, and the axial stress was monitored. Fig. 2.96 illustrates the measured data. While the axial stress at the high porosity of $\phi$ = 30 % increased to 0.3 MPa, the axial stress at the low porosity of $\phi$ = 19 % attained to 2.5 MPa. Because the pore-water pressure was nearly atmospheric, the total axial stress recorded must be equivalent to the swelling pressure in the sample.

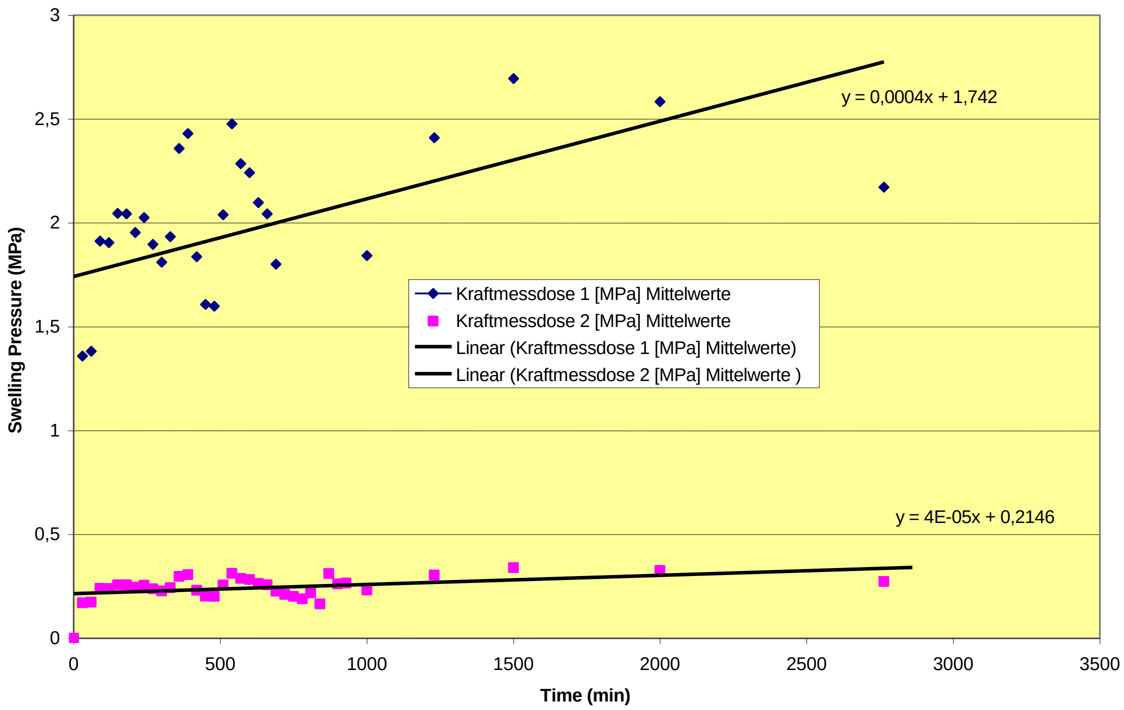


**Fig. 2.96** Swelling pressure of compacted COX claystone during wetting with synthetic pore water

### 2.8.6 Conclusions on the backfill behaviour

The hydro-mechanical behaviour of the crushed COX claystone was preliminarily investigated as backfill material for a potential repository in a clay formation. Under normal mechanical compression the air-dried aggregate with grain sizes of d < 10 mm and 16 mm can reach an initial dry density of 1.5 g/cm$^3$ at a porosity of $\phi$ = 45 %. The backfill resistance increases with compaction or porosity reduction, depending on the loading rate. At initially high porosities and at low loading rates, the support effect of the backfill is relatively low. Because of high potentials for water adsorption and associated distinct swelling properties, a certain swelling pressure can be achieved with the crushed claystone after a certain compaction. For instance, a swelling pressure of 2.5 MPa was observed on the compacted aggregate at a porosity of 19 %. The hydraulic conductivity of the backfill decreases exponentially with a decrease of the porosity. Low permeability values of $10^{-16}$ to $10^{-18}$ $m^2$ were determined at porosities of 30 % to 16 %.

Because of the favourable advantages and properties of the crushed claystone as potential backfill material, respective research work is continuing at the GRS laboratory within an extensive programme of the THM-TON project /THM 07/ including

- Characterization of the thermo-hydro-mechanical properties of the crushed claystone under repository relevant conditions;
- Investigation of the effect of various additions such as coarse-grained gravel, sand, and limestone on the THM behaviour of the mixtures;
- Modelling of the interactions between the backfill and the surrounding clay rock.

# 3 THM Modelling

With regard to the new German approach of the safe containment of radioactive waste in an isolating rock zone (IRZ) /BMU 09/ it is of paramount importance to confirm constitutive models enabling adequate prediction of the long-term processes prevailing in the host rock and the engineered barriers, particularly the evolution or self-sealing of the EDZ in interaction with the EBS. Since 2002, GRS uses the FEM code CODE-BRIGHT developed by the Technical University of Catalonia in Barcelona /OLI 94/, /GEN 98/, /UPC 04/ for the analysis of coupled thermo-hydro-mechanical processes in the multi-barrier-system around HLW repositories in clay and salt formations. Within previous projects (BURE-PRE /ZHA 04a/, /ZHA 07b/, HE-D /ZHA 07a/, NFPRO /ZHA 08a/ /WIE 08/), GRS performed a great number of modelling exercises for gathering experience with coupled THM calculations and for validating the constitutive models implemented in the code for various clay-based backfill materials and clay rocks /ZHA 04b/, /ZHA 07a/, /ZHA 08a/, /WIE 08/. In the framework of this project, the modelling work focused on validating the constitutive models for the prediction of the development and recovery of the EDZ around HLW disposal boreholes in clay formations. The model validation was conducted by modelling the following laboratory and *in situ*-experiments and by comparing the modelling results with the observations:

- EDZ simulation tests performed at the GRS laboratory on large hollow cylinders of COX claystone (section 2.7);
- REP experiment monitoring hydro-mechanical responses of the COX clay rock to the excavation of the main shaft of the MHM-URL /MOD 06/, /SU 07/;
- TER experiment investigating the thermal impact on the hydro-mechanical processes in the COX clay rock during heating/cooling in a horizontal borehole /WIL 07/;
- Scoping calculations of THM processes in a clay rock-bentonite buffer-system around a HLW disposal borehole.

First, the fundamental theories of coupled THM modelling and the main features of applied constitutive models are briefly reviewed with the determination of the associated parameters for the COX claystone. Secondly, the modelling results are compared with the results of the measurements performed during the experiments. Finally, the capabilities of the applied models (particularly the damage-elastoplastic model developed by

Vaunat et al. /VAU 03/, /VAU 04/, /VAU 09/ for argillaceous rock) are evaluated on basis of a comparison between the modelling and the measurement results.

## 3.1 Fundamental theories and constitutive models

### 3.1.1 THM coupling phenomena

Almost all geological and geotechnical materials such as rocks and backfill / buffer materials are porous media. Generally, such porous media are composed of three species: mineral, water and air, distributed as three phases: solid, liquid and gas. The liquid phase contains liquid water and dissolved air, while the gas phase is a mixture of dry air and water vapour. The mineral and solid phases are here considered coincidently. In porous media simultaneously subjected to thermal, hydraulic and mechanical conditions, complex THM phenomena and interactions take place as for instance,

a) thermal loading inducing deformation and stress variations (T → M) and expansion of pore-water as well as pore-pressure changes (T → H);

b) mechanical loading leading to changes in porosity and hydraulic conductivity (M → H) as well as thermal conductivity (M → T);

c) pore-water pressure changes directly related with the effective stress (H → M), degree of water saturation and water / gas flow influence the heat transfer and the temperature field (H → T).

All important aspects of THM coupling are illustrated in fig. 3.1 /GEN 06/. Taking into account the most important coupled THM phenomena, the FEM code CODE-BRIGHT has been developed by UPC /OLI 94/, /GEN 98/, /GEN 06/, /UPC 04/. A number of general assumptions are made in the formulation of the coupled THM problems encountered in unsaturated porous materials:

1. Dry air is considered a single species and, usually, it is the main component of the gaseous phase. Henry's law is used to express equilibrium of dissolved air.

2. Vapour concentration is in equilibrium with the liquid phase, and the psychrometric law expresses its concentration.

3. Thermal equilibrium between phases is assumed meaning that the three phases have the same temperature.

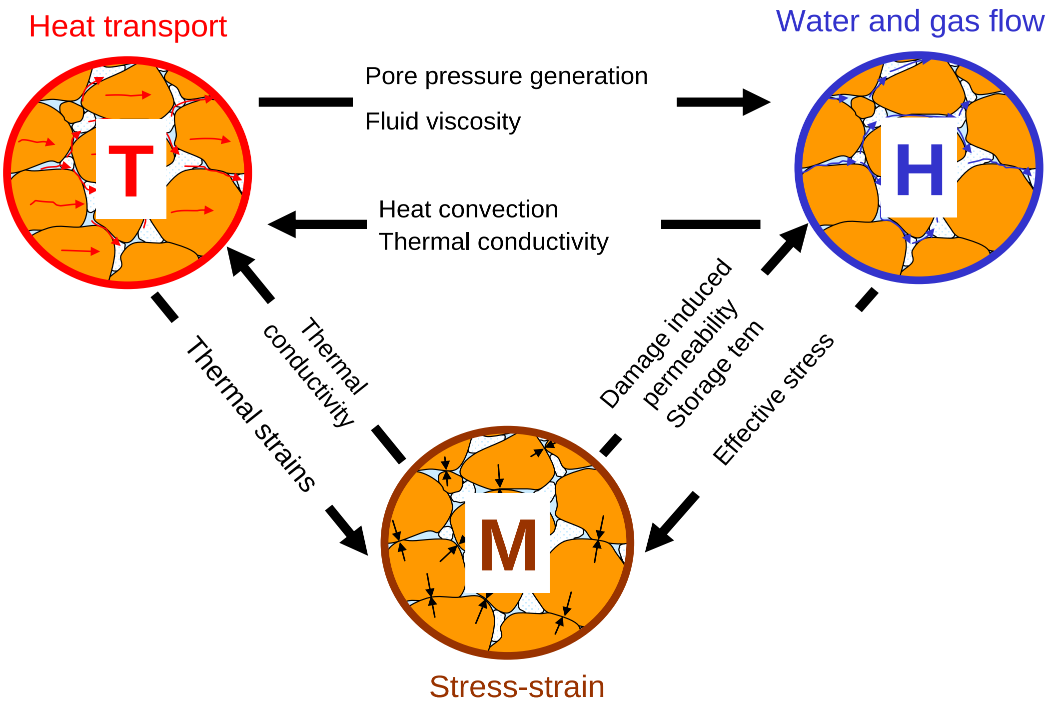


**Fig. 3.1** Relations between THM processes in porous media /GEN 06/

4. Balance of momentum for the medium as a whole is reduced to the equation of stress equilibrium together with a mechanical constitutive model to relate stresses with strains.

5. Small strains and small strain rates are assumed for solid deformation. Advective terms due to solid displacement are neglected after the formulation is transformed in terms of material derivatives. In this way, volumetric strain is properly considered.

6. State variables are solid displacements, liquid pressure, gas pressure, and temperature.

Details about the basic theories with the formulated governing equations (balance equations and constitutive models) are described in the code manual /UPC 04/ and in the literature /OLI 94/, /GEN 06/. In the following, the balance equations and constitutive models, which are to be solved in the calculations, are briefly summarized. Values of the associated parameters for the COX argillite are partly determined on the basis of GRS' tests and partly taken from literature /GEN 06/, /VAU 03/, /VAU 09/, /ZHA 04b/.

### 3.1.2 Balance equations

Generally, for the calculations of coupled THM processes in geological media, a set of balance equations for internal energy, solid mass, water mass, air mass, and stress equilibrium are to be solved in a consistent way /OLI 94/, /UPC 04/, /GEN 98/, /GEN 06/. These are

**Internal energy balance:**

$$\frac{\partial}{\partial t}[E_s p_s (1-\phi) + E_l \rho_l S_l \phi + E_g \rho_g S_g \phi] + \nabla \cdot (\mathbf{i_c} + \mathbf{j_{Es}} + \mathbf{j_{El}} + \mathbf{j_{Eg}}) = f^E \tag{3.1}$$

where $E_s$, $E_l$ and $E_g$ are specific internal energies corresponding to the solid, liquid and gaseous phases, $\rho_s$, $\rho_l$ and $\rho_g$ are the densities of the three phases, $\phi$ is the porosity, $S_l$ is the volumetric liquid fraction and $S_g$ is the volumetric gaseous fraction with respect to the pore volume, $S_l + S_g = 1$. $\mathbf{i}_c$ is the conductive heat flux and $\mathbf{j}_{Es}$, $\mathbf{j}_{El}$, $\mathbf{j}_{Eg}$ are the advective energy flux of each of the three phases with respect to a fixed reference system. The most relevant advection energy fluxes correspond to vapour and liquid water motion. For very low permeable materials, the non-advective heat flow $\mathbf{i}_c$ dominates the heat transfer. $f^E$ is the energy supply per unit volume of the considered medium.

**Water mass balance:**

$$\frac{\partial}{\partial t}(\theta_l^w S_l \phi + \theta_g^w S_g \phi) + \nabla \cdot (\mathbf{j}_l^w + \mathbf{j}_g^w) = f^w \tag{3.2}$$

where $\theta_l^w$ and $\theta_g^w$ are the mass of water per unit volume of liquid and gas, respectively, $\mathbf{j}_l^w$ and $\mathbf{j}_g^w$ denote the total mass flux of water in the liquid and gas phases with respect to a fixed reference system and $f^w$ is the external mass supply of water per unit volume of medium.

**Air mass balance:**

$$\frac{\partial}{\partial t}(\theta_l^a S_l \phi + \theta_g^a S_g \phi) + \nabla \cdot (\mathbf{j}_l^a + \mathbf{j}_g^a) = f^a \tag{3.3}$$

where $\theta_l^a$ and $\theta_g^a$ are the mass of dry air per unit volume of liquid and gas, respectively, $\mathbf{j}_l^a$ and $\mathbf{j}_g^a$ indicate the total mass flux of air in the liquid and gas phases with respect to a fixed reference system, and $f^a$ is the external mass supply of air per unit volume of medium.

**Solid mass balance:**

$$\frac{\partial}{\partial t}(\theta^s(1-\phi))+\nabla\cdot(\mathbf{j}^s)=f^s \tag{3.4}$$

where $\theta^s$ is the solid density, $\mathbf{j}^s$ is the flux of solid, and $f^s$ is the external mass supply of solid per unit volume of medium.

**Stress equilibrium:**

$$\nabla\cdot\boldsymbol{\sigma}+\mathbf{b}=\mathbf{0} \tag{3.5}$$

where $\boldsymbol{\sigma}$ represents the stresses and $\mathbf{b}$ the body forces.

The state variables are the solid displacements $\boldsymbol{u}$ (three spatial directions), liquid pressure $p_l$, gas pressure $p_g$, and temperature $T$.

### 3.1.3 Mechanical model

Recently, a damage-elastoplastic model has been developed by Vaunat et al. /VAU 03/, /VAU 04/ for argillaceous rock which is considered as a composite material composed of a clay matrix connected by bonds (fig. 3.2). The clay matrix behaves like a typical elastoplastic soil, while the bonds behave like a typical quasi-brittle material that can be represented by a damage elastic law. The stress/strain behaviour of the composite material is determined by coupling both responses of matrix and bonds under compatible conditions. In order to gain a better understanding of the model features, this model is presented below based on the publications from the model developer Vaunat et al. /VAU 03/, /VAU 04/, /VAU 09/, /UPC 04/, /GEN 06/, /GEN 07/.

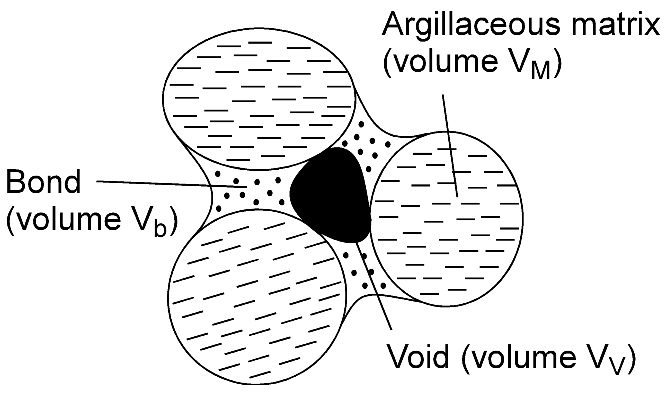


**Fig. 3.2** Schematic arrangements of clay matrix and bonds in clay rock /VAU 03/

#### 3.1.3.1 Definitions

The solid phase has two components, each one occupying a given volume fraction of the porous medium. The clay matrix volume is noted as $V_M$, the bond volume as $V_b$, and the void volume as $V_v$.

**The volume of the solid phase is**

$$V_S = V_M + V_b \tag{3.6}$$

Different void ratios and volumetric strains are defined:

**Void ratio:**

$$e = V_V / V_S \tag{3.7}$$

**Bond ratio:**

$$e_b = V_b / V_S \tag{3.8}$$

**Matrix ratio:**

$$e_M = (V_b + V) / V_S \tag{3.9}$$

**Pore volumetric strain:**

$$\varepsilon_v = \frac{-dV_v}{V_v + V_s} = -\frac{de}{1+e} \tag{3.10}$$

**Bond volumetric strain:**

$$\varepsilon_v^b = \frac{-dV_b}{V_b + V_s} = -\frac{de_b}{1+e} \tag{3.11}$$

**Matrix volumetric strain:**

$$\varepsilon_v^M = \frac{-d(V_b + V_v)}{V_v + V_s} = -\frac{de_M}{1+e} \tag{3.12}$$

**Relationships:**

$$e_M = e + e_b \tag{3.13}$$

$$\varepsilon_v^M = \varepsilon_v + \varepsilon_v^b \tag{3.14}$$

The matrix ratio $e_M$ is a measure of the amount of volume not occupied by clay particles. The bonds are assumed to behave like a porous medium and are thus (among other things) compressible (Eq. (3.1) – (3.11)). It follows that the matrix (or external) volumetric strain $\varepsilon_v^M$ is the sum of the pore volumetric strain $\varepsilon_v$ and the bond volumetric strain $\varepsilon_v^b$ (Eq. (3.1) – (3.14)). It is also extended to the shear strain by the expression:

$$\varepsilon_q^M = \varepsilon_q + \varepsilon_q^b \tag{3.15}$$

where $\varepsilon_q^M$ is the matrix (external) shear strain, $\varepsilon_q$ is the shear strain between the clay particles and $\varepsilon_q^b$ is the shear strain in the bonds.

When a load is externally applied to the medium, part of the stresses will be carried by the bonds and part by the clay matrix. The different local stresses in both materials must be in equilibrium with the external load and the resulting local strains must be compatible with the total deformations. Therefore, a constitutive model for such a composite material must include two parts, one for the clay matrix and one for the bonds and a stress distribution criterion to specify the way in which the applied stresses are shared by the matrix and bonds.

In the CODE-BRIGHT, the model equations are written adopting the conventions commonly used in soil mechanics where p > 0 and $\varepsilon_v$ > 0 depict compression.

**The concept of Biot's effective stress is adopted:**

$$\boldsymbol{\sigma}' = \boldsymbol{\sigma} - B\mathbf{I}p_l \tag{3.16}$$

where B is the Biot coefficient, $\mathbf{I}$ is the identity tensor, $p_l$ is the liquid pressure. In case of a saturated state, B = 1, while for unsaturated condition the Biot stress is switched with the total stress minus the gas pressure, $\boldsymbol{\sigma}^{Biot} = \boldsymbol{\sigma} - \mathbf{I}p_g$.

**The mean effective stress is**

$$p = \frac{1}{3}(\sigma'_x + \sigma'_y + \sigma'_z) \tag{3.17}$$

where $\sigma'_x, \sigma'_y, \sigma'_z$ are the effective stresses.

**Second stress invariant:**

$$J = \sqrt{\frac{1}{2} trace(\mathbf{s} : \mathbf{s})} = \frac{1}{\sqrt{3}} q \tag{3.18}$$

$$q = \frac{1}{\sqrt{2}} \sqrt{(\sigma'_x - \sigma'_y)^2 + (\sigma'_y - \sigma')^2 + (\sigma'_z - \sigma'_x)^2 + 6(\tau'_{xy} + \tau'_{yz} + \tau')} \tag{3.19}$$

where $q$ is the deviatoric stress, $\tau'_{xy}, \tau'_{yzy}, \tau'_{zx}$ are the shear stresses.

**Lode's angle:**

$$\theta = -\frac{1}{3} \sin^{-1}(1.5\sqrt{3} \det \mathbf{s} / J^3) \tag{3.20}$$

$\theta = -\pi/6$ means triaxial compression and $\theta = \pi/6$ extension.

#### 3.1.3.2 Elasto-plastic behaviour of clay matrix

The clay matrix is considered as a ductile material governed by an elasto-plastic law using Hoek & Brown's criterion as yield surface. Inside the yield surface the matrix behaves elastically.

**Elastic law:**

$$d\sigma_{ij}^M = D_{ijkl}^{eM} \left( d\varepsilon_{kl}^M - \delta_{kl} \frac{ds}{K_s^M} - d\varepsilon_{kl}^p \right) \tag{3.21}$$

where $\sigma_{ij}^M$ = stresses prevailing at clay particles contact

$D_{ijkl}^{eM}$ = elastic stiffness matrix of the clay

$d\varepsilon_{kl}^M$ = total strains of the clay matrix (equal to the external strains)

$K_s^M$ = bulk modulus against suction change ds (s = pg – pl).

$d\varepsilon_{kl}^{p}$ = plastic strains of the clay matrix

$\delta_{kl}$ = Kronecker delta.

Assuming linear elasticity, the elastic stiffness $D_{ijkl}^{eM}$ is determined by Young's modulus $E^{M}$ and Poisson's ratio $\nu^{M}$ of the clay matrix. Volumetric swelling or shrinking of the clay matrix is linearly related with suction change $ds$ by the bulk modulus $K_{s}^{M}$. Wetting (suction decrease) leads to swelling and in contrast drying (suction increase) results in shrinkage:

$$d\varepsilon_{v}^{s} = \frac{-ds}{K_{s}^{M}} \tag{3.22}$$

**Yield function** (Hoek & Brown criterion):

$$F^{p} = \frac{4\sin^{2}(\theta^{M} - \pi/6)}{R_{c}^{M}}(J^{M})^{2} - \frac{2m^{M}\sin\theta^{M}}{\sqrt{3}}J^{M} - m^{M}(p^{M} + p_{t}^{M}) \geq 0 \tag{3.23}$$

where $p_{t}^{M}$ = tensile strength of the clay matrix (isostatic)

$R_{c}^{M}$ = uniaxial compressive strength of the clay matrix

$m^{M}$ = $R_{c}^{M}/p_{t}^{M}$ ratio defining the shape of the yield surface.

In case of triaxial compression, $\theta = -\pi/6$, the yield function is expressed as

$$F^{p} = \frac{(q^{M})^{2}}{R_{c}^{M}} + \frac{m^{M}}{3}q^{M} - m^{M}(p^{M} + p_{t}^{M}) \geq 0 \tag{3.24}$$

The strength $R_{c}^{M}$ of the clay matrix increases with elevating suction (drying) by

$$R_{c}^{M}(s) = R_{c}^{M}(o)[(1-r^{M})\exp(-\beta^{M}s) + r^{M}] \tag{3.25}$$

where the coefficient $r^{M}$ depicts the limit strength by $r^{M} = \lim_{s\to\infty}(R_{c}^{M}(s)/R_{c}^{M}(o))$ and $\beta^{M}$ defines the change rate of the strength $R_{c}^{M}$ with suction $s$.

**Plastic potential:**

$$G^{p} = \frac{4\sin^{2}(\theta^{M} - \pi/6)}{R_{c}^{M}}(J^{M})^{2} - \frac{2m^{M}\sin\theta^{M}}{\sqrt{3}}J^{M} - \omega^{M}m^{M}(p^{M} + p_{t}^{M}) \tag{3.26}$$

where $\omega^M$ is a parameter defining the non-associativity of the plastic flow: $\omega^M$ = 1 when associated and $\omega^M$ = 0 for zero dilatancy. Taking the associativity of the plasticity ($\omega^M$ = 1) for triaxial compressive conditions ($\theta = -\pi/6$) into account, the plastic potential has the same form as eq. (3.24).

**Hardening law:**

A hardening/softening law is introduced through the following dependency of the tensile strength on the plastic strain:

$$p_t^M = \frac{R_{co}^M}{m^M}\left[1-(1-\alpha^M)\frac{\max(\varepsilon_1^{pM},\xi_r^M)}{\xi_r^M}\right]^2 \tag{3.27}$$

Where $R_{co}^M$ = uniaxial compressive strength of the intact clay;

$\varepsilon_1^{pM}$ = major principal plastic strain;

$\xi_r^M$ = accumulated major principal plastic strain at which the residual strength $\alpha^{M\,2} R_{c0}^M$ is reached;

$\alpha^M$ = brittleness parameter relating the intact and residual uniaxial compressive strength $R_{co}^M$ and $R_{cres}^M$ by

$$\alpha^M = \sqrt{\left(\frac{R_{cres}^M}{R_{c0}^M}\right)^2 + \frac{2}{3}m^M\frac{R_{cres}^M}{R_{c0}^M}} \tag{3.28}$$

$\alpha^M$ = 1 means perfect plasticity and

$\alpha^M$ = 0 indicates total degradation (residual strength $R_{cres}^M$ = 0).

**Visco-plastic strain**

The rate dependency is introduced as a visco-plastic mechanism. The plastic multiplier $\lambda^p$ is expressed as a function of the distance between the current clay matrix stress point and the inviscid plastic stress point:

$$d\lambda^p = \frac{dt}{\eta^M}\left\langle F^p \right\rangle \tag{3.29}$$

where $dt$ is the time increment, $\eta^M$ is the matrix viscosity and $\langle\ \rangle$ is the Macauley bracket. The inviscid plastic locus takes the form

$$\overline{F}^p = F^p - \frac{\eta^M}{dt}d\lambda^p \le 0 \tag{3.30}$$

where $F^p$ is the Hoek & Brown yield criterion (Eq. (3.23)).

The visco-plastic strains are computed as

$$d\varepsilon_{vp}^{M} = \frac{dt}{\eta^{M}} \frac{\partial G_{M}}{\partial p_{M}} \left\langle F^{p} \right\rangle \quad d\varepsilon_{vq}^{M} = \frac{dt}{\eta^{M}} \frac{\partial G_{M}}{\partial q_{M}} \left\langle F^{p} \right\rangle \tag{3.31}$$

The plastic strains in eq. (3.21) are replaced by the visco-plastic ones for cases of time dependency.

#### 3.1.3.3 Damage-elastic behaviour of bonds

Bonds are considered as quasi-brittle material the behaviour of which is represented by an elastic law with damage. Bond damage or degradation occurs as the result of apparition of micro-fissures within the bonds, which reduces the surface on which stresses and strains are active. The operative stresses and strains acting on the reduced surface of solid bonds are related to stresses and strains averaged over the whole bond area by a damage parameter.

***Elastic law***

$$d\sigma_{ij}^{b} = D_{ijkl}^{eb} (d\varepsilon_{kl}^{b} - d\varepsilon_{kl}^{d}) \tag{3.32}$$

Where $\sigma_{ij}^{b}$ = stresses inside bonds;
$D_{ijkl}^{eb}$ = secant damaged elastic stiffness matrix of bonds;
$d\varepsilon_{kl}^{b}$ = strains of bonds;
$d\varepsilon_{kl}^{d}$ = damage strains.

The damaged elastic matrix is related to the undamaged elastic matrix tensor $D_{ijkl}^{ebo}$ by

$$D_{ijkl}^{eb} = (1-D) D_{ijkl}^{ebo} = e^{-L} D_{ijkl}^{ebo} \tag{3.33}$$

where $D$ is a measure of damage of the material and equal to the ratio of bond fissures over the whole area of bonds, $L$ is the damage variable related to $D$ by $L = \ln(1/(1-D))$, and $D_{ijkl}^{ebo}$ is defined by Young's modulus $E^{bo}$ and Poisson's ratio $\nu^{bo}$ of the undamaged bonds through the linear isotropic elasticity. The damage parameter $D$ and variable $L$ are explicitly related to the stiffness degradation by

$$D = 1 - \frac{K^b}{K^{bo}} = 1 - \frac{G^b}{G^{bo}} = 1 - \frac{E^b}{E^{bo}} \qquad \text{(a)}$$

$$L = \ln\frac{K^{bo}}{K^b} = \ln\frac{G^{bo}}{G^b} = \ln\frac{E^{bo}}{E^b} \qquad \text{(b)} \qquad (3.34)$$

where $K^{bo}, G^{bo}, E^{bo}$ and $K^b, G^b, E^b$ are the bulk, shear and Young's modulus of the un-damaged and damaged bonds, respectively. When $D = 0$ $(L = 0)$, the material is intact and the bond stiffness is determined by $K^{bo}, G^{bo}, E^{bo}$. As $D$ increases, cracks in bonds develop and the material stiffness decreases progressively. When $D = 1$ $(L \to \infty)$ the bonds are fully damaged and the stiffness is eliminated. Change of $D$ is linked to the energy increment input to the bonds $du_b$ (equal to $(p_b - p_{bo})d\varepsilon_{vb} + (q_b - q_{bo})d\varepsilon_{qb}$ in triaxial conditions).

**Damage locus**

The current bond damage locus is defined in the stress space as a threshold of equal energy $r^b$, corresponding to the maximum energy input to the bond during its history

$$F^d = \frac{1}{2}\sigma_{ij}^b \varepsilon_{ij}^b - r^b(s) \qquad (3.35)$$

This condition draws an ellipse in the $p_b - q_b$ space. For a stress state moving inside the ellipse, no damage develops. When the ellipse is reached by the current stress state, damage occurs. The value of the energy threshold depends on suction $s$

$$r_o^b(s) = r^b(o) + r_{os}^b \cdot s \qquad (3.36)$$

where $r^b(o)$ = damage threshold at zero suction (fully saturated)

$r_{os}^b$ = parameter defining the change rate of damage locus with suction.

**Damage rule**

The damage rule gives the evolution of damage strain $d\varepsilon_{kl}^d$ with the damage variable $L$. This relation is constrained by the evolution of the bond elastic modulus and takes the form

$$d\varepsilon_{kl}^{d} = \varepsilon_{ij}^{b} dL \tag{3.37}$$

**Damage evolution law**

It defines the evolution of the damage locus $r^b$ with the damage variable $L$. A simple linear expression is considered

$$r^b = r_o^b + r_1^b L \tag{3.38}$$

Where $r_o^b$ = value of energy threshold at which damage starts (Eq. (3.36))

$r_1^b$ = parameter defining the evolution rate of damage locus, as a function of suction

$$r_1^b = r_{10}^b + r_{11}^b \cdot s \tag{3.39}$$

with parameters $r_{10}^b$ and $r_{11}^b$.

**Rate dependency**

The rate dependency is introduced by a delayed micro-cracking and uses the visco-damage formalism. The damage variable is expressed as a function of distance between the current bond stress point and the infinitely slow damage locus:

$$dL = \frac{dt}{\eta^b} \left\langle F^d \right\rangle \tag{3.40}$$

where $\eta^b$ = damage viscosity of the bonds.

The infinitely slow damage locus takes the form

$$\overline{F}^d = F^d - \frac{\eta^b}{dt} dL \leq 0 \tag{3.41}$$

#### 3.1.3.4 Stress and strain distribution in the composite material

Any load applied to an element of cemented material will distribute itself between the soil matrix and the bonds according to a ratio that depends on the geometric arrangement of both components. Following the principle of energy equivalence that establish-es the equality between the energy of the composite material and the sum of energies for all components leads to the expressions of strains and stresses:

$$d\varepsilon_{ij}^{M} = d\varepsilon_{ij} + d\varepsilon_{ij}^{b} \tag{3.42}$$

$$\sigma_{ij} = (1+\chi)\sigma_{ij}^{M} + \chi\sigma_{ij}^{b} \tag{3.43}$$

with

$$\chi = \frac{\varepsilon_v^b}{\varepsilon_v} = \frac{\varepsilon_q^b}{\varepsilon_q} = \chi_0 \cdot \sqrt{1-D} = \chi_0 \cdot \exp(-L/2) \tag{3.44}$$

where the local stresses $\sigma_{ij}^{M}$ and $\sigma_{ij}^{b}$ must be in equilibrium with the external stresses $\sigma_{ij}$ and the local strains $\varepsilon_{ij}$ and $\varepsilon_{ij}^{b}$ must be compatible with the external strains $\varepsilon_{ij}^{M}$. $\chi_0$ is a coupling parameter related to cement concentration, giving the relative importance of the bond- and matrix-behaviour in the overall response of the composite material. The structure parameter $\chi$ decreases as damage evolves inside the bonds. In case of fully damage ($D \rightarrow 1$, $L \rightarrow \infty$) the rock behaves like a de-structured soil.

#### 3.1.3.5 Parameters

In total, there are 18 independent parameters in the model. The parameter values for the COX clay rock were preliminarily established in /VAU 03/, /VAU 04/, /VAU 09/. Based on GRS's new test results, some of the parameters were re-examined herein. Tab. 3.1 summarizes the newly determined parameters. It is to be pointed out that the respective parameters for the clay matrix and the bonds in the rock mass can hardly be determined independently. This may lead to some degrees of uncertainty with the parameters and thus may limit the application of the model.

Some related parameters in Tab. 3.1 are deduced from the following relationships:

$$K = \frac{E}{3(1-2\nu)}; \; G = \frac{E}{2(1+2\nu)} \tag{3.45}$$

$$E^{Ro} = (1+\chi_o)^2 E^M + \frac{\chi_o^{\,2}}{1+\chi_o} E^{bo}; \; R_c^{\,Ro} = (1+\chi_o) R_c^{\,M} \tag{3.46}$$

where $E^{Ro}$ and $R^{Ro}$ are Young's modulus and the uniaxial compressive strength of the natural clay rock, respectively.

In case of triaxial compression, $\theta = -\pi/6$, the Hoek & Brown's yield function for the composite clay rock can be expressed as

$$F^{p} = \frac{(q^{M})^{2}}{(1+\chi)R_{c}^{M}} + \frac{m^{M}}{3} q^{M} - m^{M} p^{M} - (1+\chi)R_{c}^{M} \geq 0 \qquad (3.47)$$

The parameters are re-examined as follows. First, the damage threshold of bonds, the yield locus of clay matrix, and the failure boundary of the saturated clay rock ($s = 0$) are depicted in the $p$–$q$ stress plane in fig. 3.3 together with the strength data obtained on the COX argillite. The bond damage threshold (Eq. (3.36)) at $s = 0$ draws in the $p$–$q$ plane an ellipse with the initial stress state at the -490 m level in the MHM-URL ($\sigma_1$ = 16 MPa, $\sigma_2 = \sigma_3$ = 12 MPa), the major axis of $\sqrt{2K^{bo}r^{b}(o)}$ and the minor axis of $\sqrt{2G^{bo}r^{b}(o)}$. When the stress state reaches the ellipse, damage of bonds occurs and developes with increasing stress beyond the locus. The lower limit of the rock strength is assumed to be the yield boundary of the clay matrix (Eq. (3.23)). When this boundary is reached by the current stress state, plastic deformation takes place. The mean curve of the peak strength data represents the failure envelope (Eq. (3.47)) for the rock mass. It is obvious that the existence of bonds enhances the strength of the material. The post-failure behaviour appears when the stress exceeds the failure envelope. Since the test data do not indicate a significant impact of temperature on the rock strength, the above mentioned boundaries may be applicable for high temperatures up to 100 °C.

The strength of the clay matrix and thus the clay rock increases with drying or suction. This suction effect is taken into account in the model (Eq. (3.25)). Fig. 3.4 compares the model curves with the strength data obtained on COX and OPA samples with different water contents at a confining stress of 10 MPa /BLU 07/. By fitting the data, the model parameters are determined to $R_c^M(o)$ = 35 MPa, $r^M$ = 2.5, $\beta^M$ = 0.02 for the COX clay, $R_c^M(o)$ = 41.5 MPa, $r^M$ = 2.0, $\beta^M$ = 0.02 for the OPA clay at Mont Terri, and $R_c^M(o)$ = 33.3 MPa, $r^M$ = 2.0, $\beta^M$ = 0.02 for the OPA clay at Benken. The effect of the water content on the strength is apparently well represented by the model.

Using the parameters, some typical triaxial compression tests are simulated. Fig. 3.5 compares the simulation results with the test data of COX samples under lateral confining stresses of 1 and 3.3 MPa, respectively. A reasonable agreement between them is achieved, particularly for the linear elastic strain and the subsequent plastic strain with hardening. However, the post-failure behaviour observed could not be represented by the model. As the peak strength is reached, computing ceases. This problem has to be solved with support from the code developer UPC.

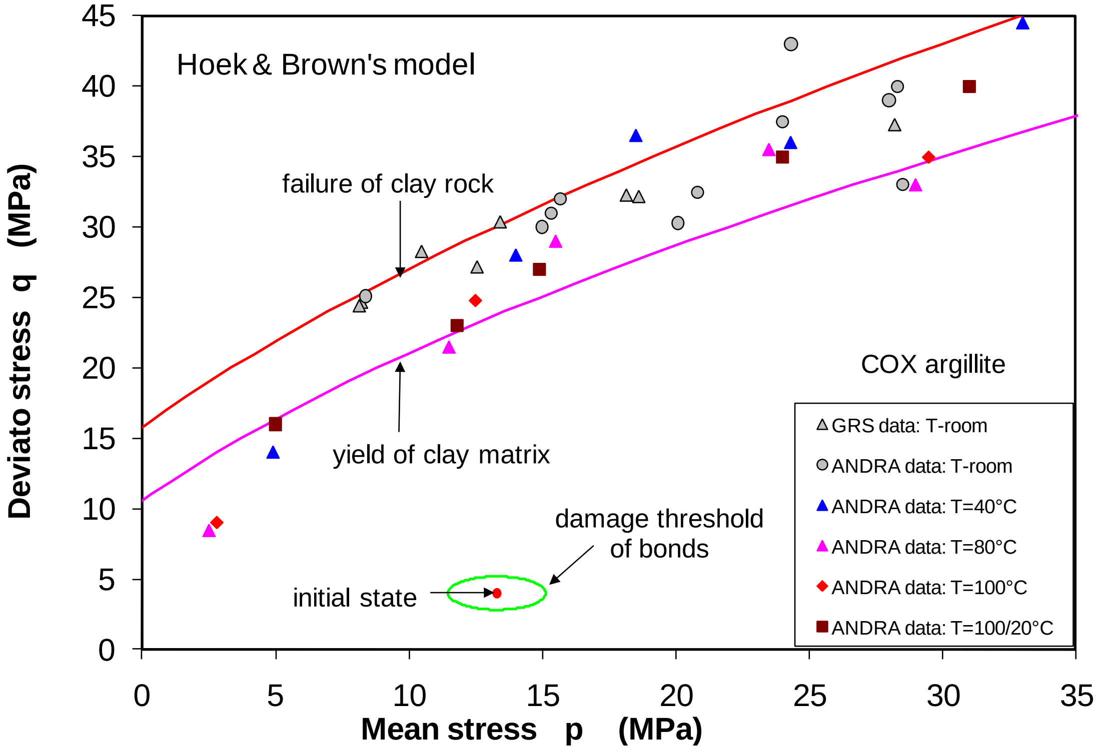


**Fig. 3.3** Damage, yield and failure boundaries of the COX claystone

**Tab. 3.1** Parameters of the damage-elastoplastic model for the COX claystone

| Symbol | Unit | Equation | COX clay |
|---|---|---|---|
| $E^M$ | MPa | (3.21) | 2000 |
| $\nu^M$ | - | (3.21) | 0.28 |
| $K_s^M$ | MPa | (3.22) | 30000 |
| $m^M$ | - | (3.23) | 3 |
| $R_c^M(o)$ | MPa | (3.25) | 17 |
| $r^M$ | - | (3.25) | 2.5 |
| $\beta^M$ | $MPa^{-1}$ | (3.25) | 0.02 |
| $\varpi^M$ | | (3.26) | 0.25 |
| $\xi_r^M$ | - | (3.27) | 0.02 |
| $\alpha^M$ | - | (3.27) | 0.5 |
| $\eta^M$ | MPa·s | (3.29) | $10^6$ |
| $E^{bo}$ | MPa | (3.33) | 4500 |
| $\nu^{bo}$ | - | (3.33) | 0.28 |
| $r^b(o)$ | MPa | (3.36) | 0.7 |
| $r_{os}^b$ | - | (3.36) | 0.0001 |
| $r_{10}^b$ | MPa | (3.39) | 0.04 |
| $r_{11}^b$ | - | (3.39) | 0.7 |
| $\eta^b$ | MPa·s | (3.40) | $10^6$ |
| $\chi_0$ | - | (3.44) | 0.50 |
| **Related parameters** | **Unit** | **Equation** | **COX clay** |
| $K^M$ | MPa | (3.21) | 1515 |
| $G^M$ | MPa | (3.21) | 640 |
| $K^{bo}$ | MPa | (3.33) | 3410 |
| $G^{bo}$ | MPa | (3.33) | 1440 |
| $E^{Ro}$ | MPa | (3.46) | 5250 |
| $\nu^R$ | - | (3.46) | 0.28 |
| $K^{Ro}$ | MPa | (3.46) | 3980 |
| $G^{Ro}$ | MPa | (3.46) | 1680 |
| $R_c^{Ro}$ | MPa | (3.46) | 25.5 |

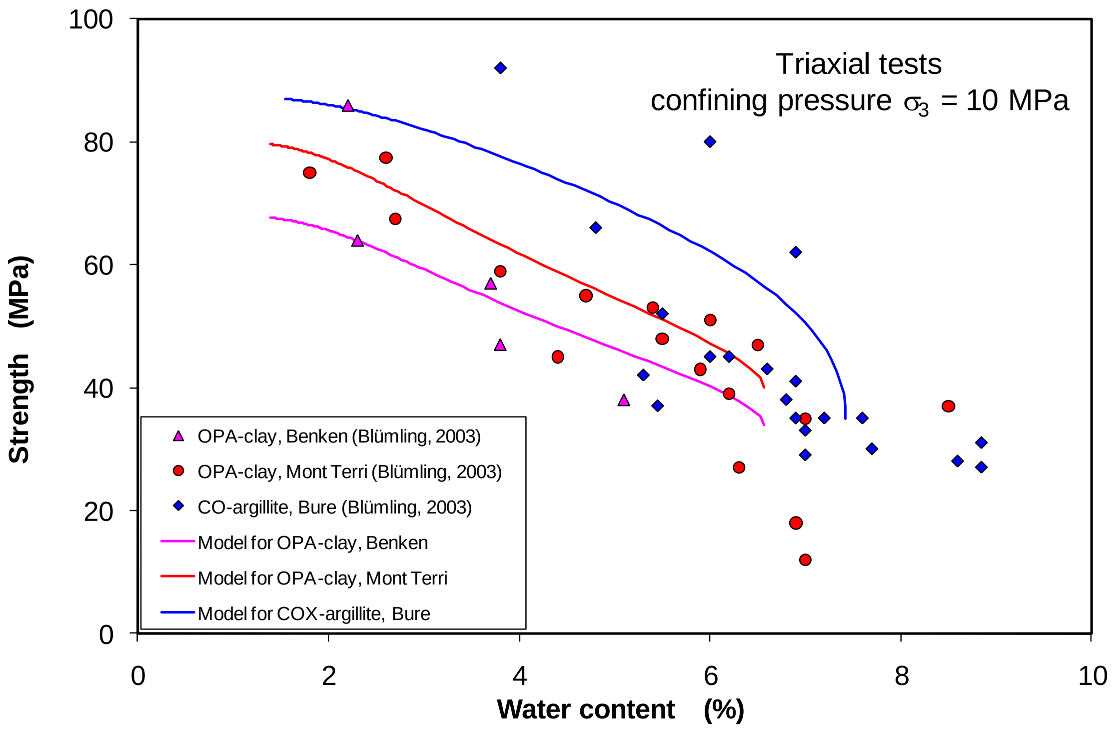


**Fig. 3.4** Dependency of the clay rock strength on the water content

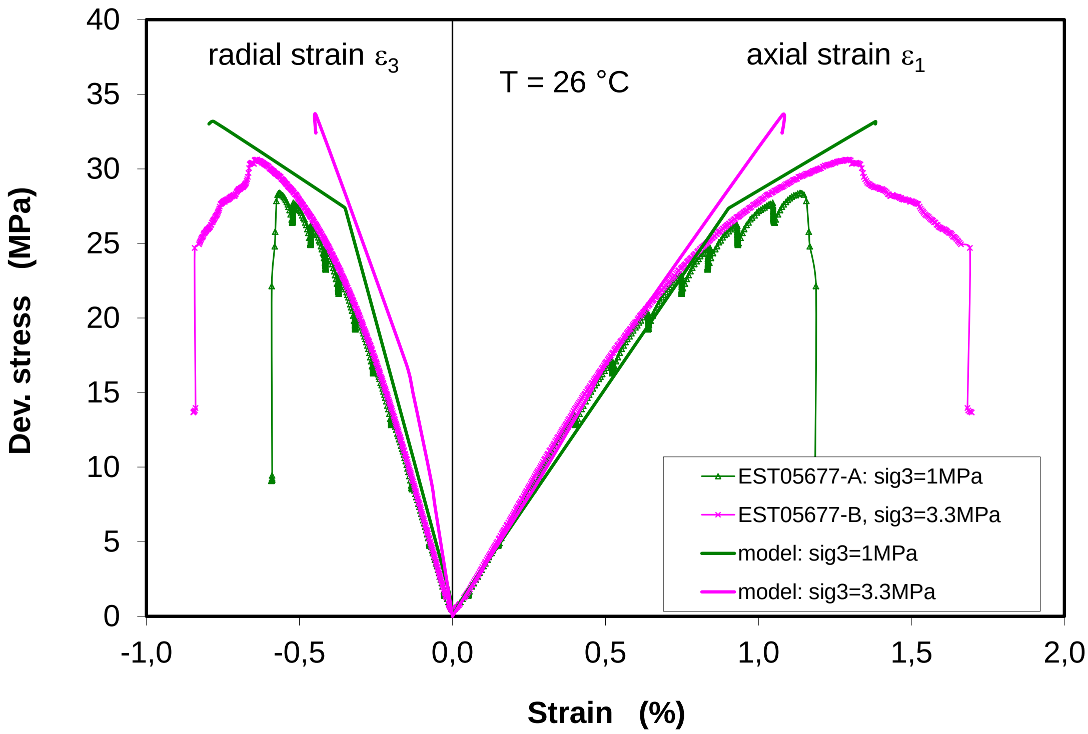


**Fig. 3.5** Simulation of triaxial compression tests on COX samples

In order to get a better fitting for the radial strain and thus the volumetric strain, a variation of Poisson's ratio from $\nu^M = \nu^b = \nu^R = 0.1$ to 0.4 was taken into account in modelling a test. Fig. 3.6 shows the results. While the axial strain predicted by the model increases with decreasing Poisson's ratio, the modelled radial strain seems to be independent from the $\nu$-value. This conflicts with the elasticity theory and has to be checked in the code.

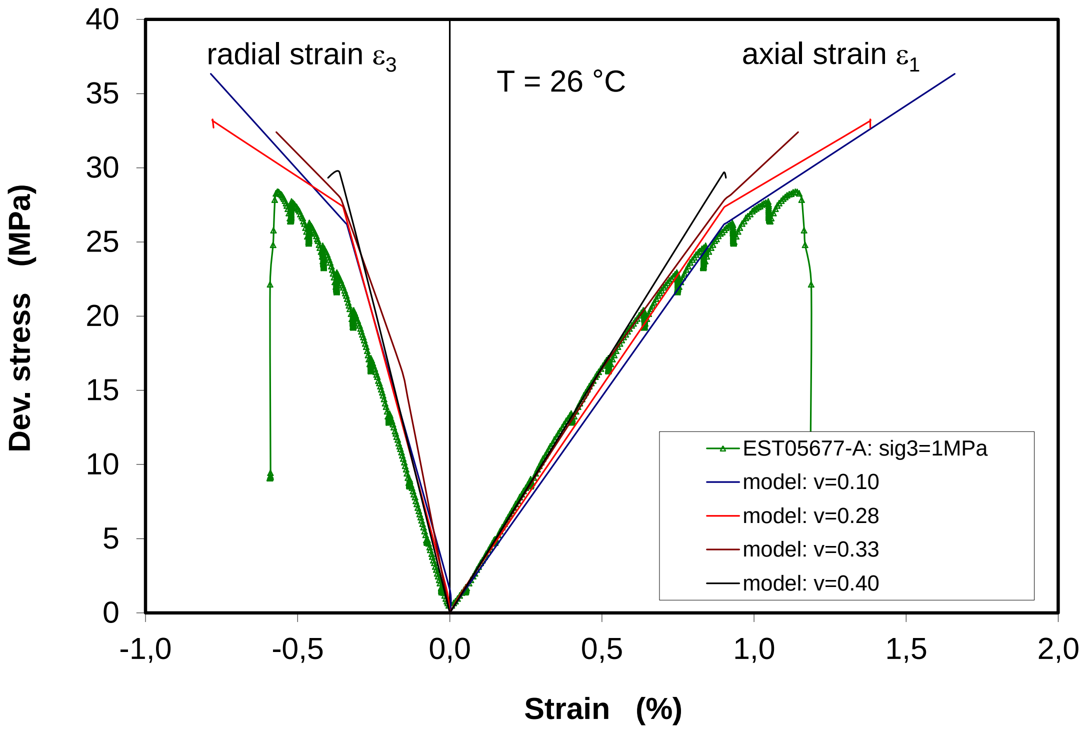


**Fig. 3.6** Modelled strains in response to variations of Poisson's ratio

The stress-strain behaviour of clay rock at different confining stresses is also simulated, as shown in fig. 3.7. The modelling results suggest that the linear elastic deformation seems to be less dependent on the confining stress, but the yield and peak failure stresses increase with the confining stress.

A triaxial compression test performed on a COX sample at an elevated temperature of 90 °C was modelled, too. A lateral stress of 3 MPa and a water back-pressure of 0.2 MPa were applied to the sample ends. Fig. 3.8 compares the stress-strain curves of the modelling and the test data. While the elastic part of the axial strain is well represented by the model, the radial strain and the resulting volumetric strain are under-predicted. Moreover, the yielding point is largely over-predicted, so that the subsequent plastic deformation is practically not represented by the model.

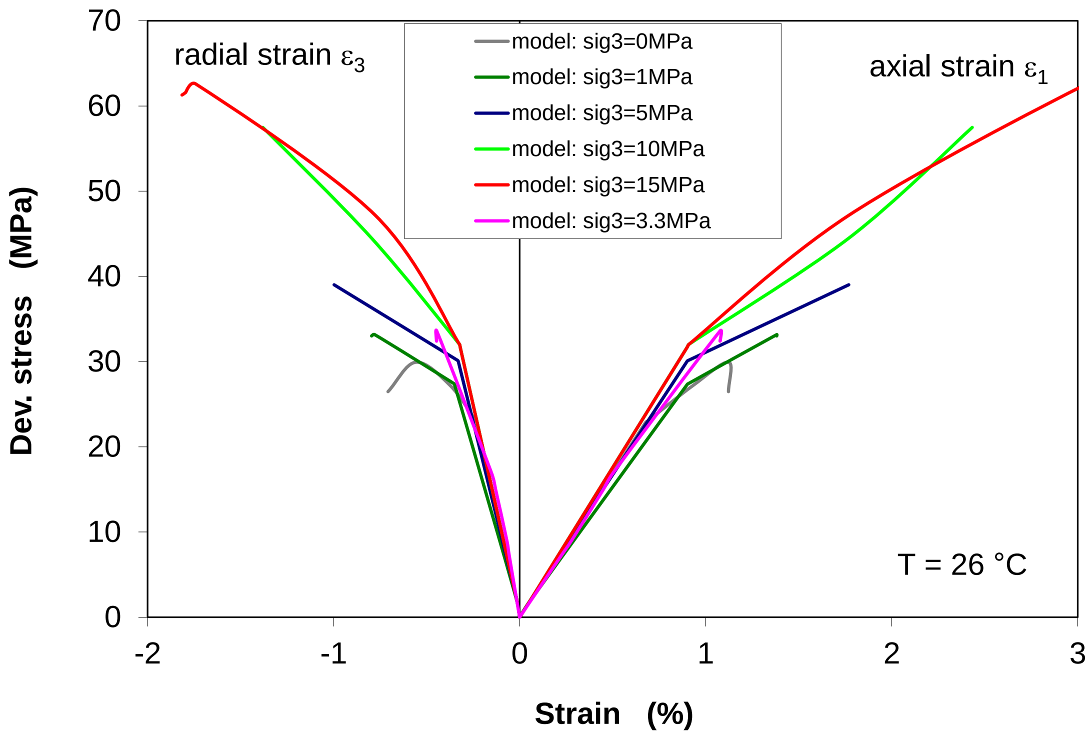


**Fig. 3.7** Stress-strain behaviour predicted by the damage-elastoplastic model at various confining stresses

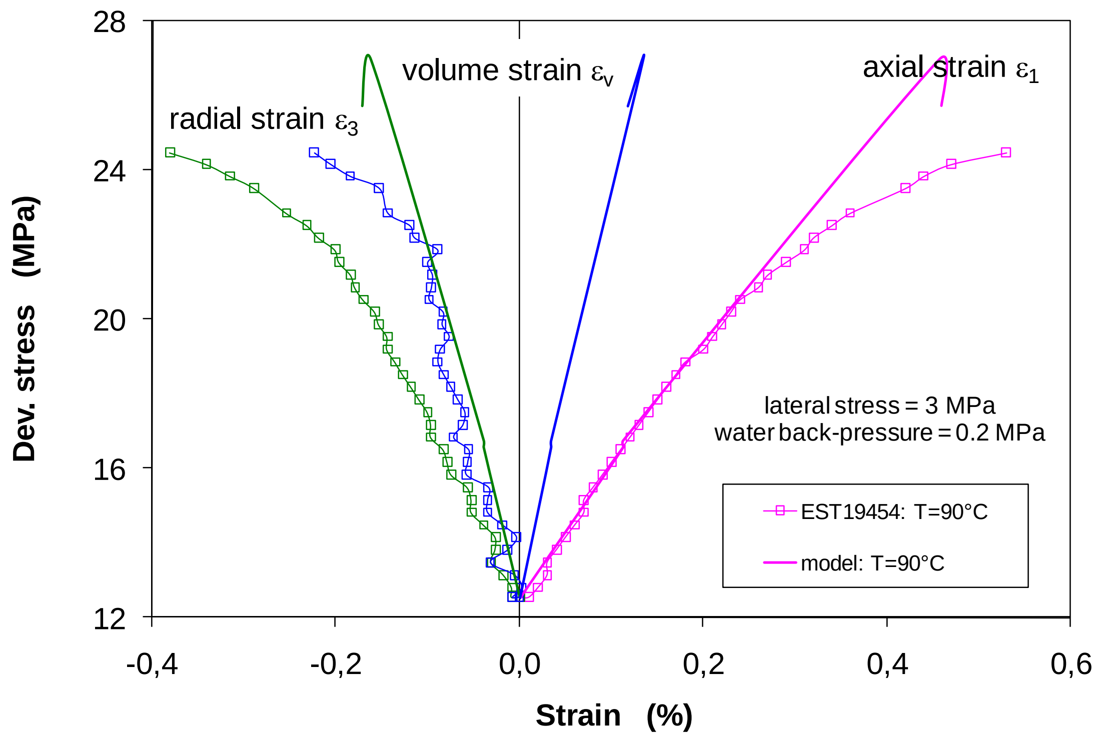


**Fig. 3.8** Model prediction of the stress-strain behaviour of COX claystone at 90 °C

### 3.1.4 Hydraulic models

In highly-consolidated clay rocks, a very significant portion of the water content is adsorbed on mineral surfaces and may not be able to participate in advective transport under normally-encountered pressure gradients. However, the adsorbed water is able to move out thermodynamically from the pores at high external suction, and in contrast, external water can also be taken-up by clays. The process of de- and re-hydration is controlled by the relationship between suction and water content, which was determined on the COX and OPA claystone using the vapour equilibrium technique, as presented in fig. 2.29 in section 2.4.1. The water retention curve is expressed by the Van Genuchten model (Eq. (2.10)) and the parameters are given in tab. 2.3.

Liquid and gas advection in a rock mass follow Darcy's law, as represented in tab. 3.2. The hydraulic conductivity $\boldsymbol{K}_\alpha$ of each phase ($\alpha = l$ for liquid, $\alpha = g$ for gas) is a tensor, depending on the intrinsic permeability $\boldsymbol{k}$, the relative permeability $k_{r\alpha}$, and the dynamic viscosity $\mu_\alpha$. In the modelling, the hydraulic properties of the COX claystone are assumed to be isotropic and thus the permeability as well as the hydraulic conductivity becomes scalar quantity. The intrinsic permeability $k$ decreases with decreasing porosity $\phi$. Kozeny's model is employed for the relationship,

$$k = k_o \frac{\phi^3}{(1-\phi)^2} \frac{(1-\phi_0)^2}{\phi_0^3} \tag{3.48}$$

with an initial permeability value of $k_o = 2 \cdot 10^{-20}$ m$^2$ at an initial porosity of $\phi_o$ = 15 % for the COX argillite (see fig. 3.9).

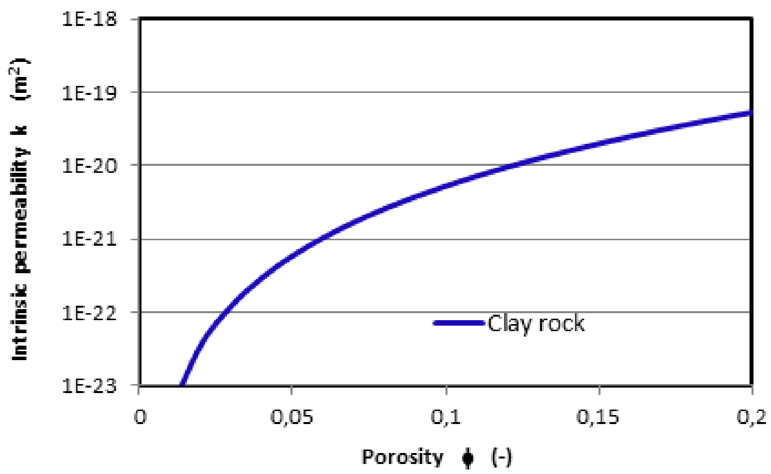


**Fig. 3.9** Permeability related to the porosity of the COX claystone

It is to be noted that this model may not be adequate for description of permeability changes induced by fracturing. Currently, GRS has investigated on permeability changes in relation with fracture closure in the frame of the THM-TON project /THM 07/. Based on laboratory compression tests on fractured COX and OPA claystone as shown in fig. 3.10, Zhang /ZHA 10b/ proposed an exponential model for the fracture closure induced by increasing normal stress as follows:

$$\Delta b = b_m[1-\exp(-\alpha\sigma_n^{\beta})] \tag{3.49}$$

where $\Delta b$ is the aperture closure, $b_m$ is the possible maximum aperture closure (equal to the initial aperture), $\sigma_n$ is the normal stress, $\alpha$ and $\beta$ are constants. If the stress tends to infinity, $\sigma_n \to \infty$, the fractures will be fully closed, i. e., $\Delta b \to b_m$.

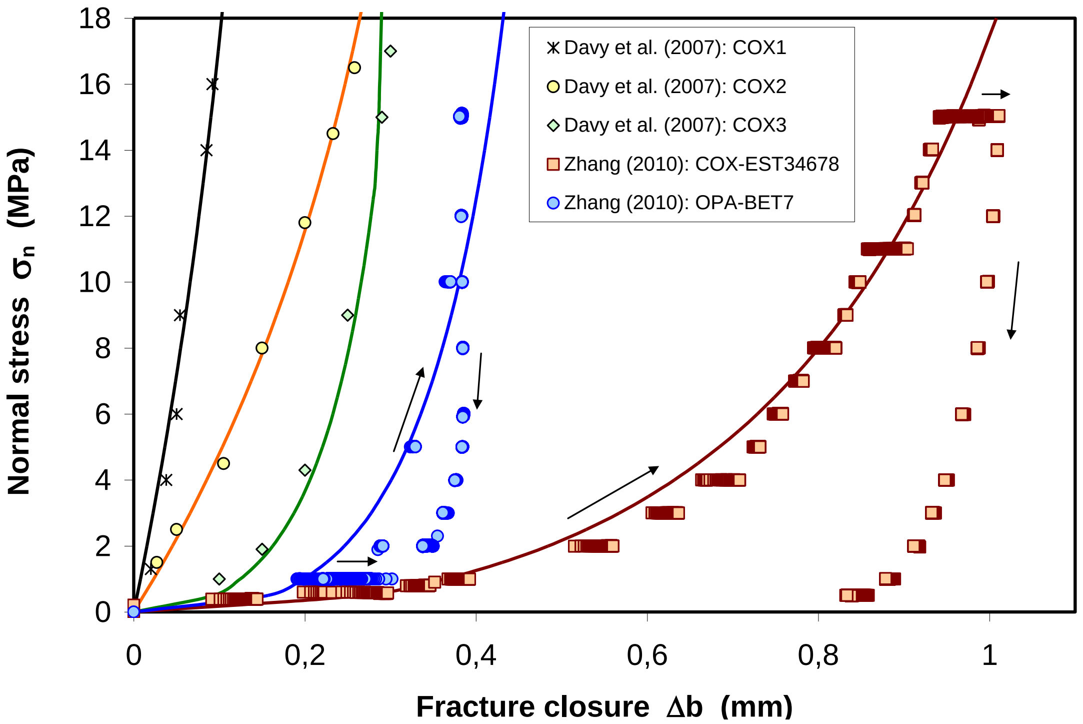


**Fig. 3.10** Fracture closure in relation with normal stress

For the permeability change by fracture closure the following is model is proposed with

$$K = K_{mat} + \frac{R \cdot b_{eff}^3}{12s} = K_{mat} + \frac{R \cdot (b-b_c)^3}{12s} \tag{3.50}$$

where $b_c$ denotes a critical aperture, $R$ represents the influence of the other fracture features (surface roughness, tortuosity, filling and others), and $K_{mat}$ is the permeability of the rock matrix. As the geometric fracture aperture b decreases with increasing normal stress to a very low magnitude($b < b_c$), some parts of the fractures may be separated and isolated by more compacted areas thus eliminating geometric connectivity and hydraulic conductivity of the dead-end fractures. This means that the cubic law is limited to “macro-cracks” ($b > b_c$). Kozeny’s model (Eq. (3.48)) may be suitable for the permeability $K_{mat}$ of the matrix. This “fracture closure-permeability model” has not been used in the frame of this project. It is planned to improve this model within the new programme /THM 10/ and to implement it in the CODE-BRIGHT.

In addition to the advective transport of water and air, vapour diffusion in air and the solubility of air in liquid water are controlled by Fick’s law and by Henry’s law, respectively. The changes of liquid and gas phases are represented by the psychrometric law. The density and viscosity of liquids and gases are dependent on pressure and temperature. The hydraulic models and parameters for the claystone are listed in tab. 3.2. Details of these models can be found in the manual of the CODE-BRIGHT /UPC 04/.

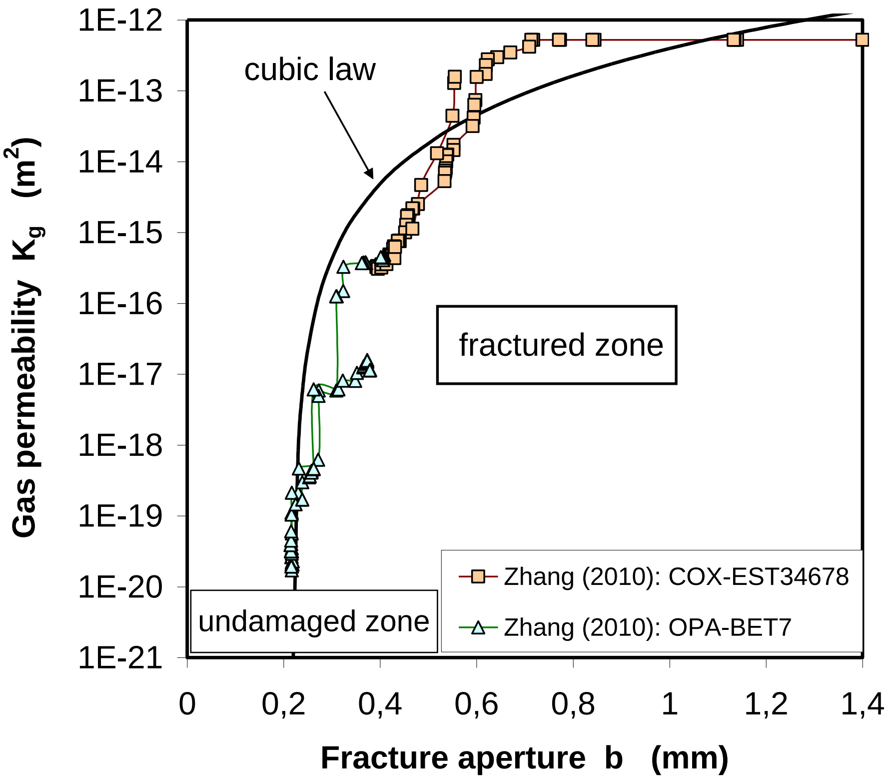


**Fig. 3.11** Fracture permeability as function of fracture aperture

**Tab. 3.2** Hydraulic constitutive laws and parameters for the COX clay rock

| Law | Equation | Parameter |
|---|---|---|
| Darcy's law for advective flux of liquid and gas | $\mathbf{q}_\alpha = -\mathbf{K}_\alpha (\nabla P_\alpha - \rho_\alpha \mathbf{g})$<br>$\mathbf{K}_\alpha = \mathbf{k} k_{r\alpha} / \mu_\alpha$<br>$\alpha$ = $l$ for liquid, $\alpha$ = $g$ for gas | $\boldsymbol{k}$ = permeability tensor<br>$k_{r\alpha}$ = relative permeability<br>$\mu_\alpha$ = dynamic viscosity |
| Intrinsic permeability | $\mathbf{k} = \mathbf{k}_0 \frac{\phi^3}{(1-\phi)^2} \frac{(1-\phi_0)^2}{\phi_0^3}$ | $\boldsymbol{k}_o = \mathrm{k}_o = 2{\cdot}10^{-20}$ m$^2$<br>$\phi$ = porosity, $\phi_o$ = 0.15 |
| Relative permeability | $k_{rl} = A \cdot S_e^B$, $k_{rg} = 1 - k_{rl}$<br>or $k_{rl} = \sqrt{S_e}[1-(1-S_e^{1/\lambda})^\lambda]^2$ | $A$ = 1, B = 5<br>$\lambda$ = 0.6 |
| Saturation of liquid and gas | $S_e = \frac{S_l - S_{lr}}{S_{ls} - S_{lr}}$<br>$S_g = 1 - S_l$ | $S_{lr}$ = residual saturation = 0.01<br>$S_{lr}$ = maximum saturation = 1<br>$S_l$ = actual saturation<br>$S_e$ = effective saturation |
| Suction / saturation – relationship | $S_e = \left[1 + \left(\frac{s}{P_0}\right)^{1/(1-\beta)}\right]^{-\beta}$ | $P_o$ = 28 MPa<br>ß = 0.37 |
| Fick's law for vapour non-advective flux | $\mathbf{i}_g^w = -\mathbf{D}_g^w \nabla \omega_g^w$<br>$= -(\phi\ \rho_g\ S_g \tau\ \mathbf{D}_m^w\ \mathbf{I}) \nabla \omega_g^w$ | $D_m^w = 5.9 \cdot 10^{-12} \cdot \frac{(273.15+T)^{2.3}}{P_g}$ $m^2/s$<br>$\tau$ = tortuosity = 1 |
| Psychrometric law for vapour mass per unit gas volume | $\theta_g^w = (\theta_g^w)^0 \exp\left[\frac{-(P_g - P_l) M_w}{R(273.15+T)\rho_l}\right]$ | $M_w$ = molecular mass of water = 0.018 kg/mol<br>$R$ = gas constant =8.314 J/(mol K) |
| Henry's law for solubility of air in water | $\omega_l^a = \frac{P_a}{H} \frac{M_a}{M_w}$ | $M_a$ = molecular mass of air = 0.02895 kg/mol<br>$H$ = 10000 MPa |
| Liquid density | $\frac{\rho_l}{\rho_{lo}} = 1 + \beta(P_l - P_{lo}) + \alpha_l T$ | $\rho_{lo}$ = 1025 kg/m$^3$, $\alpha_l$ = $-3.4{\cdot}10^{-4}$ K$^{-1}$<br>ß = $4.5{\cdot}10^{-4}$ MPa$^{-1}$, $P_{lo}$ = 0.1 MPa |
| Liquid viscosity | $\mu_l = A \exp\left(\frac{B}{273.15+T}\right)$ | $A$ = $2.1{\cdot}10^{-12}$ MPa s<br>$B$ = 1808.5 K |
| Ideal gas law | $P_g = \frac{\rho_g}{m} TR$ | $m$ = 28.966 kg/kmol for air<br>$m$ = 18.016 kg/kmol for vapour |
| Gas viscosity | $\mu_g = A \exp\left(\frac{B}{273.15+T}\right)$ | $A$ = $1.48{\cdot}10^{-12}$ MPa s<br>$B$ = 119.4 K |

### 3.1.5 Thermal models

Heat transport in porous media is governed by conduction and by advective flow of liquid water and vapour. Thermal conduction is expressed by Fourier's law

$$\mathbf{i}_c = -\lambda \nabla T \tag{3.51}$$

where $\Delta T$ is the temperature change and λ is the thermal conductivity. Because of stratification, argillaceous rocks usually exhibit thermal anisotropy. The thermal conductivity values measured along the directions parallel ($\lambda_{//}$) and perpendicular ($\lambda_{\perp}$) to the bedding plane are: $\lambda_{//}$ / $\lambda_{\perp}$ = 1.9 / 1.3 $W \cdot m^{-1} \cdot K^{-1}$ for the COX claystone and $\lambda_{//}$ / $\lambda_{\perp}$ = 2.1 /1.0 $W \cdot m^{-1} \cdot K^{-1}$ for the OPA clay /D02 07/. This anisotropic property may be not so significant for the clay rocks under confining stresses and is therefore not considered in this modelling work. A mean value of $\lambda = (\lambda_{\perp} + 2 \cdot \lambda)/3$ = 1.7 $W \cdot m^{-1} \cdot K^{-1}$ is adopted for both types of rocks. A value of the specific heat capacity $C_s$ = 800 $J \cdot kg^{-1} \cdot K^{-1}$ is adapted for the solid phase, while $C_l^w$ = 4184 $J \cdot kg^{-1} \cdot K^{-1}$ is taken into account for liquid water and $C_g^w$ = 1900 $J \cdot kg^{-1} \cdot K^{-1}$ is taken into account for water vapour.

The thermal expansion of clay rocks is also characterized by anisotropy with different coefficient values, as for instance, $\alpha_{//}$ = $1.2 \cdot 10^{-5}$ $K^{-1}$ parallel to the bedding and $\alpha_{\perp}$ = $1.9 \cdot 10^{-5}$ $K^{-1}$ perpendicular to the bedding for the COX claystone /D02 07/. Neglecting anisotropy, these data yield an average coefficient of $\alpha_m$ = $1.6 \cdot 10^{-5}$ $K^{-1}$. In saturated condition, the thermal expansion of a porous medium is governed by the expansion of both the solid minerals and the pore water. Neglecting anisotropy, a linear thermal expansion coefficient for the saturated porous medium may be expressed by

$$\alpha_m = \alpha_s (1 - \phi) + \frac{\alpha_w}{3} \phi \tag{3.52}$$

where $\phi$ is the porosity in the rock, and $\alpha_s$, $\alpha_w$, $\alpha_m$ are the expansion coefficients of the solid grains, the pore water, and the saturated rock mass, respectively. The expansion coefficient for clay minerals have a low value of $\alpha_s$ = $2 \cdot 10^{-6}$ $K^{-1}$ /NOY 00/. Using $\alpha_w$ = $3.4 \cdot 10^{-4}$ $K^{-1}$ for water, the coefficient is calculated to $\alpha_m$ = $1.65 \cdot 10^{-5}$ $K^{-1}$ for $\phi$ = 13 % and $\alpha_m$ = $1.75 \cdot 10^{-5}$ $K^{-1}$ for $\phi$ = 15 %. Because the expansion coefficient of the pore water is two orders of magnitude higher than that of the solid grains, the thermal expansion of a saturated clay rock is dominated by the water expansion. Fig. 3.12 compares the theoretic model with the data obtained on OPA samples /ZHA 07c/, /ZHA 08c/ and the averaged thermal expansion curve of the COX claystone. The comparison shows that:

a) the thermal expansion behaviour is nearly the same for both the claystone;
b) the measured data are well represented by the theoretic model for a porosity range of $\phi$ = 13 – 15 %; and
c) the numerical calculation with CODE-BRIGHT gives a slight over-prediction. In case of an unsaturated state, thermal contraction may take place under certain confining stresses, as predicted by the numerical modelling in fig. 3.13.

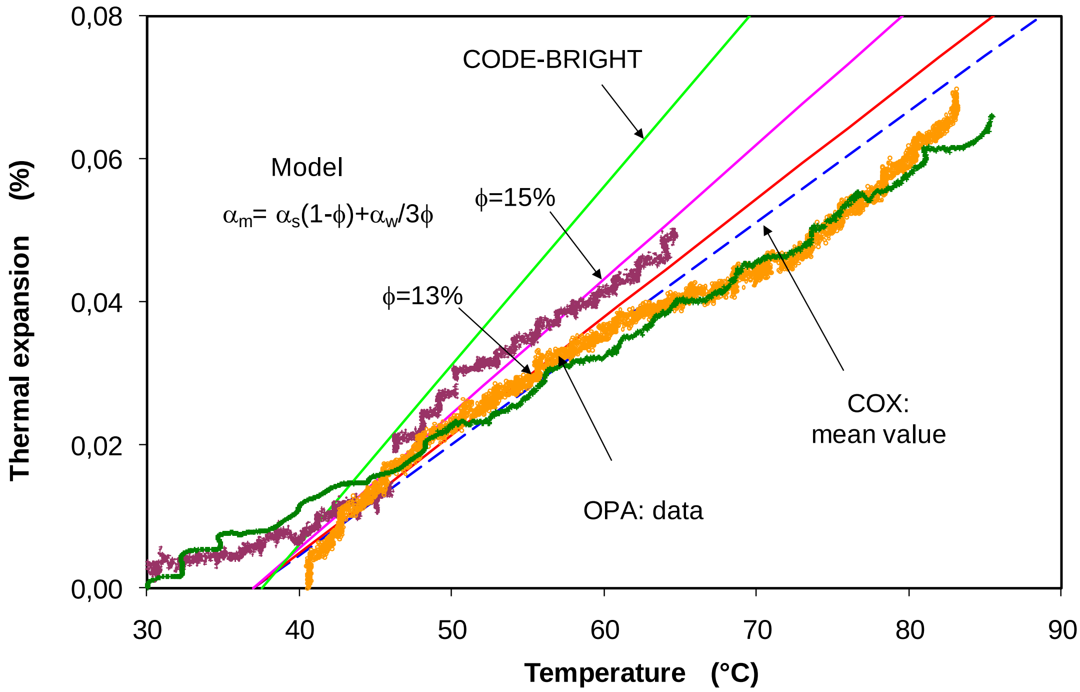


**Fig. 3.12** Thermal expansion of claystone: comparison between model and test data

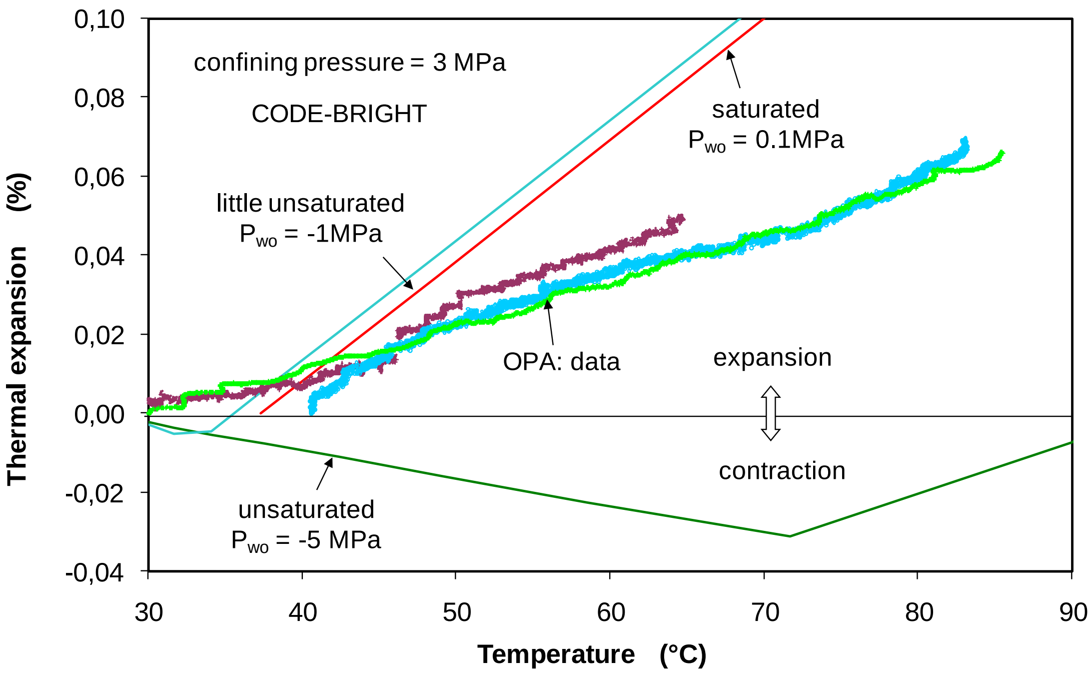


**Fig. 3.13** Thermal contraction and expansion of unsaturated clay given by modelling

**Tab. 3.3** Thermal laws and parameters for the COX clay rock

| Law | Equation | Parameter |
|---|---|---|
| Fourier's law for conductive heat flow | $\mathbf{i}_c = -\lambda \nabla T$ | $\lambda$ = 1.7 W/(m·K) |
| Internal energy of solid | $E_s = C_s \cdot T$ | $C_s$ = 800 J/(kg·K) |
| Internal energy of liquid | $E_l = E_l^w\, \omega_l^w + E_l^a\, \omega_l^a$<br>$E_l^w = C_l^w \cdot T$<br>$E_l^a = C_l^a \cdot T$ | $C_l^w$ = 4184 J/(kg·K)<br>$C_l^a$ = 1006 J/(kg·K) |
| Internal energy of gas | $E_g = E_g^w\, \omega_g^w + E_g^a \omega_g^a$<br>$E_g^w = E_v + C_g^w \cdot T$<br>$E_g^a = C_g^a \cdot T$ | $E_v$ = 2.5·10$^6$ J/kg<br>$C_g^w$ = 1900 J/(kg·K)<br>$C_g^a$ = 1006 J/(kg·K) |
| Linear thermal expansion coefficient of solid grains | | $\alpha_s$ = 2.0·10$^{-6}$ K$^{-1}$ |
| Volumetric thermal expansion coefficient of the pore water | | $\alpha_w$ = 3.4·10$^{-4}$ K$^{-1}$ |
| Linear thermal expansion coefficient of the rock mass | | $\alpha_m$ = 1.7·10$^{-5}$ K$^{-1}$ |

## 3.2 Benchmark modelling of large hollow cylinder tests

Within work package WP5.2 of the TIMODAZ project /D13 10/, GRS participated in a benchmark modelling of laboratory tests on large hollow cylinders of the COX clay rock by using CODE-BRIGHT (version cdv3, /UPC 04/). The main purpose of the modelling work was to validate the constitutive models, particularly the damage-elastoplastic model (section 3.1.3) for the development and recovery of the EDZ around HLW disposal boreholes in the clay formation. The relevant processes such as borehole excavation, backfilling, water transport, heating and cooling were simulated in the tests (section 2.7.2). Two of them, BMT1 and BMT4 were numerically simulated.

Considering the complex testing procedure and boundary conditions of the large hollow cylinder tests, coupled THM calculations were carried out by solving a set of balance equations of energy, solid mass, water mass, air mass and stress equilibrium with selected constitutive models. The main assumptions were as follows:

- The COX clay rock is isotropic and homogeneous because of the insignificance of bedding planes;
- Heat transport includes conduction (Fourier's law) in the porous medium and advection of liquid water and vapour flow;
- Water transport is controlled by liquid water advection (Darcy's law), vapour diffusion in air (Fick's law), and liquid / gas phase changes (psychrometric law);
- Gas migration is governed by advection (Darcy's law), dissolution in liquid (Henry's law) and the ideal gas law;
- The damage-elastoplastic model is applied for the description of the mechanical behaviour of the COX claystone.

### 3.2.1 HM modelling BMT1

The simulation test BMT1 was performed on a COX hollow cylinder (DIR2003-K4) of D/d/L= 280/100/525 mm at an ambient temperature of 26 °C in four steps (fig. 2.71):

1. **Initial state** was adjusted to the same outer and inner borehole pressure of $\sigma_R = \sigma_r$ = 15 MPa and axial stress of $\sigma_a$ = 17 MPa;
2. **Borehole excavation** was simulated by decreasing the inner pressure down to $\sigma_r$ = 2.6 MPa;
3. **Unloading** in radial direction was performed by decreasing the radial stress down to $\sigma_R$ = 3 MPa for 4 days;

4. **Loading** in axial direction was carried out by increasing the axial stress to failure.

During the test, gas flow was recorded at an injection pressure of 1.5 MPa at the bottom. This test was simulated in a hydro-mechanical coupling way using an axisymmetric model. Because the sample was initially not saturated at a degree of 82 %, a corresponding suction of $s$ = 22 MPa was adapted for the sample. The modelling steps with application of corresponding boundary conditions are illustrated in fig. 3.14.

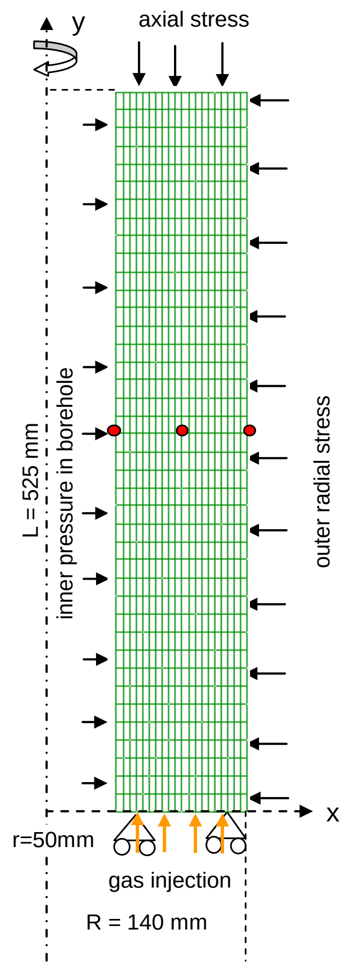


Calculation procedure:

– **Step 1**: t = 0 – 0.9 day
  pre-consolidation
  temperature T = 26 °C
  pore water pressure pl = -22 MPa
  gas injection pressure pg = 1.5 MPa
  vertical stress $\sigma_y$ = 17 MPa
  outer radial stress $\sigma_R$ = 15 MPa
  inner radial stress $\sigma_r$ = 15 MPa

– **Step 2**: t = 0.9 – 1.8 day
  borehole excavation
  inner radial stress from $\sigma r$ = 15 to 2 MPa

– **Step 3**: t = 1.8 – 5.9 day
  radial unloading
  outer radial stress from $\sigma_R$ = 15 to 3 MPa

– **Step 4**: t = 5.9 – 6.0 day
  axial loading
  axial stress from $\sigma y$ = 17 MPa up to failure

**Fig. 3.14** Model geometry and boundary conditions for simulation of the benchmark test BMT1 on a large hollow claystone cylinder

The modelling results are compared with the test data in terms of time evolution of the applied temperature, confining stresses and gas injection pressure in fig. 3.15, the resulting displacements in fig. 3.16, changes of the stress state in fig. 3.17, and variations of the porosity and the permeability near the borehole wall in fig. 3.18, respectively.

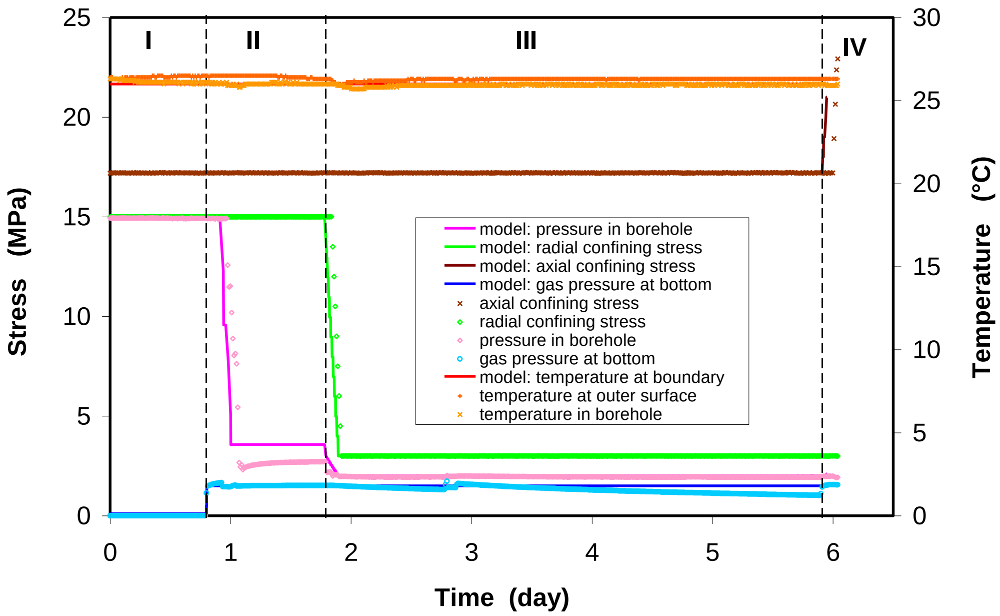


**Fig. 3.15** BMT1 – Applied boundary conditions of temperature, stress and gas pressure and comparison of modelling and test data

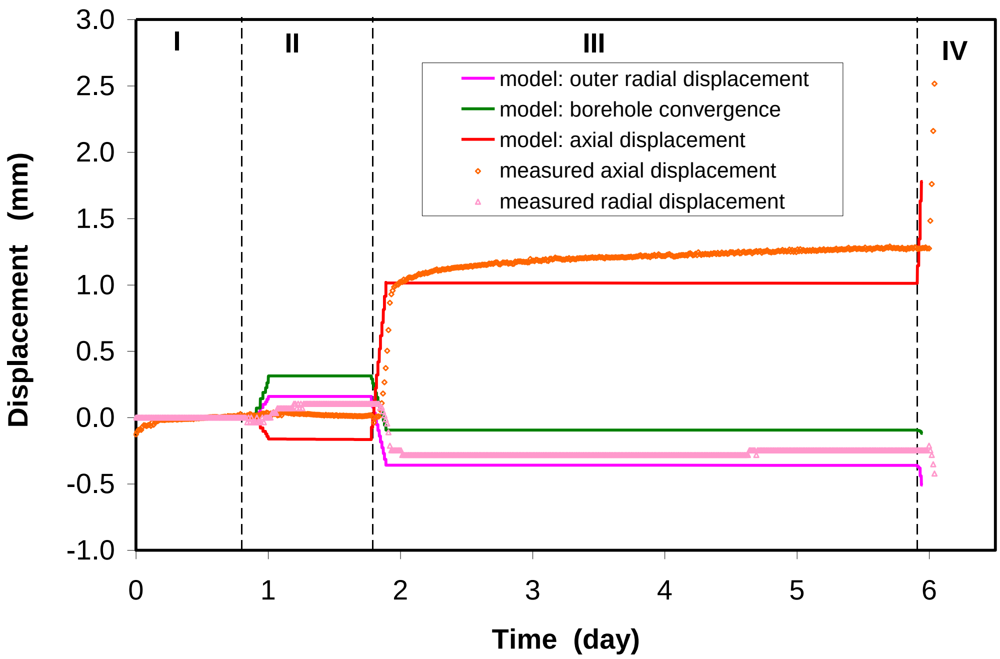


**Fig. 3.16** BMT1 – Response of deformation to the mechanical loading; comparison between modelling results and test data

Comparing the recorded data of axial and outer radial displacements with modelling data one can recognize from fig. 3.16 that the short-term deformations induced by the stress changes are reasonably represented by the model. The time-dependent deformation on the contrary cannot be captured because the model allows the visco-plastic deformation only after yielding.

Fig. 3.17 indicates that after the borehole excavation simulated by reducing the inner borehole pressure from $\sigma_r$ = 15 to 2 MPa, the deviatoric stress near the borehole wall increases largely but remains below the yield criterion. Far from the wall the deviatoric stresses are much lower. A further increase of the axial stress during the last loading phase, however, let the stress rising at all points in the hollow cylinder. In the calculation, an upper limit of the loading was encountered, at which the computation ceased. This computed maximum stress of $\sigma_y$ = 22 MPa is lower than the realistic value of 27 MPa. Further computation for the failure and the post-failure behaviour could not be performed.

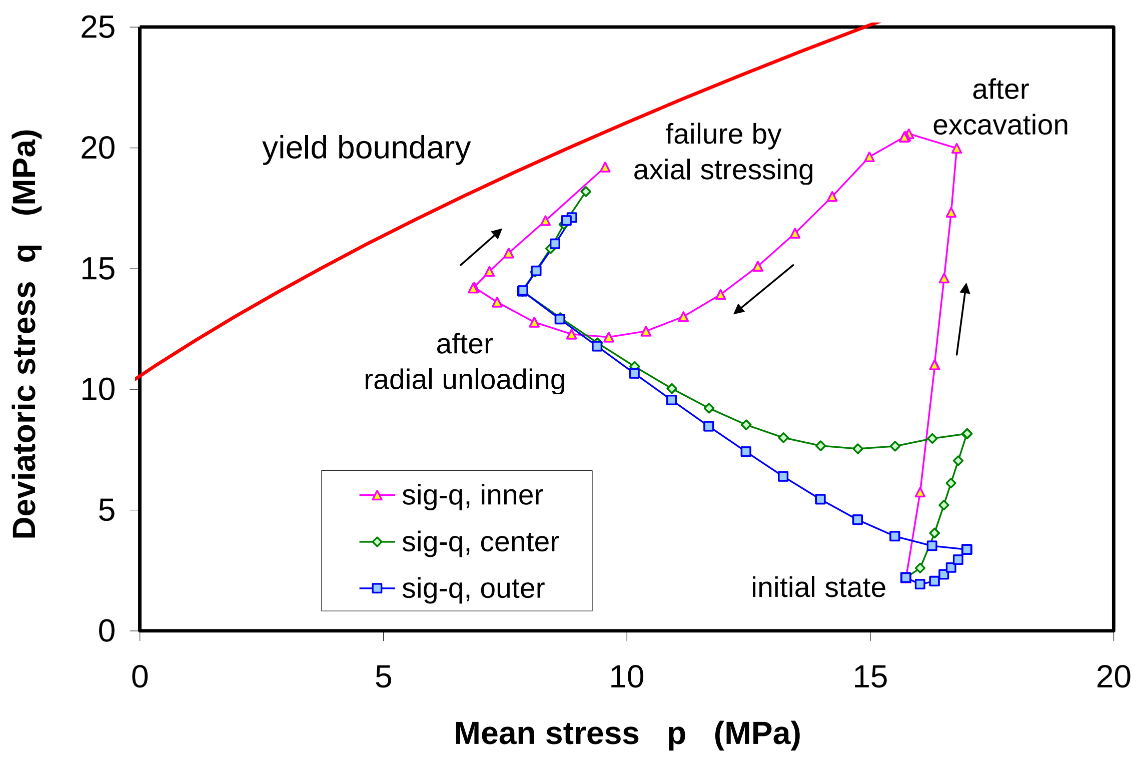


**Fig. 3.17** BMT1 – Calculated stress paths at typical points in the middle section of the sample

According to Kozeny's model adopted for the modelling, the permeability change in the damaged zone near the borehole wall is calculated based on the modelled porosity at that location and compared with the recorded data in fig. 3.18. It is obvious that the permeability – porosity model is not able to capture the dramatic increase in the permeability due to fracturing. Obviously, adequate models are needed for description of such a percolation flow during the fracturing process.

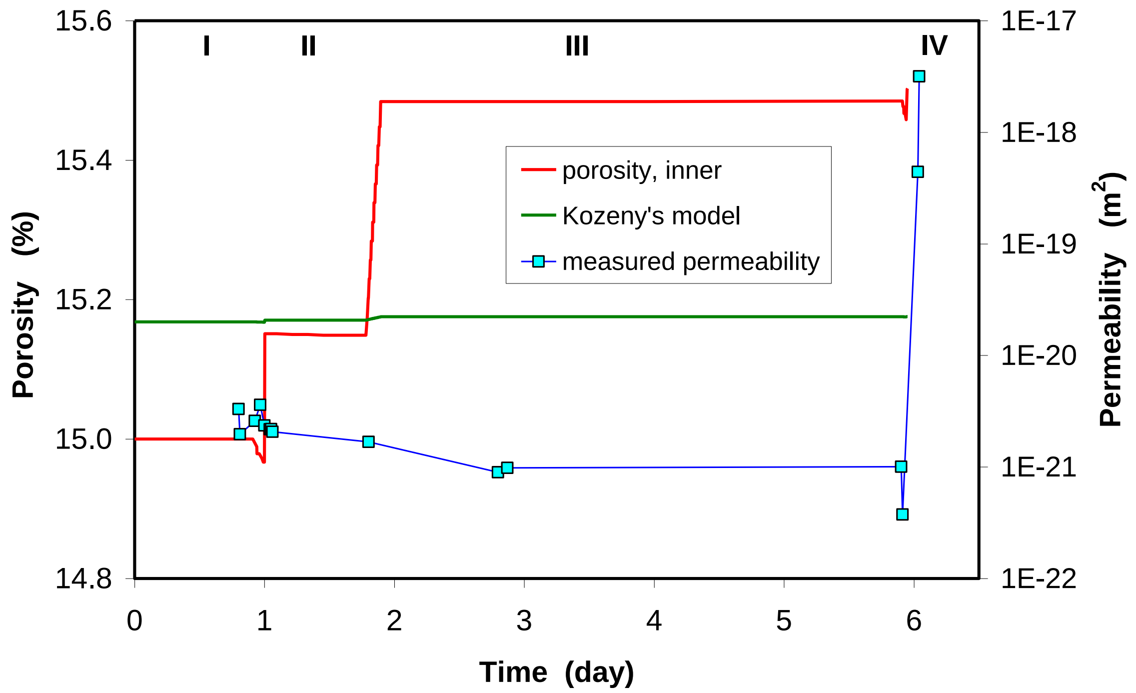


**Fig. 3.18** BMT1 – Calculated permeability variations in comparison to the data

### 3.2.2 THM modelling of BMT4

The benchmark test BMT4 was performed on a COX hollow cylinder (DIR1004-EST27312) of D/d/L= 280/100/460 mm. The test layout and the pictures of the sample before and after testing are shown in fig. 2.74. The test procedure involved six phases with the following boundary conditions:

1. Initial state: same outer and inner borehole pressure of $\sigma_R = \sigma_r = 15$ MPa and at fixed axial strain ($\Delta\varepsilon_a = 0$);
2. Borehole excavation: simulated by reducing the borehole pressure down to $\sigma_r = 1.0$ MPa;
3. EDZ-intensification: by increasing the external radial load till gas breaking through;
4. Water injection to the top of the fractured sample at pressures of 0.5 to 0.3 MPa for 17 days;

5. Temperature increase by heating from 29 °C to 74 °C at the outer surface during 3 days and then kept constant for 19 days;

6. Cooling down to the initial level of 29 °C over 3 days and then kept for 18 days.

Considering the complex testing procedure and conditions, coupled THM calculations were carried out. The initial porosity of 15.8 % and a saturation degree of 90 % (suction $s$ = 10 MPa) were taken into account. An axisymmetric model was adopted for the hollow cylinder (fig. 3.19). The realized test procedure with the above mentioned steps was simulated by applying the corresponding conditions to the model. Fig. 3.20 illustrates the applied boundary stresses and temperatures in comparison with the data.

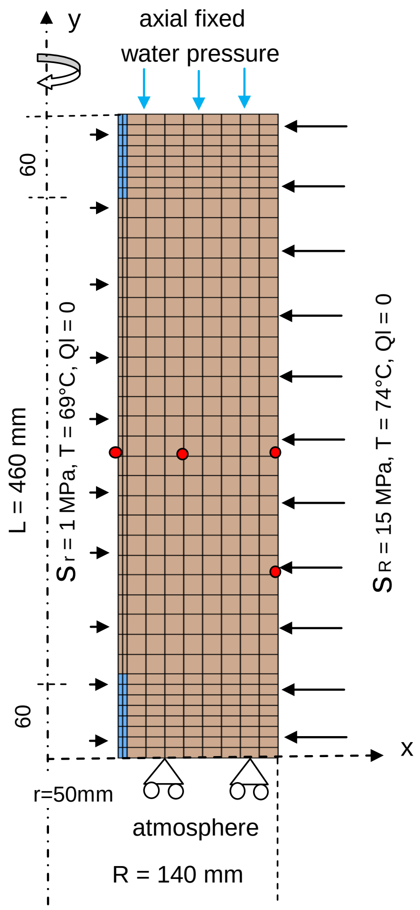


Calculation procedure:

- **Step 1**: pre-consolidation, t = 0 – 1 day,
  T = 29 °C, $p_l$ = -10 MPa, $p_g$ = 0.1 MPa
  $\sigma_y$ = 1.7 MPa, $\sigma_R = \sigma_r$ = 15 MPa
- **Step 2**: borehole excavation, t = 1 – 4.85 day
  $\sigma_r = 15 \rightarrow 1$ MPa
- **Step 3**: fracturing, t = 4.85 – 5.0 day
  $\sigma_R = 15 \rightarrow 17$ MPa ($\sigma_{R\text{-}max}$ limited before failure)
- **Step 4**: unloading, t = 5.0 – 7.9 day
  $\sigma_R = 17 \rightarrow 15$ MPa
- **Step 5**: water injection, t = 7.9 – 26 day
  $p_{in}$ = 0.5 – 0.3 MPa or $Q_{in}$ = 0, $p_{out}$ = 0.1 MPa
  at T = 29 °C, $\sigma_R$ = 15 MPa, $\sigma_r$ = 1 MPa, $\Delta\varepsilon_y = 0$
- **Step 6**: ramp heating, t = 26 – 28 day
  T = 29 °C $\rightarrow$ $T_{out}$ = 74 °C, $T_{in}$ = 69 °C
  at $p_{in}$ = 0.3 MPa, $p_{out}$ = 0.1 MPa
- **Step 7**: heating continues, t = 28 – 48 day
  $T_{out}$ = 74 °C, $T_{in}$ = 69 °C, $p_{in}$ = 0.3 MPa or $Q_{in}$ = 0
- **Step 8**: ramp cooling, t = 48 – 50 day
  $T_{out}$ = 74 °C, $T_{in}$ = 69 °C $\rightarrow$ T = 29 °C
- **Step 9**: cooling down, t = 50 – 69 day
  T = 29 °C, $p_{in}$ = 0.3 MPa or $Q_{in}$ = 0

**Fig. 3.19** Model geometry and boundary conditions for simulation of the benchmark

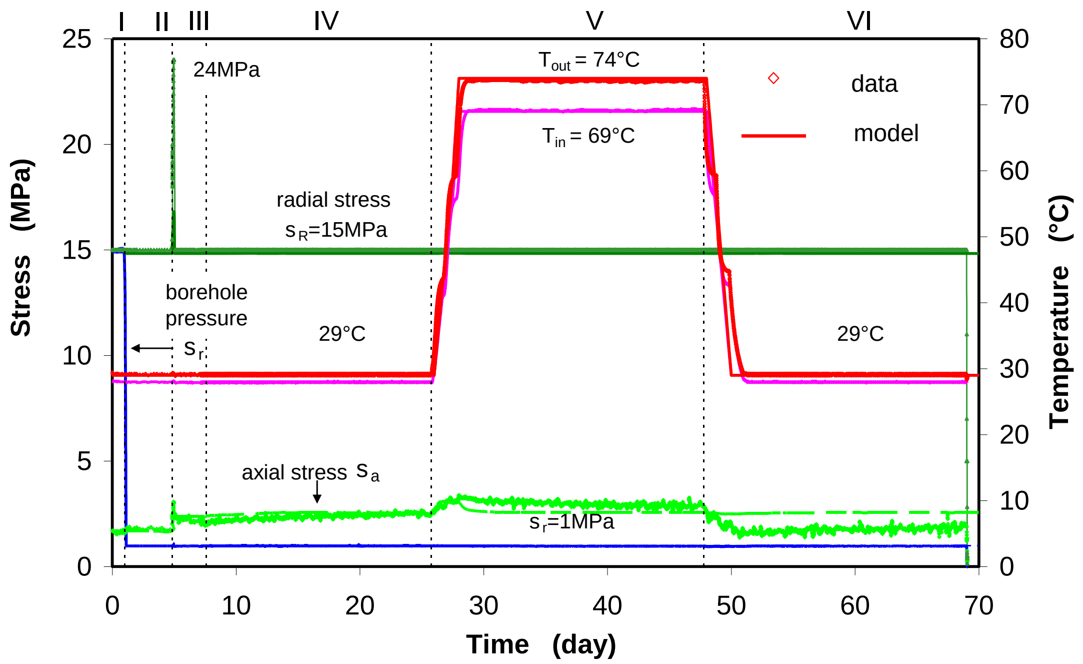


**Fig. 3.20** BMT4 – Applied temperatures and stresses in comparison to modelling and test data

The following boundary conditions are applied:

1) instead of fixed axial strain, the recorded axial stress of 1.7 MPa is applied in the model for the first three steps (I – III) because the poor control of the axial strain and possible weak contacts between the load pistons and the end faces of the sample;
2) the gas migration test during the first three steps (I – III) was not simulated by keeping the gas pressure at atmospheric level;
3) the temperature measured at the inner borehole wall was applied as a boundary condition because of some heat lost from the sample ends; and
4) various values of intrinsic permeability between $4 \cdot 10^{-20}$ and $5 \cdot 10^{-18}$ $m^2$ were examined by comparing water flow and pressure with measured data.

First, the modelled deformations due to the borehole excavation and the EDZ intensification (steps I-III) are compared with the measurements. Fig. 3.21 shows that the deformations at the measuring points and the borehole convergence due to the borehole excavation ($\sigma_r = 15 \rightarrow 1$ MPa) which are reasonably represented by the model, thereby confirming the elastic parameters. After that, the calculated deformations remain constant. The time-dependent deformation cannot be simulated by using the damage-elastoplastic model. Further increasing the external load in radial direction to $\sigma_R$ =

24 MPa resulted in a large convergence of the borehole and fracturing in the sample which was detected by an increased gas flow during the test. However, this failure stress is not matched by the modelling because the computation ceased at $\sigma_R$ = 17 MPa. As mentioned before, the failure and the post-failure behaviour could not be modelled. Inevitably, for the next modelling steps the outer radial stress was reduced to 15 MPa.

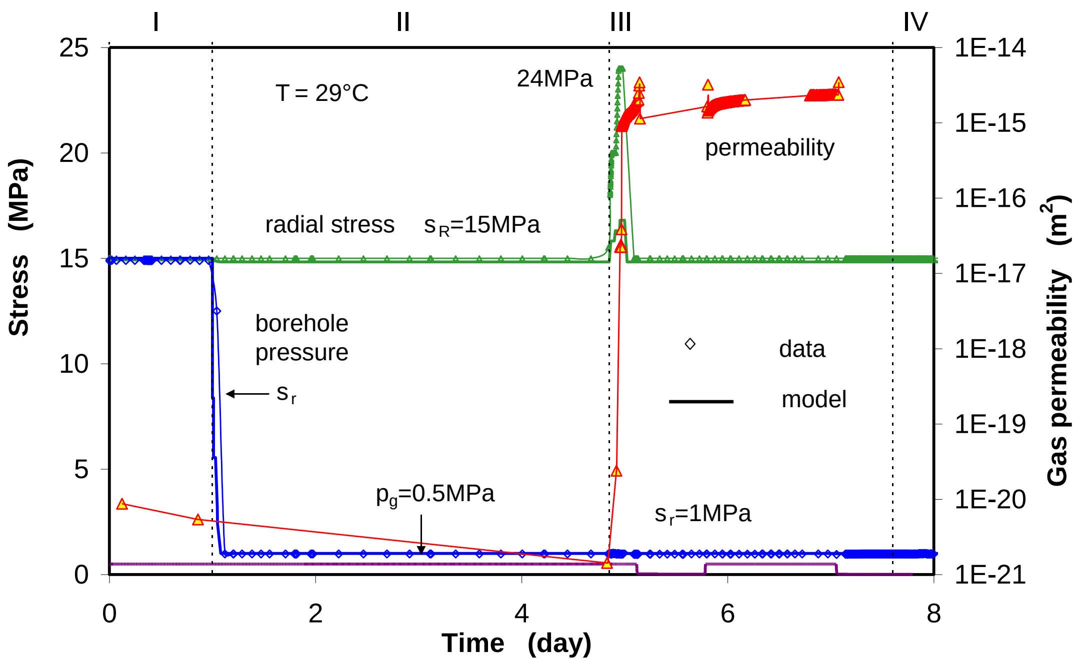


(a) applied stresses and permeability change by fracturing

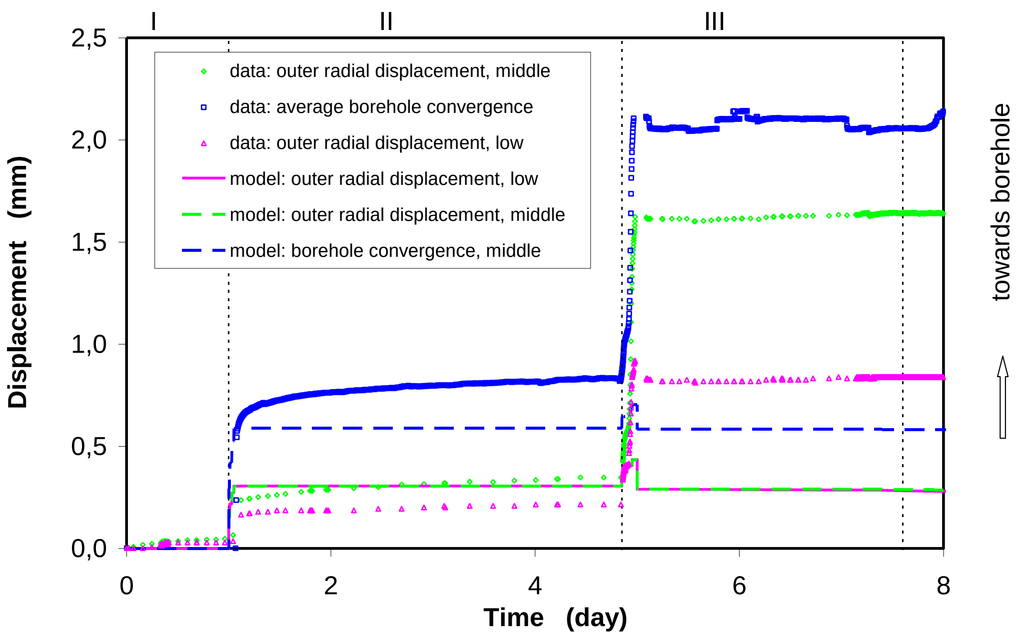


(b) response of deformation to loading

**Fig. 3.21** BMT4 – Calculated and measured mechanical behaviour of a COX hollow cylinder

Fig. 3.22 indicates that, after the borehole excavation, the deviatoric stress near the borehole wall increases subsequently over both yield boundaries of the composite clay rock at suction of zero (saturated) and the initial suction of 10 MPa (unsaturated). The claystone near the borehole wall is more damaged than the inner part of the sample where only the bonds are damaged but the clay matrix does not yield.

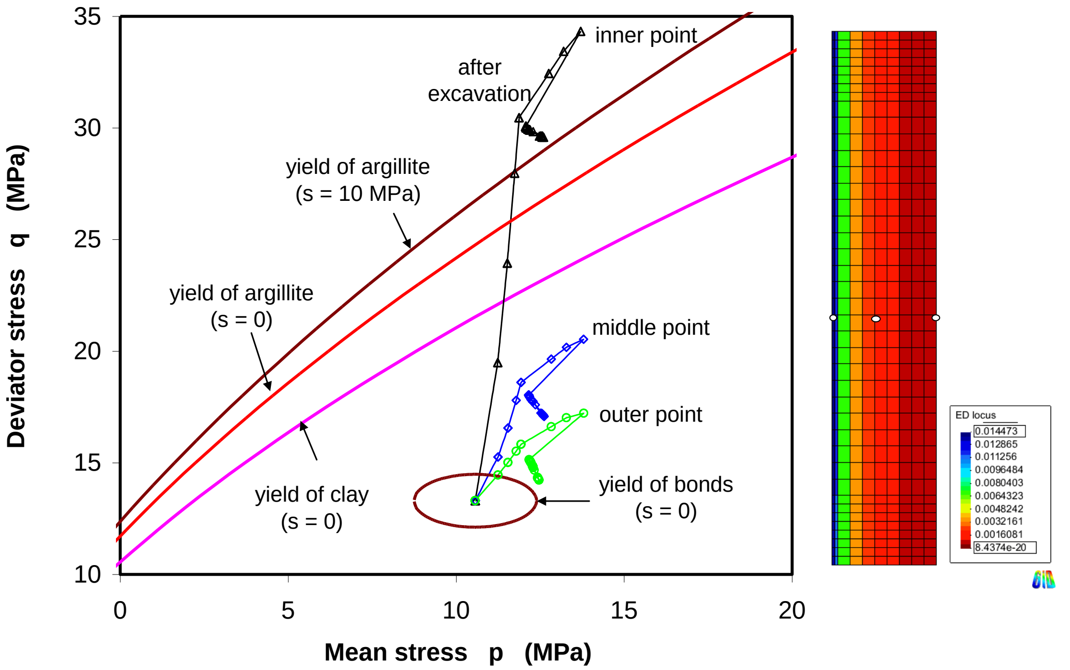


(a) stress paths and yield boundaries (b) damage distribution

**Fig. 3.22** BMT4 – Left: Stress evolution calculated for typical points in the large cylinder in comparison with the yield boundaries of bonds, clay matrix, and the argillite in saturated (s = 0) and unsaturated state (s = 10 MPa) (a); right: damage distribution at external radial load of 17 MPa (b)

After damaging, the water injection (IV), the heating (V) and the cooling (VI) phases followed at a fixed axial strain of $\Delta\varepsilon_y = 0$ and constant outer / inner radial stress of $\sigma_R$ = 15 MPa / $\sigma_r$ = 1 MPa. In the modelling, different permeability values of $4{\cdot}10^{-20}$ and $5{\cdot}10^{18}$ $m^2$ were accepted to fit the observed water inflow and outflow as well as the water back-pressure at the inlet side. Fig. 3.23 compares the calculated and observed water inlet pressure $p_{in}$ and outlet pressure $p_{out}$, while the modelled water inflow $Q_{in}$ and outflow $Q_{out}$ are compared with the measurements in fig. 3.24. During the water injection, the inlet was closed several times to examine the response of the water back-pressure. From fig. 3.23 one can see that the modelled inlet pressure evolution with k = $4{\cdot}10^{-20}$ $m^2$ agrees well with the data. However, the corresponding water inflow and outflow are significantly underestimated (fig. 3.24a). In contrast, the water flow rates (slop of the flux-time curve) are well represented with a high permeability of k = $5{\cdot}10^{18}$ $m^2$ (fig. 3.24b), but the corresponding water back-pressure calculated being much lower than that observed (fig. 3.23). Obviously, these modelled hydraulic parameters are not consistent with each other and also disagree with the measurements. This may suggest that the applied hydraulic models being validated for homogeneous porous materials are not adequate for strongly-fractured clay rocks. Additionally, a great amount of the water inflow at the beginning was recorded in the test, probably filling the space of interconnected fractures. This observation is also not represented by the modelling using the hydraulic models for undamaged materials.

Moreover, the deformation and borehole convergence after fracturing can also not be matched by the modelling (Fig. 3.25). The calculated thermal deformations during the heating and cooling phases are rather small compared with the measured data.

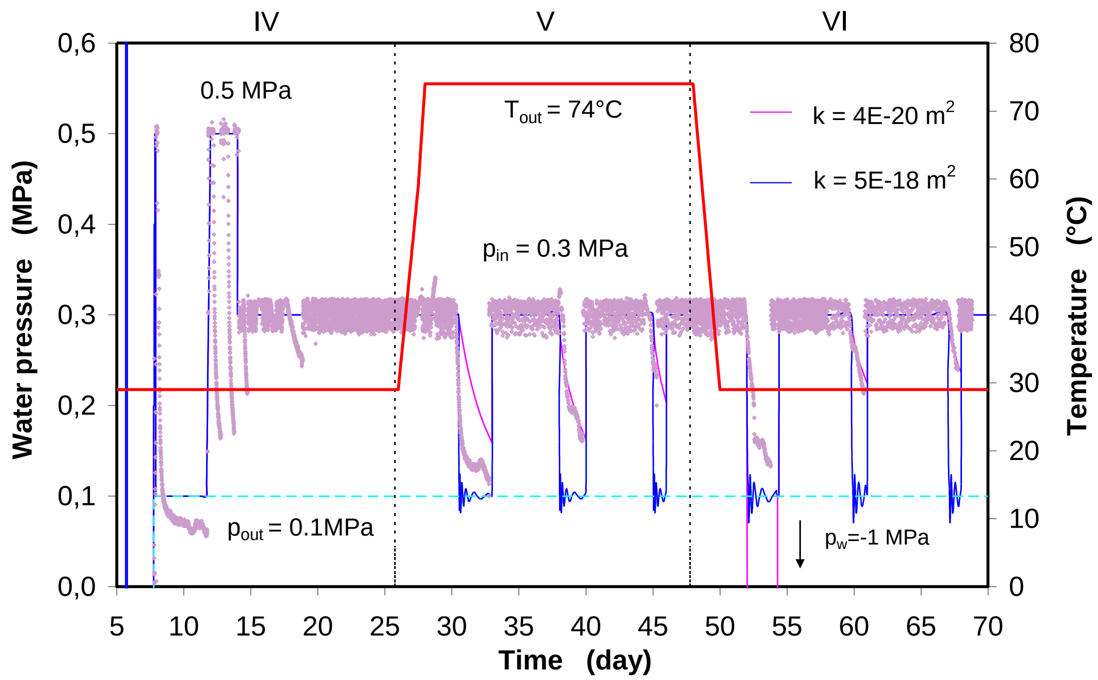


**Fig. 3.23** BMT4 – Comparison of calculated and observed water back-pressure at the inlet before, during and after the heating phase

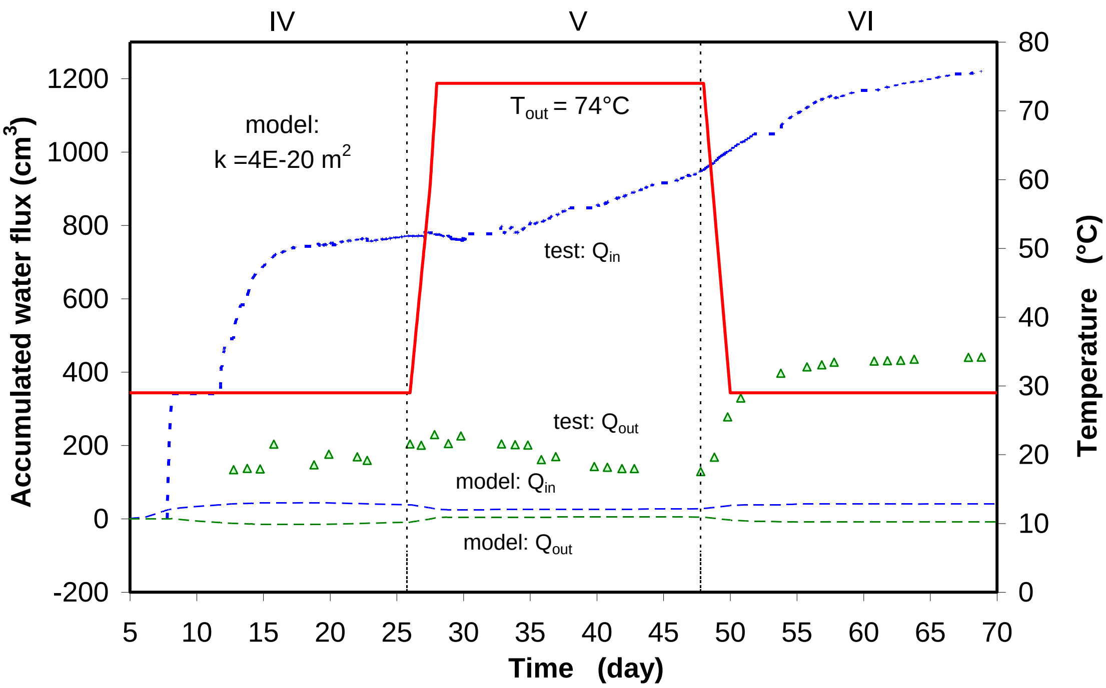


(a) calculated water inflow at k = $4 \cdot 10^{-20}$ m$^2$

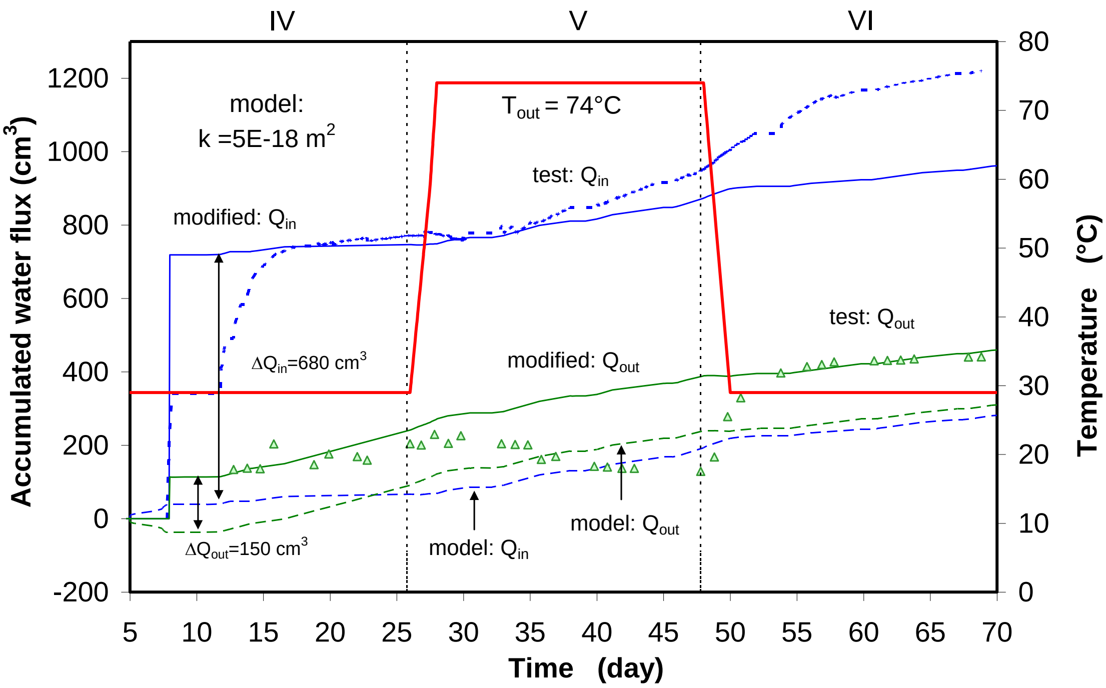


(b) calculated water inflow at k = 5·10-18 m2

**Fig. 3.24** BMT4 – Comparison of calculated and observed water inflow and outflow before, during and after the heating phase

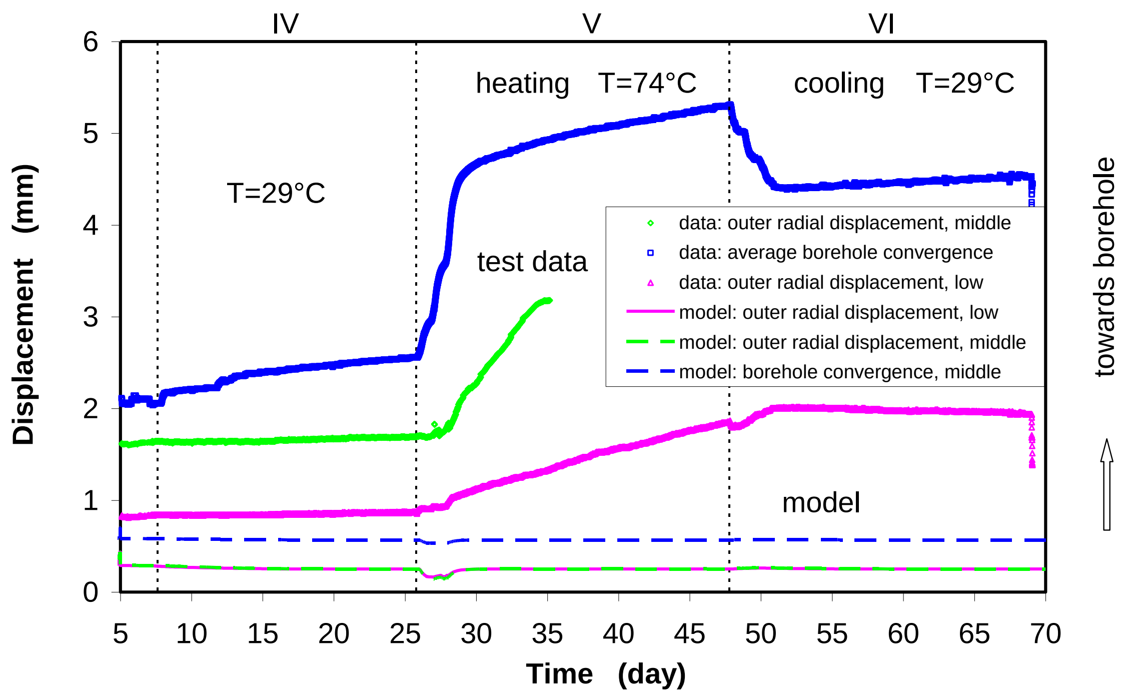


**Fig. 3.25** BMT4 – Comparison of calculated and observed deformations before, during and after the heating phase

#### 3.2.2.1 Conclusions on the benchmark modelling

In the GRS benchmark modelling, the capabilities of the THM constitutive models in CODE-BRIGHT (cdv3), particularly the damage-elastoplastic model for argillaceous rocks, were examined by a comparison of test results obtained from the laboratory creation and recovery of an EDZ around a borehole in a large of a COX claystone test sample. The results indicate that

- The short-term deformation behaviour of the hollow cylinders is reasonably represented by the model with indication of micro-damage evolution. The post-failure behaviour on the contrary could not be modelled due to a premature stop of the computation.
- The drastic increase of permeability by fracturing and the permeability decrease due to re-compaction of the fractures cannot be captured by Kozeny's permeability-porosity relationship for porous media without fractures.
- The observed water inflow into the fractured claystone is significantly underestimated by the modelling even though a real permeability value of the fractured claystone was used.

- The significant responses of deformation in the damaged claystone to heating and cooling are weakly represented by the modelling.

Generally speaking, the THM behaviour of damaged claystone cannot reasonably be approached by the constitutive models for continuum porous media without involving effects of discontinuities. According to our knowledge, the behaviour of damaged claystone is not yet well characterized and understood. The research work has to continue to improve the constitutive models with regard to the prediction of the development and recovery of the EDZ and to enhance the certainty of the long-term safety assessments of HLW repositories in argillaceous formations.

## 3.3 Simulation of shaft sinking

### 3.3.1 Overview of the REP shaft sinking experiment

During the excavation of the main access shaft at the MHM-URL a large scale experiment entitled REP experiment was performed. The REP experimental zone is situated at a depth between z = -460 m and z = -476 m, in which an extensive instrumentation was installed in boreholes drilled from a niche constructed at a level of z = -447 m. Fig. 3.26 shows the layout of the REP experimental zone.

In order to investigate the mechanical and hydro-mechanical behaviour of the rock observed during shaft sinking predictive modelling and interpretive modelling was performed by seven modelling teams (CGES, ITASCA France, CIMNE/ENRESA, NAGRA, ANDRA, Coyne-Bellier, SCK/CEN) using various computer codes /MOD 06/, /SU 07/. The results of the numerical simulations in comparison with the *in situ* experimental findings together with lessons learned from the comparison have been published within the EC-Deliverable 5-6-7 entitled “MODEX-REP – Hydromechanical Modelling of the clay rock response to shaft sinking” of the EURATOM 5$^{th}$ European framework programme /MOD 06/.

Beside the others, GRS modelling exercises were carried out using CODE-BRIGHT. In order to validate the applied constitutive model, interpretive calculations were performed and compared with selected measurement data. Due to the lack of the detailed files of ANDRA’s data only results from physical modelling and numerical simulation are presented below.

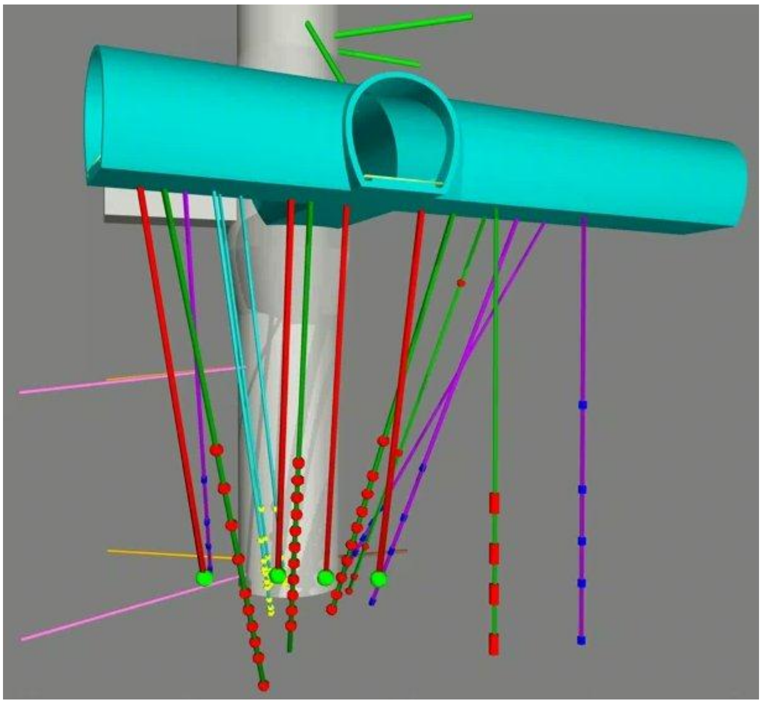

**Fig. 3.26** 3D view of the REP experimental zone with instrumentation boreholes

### 3.3.2 Model and boundary conditions

The HM processes occurring in the clay rock during shaft excavation were calculated in a coupled way by solving a series of balance equations (Eq. (3.1) to (3.5)) for energy, solid, water, air and stress. The balance equations were completed by constitutive equations and equilibrium restrictions which provide the link between the state variables and the dependent variables. In the modelling, the clay rock was assumed to be isotropic and homogeneous, horizontal bedding planes were neglected. Water transport was controlled by liquid water advection (Darcy's law), vapour diffusion in air (Fick's law), and liquid / gas phase changes (psychrometric law). Temperature effects were neglected.

Due to previous experiences in the framework of the numerical simulation of laboratory tests using the damage-elastoplastic model, it has been decided to use a simple elastic approach to describe the hydro-mechanical behaviour of the clay, being aware of the fact that the total deformation might be underestimated.

For numerical analysis of the behaviour of the clay rock during shaft excavation an axisymmetric configuration centred on the axis of the shaft has been considered. The geometry analysed corresponds to a vertical slice of the rock of 100 m in height and 50 m in width. The upper boundary of the slice corresponds to level z = -417 m, the lower boundary to level z = -517 m. Due to the axis convention of the axisymmetric model the z-axis corresponds to the vertical axis oriented upwards, whereas the r-axis corresponds to the horizontal axis.

The geometry of the shaft is modelled with an outer diameter of d = 3 m including a final concrete lining of d = 0.5 m in thickness, that is put in place successively with a distance to the excavation front between 18 m to 22 m. Due to the advanced lining in the shaft, convergence is not allowed by fixing the radial displacement ($\Delta u_r = 0$) along the shaft wall.

The geometry is shown in fig. 3.27, whereas the shaft excavation scheme as well as the final lining advance is shown in fig. 3.28.

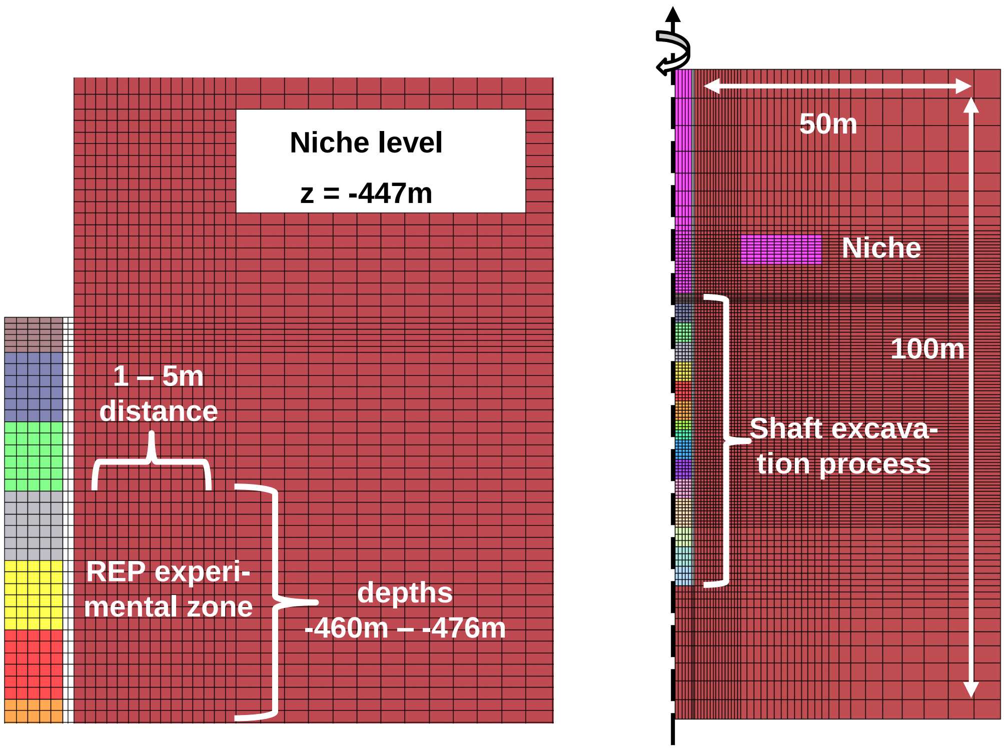


**Fig. 3.27** FE model (axisymmetric) used for numerical simulation of REP experiment

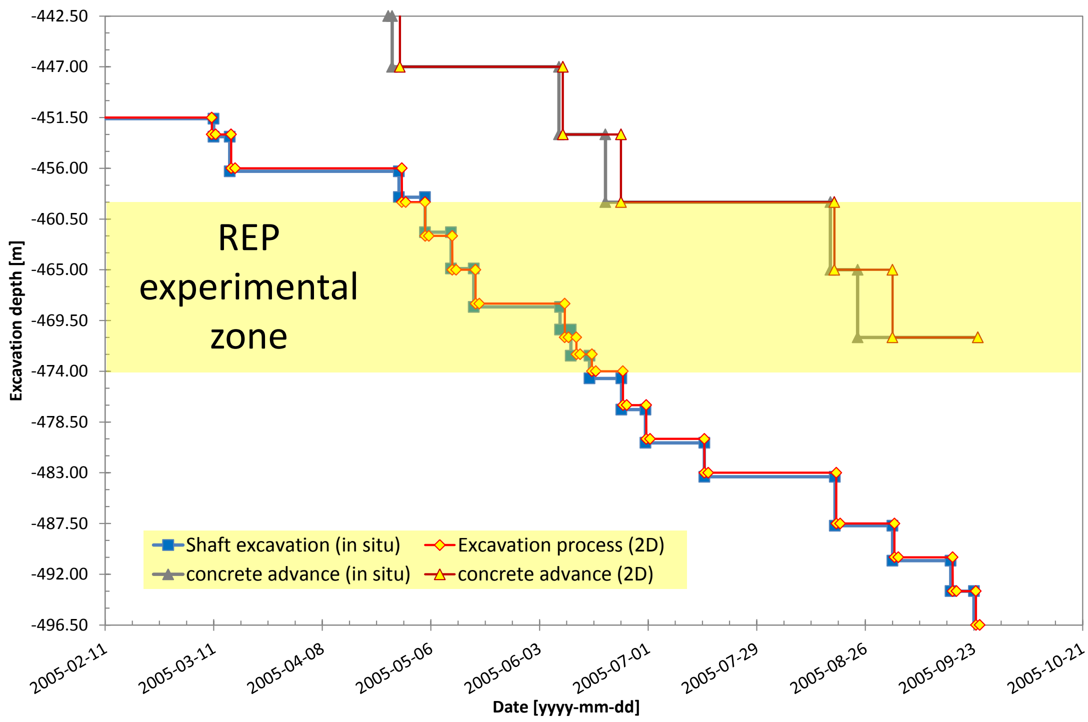


**Fig. 3.28** Shaft excavation scheme used for numerical simulation

The shaft excavation scheme is simulated by removing the corresponding rock volume from the mesh that automatically sets the radial stress equal to 0. The hydraulic conditions at the clay rock contour are somewhat complicated. The shaft has been actively ventilated during each excavation step, and also after the lining is put in place it has to be assumed that water flow out of the rock is still possible. Therefore the ventilation process has been abstracted and modelled as atmospheric pressure of $p_W$ = -0.1 MPa acting at the contour zone.

According to the lithostatic distribution specified by /MOD 06/ an orthotropic initial stress state is characterised by the vertical stress ranking from $\sigma_z$ = -9.7 MPa at the upper boundary to $\sigma_z$ = -13.3 MPa at the lower boundary of the mesh. Between the same levels, the horizontal stress varies from $\sigma_r$ = -13.3 MPa to $\sigma_r$ = -15.3 MPa. For initial water pressure a hydrostatic distribution is considered, that is between $p_W$ = 4.17 MPa at the upper boundary and $p_W$ = 5.17 MPa at the lower boundary.

A constant porosity $\phi$ = 0.15 is considered for the rock. The material parameters associated with the constitutive equations were determined for the COX clay and used in the documented calculations. The values of the parameters are represented in chapters 3.1.3 and 3.1.4.

### 3.3.3 Modelling results and field observations

In the following, selected field observations taken from /MOD 06/ are discussed and compared to the achieved modelling results.

**Extensometer measurements**

Two boreholes were equipped with multi-point extensometers for measuring rock displacements on the borehole axis. The boreholes REP2201 and REP2202 are oriented perpendicular and parallel towards the maximum horizontal stress, respectively. In fig. 3.29 the evolution of displacements within the rock as measured in borehole REP2202 compared with the head of the extensometer is shown. Excavation was carried out with the drill and blast method. For each blast, instantaneous displacement was measured on the extensometer. As the working face progressed towards the REP zone, an initial compression phase was observed, followed by an extension phase. As long as shaft sinking operations had not reached the anchoring level, the extensometer remained under compression. However, as soon as the shaft passed the anchoring level the extensometer started to expand. After the excavation face had gone past, the measuring points did not return to their initial positions. Permanent extension was observed on all the sensors. However, relative positions between sensors no. 1 to no. 8 were only slightly altered, whereas the performance of the sensors no. 9 and no. 10 close to the shaft wall at a distance of about 0.8 m and 0.5 m, respectively, suggests that inelastic deformations are caused in the rock in the shaft wall vicinity. From a depth of about z = -480 m, increases in instantaneous displacements due to the drill and blast excavation method were very insignificant. Therefore displacements measured after the mid of July were no longer related to the shaft excavation progress but to its convergence.

Using a simple hydro-mechanical coupled physical modelling approach the compressive deformation in front of the shaft excavation face is followed by an increase in pore water pressure as long as no rock damage occurs. Therefore the extensometer measurements results suggest that the sensors might show a visible increase in pore water pressure before the shaft excavation front passes by.

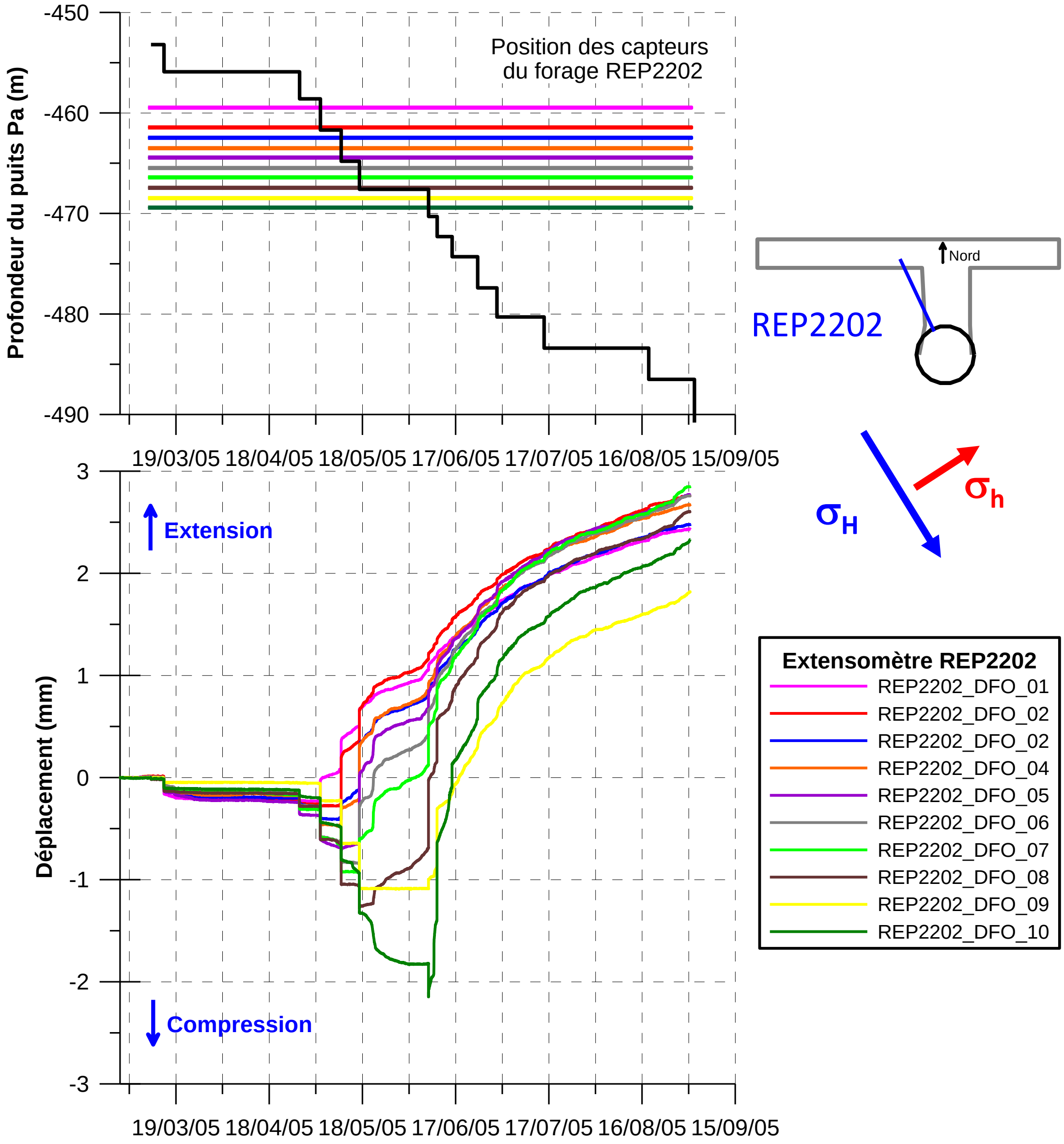


**Fig. 3.29** Evolution of axial displacements in borehole REP2202 /MOD 06/

## Pore water pressure measurements

Four boreholes are dedicated to pore-water pressure measurement. In three of them, the measuring points are located around the shaft at distances of about 1 m to 5 m from the contour. The fourth borehole is located outside the influenced zone around the shaft and serves as a reference point at a distance of more than 13 m. After the installation was completed, the pore water pressure was restored and stabilised at almost at 3.4 MPa to 3.9 MPa. In fig. 3.30 *in situ* measurements on pore water pressure evolution in borehole REP2202 during the sinking of the access shaft are shown.

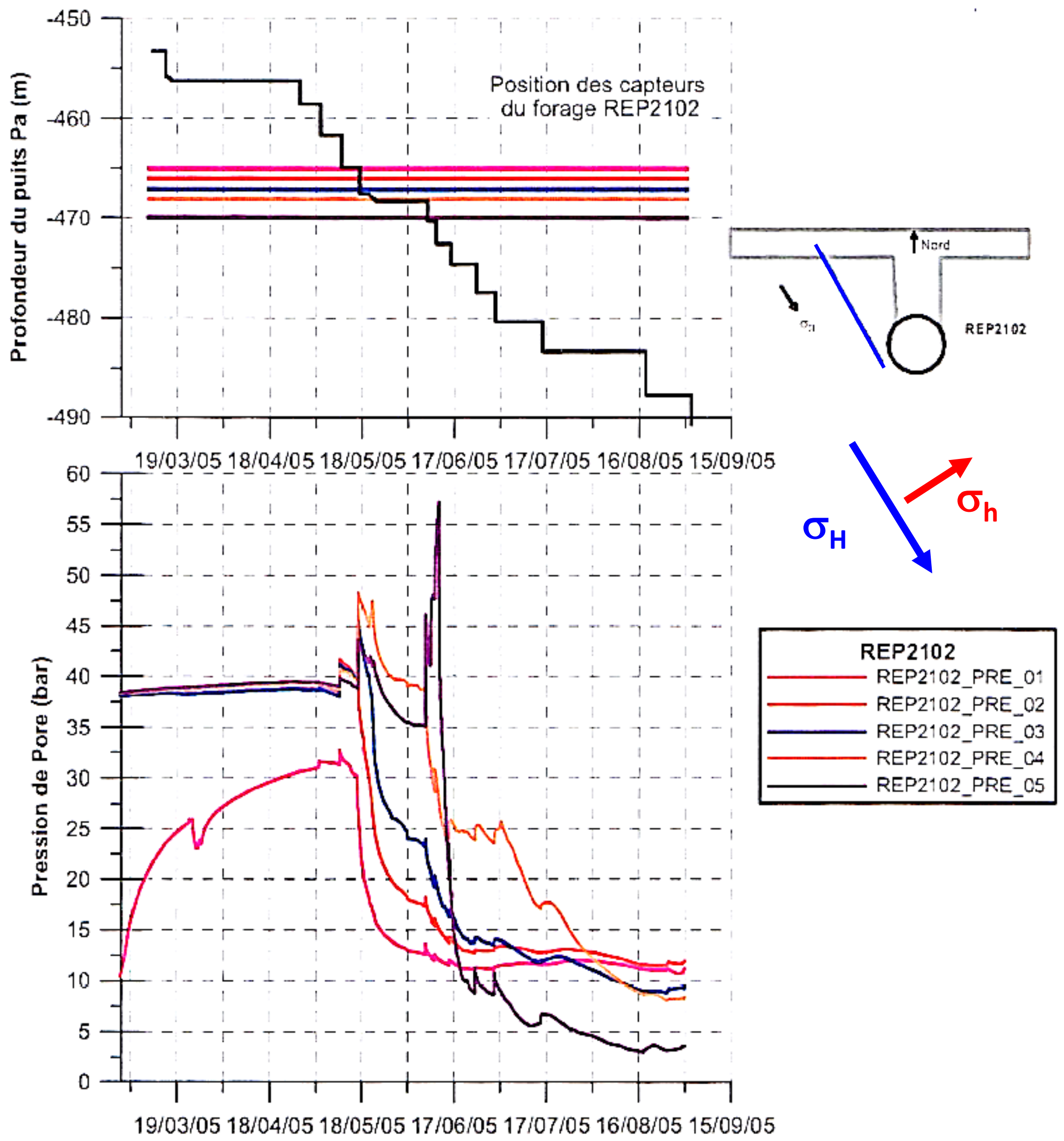


**Fig. 3.30** Evolution of pore water pressures in borehole REP2102 /MOD 06/

The borehole REP2202 is located towards the maximum horizontal stress. When the excavation was approaching the level of the sensor, overpressure was observed. This overpressure was all the higher, the closer the sensor was located to the shaft wall. When the level of the sensor was overtaken by the excavation process, the pore water pressure started to fall. After the excavation face had gone past, the measurement results of sensors no. 1 to no. 4 stabilised again at almost 1.0 MPa, whereas the results of sensor no. 5 tended towards atmospheric pressure.

Though overpressures were also observed in some sensors in borehole REP2103, which is located in the area towards the minimum horizontal stress, this type of coupled hydro-mechanical behaviour could not be observed systematically in all of the three boreholes located around the shaft.

In borehole REP2101, with similar orientation to maximum horizontal stress as borehole REP2102, instead of an overpressure a slight decrease in pore water pressure before the passage of the excavation could be observed. A possible explanation could be the existence of damaged rock zones.

**Numerical simulation**

The aforementioned measurement results show that the applied constitutive model should reflect the hydro-mechanical behaviour of the clay rock as follows:

- Level of pore water pressure below hydrostatic value before shaft excavation,
- Overpressure due to compressive loading resulting from shaft excavation process,
- Pressure decrease due to extensional deformation when shaft excavation front passes,
- Level of pore water pressure after the excavation face has gone past.

The applied model might not show the pressure decrease towards atmospheric pressure measured in REP2102 sensor no. 5 due to the fact that rock damage was not considered. The displacements measured in extensometer REP2202 after mid of July that were related to the shaft convergence process could also not be simulated with the applied modelling approach, because mechanical time-dependent deformation behaviour besides the consolidation process was not considered.

For comparison several nodes within the finite element mesh were selected with respect to depth and distance to the shaft contour zone and their results of hydro-mechanical simulation were compared to the experimental findings on pore water pressure at borehole REP2102 as well as extensometer measurements at borehole REP2202. Fig. 3.31 shows the position of the sensor intervals and the selected nodes of the finite element mesh.

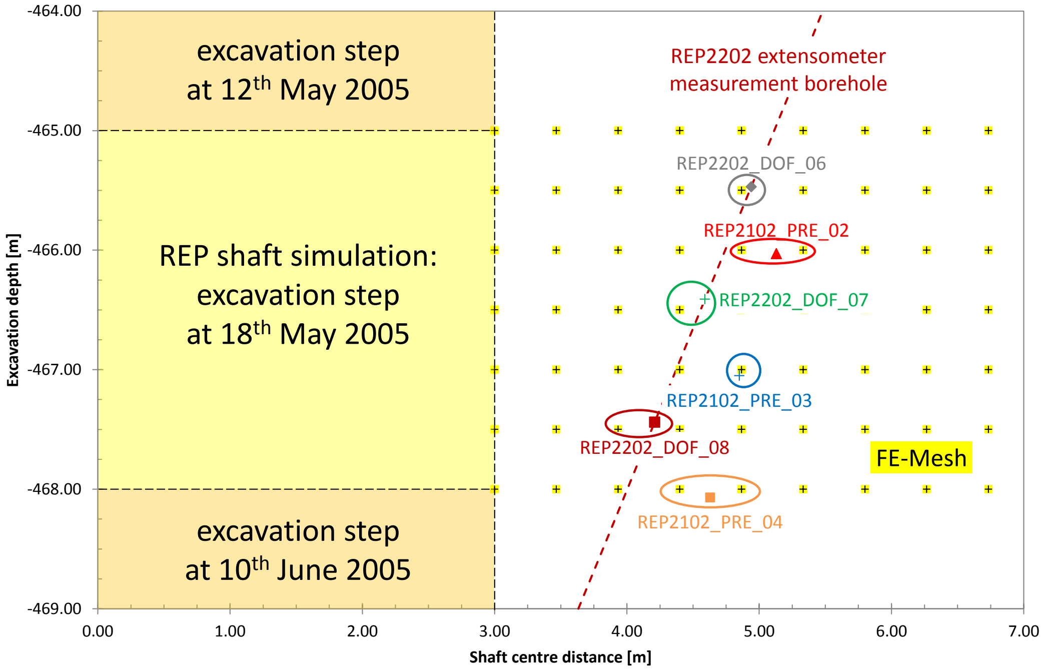


**Fig. 3.31** Position of the REP2102 and REP2202 sensor intervals and the selected nodes of the finite element mesh used for comparison of simulation results and experimental findings

Calculation results on pore-water pressure propagation with time for selected REP2102 test intervals as a result of hydro-mechanical coupled simulation before the shaft excavation front reaches the REP experimental zone are shown in Fig. 3.3.7. Considerations of desaturation effects caused by the niche excavation lead to a reduced pore water pressure of about 3.8 MPa with respect to the expected hydrostatic pressure at REP2102 interval level.

Before the shaft excavation front has nearly reached the position of the sensor intervals an increase in pore water pressure of almost 4 bar to 7 bar can be observed in fig. 3.32, followed by an instantaneous decrease in pore water pressure of about 1.0 MPa when the excavation front passes the sensor level.

After the shaft excavation front has passed the REP experimental zone at mid of June 2005 the REP2102 sensor no. 2 and no. 3 stabilised at values of 2.7 MPa and 2.5 MPa respectively (see fig. 3.33), showing a slight linear decrease of about 7 bars within the next 3 months. REP2102 sensor no. 4 shows a delayed decrease in pore water pressure stabilising at about 2.1 MPa due to the sensor position with a minor distance to the shaft contour as well as a minor linear decrease of about 5 bars within the next 3 months.

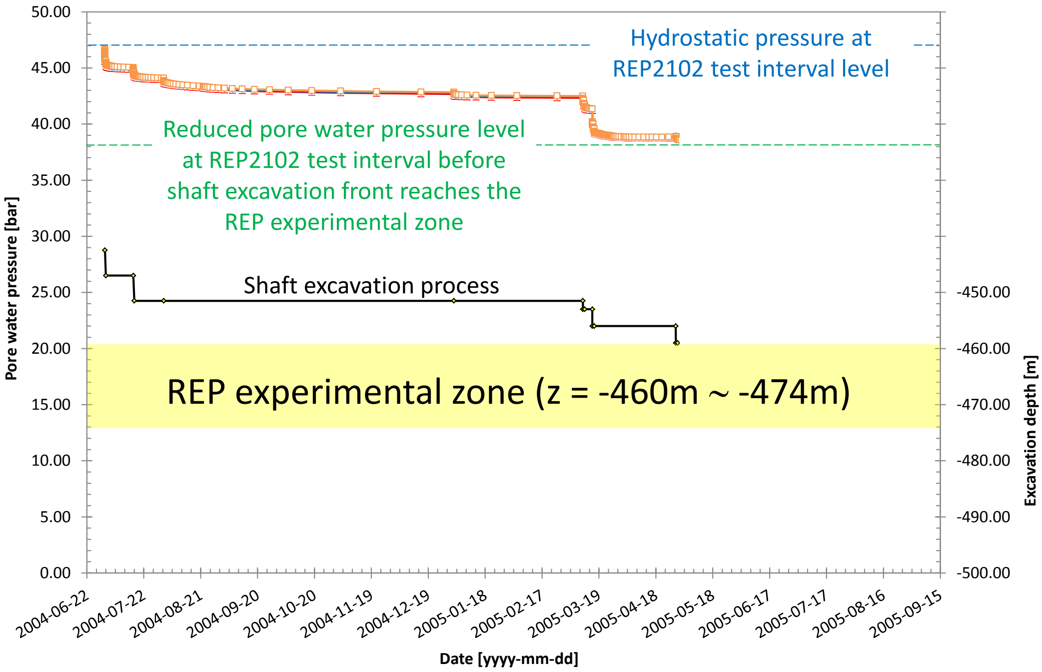


**Fig. 3.32** Calculation results on pore water pressure propagation with time for selected REP2102 test intervals as a result of hydro-mechanical coupled simulation before the shaft excavation front reaches the REP experimental zone

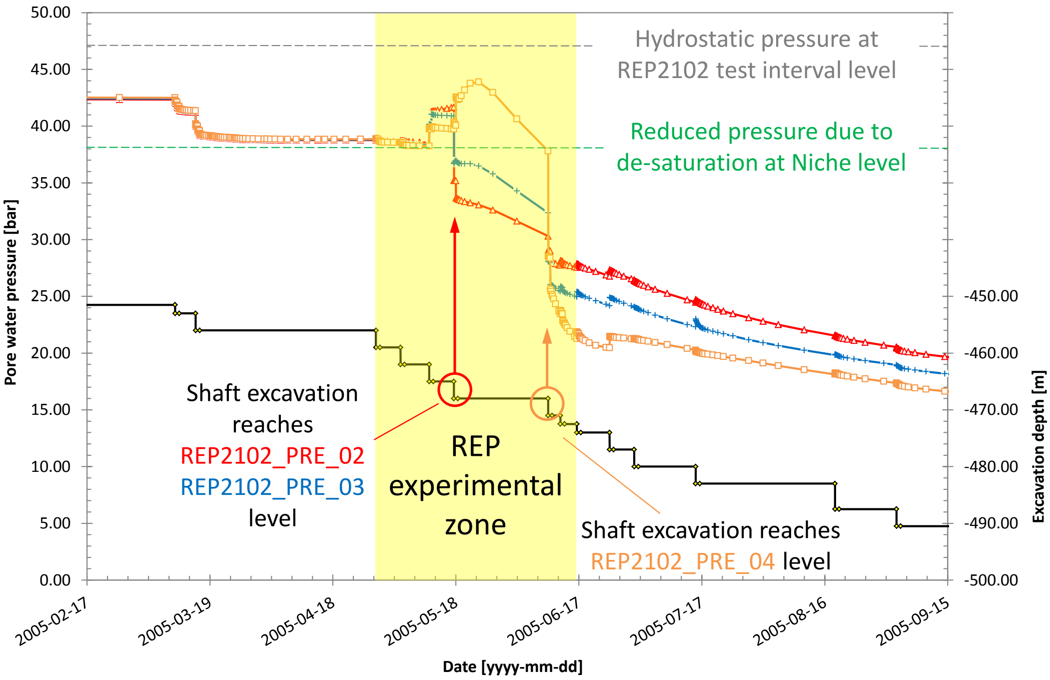


**Fig. 3.33** Calculation results on pore water pressure propagation with time for selected REP2102 test intervals as a result of hydro-mechanical coupled simulation of shaft excavation

With respect to the experimental findings of borehole REP2102 the results of the hydro-mechanical simulation could represent the basic reaction of pore water pressure due to the shaft excavation process, though the total value of the pressure decrease has been underestimated, because rock damage has not been considered.

Due to the lack of the detailed data file of the REP2202 extensometer reference point only total deformation data are presented below, with regard to the global axis. In fig. 3.34 calculation results on horizontal and vertical deformation with time for selected REP2202 test intervals as a result of hydro-mechanical coupled simulation of shaft excavation are shown. The calculation results for the selected test intervals show a significant increase in horizontal deformation only when the shaft excavation front reaches the REP experimental zone, showing the highest convergence values of about 3 mm when the excavation front passes by.

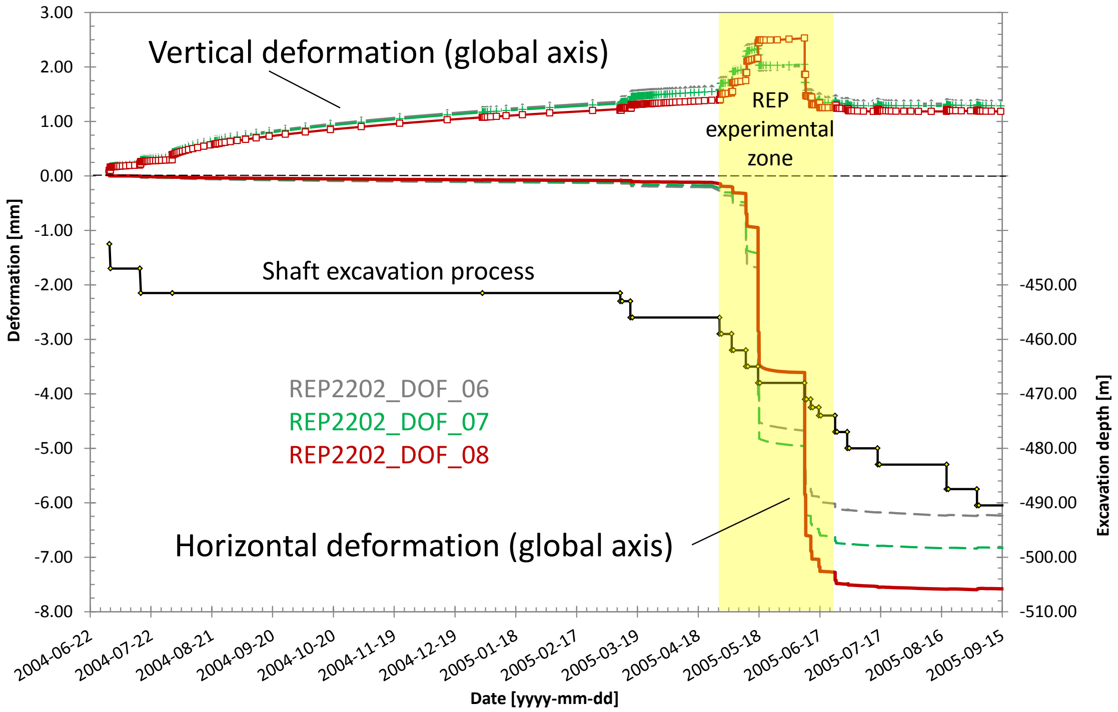


**Fig. 3.34** Calculation results on deformation (global axis) with time for selected REP2202 test intervals as a result of hydro-mechanical coupled simulation of shaft excavation

In contrast to the behaviour of the total horizontal deformation of about 8 mm in the direction of the symmetry axis due to the possible convergence deformation into the opening, the vertical deformations show a different behaviour. As long as the excavation front has not reached the REP experimental zone vertical deformations increase with time showing nearly a linear uplift trend of about 1 mm in the first 10 month. When the REP experimental zone is reached the calculation values show a significant reaction in uplift due to the shaft excavation process in the same order of magnitude. When the excavation front passes by the deformation trend is being reversed and reaches nearly the same level of deformation as before.

In order to compare the achieved calculation results with experimental findings only the simulation values assigned to the excavation process within the REP experimental zone are selected and shown in fig. 3.35 with respect to geotechnical convention of compressive and extensile deformation. The deformation values within the first 10 month are neglected.

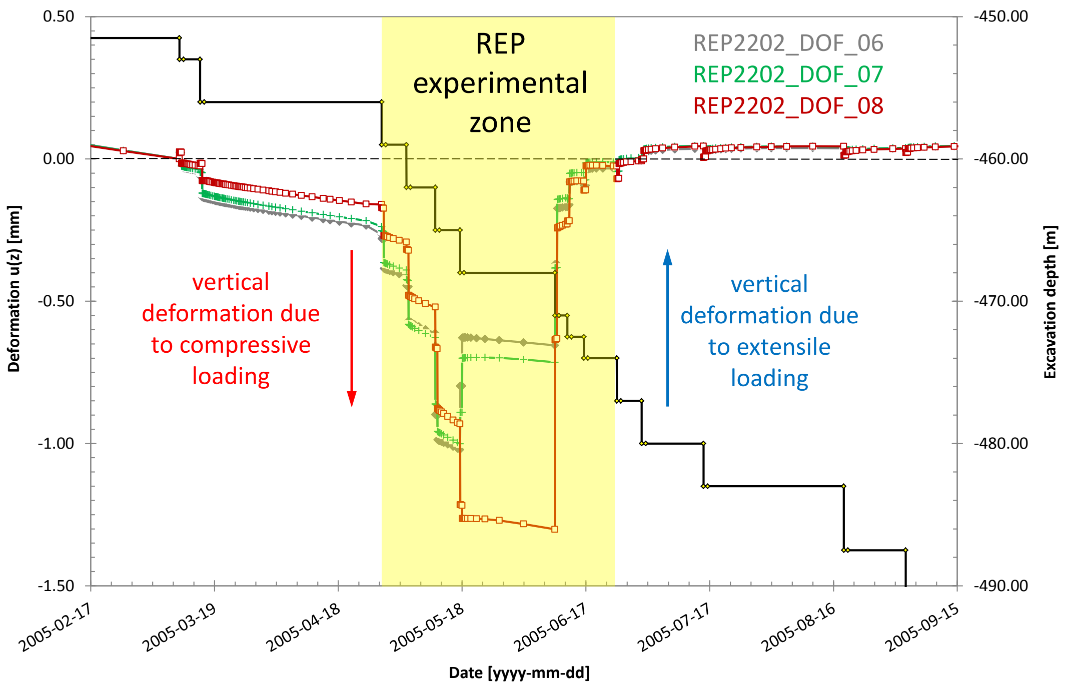


**Fig. 3.35** Calculation results on vertical deformation (geotechnical convention) with time for selected REP2202 test intervals as a result of hydro-mechanical coupled simulation of shaft excavation

With respect to the experimental findings of borehole REP2202 the results of the hydro-mechanical simulation could represent the basic deformation behaviour of the clay rock due to the shaft excavation process though the displacements related to the shaft convergence process could not be simulated with the applied modelling approach, because mechanical time-dependent viscous behaviour has not been considered.

## 3.4 Modelling of rock response to heating

### 3.4.1 Overview of the TER heating experiment

In order to investigate the thermal properties and to enhance the knowledge about the THM processes of the Callovo-Oxfordian clay rock, an *in situ* heating experiment called TER was performed in the MHM-URL from the beginning of 2006 to the end of 2009. The concept of the heating experiment was designed to heat the clay formation in an undisturbed zone by using an electric heater. The experiment was located at the main level at 490 m depth. Fig. 3.36 shows the location and layout of the test field.

The heater borehole TER1101 of 145 mm diameter and a length of 10 m was horizontally drilled from the GEX drift into the rock mass with the bedding plane oriented horizontally (see fig. 3.37). At a borehole depth of 6 m to 9 m, a heater packer was installed. Thermal power and inflation pressure of the heater packer were regulated remotely from the drift. The heater device was equipped with several temperature sensors in order to control the homogeneity of the temperature distribution along the heater axis. A steel and a plastic liner were inserted in the borehole in the heater section and in the other part, respectively, in order to protect the borehole from the falling of debris.

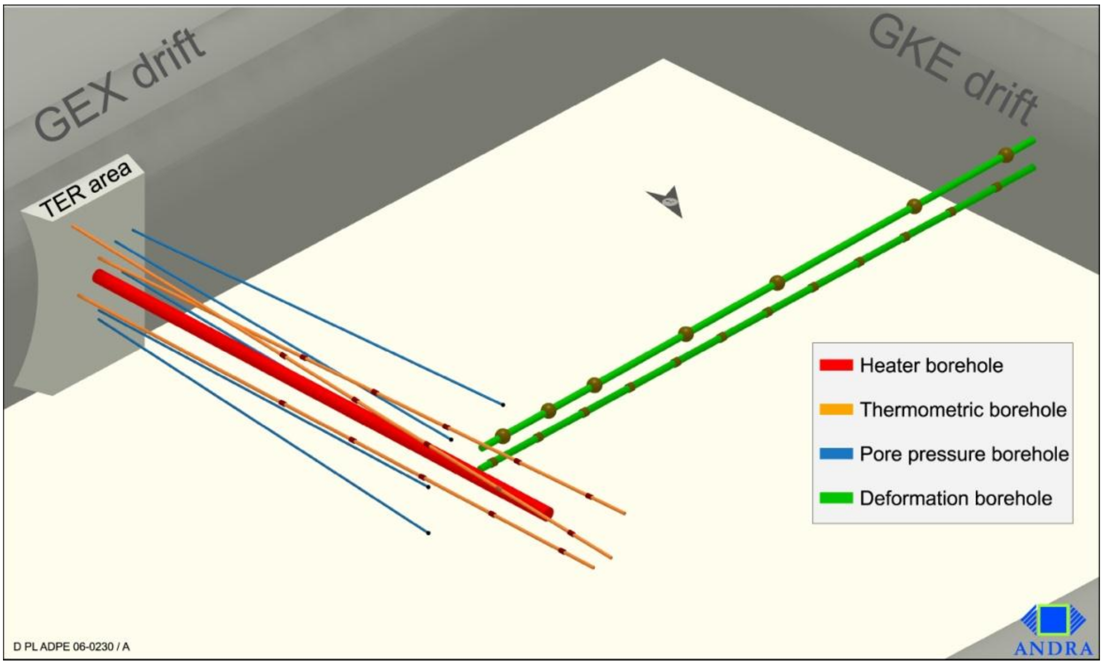


**Fig. 3.36** 3D view of the TER test arrangement with heater and instrumentation boreholes

Three boreholes, TER1201/02/03, were drilled beside, above and at an angle of 45° to the heater borehole for monitoring the temperature in the test area (fig. 3.38). Their distances to the heater borehole ranged from 0.6 m to 0.8 m. In each borehole five sensors were installed with a distance of 1.5 m between each neighbouring points. The instrumentation layout allowed the examination of heat transfer in different directions with regard to the bedding plane (TER1201 sensors C1 to C5 parallel, TER1203 sensors C1 to C5 perpendicular, and TER1202 sensors C1 to C5 at an angle of 45° to the bedding plane).

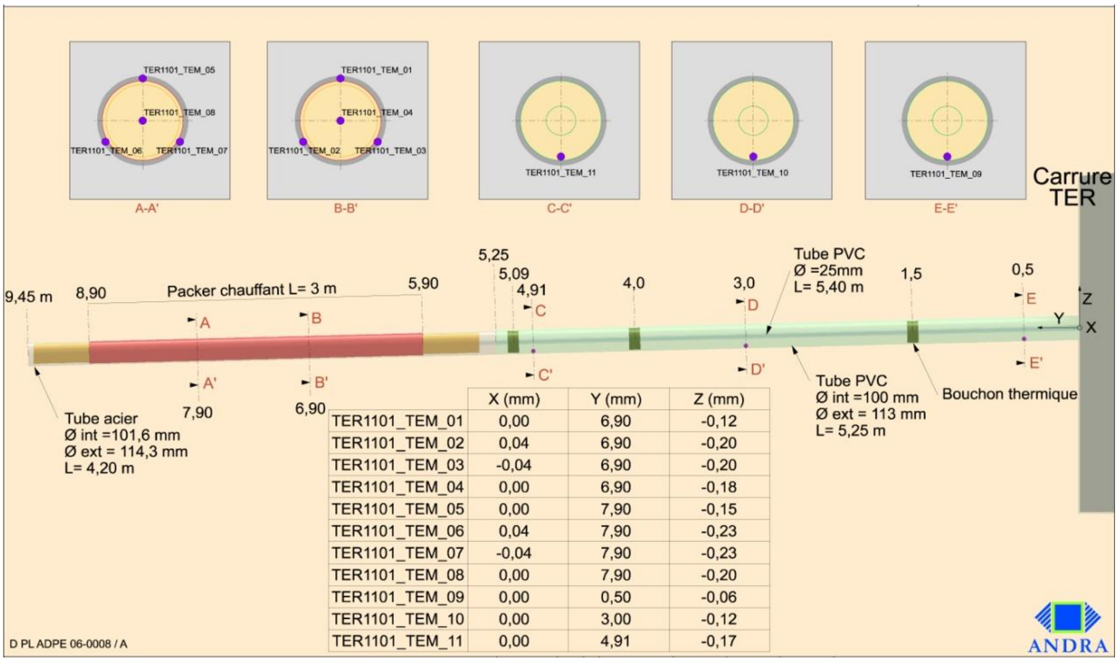


| | X (mm) | Y (mm) | Z (mm) |
|---|---|---|---|
| TER1101_TEM_01 | 0,00 | 6,90 | -0,12 |
| TER1101_TEM_02 | 0,04 | 6,90 | -0,20 |
| TER1101_TEM_03 | -0,04 | 6,90 | -0,20 |
| TER1101_TEM_04 | 0,00 | 6,90 | -0,18 |
| TER1101_TEM_05 | 0,00 | 7,90 | -0,15 |
| TER1101_TEM_06 | 0,04 | 7,90 | -0,23 |
| TER1101_TEM_07 | -0,04 | 7,90 | -0,23 |
| TER1101_TEM_08 | 0,00 | 7,90 | -0,20 |
| TER1101_TEM_09 | 0,00 | 0,50 | -0,06 |
| TER1101_TEM_10 | 0,00 | 3,00 | -0,12 |
| TER1101_TEM_11 | 0,00 | 4,91 | -0,17 |

**Fig. 3.37** Layout of the TER heater borehole with heater packer and temperature sensors

Thermally-induced pore pressure changes were recorded by means of the GRS mini-packer-systems which were successfully used in the HED heating experiment in the Mont-Terri-URL /ZHA 05/, /ZHA 06/, /ZHA 07a/, /ZHA 09a/. Fig. 3.39 shows the positions of the measuring points. Five small mini-packer systems were installed in five slim boreholes of 20 mm diameter. They were located in the same vertical plane crossing the heater axis, at 0.5 m to 1.5 m distance from the heater. At each position, both the pore pressure and the temperature were measured. The instrumentation layout made it possible to monitor the temperature at the pore pressure sensor locations in three directions: In borehole TER 1401/02 parallel, in borehole TER1404/05 perpendicular, and in borehole TER1403 at an angle of 45° to the bedding plane. Additionally, some pulse tests were carried out for determining the permeability at each location before and after heating.

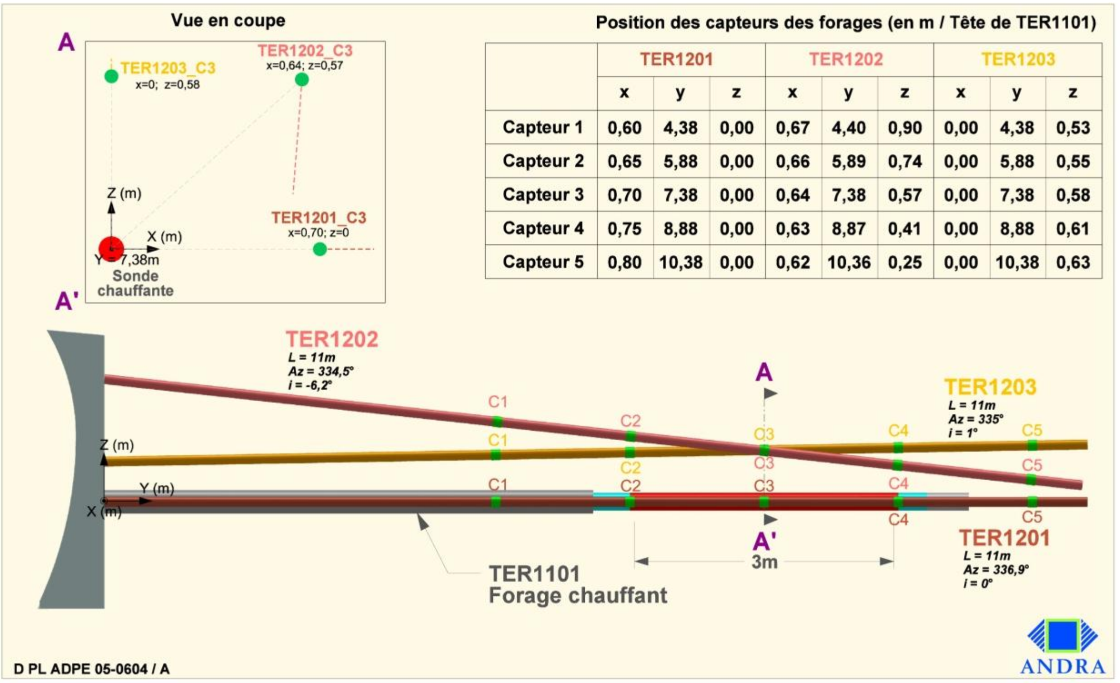


**Fig. 3.38** Positions of temperature sensors in the TER experiment

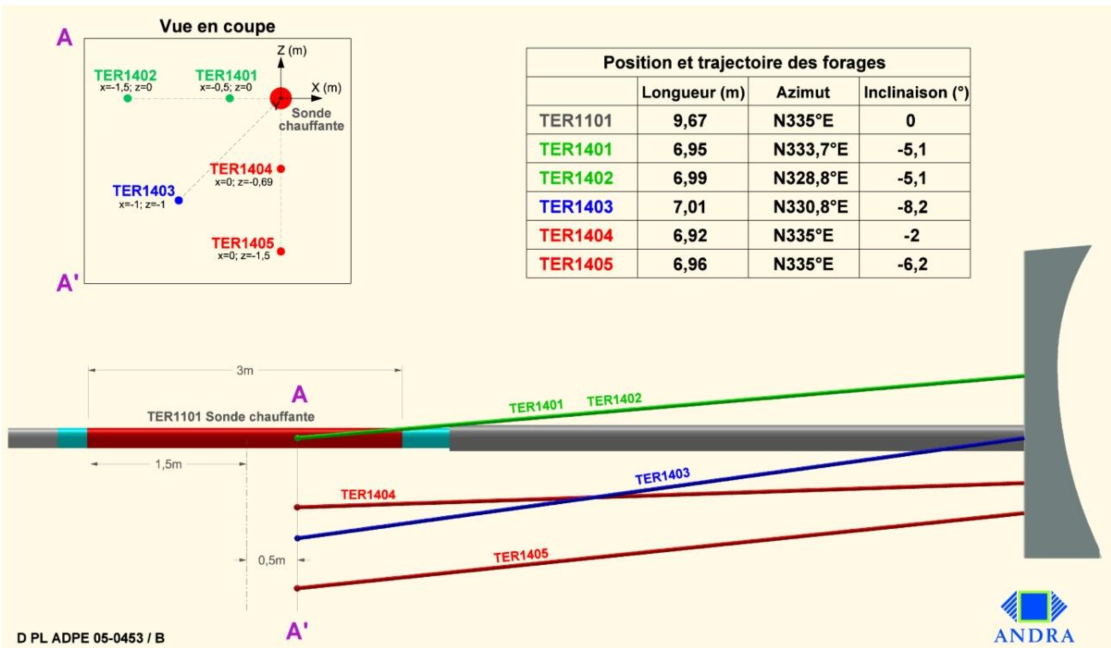


**Fig. 3.39** Positions of pore pressure and temperature sensors in five boreholes in the TER experiment

The rock deformation during the experiment was observed by means of two kinds of extensometers which were installed in two horizontal boreholes TER1301/02 perpendicular to the heater axis in the middle section (fig. 3.40). In borehole TER1301 the sliding micrometer developed by the company SOLEXPERTS already used in the HE-D experiment was installed. Using a displacement transducer between two metallic rings, the relative displacement was measured. Totally, 13 rings were installed in the borehole with a distance of 1 m between neighbouring points. In the other borehole TER1302 an automatic classical extensometer was installed 50 cm above borehole TER1301 in order to continuously record the displacement of the measuring anchors relative to the fixed point at the borehole mouth. 7 anchors were installed along the borehole at different distances to the borehole mouth.

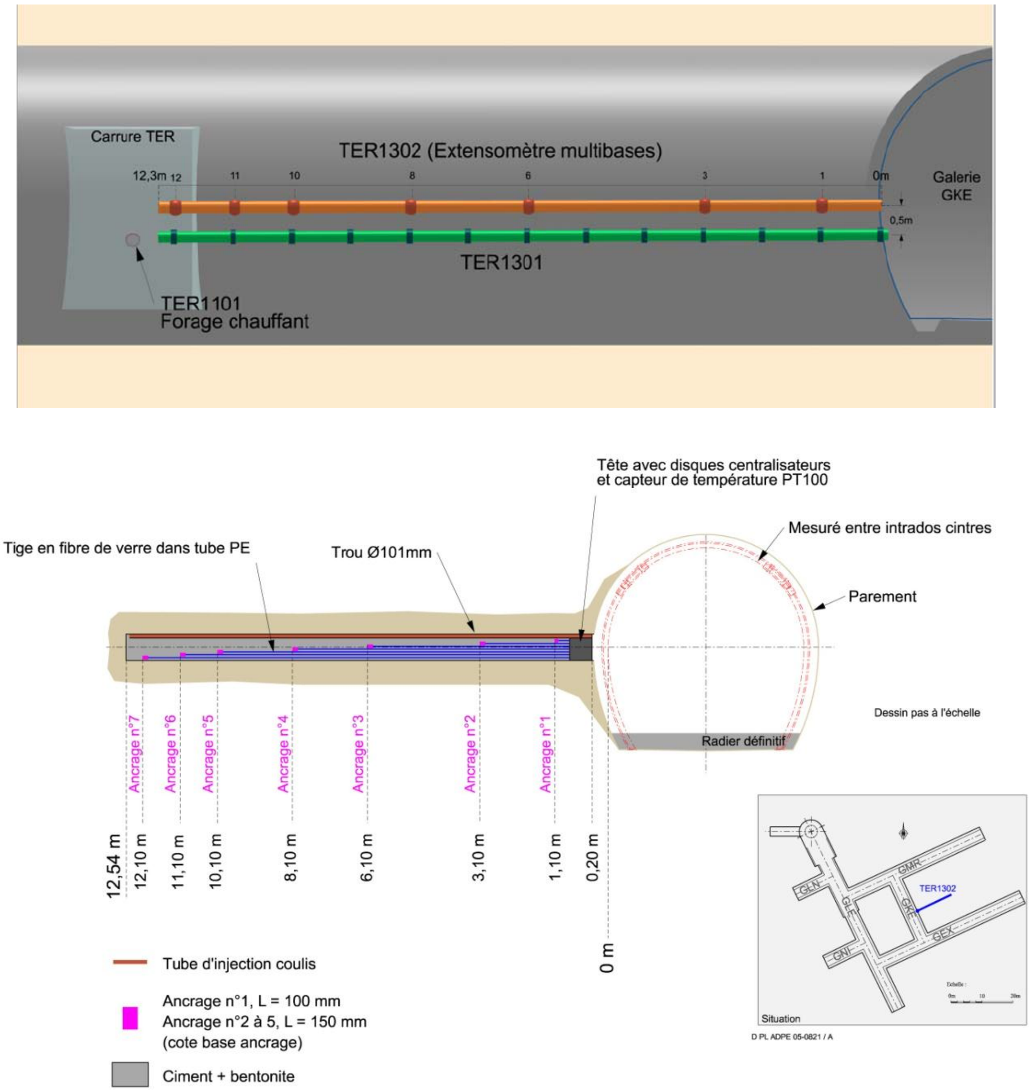


**Fig. 3.40** Positions of extensometer anchors in two boreholes

The installation of the sensors and the heater were performed during the last quarter of 2005. The first heating phase was launched at the beginning of 2006. Fig. 3.41 illustrates the heating phases with four heating / cooling cycles. Unfortunately, in each cycle several heating interruptions happened for days to months due to heater failures because of different reasons. Additionally, some uncertainties were recognized during the experiment, as for instance the correct measurement of the heater power and the quality of the of the heater contact to the rock. This yielded some difficulties for the precise determination of the thermal parameters from the measurements, for the definition of the model conditions, and for the interpretation of the observed THM processes.

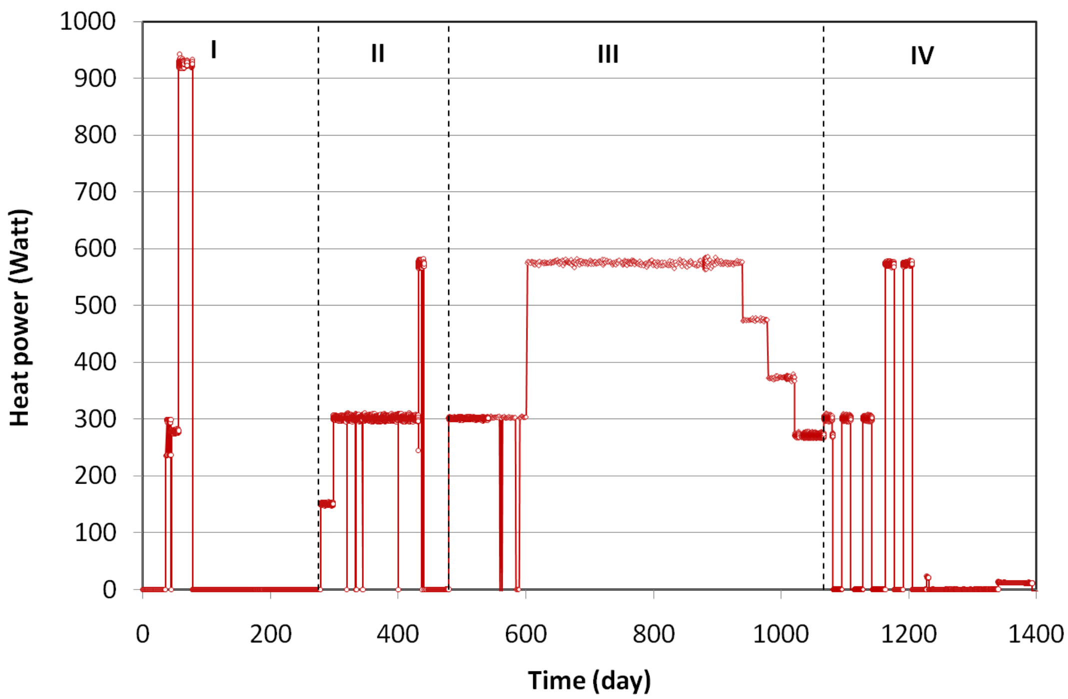


**Fig. 3.41** Heat power applied during the TER experiment with heating/cooling cycles

### 3.4.2 Model and boundary conditions

The TER experiment was simulated by modelling teams of CEA, DBE-TEC, GRS, and UPC using various computer codes. Among the others, GRS' modelling exercises were carried out by using the CODE-BRIGHT. In order to support the design of the experiment, predictive calculations were performed before testing. After the experiment, interpretive calculations were conducted and the results of which were compared with the measured data. The modelling results and the measurements are presented below.

The THM processes occurring in the clay rock during the heating / cooling cycles were calculated by coupled modelling with solving the series of balance equations (Eq. (3.1) – (3.5)) for energy, solid, water, air and stress. The set of the balance equations is completed by constitutive equations and equilibrium restrictions which link the state variables and the dependent variables. In the modelling, the following main assumptions are made:

- The clay rock is assumed isotropic and homogeneous because of the insignificance of the bedding planes;
- Heat transport in the porous medium includes conduction (Fourier's law) as well as heat transport by advection of liquid water and vapour flow;
- Water transport is controlled by liquid water advection (Darcy's law), vapour diffusion in air (Fick's law), and liquid / gas phase changes (psychrometric law);
- Gas pressure is kept at atmospheric level;
- The mechanical behavior of the clay is described by the damage-elastoplastic model (see section 3.1-3).

Fig. 3.42 shows a simplified axisymmetric model of 24 m length and 12.5 m radius. In fact, this model represents a cylindrical rock mass with the heater borehole axis being the symmetry axis. The borehole has a radius of 75 mm and a total length of 10 m, including a heater of 3 m length. The *in situ* prevailing conditions are applied to the initial state of the rock as follows: porosity $\phi$ = 15 %, full saturation (suction $s$ = 0), temperature $T$ = 22 °C. A hydrostatic stress of $\sigma$ = 13.5 MPa was averaged from the anisotropic stress state of the major horizontal component $\sigma_H$ = 16 MPa, the minor horizontal component $\sigma_h$ = 12 MPa and the vertical component $\sigma_v$ = 12 MPa. The axis of the heater borehole was oriented parallel to the direction of the major horizontal stress. The pore water pressure in the rock at the main level is estimated to about 4.5 MPa. But, the observation in the TER test field before testing suggested a value of $P_l \approx$ 2.6 MPa, which is taken into account in the modelling. Because of the lining of the borehole, convergence is suppressed by fixing the radial displacement ($\Delta u_x$ = 0) along the borehole boundary. Considering the possible existence of gaps between the borehole wall and the liner, water flow out of the rock is allowed by adopting atmospheric pressure for the pore pressure ($P_l$ = $P_g$ = 0.1 MPa) at the borehole wall. Obviously, this simplified model cannot represent the realistic situation, particularly the impact of the three surrounding drifts on the THM processes in the test field. The experiment was simulated by sequential calculation steps considering the power supplies within the four heating/cooling cycles. Because of the above mentioned uncertainties regarding the power supply and the heater/rock interface, various power values differing from the given data (fig. 3.41) were considered for fitting the temperature data measured the test field.

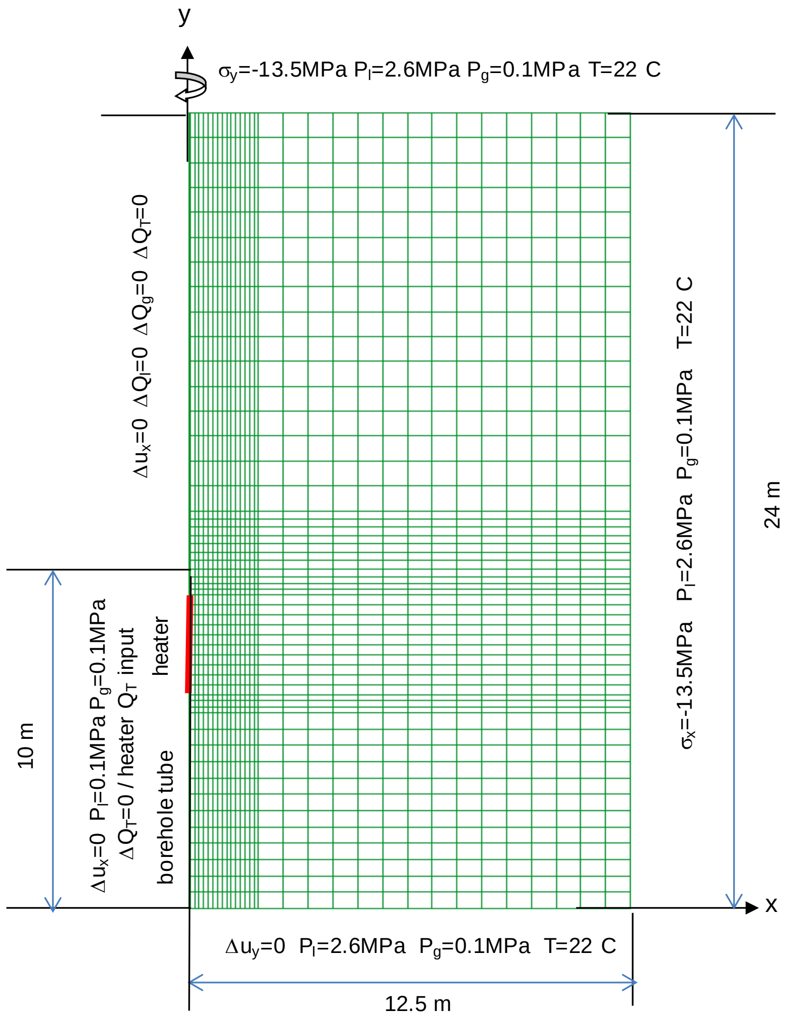


**Fig. 3.42** Axisymmetric model with boundary conditions prevailing around the heater borehole

### 3.4.3 Modelling results and field observations

Three input values for the heat power were examined for fitting the modelling results with the temperature data measured at the different locations: a) the given power data presented in fig. 3.41, b) two times the given power, and c) three times the given power. Using the given power data, the temperatures are underestimated by the calculation for all the measuring points. While the value of 2 times the given power leads to a better matching with the temperature measured at the heater surface (see fig. 3.43), the value of 2 times the given power produced the best results for all the other positions in the rock. Therefore, the power input with two times the given value was considered for the calculation of the pore pressure and the deformation.

### 3.4.3.1 Temperature

Fig. 3.43 shows the temperature data measured at the heater surface and the calculation results with the three input values for the heat power. During the first heating phase, the temperature reached a maximum of 100 °C. After cooling down deduced by the heater failure, the further power supply was limited to a heater temperature below 80 °C. The comparison indicates that the value of 2 times the given power fits the model with the measurement relatively well.

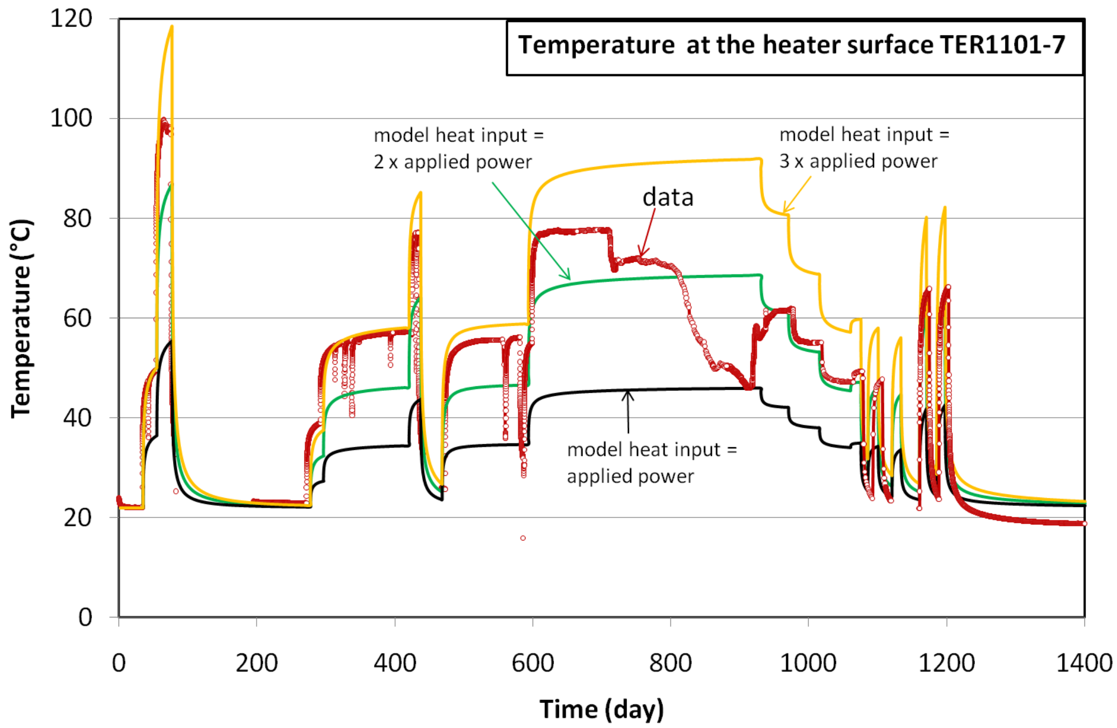


**Fig. 3.43** Measured and calculated temperature evolution at the heater/rock interface

In fig. 3.44 the temperatures recorded inside the rock are compared with the modelling results for sensors TER1201/2/3-C2/C3/C4/C5. Their positions are shown in fig. 3.38.

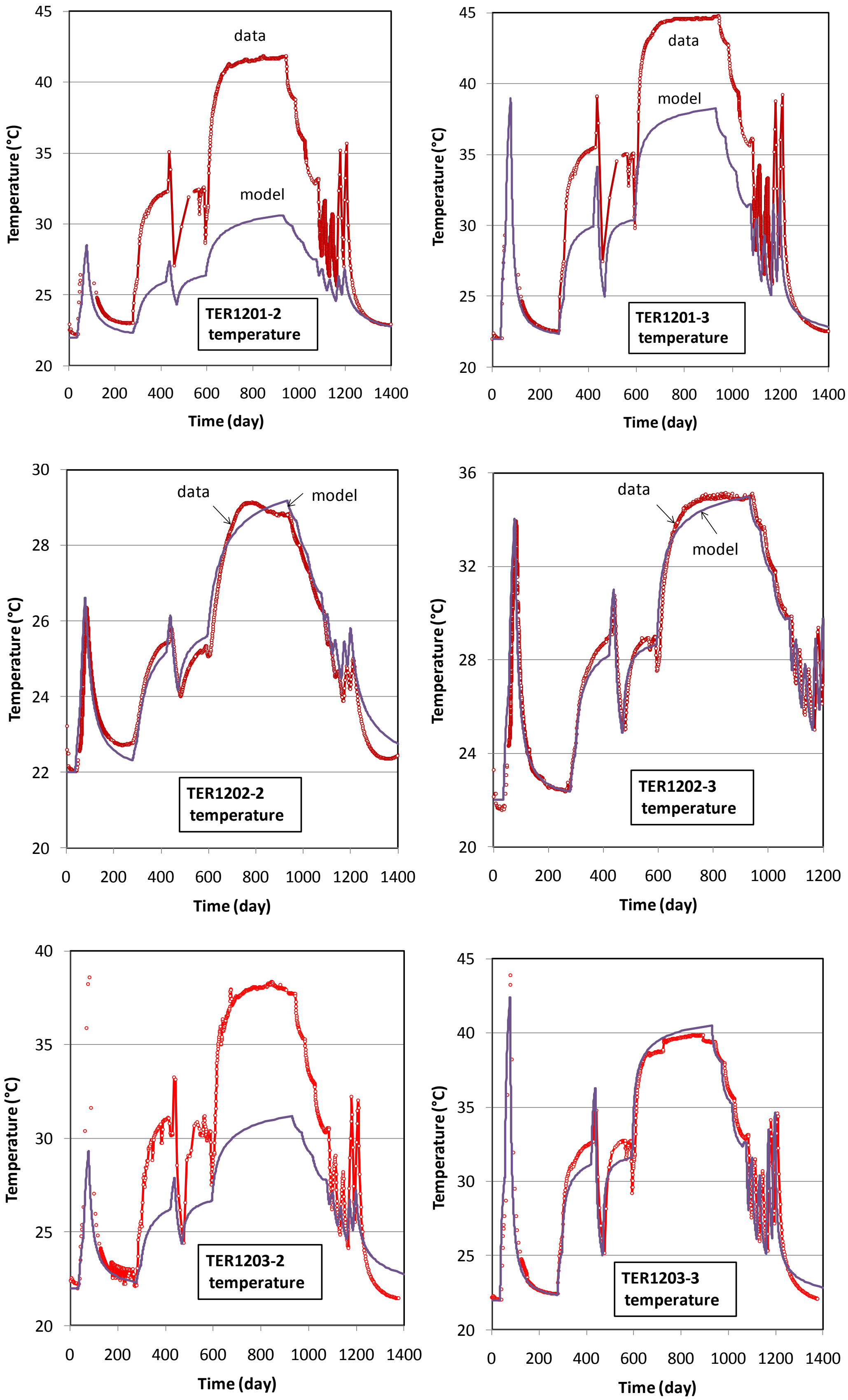


Section C2 Section C3

**Fig. 3.44** Temperature evolution observed and calculated inside the surrounding rock

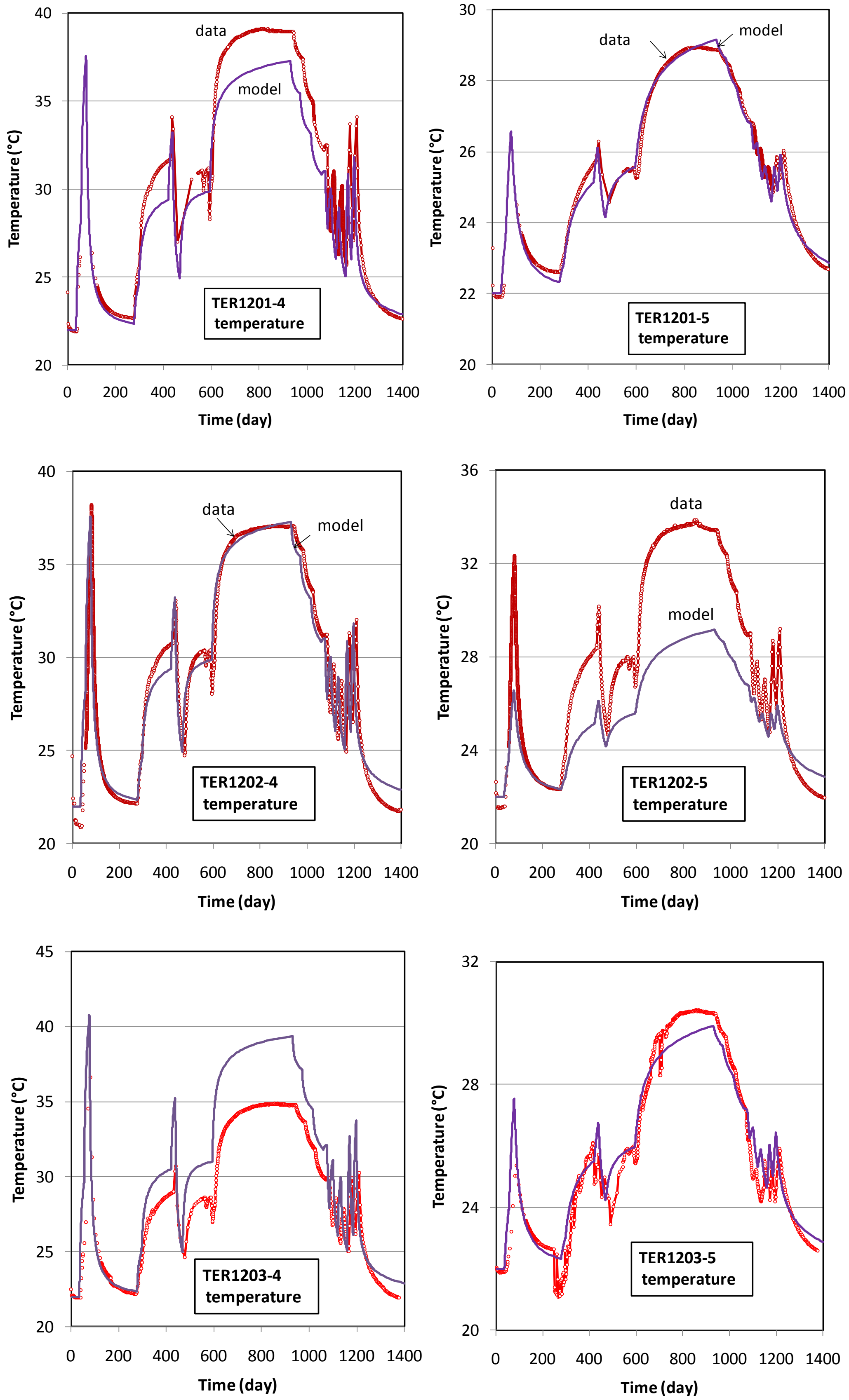


Section C4 Section C5

**Fig. 3.44** Temperature evolution observed and calculated inside the surrounding rock [continued]

The measurements indicate that the maximum temperatures at all the points were reached during the third heating phase at ~1000 days, but being not coincident with that observed at the heater surface. Section C3 in the middle of the heater was heated up to 35 °C at TER1202-C3, to 40 °C at TER1203-C3, and to 45 °C at TER1201-C3 respectively, depending on the distances of 0.6 to 0.9 m to the heater. In the farther section C5, the maximum temperature ranged between 29 °C and 34 °C. On the other hand, the sensors TER1201-C2/3/4/5 located horizontally beside the heater and parallel to the bedding plane provided higher temperature values than those recorded by the sensors TER1203-C2/3/4/5 which were positioned vertically above the heater and perpendicular to the bedding plane. This may indicate the anisotropic thermal transfer in the rock. Even though the applied isotropic model can only provide the average thermal process, the modelling results agree quite well with the temperatures measured at the most locations. The thermal anisotropy will be experimentally characterized and modelled by 3D modelling within a new programme /THM 10/.

#### 3.4.3.2 Pore pressure

The positions of pore pressure measurements are shown in fig. 3.39. Correlated with the temperature changes, the pore-water pressure in the heated area varied largely due to the very low permeability of the clay rock and the relatively high thermal expansion of the pore-water. Fig. 3.45 illustrates the evolution of the pore water pressure and the temperature measured at the same locations in the near-field of 0.5 – 1.5 m around the heater together with the modelling results. Before heating, lower initial pore water pressure values than the given value of 4.5 MPa of 2.0 and 3.5 MPa were measured. Consequently, an averaged pore pressure of 2.6 MPa was applied in the model. The measurements show that, in each heating / cooling cycle the temperature increase leads to a rising pore pressure and the temperature decrease causes a reduction of the pore pressure. During the first heating phase, a maximum pore pressure of up to 4.0 to 6.5 MPa was reached, depending on the distance to the heater. During the last cooling phase, the measured pore pressure dropped down to zero. The cooled area might be slightly de-saturated, as indicated by the calculated negative values of pore pressure. Except for the point TER1405, the observed response of pore pressure can be reasonably represented by the isotropic model.

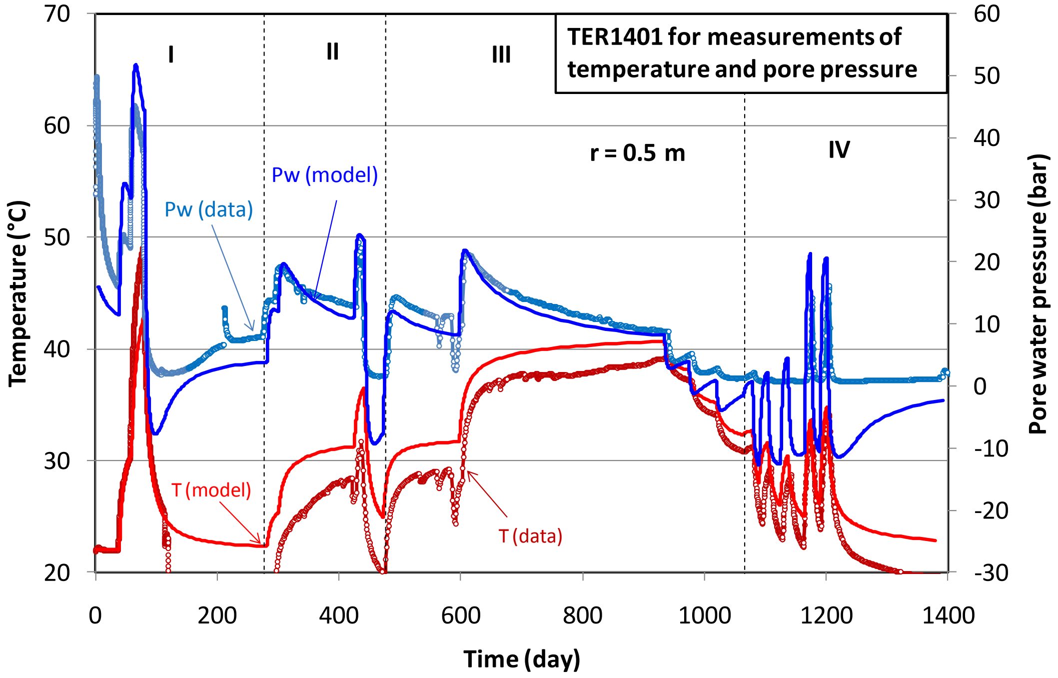


(a) TER1401

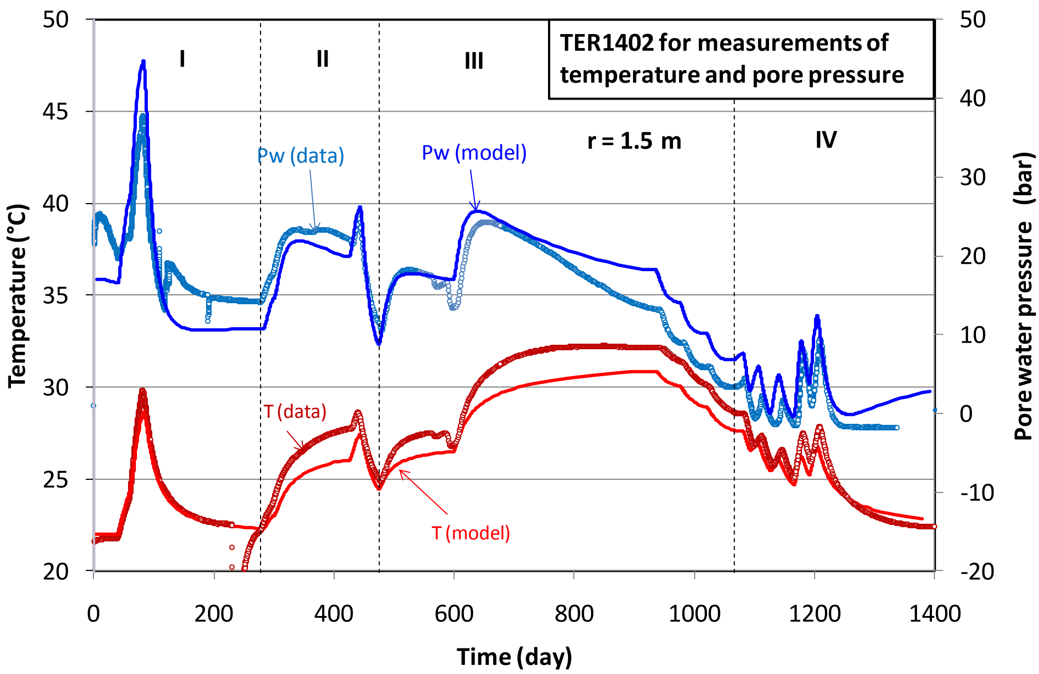


(b) TER1402

**Fig. 3.45** Thermally induced changes in pore pressure in the heated area; comparison of measured and calculated data

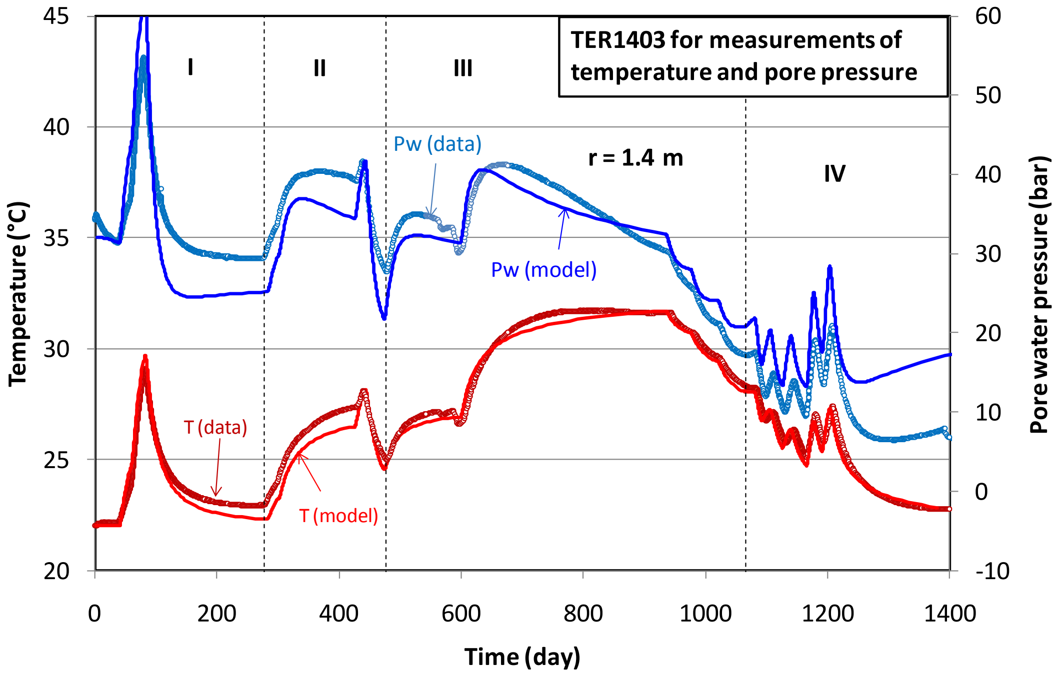


(c) TER1403

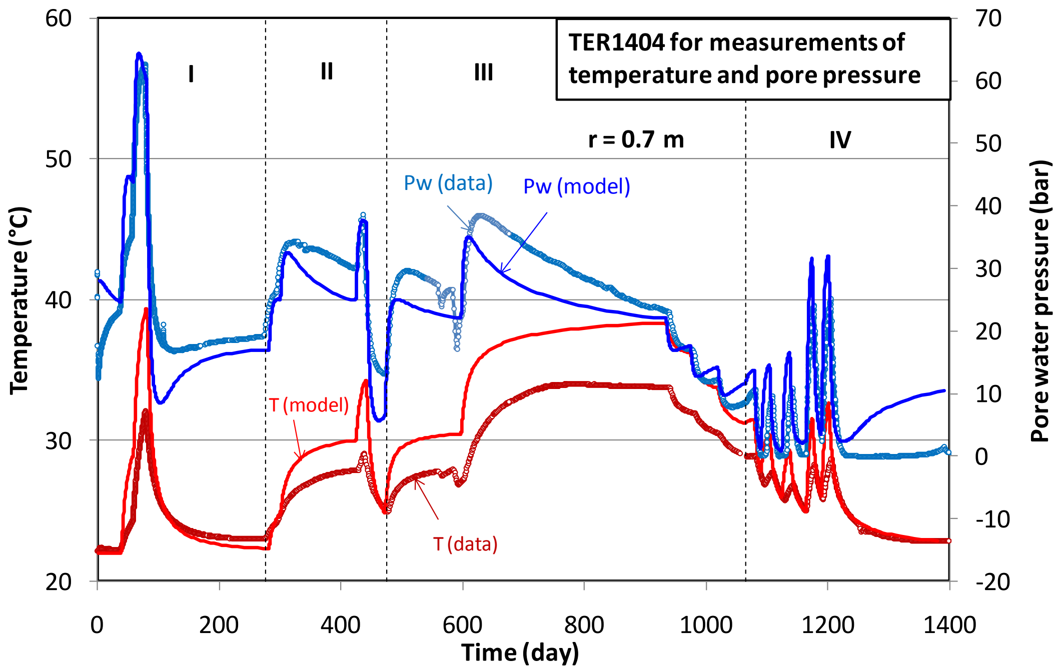


(d) TER1404

**Fig. 3.45** Thermally induced changes in pore pressure in the heated area; comparison of measured and calculated data [continued]

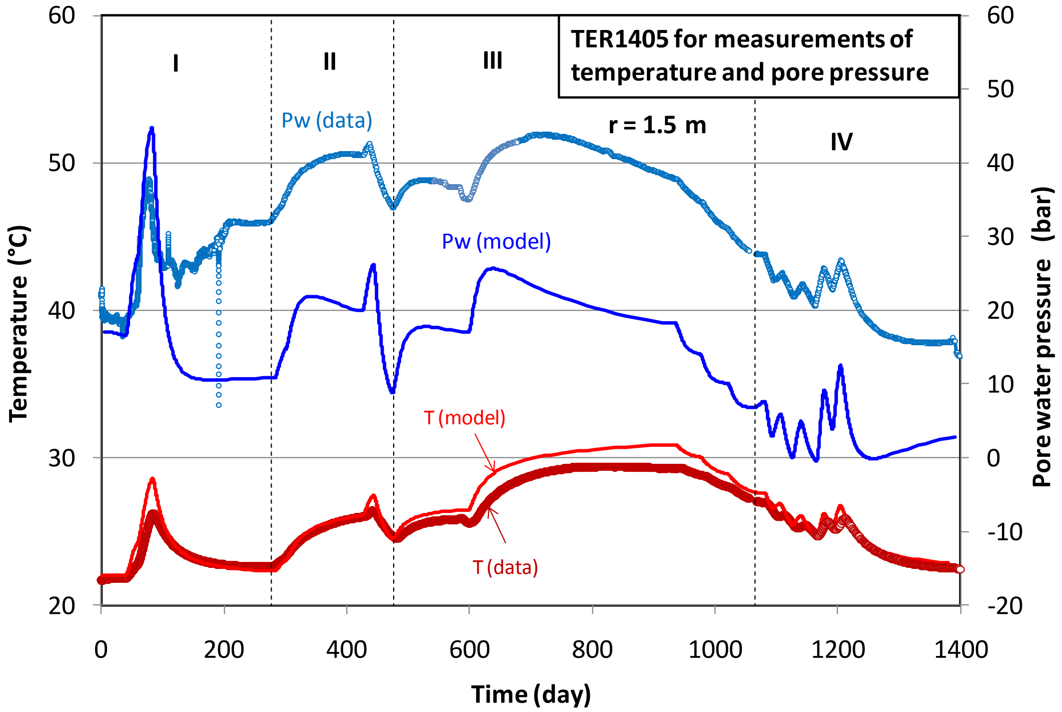


(e) TER1405

**Fig. 3.45** Thermally induced changes in pore pressure in the heated area; comparison of measured and calculated data [continued]

#### 3.4.3.3 Deformation

The relative deformation between two neighbouring points along an extensometer is calculated by

$$\varepsilon_{i-j} = \frac{u_j - u_i}{d_{i-j}} \tag{3.53}$$

where $u_i$ and $u_j$ are the displacements of points $i$ and $j$, and $d_{i\text{-}j}$ being the interval distance between both points. As a convention in rock mechanics, compression is signed positive and conversely extension negative.

In the modelling of the thermal strains, three values of the thermal expansion coefficient were applied to the rock mass consisting of solid grains and pore-water as follows: $\alpha_m$ = 1.7·10$^{-5}$, 3·10$^{-5}$, and 8·10$^{-5}$ K$^{-1}$. The low value of $\alpha_m$ = 1.7·10$^{-5}$ was used for the saturated clay rock according to the theoretical model (Eq. (3.52)) and confirmed by the tests, while the other higher values were used to fit the measured data. Fig. 3.46 compares the modelling results with the measured data in borehole TER1302 (see fig.

3.40). It is clearly to be seen that the magnitudes of the thermal deformations at all the locations are significantly underestimated by the modelling, while the pattern of the strain evolution is reasonably represented by the model for most locations. The reasons for the discrepancy are unknown. The investigation of the thermal impact on the deformation in the claystone is continuing in the frame of the ongoing THM-TON project /THM 07/.

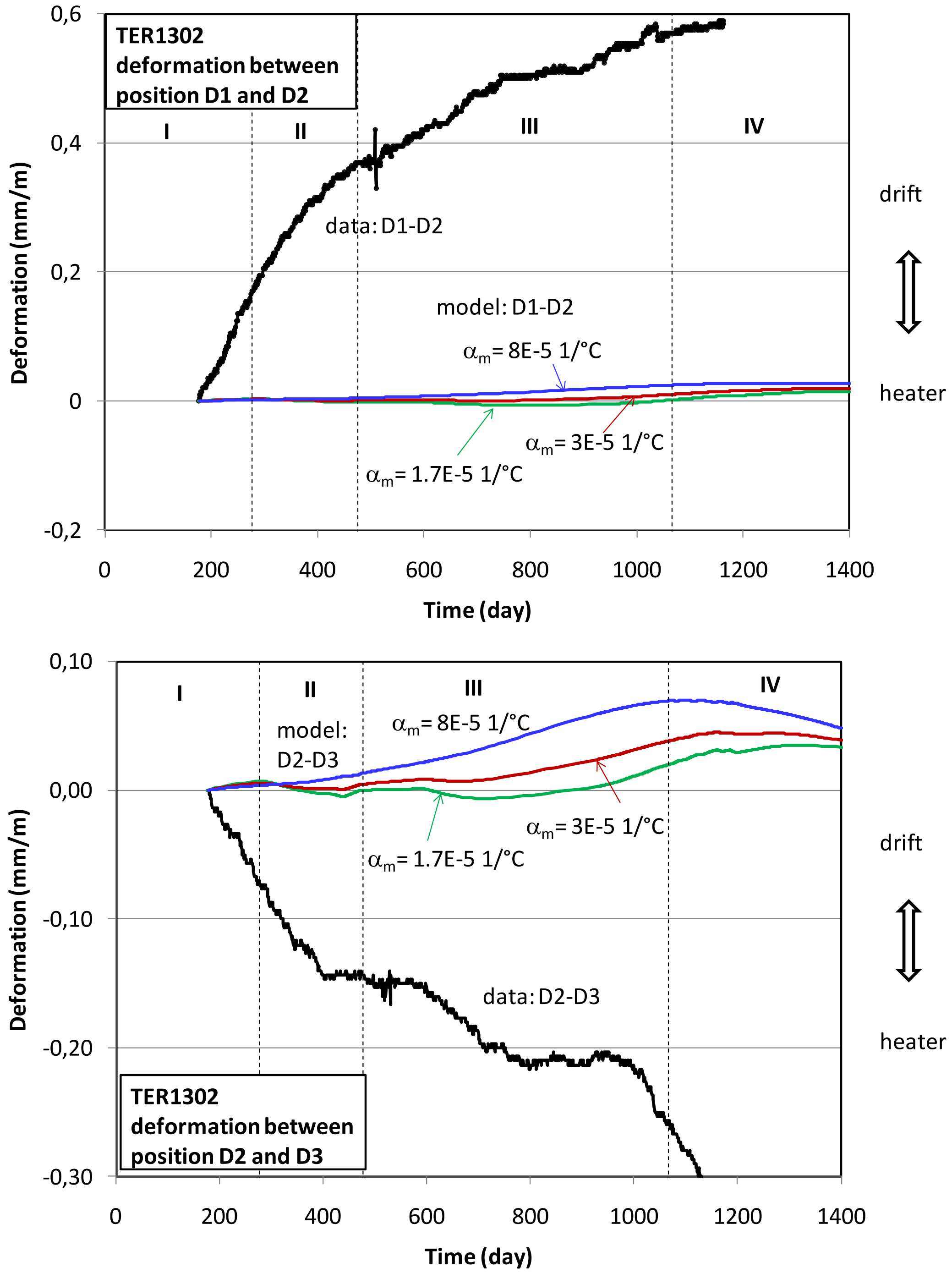


**Fig. 3.46** Measured and calculated deformations along borehole TER1302

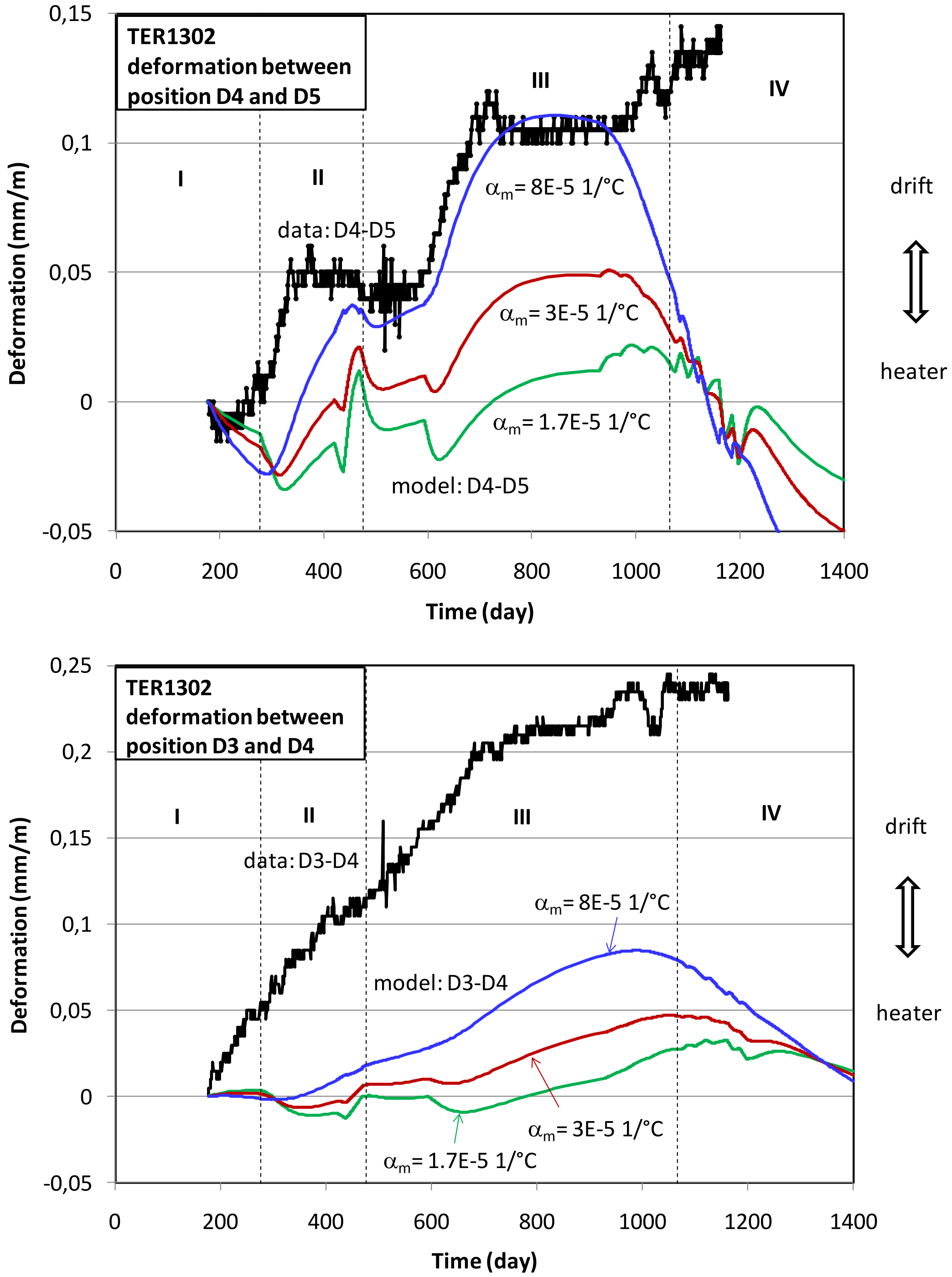


**Fig. 3.46** Measured and calculated deformations along borehole TER1302 [continued]

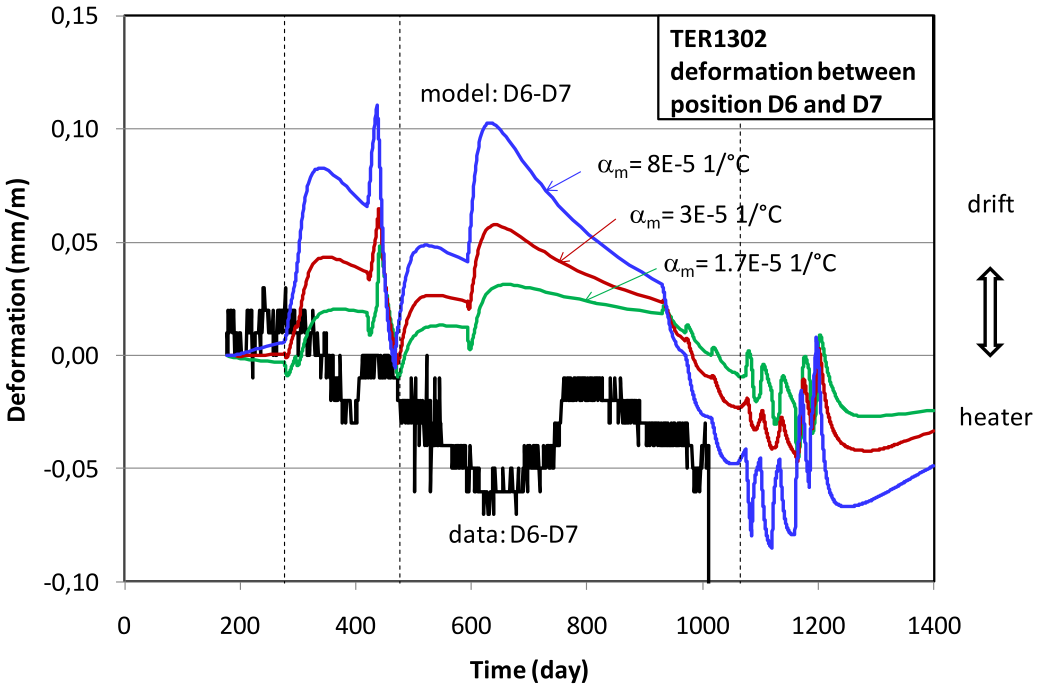


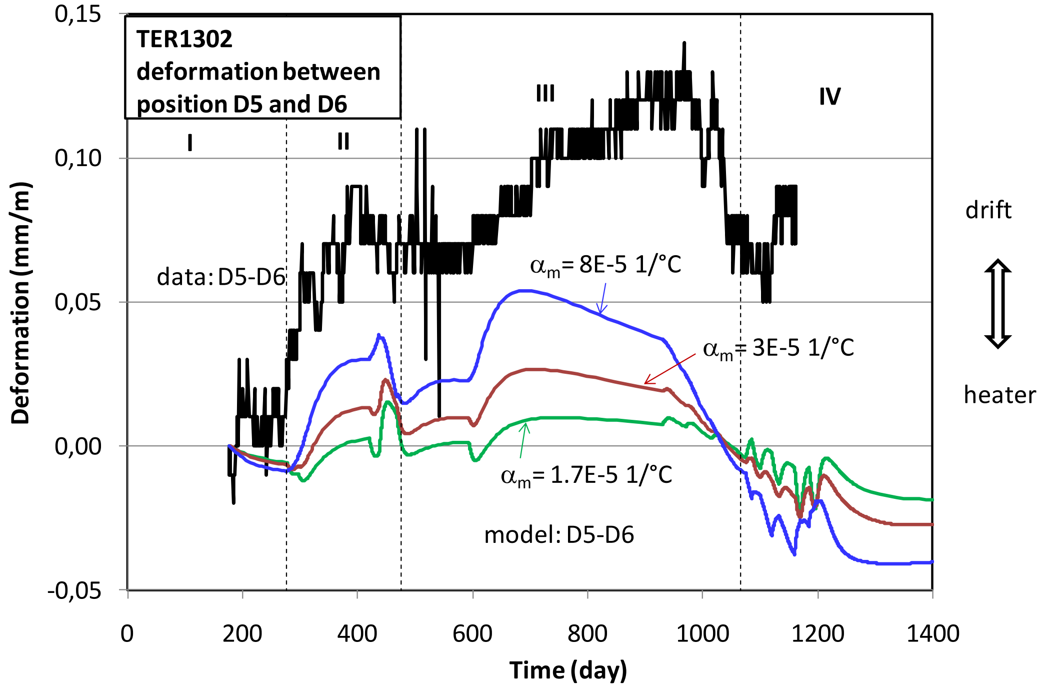


**Fig. 3.46** Measured and calculated deformations along borehole TER1302 [continued]

## 3.5 Modelling of THM processes in a rock-buffer system

According to the ANDRA's concept /AND 05/, the vitrified HLW containers (C-type) will be emplaced in dead-end lined horizontal boreholes of 700 mm diameter and 40 m length, while spent fuel (SF) will be directly disposed together with compacted bentonite-based buffer in dead-end drifts of ~2.5 m diameter and 40 m length. In order to prevent any alteration of the host rock barrier the number of containers per disposal cell and the distance between adjacent cells are determined so as to limit the temperature below 90 °C in the rock. A similar concept considering a disposal at a depth of ~650 m below the surface is also proposed by the Swiss NAGRA for the disposal of HLW in the Opalinus clay in Switzerland /NAG 02/. The HLW containers will be emplaced on compacted bentonite blocks positioned on the drift floor and the remaining space is backfilled with granular bentonite. Fig. 3.47 illustrates these concepts for the HLW/SF disposal in drifts.

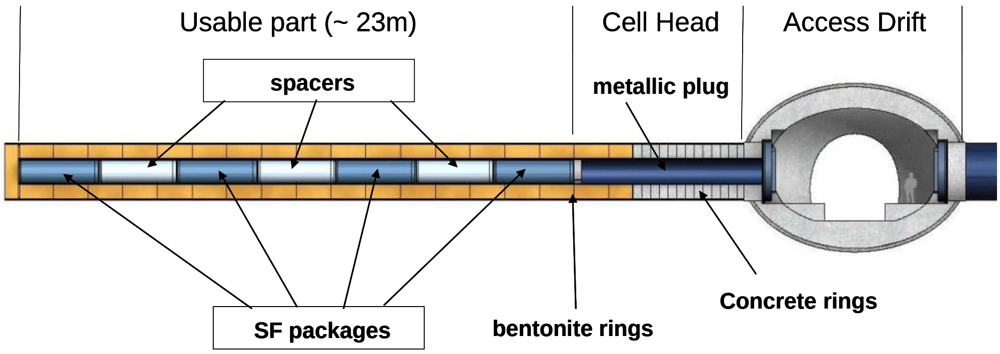


(a) ANDRA concept

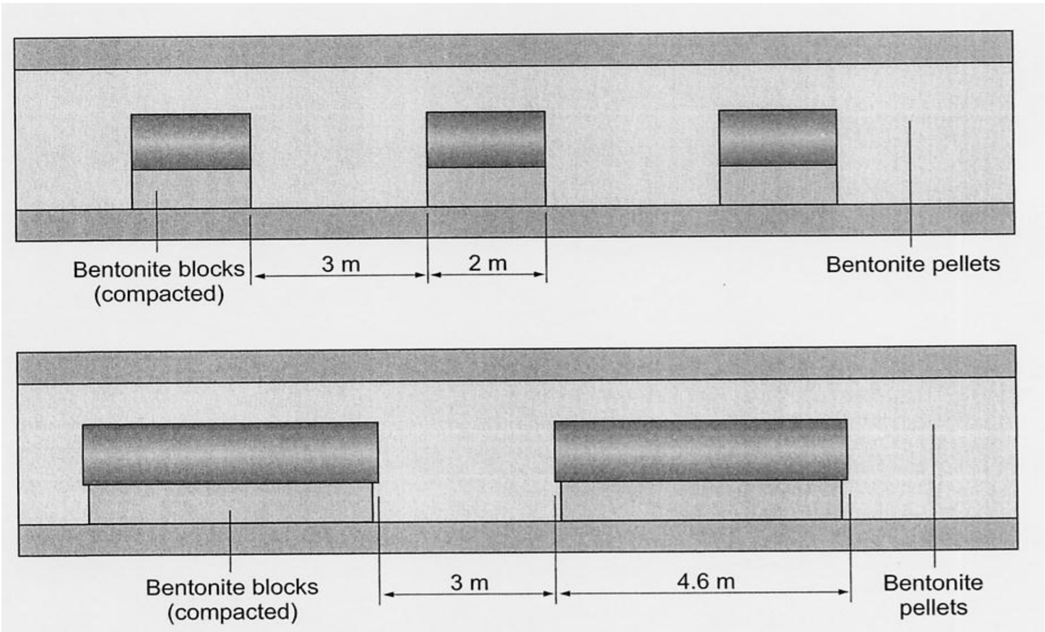


(b) NAGRA concept

**Fig. 3.47** Concepts for HLW/SF disposal in horizontal drifts with bentonite-based backfill (after ANDRA /AND 05/ and NAGRA /NAG 02/)

In order to highlight the thermo-hydro-mechanical processes in the rock-buffer-system and the interactions between the clay rock and the bentonite-buffer, scoping calculations were performed by using CODE-BRIGHT /LI 09/.

### 3.5.1 Model and boundary conditions

According to ANDRA's concept a drift is considered to be excavated at a depth of 500 m below the surface. It has a diameter of 2.2 m and a length of 20 m. Four SF containers of 0.39 m diameter and 1.7 m length are emplaced in the 13.6 m long middle space with a distance of 2.3 m to each other. The remaining space in the drift is backfilled with compacted bentonite-buffer. The buffer thickness between the container and the drift wall is 0.9 m. An axisymmetric model was chosen involving a large rock mass of 100 m radius and 100 m length (see fig. 3.47). In fact, this model represents a cylindrical rock-buffer-system with the central axis being the container axis. For the analysis of the THM processes in the system, some typical points were selected in the buffer and the rock along a radial line (dash yellow line) in the middle of the drift for determining the THM parameters with time.

The materials are assumed homogeneous and isotropic for focusing on the THM coupling processes in the rock-buffer-system, even though the COX clay rock exhibits some anisotropic properties. Initially, the host rock with 15 % porosity is saturated by the formation water. The *in situ* prevailing conditions in the MHM-URL are applied to the model. An isotropic rock stress state is prescribed with a magnitude of 12.5 MPa at a depth of 500 m. A pore-water pressure of 4.5 MPa is adopted. The rock temperature is about 27 °C. The atmospheric gas pressure of 0.1 MPa is kept constant, i. e., possible gas generation and migration is neglected in this model. The initial conditions are fixed at the boundaries of the rock mass over the modeling period including drift excavation, ventilation, backfill, and the heat emission from the waste.

In the first calculation step, the drift excavation and ventilation is simulated by (1) reducing the stress normal to the drift wall down to zero and (2) by circulating gas along the drift wall with a relative humidity of 85 % and a turbulence coefficient of $10^{-5}$ m/s. Drift excavation and ventilation will take a time period of 100 days.

Following the drift excavation and ventilation, the SF containers and the bentonite are emplaced in the drift. This is simulated by simultaneously applying the initial conditions of the buffer and the decayed heat emitting from the waste as thermal boundary conditions. The bentonite is initially unsaturated with a degree of water saturation of 52 %, corresponding to a negative pore-water pressure or suction of 105 MPa. The initial porosity of the buffer is 41.5 %. The initial stress in the buffer is zero. The thermo-elastoplastic model (BBM) is adopted for the description of the mechanical behavior of the compacted bentonite. The other thermal and hydraulic models as well as the parameters for the FEBEX bentonite /GEN 98/ are applied in the modelling. The main features of the THM models and the set of the parameters are also summarized in /ZHA 04b/.

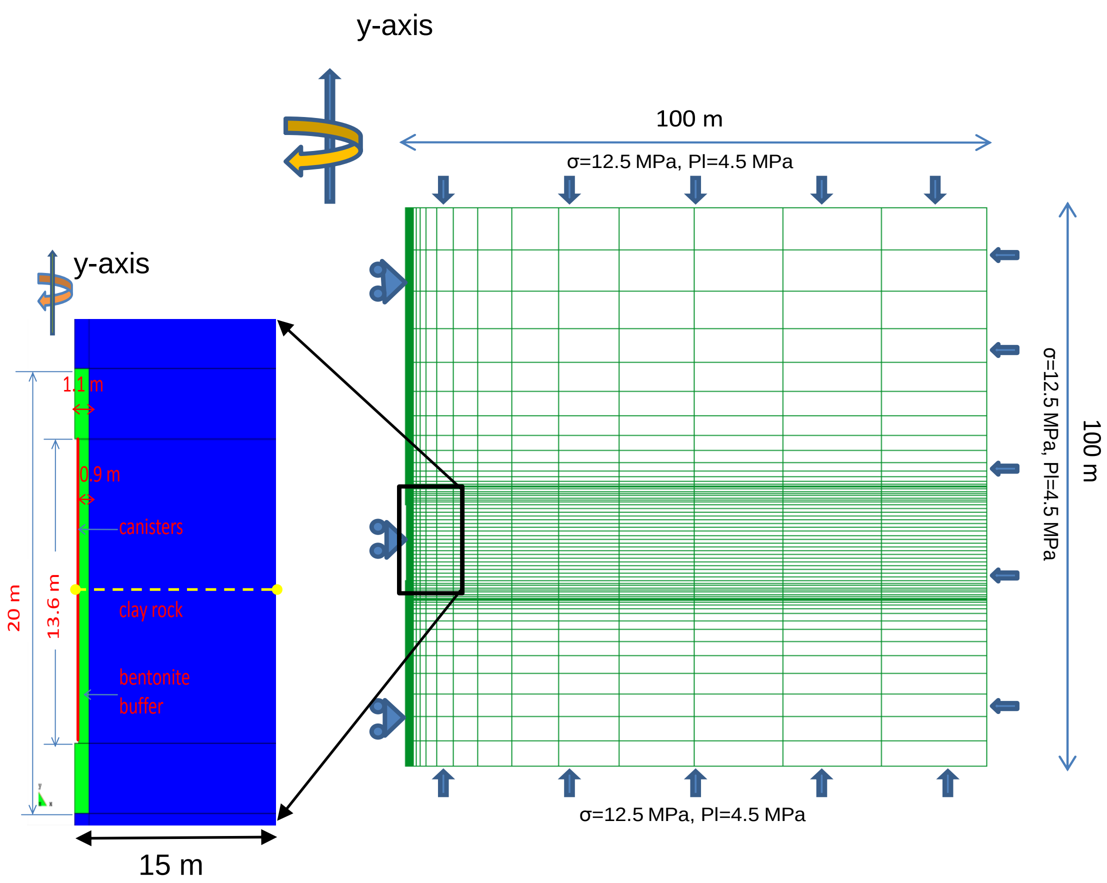


**Fig. 3.48** Axisymmetric model for the rock-buffer-system surrounding SF containers in a horizontal drift

The evolution of the heat power per container is illustrated in fig. 3.49 according to the data from /GEN 06/. In the modeling, the total heat from 4 containers is homogeneously distributed over the surfaces of the containers and also over the buffer bodies along the whole section of 13.6 m length. Considering a cooling phase of the SF containers of 30 years before emplacement in the repository, the initial heat output is estimated to 670 W per container. So the initial heat output per meter length of the container/buffer surface is determined by

$$j_e = \frac{670W \cdot number\,of\,canisters}{total\,length} = \frac{670W \cdot 4}{13.6m} \approx 200W/m \tag{3.54}$$

According to /GEN 06/ the variation of the heat emission can be described by the following decay function:

$$j_e = j_{eo} \cdot \exp[-abs(\lambda_e) \cdot t] \tag{3.55}$$

where $\lambda_e$ = 6.67E-10 $s^{-1}$.

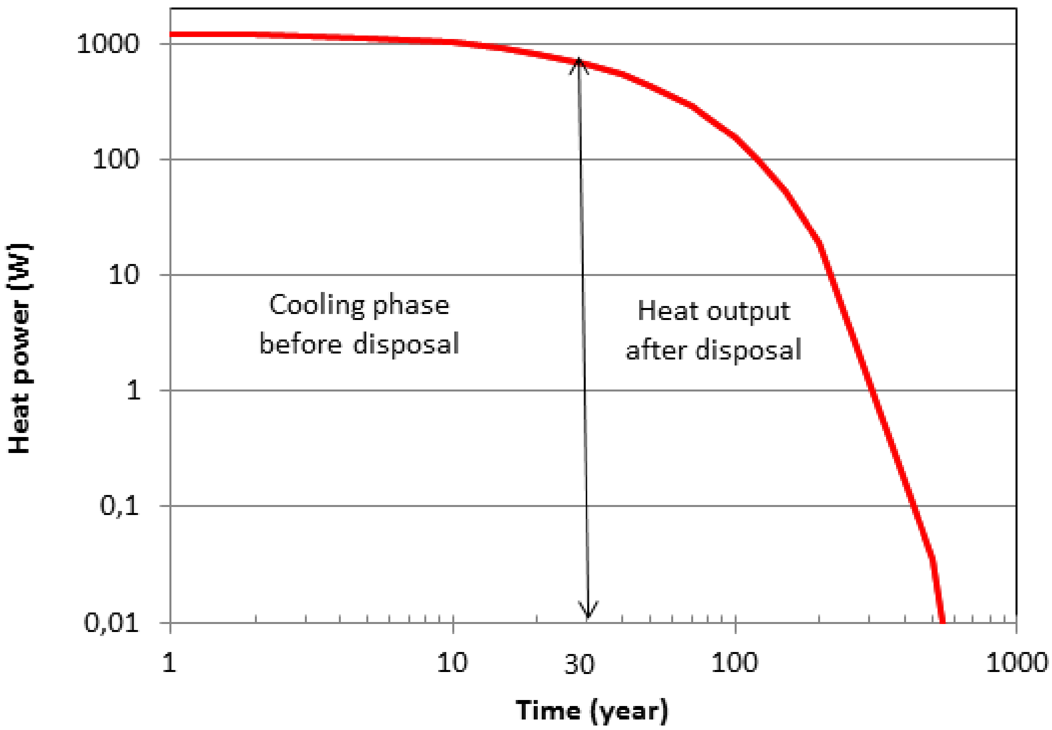


**Fig. 3.49** Evolution of the heat power of a vitrified waste container with time /GEN 06/

### 3.5.2 Results and analysis

In the modelling, long-term processes over 1000 years after SF disposal operation should be computed. However, because of the very complex THM coupling calculations in the two different materials and the limited capacity of the computer used, the computing speed was slow and hence, the time period considered in the computing time of 3 months is only about 5 years. That is why it is only possible to present the modelling results achieved for this first disposal period. The modelling results for the first heating phase of about 5 years are illustrated and analysed below.

#### 3.5.2.1 Temperature

The heat emitting from the HLW containers is gradually transferred into the buffer and the rock, forming a temperature field with varying gradient. fig. 3.50 shows the time evolution of temperatures at some selected points in the buffer and in the rock, while the temperature distribution at various times is illustrated in fig. 3.51. The temperature fields at 1, 2, 3 years are depicted in fig. 3.52. Immediately after the disposal of the containers, the temperature in the buffer rises very quickly.

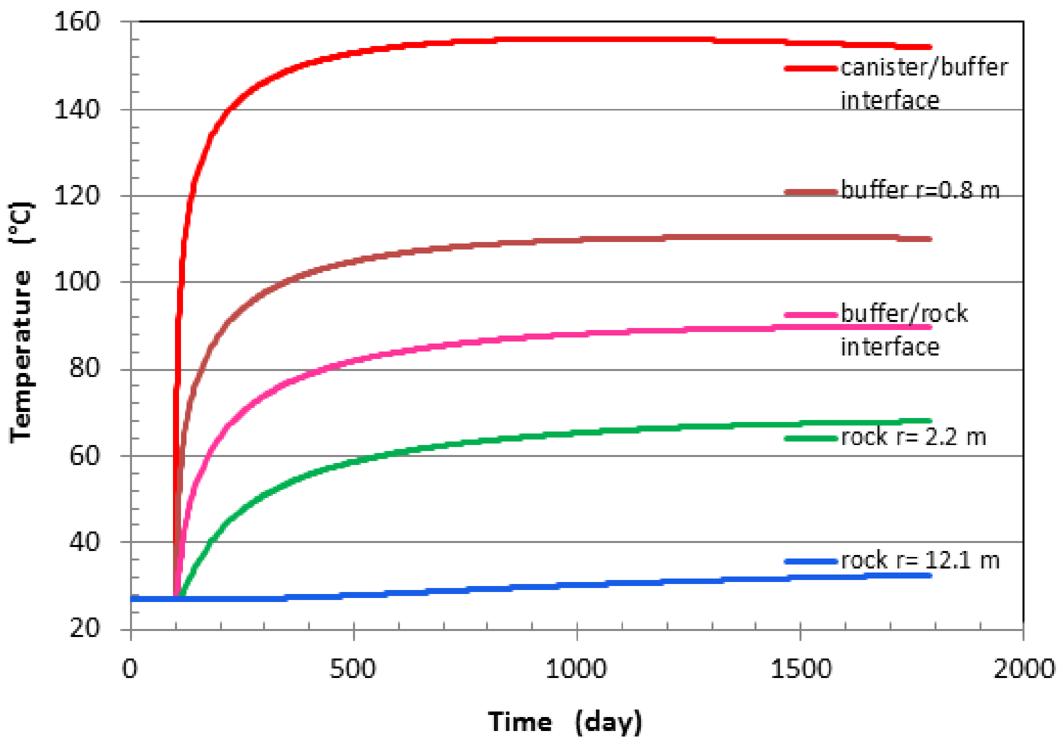


**Fig. 3.50** Evolution of temperatures at different points in the buffer-rock-barriers

The maximum temperature of 157 °C is reached at the surface of the containers after 2.6 years of heating. After that, the temperature at the container surface tends to decrease slowly with time. At the interface between buffer and rock, the temperature reaches the maximum of 93 °C after 4 years of heating and then begins to decrease. Far away from the interface, the temperature in the rock is lower than that determined by the conceptual criterion of 90 °C. Over the first heating phase of 4.5 years, the heated area extends from the containers to about 15 m into the rock mass. Based on similar modelling results reported in /GEN 06/, it can be expected that the temperature field will extend further into the rock. But due to the decay of heat output from the HLW containers, the critical temperature will not be exceeded in the rock and a cooling down phase will follow.

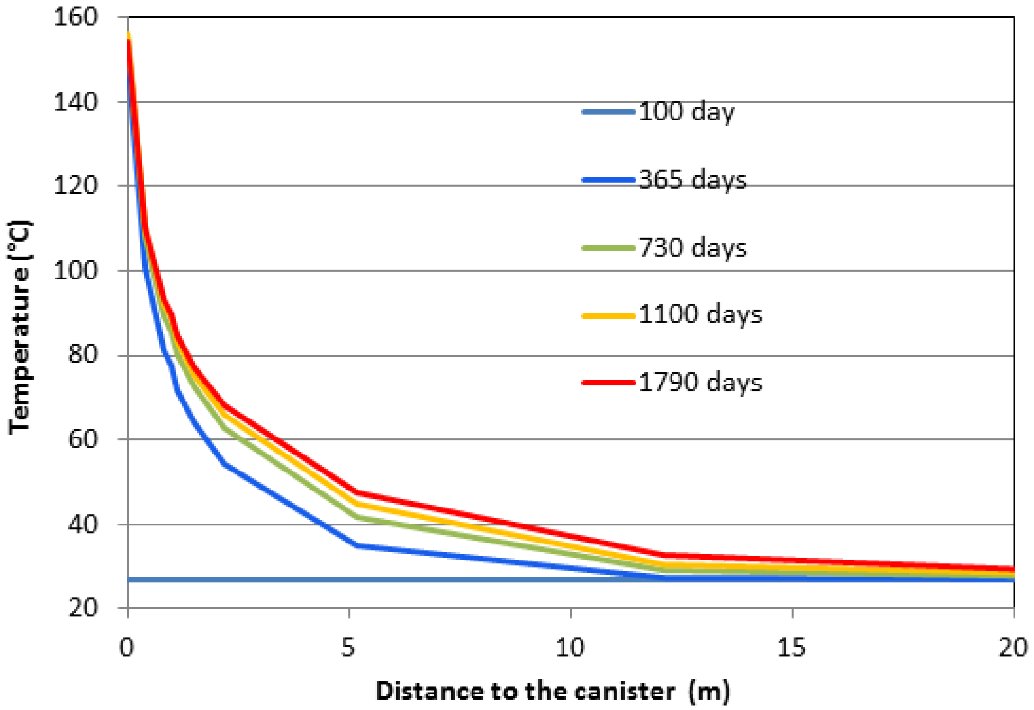


**Fig. 3.51** Distribution of temperature in the buffer-rock-barriers

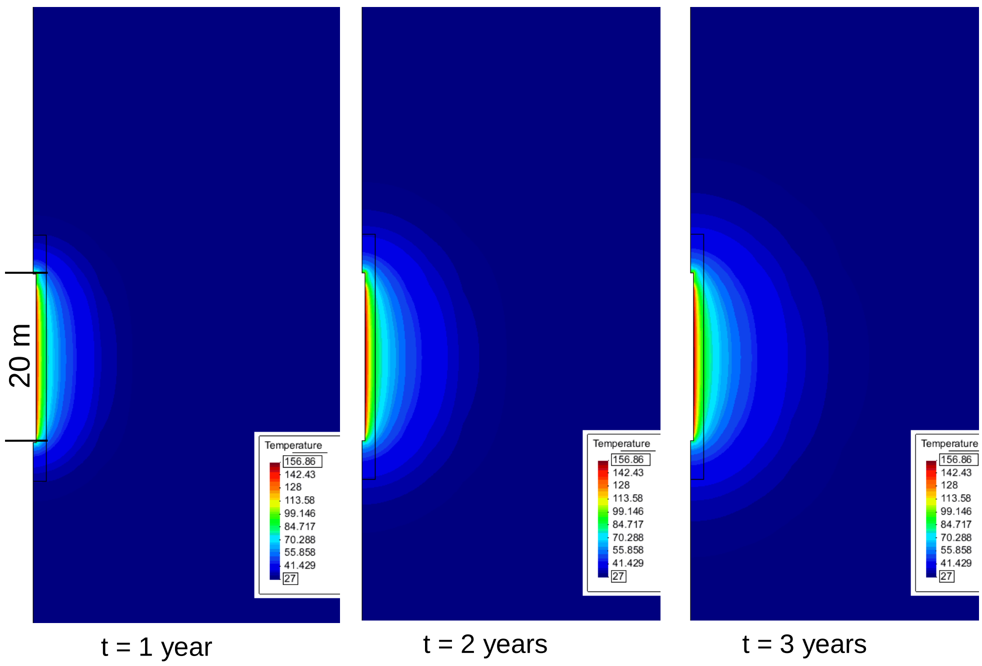


**Fig. 3.52** Temperature field in the buffer-rock-system

#### 3.5.2.2 Hydraulic Responses

The most important hydraulic process in the buffer after its emplacement is the hydration of the very dry bentonite. Fig. 3.53 shows the time evolution of the degree of water saturation at the container/buffer interface, the buffer centre, and the buffer/rock interface. By the effect of high suction, the buffer near the rock takes up water quickly from the initially saturated rock. At the opposite side, the buffer near the container is desaturated due to the evaporation of the pore water by the rapidly elevated temperatures. The water vapour from the hot inner part and from the wetted outer part migrates towards the middle of the buffer, thereby increasing the water saturation. After the transient phase of about 1 year, the degree of water saturation in the whole buffer increases gradually with time. Because the bentonite buffer is initially very dry and the permeability of the buffer and the rock is quite low, the hydration process in the buffer is very slow.

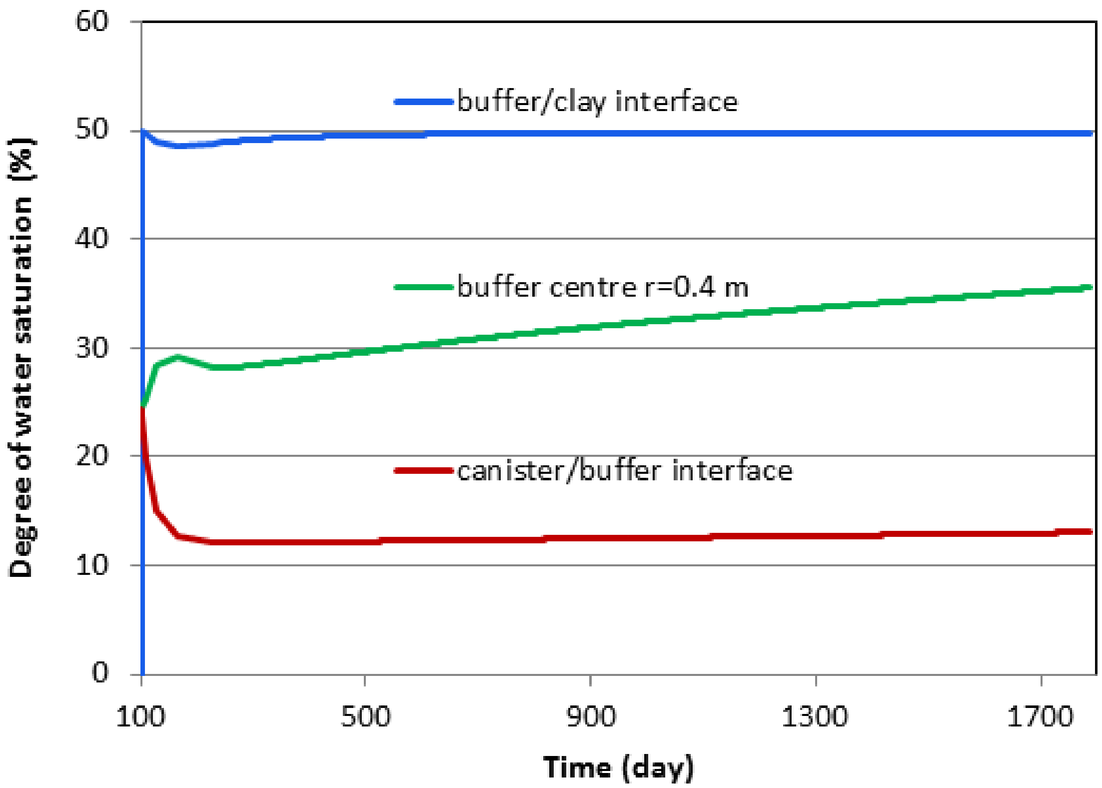


**Fig. 3.53** Evolution of water saturation at selected points in the bentonite buffer

In the clay rock with very low permeability, the most significant hydraulic process is changes of pore-water pressure. Fig. 3.54 shows the evolution of pore-water pressure at selected points along the middle section in the rock, while the pressure distributions at 1, 2, 3 years are depicted in fig. 3.55. Fig. 3.54 indicates that the drift excavation results in a sudden increase of the pore pressure up to 9 MPa near the drift wall (r = 0 – 0.2 m). During the ventilation, the pore pressure falls down to negative values, indicating a de-saturation. The dry buffer causes a higher de-saturation in this near-field. In contrast to that, the heating gives a rise of the pore pressure in the saturated region (r > 0.3 m). Within the area of r < 1.5 m to the drift wall, the pore pressure increases to the maximum values of 3 to 7 MPa during the first month and then decreases gradually with time. The increase in pore-water pressure is caused by the difference of the water expansion coefficient ($3.4 \cdot 10^{-4}$ $K^{-1}$) to the significantly lower expansion coefficient ($1.5 \cdot 10^{-6}$ $K^{-1}$) of the solid, whereas the gradual reduction of the pore pressure is due to the migration of the pore water (vapour and liquid flow) towards the dry buffer. The increase rate of the pore pressure becomes smaller in the far-field. The maximum pore pressure of 8.8 MPa is reached at the distance of r = 4.4 m after 1 year. At the distance r = 11.3 m, a lower peak pressure of 7 MPa is obtained. Fig. 3.55 shows clearly that the overpressure zone extends with time from the near-field into the far-field but with a decreased magnitude of the peak pressure.

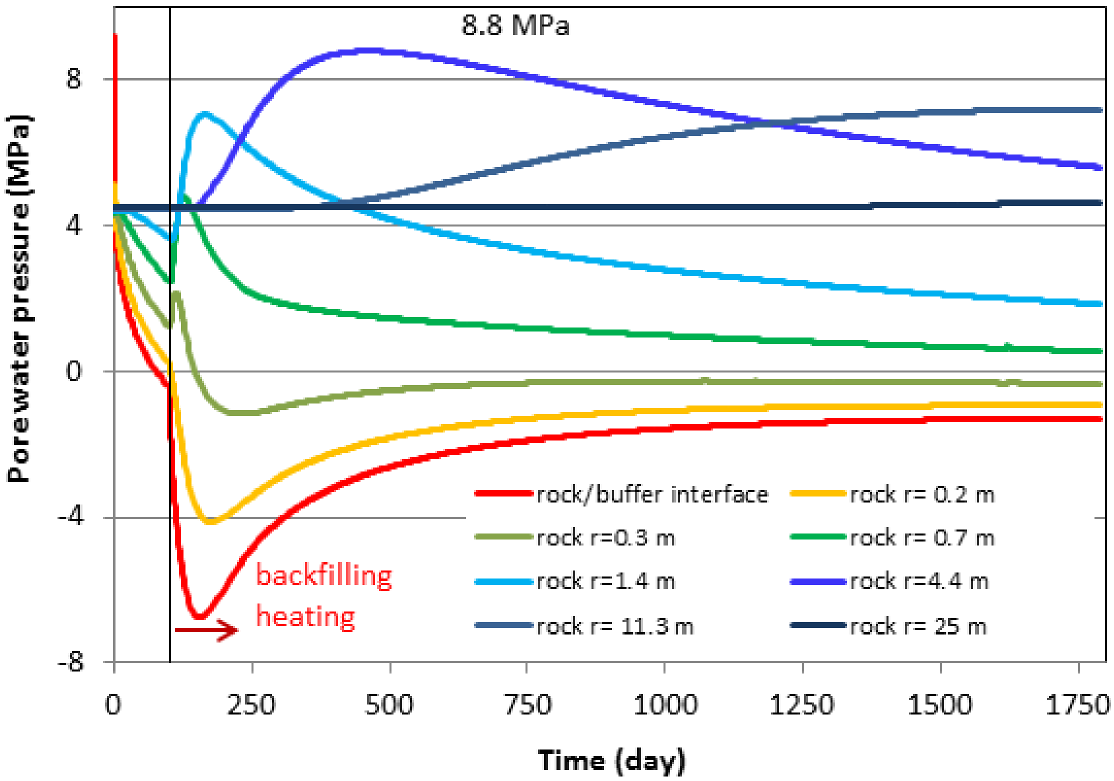


**Fig. 3.54** Evolution of pore-water pressure at selected points in the surrounding rock

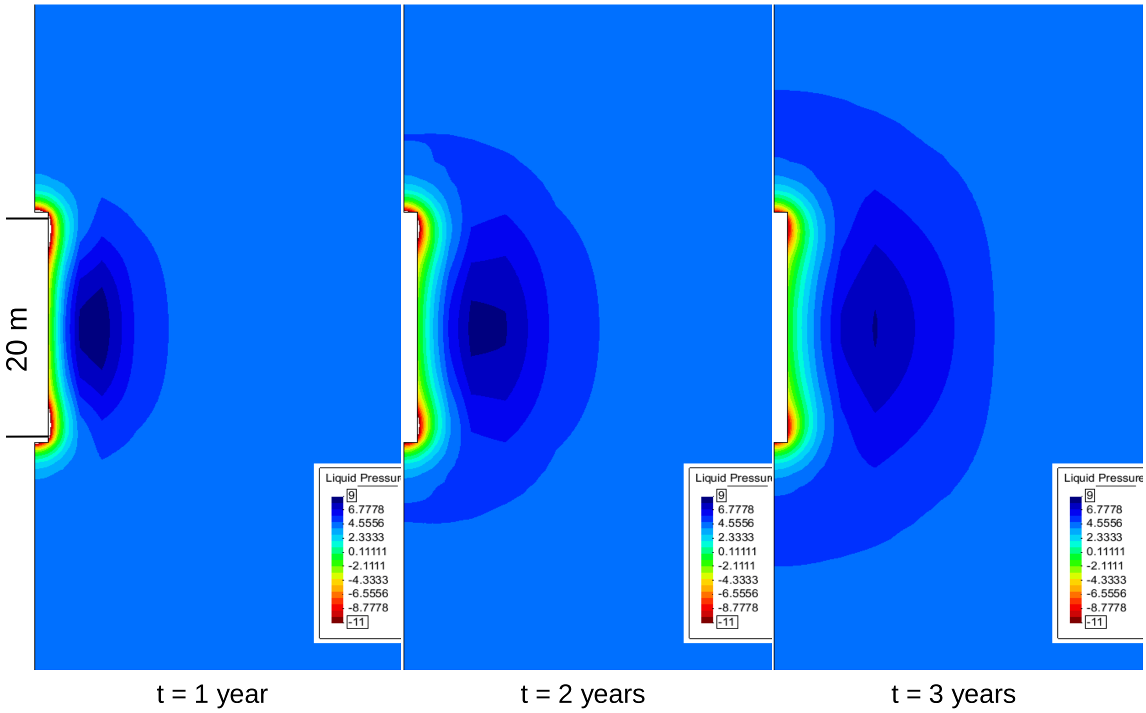


**Fig. 3.55** Distribution of pore-water pressure in the rock during the heating phase

### 3.5.2.3 Mechanical Responses

The temperature increase and the hydraulic processes in the rock and the buffer have effects on the stress-strain behaviour of both clay materials, which also interact on each other.

Fig. 3.56 illustrates thermally-induced variations of the total radial stress in the clay rock. Due to the thermal expansion of the rock mass and the confined load conditions an excess stress builds up in the area near and beyond the heated region (compare fig. 3.52 and fig. 3.55). The high stress zone extends faster and larger than the elevated temperature and pore pressure zones (compare fig. 3.52, fig. 3.55, fig. 3.56). The maximum value of the total stress is about 16 MPa (negative value indicating compression). Because the total stress is still higher than the maximum pore pressure of ~9 MPa, no hydraulic fracturing can take place.

The stress in the compacted bentonite buffer is mainly controlled by the swelling during the hydration. Fig. 3.57 indicates that the stress in the buffer increases with time to about 2 MPa after 3 years. The magnitude of the stress in the rock does not vary significantly with time.

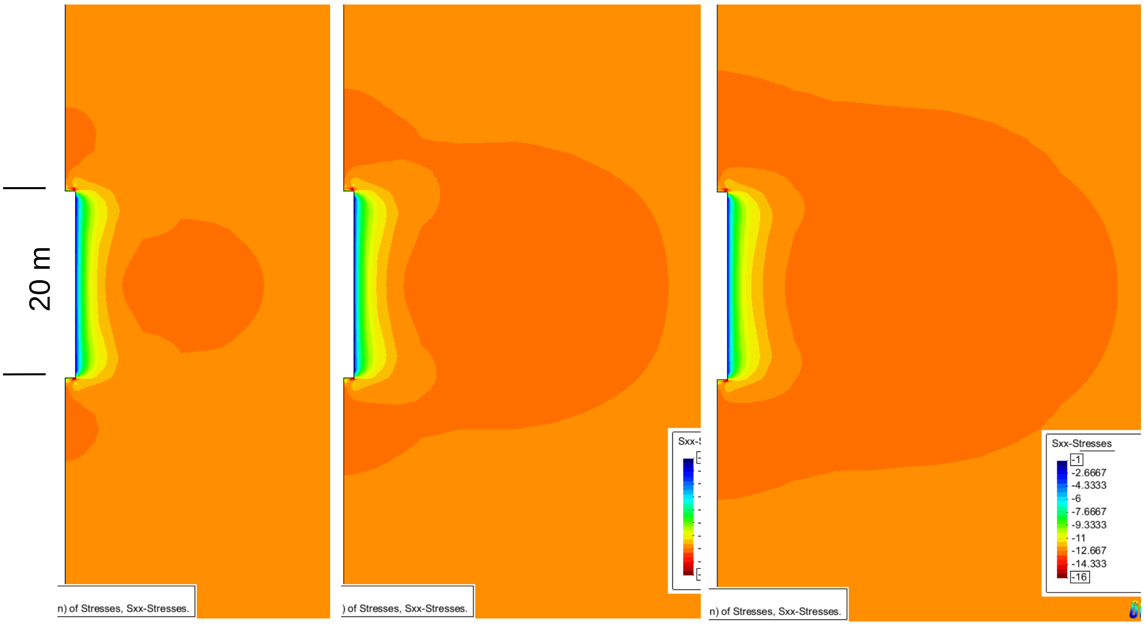


**Fig. 3.56** Distribution of total radial stress in the rock during the heating phase

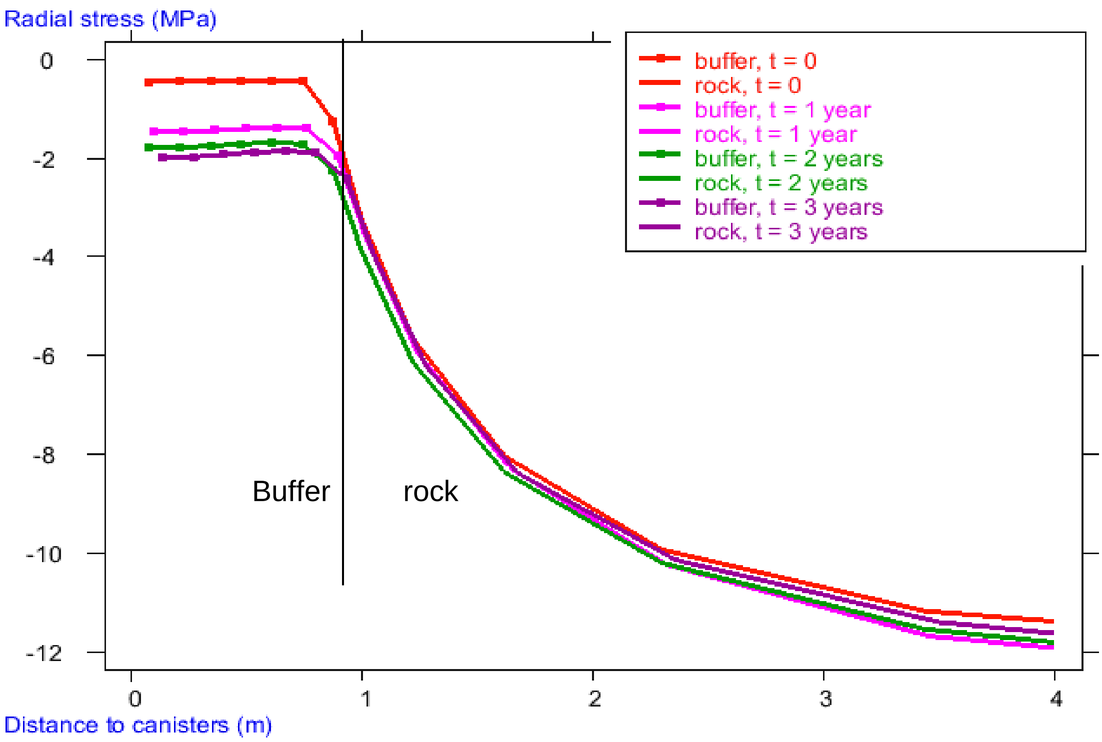


**Fig. 3.57** Variations of total radial stress in buffer and rock

Because of the variations of temperature and water saturation in the buffer, the deformation is inhomogeneous. This can be recognized from fig. 3.58 showing the distribution and evolution of the porosity as a function of the distance to the container. The buffer near the more saturated rock (r > 0.6 m) expands with increasing hydration, while the buffer on the opposite near the hot containers shrinks mainly due to the thermally-induced de-saturation. The middle area is more compacted.

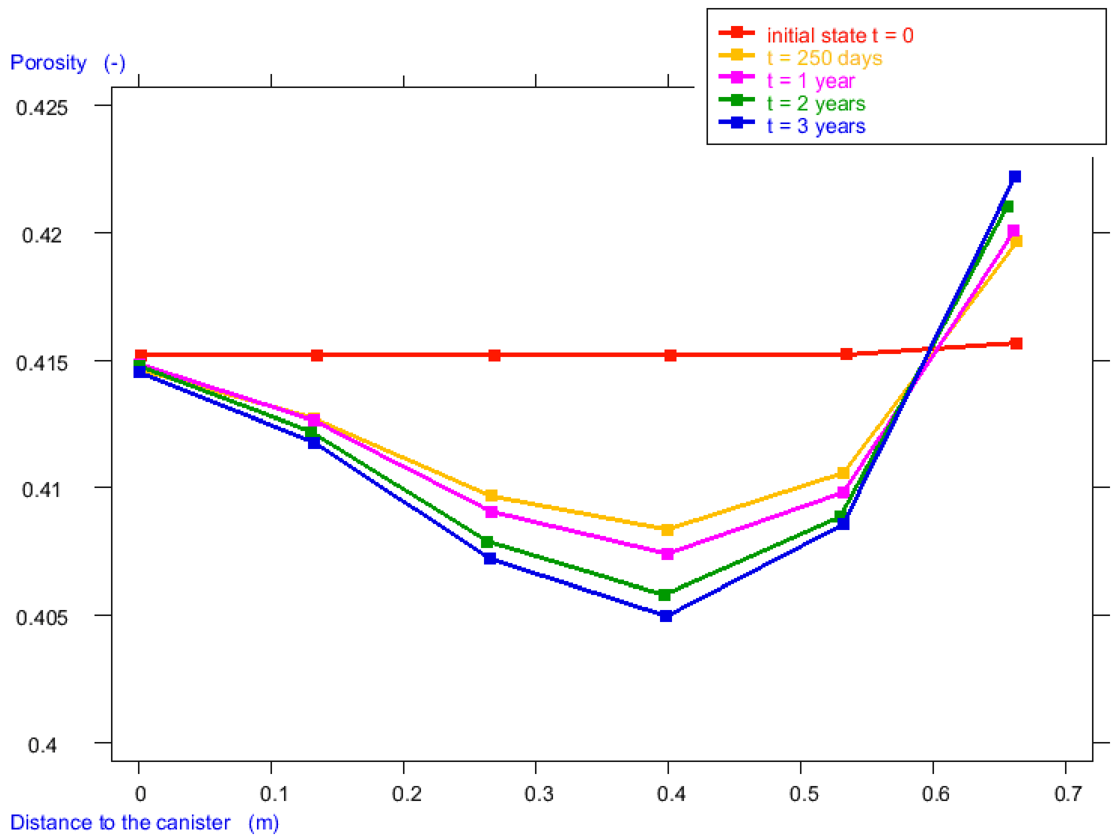


**Fig. 3.58** Variations of porosity in the bentonite buffer during the heating phase

The variations of the THM conditions and the backfill resistance have an impact on the rock deformation. Fig. 3.59 compares the displacements at different locations. The heating produces a short convergent deformation of the rock near the drift (r < 0.2 m). Because of the build-up of the backfill pressure, the deformation in this area turns back slowly. In the saturated far-field (r > 1.1 m), the temperature increase results in an expansion in all directions, i. e., not only towards the backfilled drift (positive increment), but also towards the rock depth (negative increment). Fig. 3.60 shows the directions of the rock deformation at 3 years. The thermal expansive zone moves with time and seems to be coincident with the high pore-pressure zone (compare fig. 3.60 and fig. 3.55).

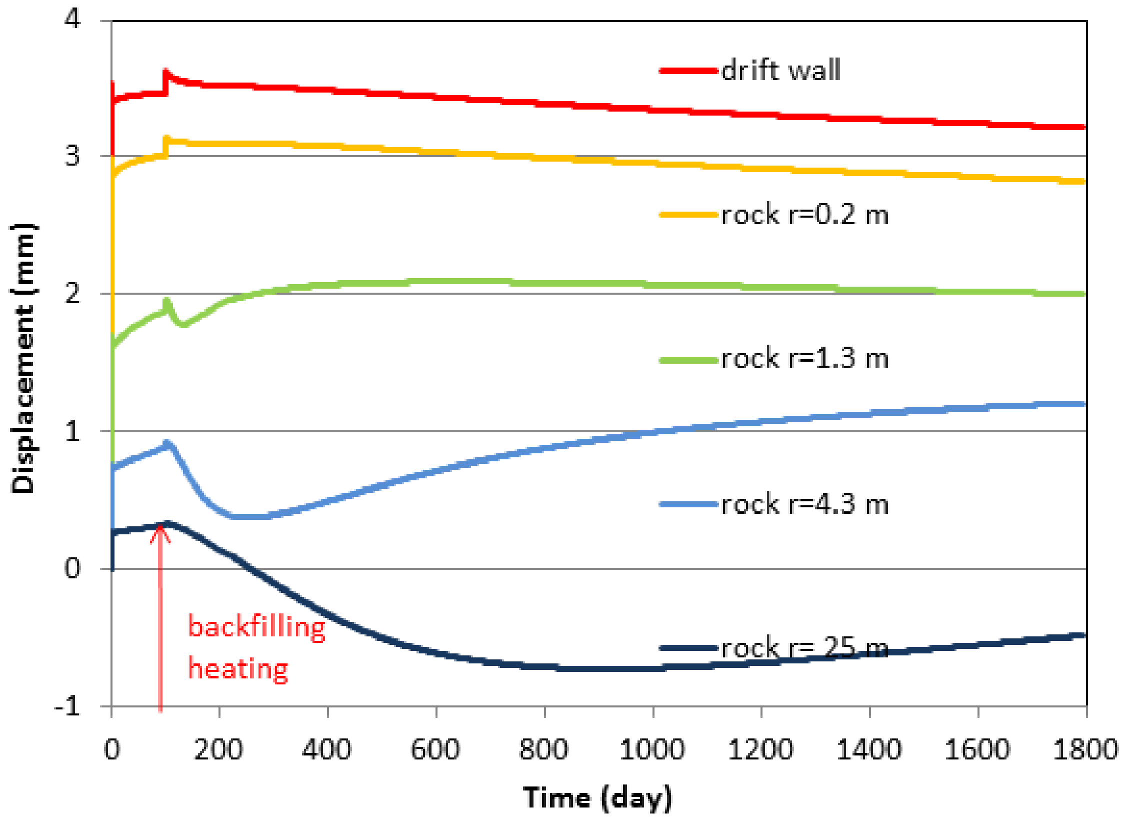


**Fig. 3.59** Evolution of radial displacements at different locations in the rock

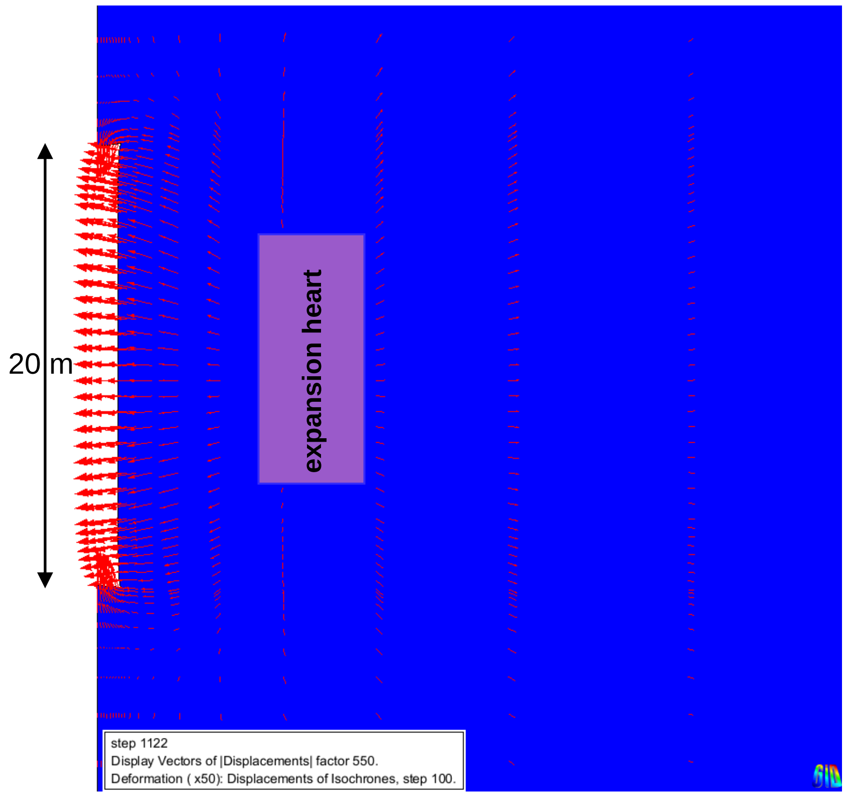


**Fig. 3.60** Rock expansion due to the thermal loading after 3 years

It is also interesting to examine the damage of the rock by comparing the stress state in the near-field with the damage locus and the yield boundary (see fig. 3.61). It is obvious that the deviatoric stresses in the near-field within a radius of ~1 m are beyond the damage locus, indicating that the bonds in the rock are more or less destroyed. The deviatoric stress at the drift wall (r < 0.2 m) first rises immediately after the excavation and even exceeds the yield limit, where plastic deformation occurs. After backfilling, the deviatoric stress reduces gradually due to the backfill pressure against the rock. This prevents further development of the damaged zone and leads the rock to heal with time.

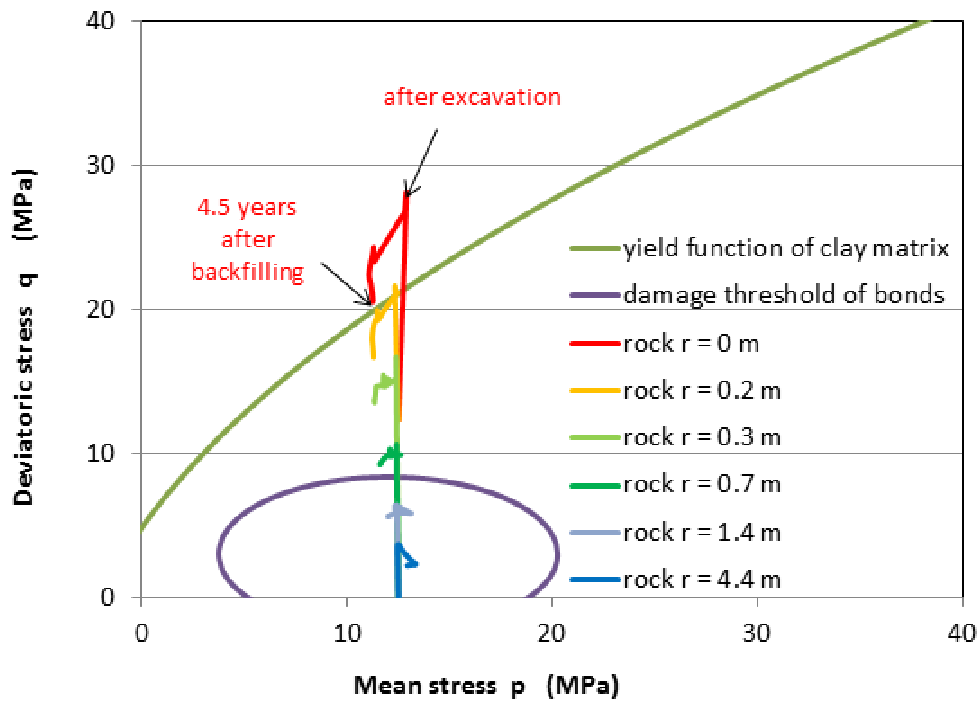


**Fig. 3.61** Rock stress states compared with the damage and yield boundaries

### 3.5.3 Conclusions on the THM modelling of rock-buffer-system

From the scoping calculations of the THM processes occurring in the rock-buffer-system during the first heating phase, some significant phenomena can be identified:

- The drift excavation induces a redistribution of the rock stress with a minimum radial component, a maximum tangential component, and a middle component in the drift direction. The deviatoric stress results in deformation of the rock towards the open drift. In the area near the drift wall, the rock is damaged. The damaged zone extends into the rock mass up to a distance of about 1.5 m.

- The drift ventilation and the subsequent backfill with unsaturated bentonite lead to a reduction of the pore pressure and even to a de-saturation in the surrounding rock to a depth of ~0.3 m. On the other side, the water saturation in the backfill increases gradually by taking up water from the initially saturated rock. The re-saturation results in build-up of the swelling pressure in the backfill against the deformation and the damage of the surrounding rock.

- The heat from the HLW containers transfers gradually into the buffer and the rock, increasing the temperatures there. The maximum temperature of 157 °C is reached at the interface between the backfill and the container at 2.5 years. The temperatures in the rock are limited below the conceptual criterion of 90 °C.

- Heating causes evaporation of the pore water in the buffer near the containers and thus de-saturation. At the opposite side, the water saturation in the buffer near the rock increases.

- The increase of temperature in the saturated rock generates a significant rise of the pore-water pressure up to 9 MPa due to the very low porosity and permeability as well as the large difference of the water expansion and the solid expansion. Simultaneously, the total rock stress increases, too. Because the effective stresses during the heating phase are still compressive, fracturing cannot take place during the heating period.

- Although only a single disposal drift is considered in the modelling, the preliminary understanding and the modelling results provide a basis for additional advances in the design, the assessment and the validation of the HLW repository concept with more disposal drifts. For this purpose, further modelling work will be done in the frame of the ongoing THM-TON project /THM 07/ with improved constitutive models, higher certainty of parameters, more realistic conditions, and an increased computing capacity.

# 4 Summary and Conclusions

## 4.1 Objectives

Within the framework of the co-operation agreement between BMWi and ANDRA, GRS has participated in ANDRA's research programme conducted in the underground laboratory MHM-URL at Bure in France since 2000. The overall objective of the research activities in the URL is to study the suitability of the Callovo-Oxfordian argillaceous formation for disposal of high-level and long-lived radioactive waste. From July 2005 to September 2010, GRS performed the BURE-HAUPT project to investigate the thermo-hydro-mechanical (THM) behaviour of the Callovo-Oxfordian clay rock and to validate the modelling capabilities of constitutive models implemented in the computer code CODE-BRIGHT for analysis of coupled THM processes occurring in clay host rocks during the repository operation and post-closure periods of tens of thousands of years.

The EC TIMODAZ project was launched in October 2006 and completed at the end of September 2010. The main purpose of this project was to study thermal impact on the excavation damaged zone (EDZ) around radioactive waste disposal cells in clay host rocks. Totally, 14 participating organisations representing 8 European countries (BE, FR, CH, DE, NL, ES, CZ, UK) were involved in the project. As the representative of Germany, GRS took part in it. The plastic Boom clay, the argillaceous Opalinus (OPA) and Callovo-Oxfordian (COX) clay rocks, which are being considered as potential host formations for repositories, were investigated in the TIMODAZ programme by conducting

- Laboratory experiments for determination of the thermo-hydro-mechanical-chemical (THMC) behaviour, particularly the fracturing and sealing behaviour of the clay rocks under relevant repository conditions;
- *In situ* heating experiments in the URLs at Mont-Terri in Switzerland, HADES in Belgium, and Josef UEF in Czech for characterization of coupled THMC processes in the rock mass;
- Benchmark modelling of the specific laboratory and *in situ* experiments for validation and improvement of the predictability of the constitutive models and computer codes used for the long-term THM processes in clay host rocks;
- Assessment of the significance of the thermally-impacted EDZ for the Performance and Safety Assessment (PA, SA) of repositories in clay formations.

GRS has contributed to the TIMODAZ programme with laboratory experiments and numerical modelling of the THM behaviour of the COX clay rock within 5 work packages:

WP2: State of the art of the THMC behaviour for the clay rocks
WP3.1: Laboratory characterization of the THMC behaviour of the clay rocks
WP3.3: Laboratory simulation tests on large hollow cylinders of the clay rocks
WP5.1: Improvement and development of constitutive models for clay rocks
WP5.2: Benchmark modelling of the laboratory and *in situ* experiments.

The results and conclusions achieved from the GRS's work within both the BURE-HAUPT and TIMODAZ projects are summarized in this report.

## 4.2 Experimental results

The thermo-hydro-mechanical behaviour of the COX clay rock has been comprehensively investigated in the GRS geo-laboratory on a large number of samples of different sizes by means of various kinds of testing methods. The tests on normally-sized samples focused on short- and long-term deformation response to mechanical loads, swelling and shrinkage induced by variations of environmental moisture, permeability changes caused by damage and re-compaction, and thermal effects on the hydro-mechanical properties. The large hollow cylinder tests simulated the fracturing and sealing processes in the EDZ around disposal cells during the excavation, ventilation, backfilling, water inflow, heating and cooling. Additionally, crushed claystone produced from the drift excavation was preliminarily characterized as a favourable alternative backfill/buffer material instead of expensive bentonite-based mixtures.

**Deformation behaviour**

Sufficient knowledge of the **short-term deformation, damage, and strength behaviour** of a clay host rock in consequence of deviatoric loading due to excavation is required for the design of an underground repository with regard to the stability and safety of its construction during the operation phase. The short-term deformation behaviour of the COX claystone was investigated by increasing axial deviatoric load on the samples at constant lateral confining stresses. The consolidated claystone behaves elasto-plastically. The elastic stiffness and the wave velocity observed increase with applied deviatoric stress until yielding, indicating the compaction of the pre-existing micro-cracks in the samples. Further increasing the deviatoric stress results in re-opening/creation, propagation and coalescence of micro-cracks forming shear fractures. The peak strength increases with the lateral confining stress and can be reasonably approached by the Mohr-Coulomb criteria. The parameters determined for the peak strength parallel to bedding plane are the cohesion of 6.5 MPa, the internal friction angle of 24°, and the major principle strain of 1 – 2 %. By comparing with the previous data, the strength perpendicular to bedding is relatively higher than that parallel to bedding with a mean anisotropic ratio of 1.25. Whereas the elasto-plastic yield occurs at ~70 % of the peak strength, the dilatancy onset detected by volumetric strain is closer to the failure point. After failure, a certain residual bearing capacity still remains in the fractured claystone.

The **long-term deformability** of a clay host rock is one of the most important factors governing the sealing process of fractures in the EDZ, the compaction of the backfill/buffer surrounding waste canisters, and finally the safe sealing of the whole repository. The experimental study of the time-dependent deformation of the COX claystone was carried out in uniaxial and triaxial creep tests under multi-step loads.

The *uniaxial creep* tests were performed on the samples at loads of 1 to 13 MPa over exceptionally long durations of 1 to 4.5 years with each phase between 4 and 18 months. All the samples with water contents of 4.7 – 6.4 % (not fully-saturated with degrees of 73 – 93 %) were sealed in rubber jackets to prevent water loss during the tests. The main findings from the uniaxial creep tests are that:

- The claystone deforms continuously with time even at low stresses of 1 – 2 MPa, indicating negligible threshold for the onset of creep.
- The creep behaviour is dependent upon the loading path, i. e. raising or lowering the load in uniaxial tests. After elevating the load to a desired level, the claystone deforms gradually with time at decreasing rates and then a (quasi-) stationary creep phase follows with a nearly constant rate. In contrast, after lowering the load to a desired level, the creep strain evolves first with negative but increased rates until a constant positive rate is reached. The duration of the transient creep at lowered load is relatively shorter than that at increased load, depending on the magnitude of load increments.
- The creep rate seems to be less dependent on the stress level. The quasi-steady state creep rates determined at elevated stresses of 1 to 13 MPa range from $2 \cdot 10^{-11}$

to $7 \cdot 10^{-11}$ $s^{-1}$, whereas the steady state creep rates observed at lowered stresses lie between $7 \cdot 10^{-12}$ and $1 \cdot 10^{-11}$ $s^{-1}$. The steady state creep rate at a lowered stress is 1 to 3 times lower than that quasi-steady state rate at the same stress increased.

- The creep rate is less or independent of the loading directions parallel or perpendicular to bedding plane, i. e., insignificant anisotropy effect on creep.
- The higher carbonate content and/or the lower water content, the slower the creep.

The **triaxial creep** tests were carried out on both COX and OPA claystone. The samples were firstly consolidated at a high isostatic stress of 40 MPa to achieve the original intact state with full water saturation. The following creep phases were conducted at constant axial stress of 15 MPa and lowered radial stress of 12, 9 and 6 MPa over 2 to 4 months each. A gradual increase in axial strain was recorded on OPA sample during each phase, but no axial strain could be detected on COX sample at the first phase at $\sigma_1$= 15 MPa / $\sigma_1$= 12 MPa. It is interesting to note that the quasi-steady state creep rates determined on OPA sample are very close to each other in a narrow range from $1.1 \cdot 10^{-11}$ to $1.7 \cdot 10^{-11}$ $s^{-1}$, indicating no or insignificant dependence of creep on the applied stress range of 3 to 15 MPa.

Different mechanisms may lie behind the creep, such as

a) rebalancing of pore pressure because of the very low permeability;

b) deformation of the mineral skeleton by sliding clay flakes;

c) subcritical propagation of fissures and the possible creation of new fissures;

d) stress-induced solution transfer because of the presence of carbonates in the argillaceous rocks;

e) deformation and state changes of water-films adsorbed on the internal and external surfaces of clay particles. Which mechanisms dominate the creep in clay rock is still unclear and thus necessary to be studied further for improvement and development of constitutive models for the long-term deformation of clay host rocks.

**Swelling behaviour**

The drift ventilation will lead to de- and re-saturation of the surrounding clay rock and result in shrinking and swelling and even fracturing near the drift wall. After closing the repository, the previously de-saturated clay rock will be gradually re-saturated again by taking up water from the saturated far-field, accompanied by swelling of clay minerals into fracture voids. The swelling capabilities of both COX and OPA claystone with different clay contents of about 12 %, 40 % and 65 %, respectively were examined by drying and wetting samples with measurements of water adsorption, free swelling strain in unconstrained conditions, and swelling pressure under axially-fixed and laterally-unconstrained conditions. The drying and wetting conditions were adjusted by changing the relative humidity of the surrounding air from 23 % to 100 % (suction = 0 – 206 MPa). The most important observations are that:

- The studied claystone exhibit high adsorption potentials, under which a great amount of water can be taken up from the humid environment to water contents of 10 – 18 % in unconstrained conditions, about two to three times that in the naturally-confined and saturated rock mass. The higher the clay content, the higher is the water adsorption potential.

- The water uptake enlarges the distance or pore space between solid particles, resulting in swelling. The claystone in unconstrained and humid conditions can expand largely up to 8 – 12 %. Because of the sedimentary structure, the swelling strain is more significant in direction perpendicular to bedding plane and even fractures appear along the weak plane. The higher the clay content, the larger the swelling strain.

- The adsorbed water-films in the claystone are capable of bearing externally applied loads and even carrying the lithostatic stress, as indicated by the measured swelling pressures up to 10 – 12 MPa on COX samples with a clay content of ~40 % from the depth of 490 m and 5.5 MPa on OPA samples with a clay content of ~65 % from the depth of 230 m, respectively. This conclusion is also supported by the swelling strain observed on a COX sample at the stress state at the MHM-URL with high confining stresses of 12 – 15 MPa and pore pressure of 4.5 MPa.

- Conversely, a dry condition causes evaporation of pore water and release of the stress-supporting elements, leading to collapse of the pore structure. The macroscopic shrinkage increases with decreasing moisture, but is limited to 0.3 % at COX to 1.7 % at OPA claystone in a dry condition of 23 % air humidity. A higher clay content results in a larger shrinkage.

- The saturated claystone with clay contents of more than 40 % seemed to behave as compacted colloid without direct bonds between solid particles. Consequently, the swelling pressure acting in interparticle water-films is equal to the effective stress (total external stress minus free pore water pressure). This so-called dense clay-colloid model may be helpful to improve the understanding and modelling of strongly-coupled hydro-mechanical processes in natural clay rocks and engineered clay barriers, such as water and gas transport, rheological deformation, self-sealing and healing of fractures, etc.

**Permeability changes by damage and re-compaction**

Excavation of a repository produces fractures in the surrounding host rock acting as preferential pathways for fluid transport and radionuclide migration. However, a self-sealing process of the fractures can be expected due to combined impact of the rock compression, backfill support, and the swelling of clay minerals during the long post-closure period. The knowledge of permeability changes induced by the damage and the re-compaction is the fundamental input for assessment of the significance of the EDZ for the repository safety. This issue was investigated on the COX claystone by conducting a series of combined damage-compaction tests with measurement of gas permeability. The observations suggest that:

- **Intact state**: Very low gas permeabilities of $10^{-22}$ – $10^{-20}$ $m^2$ were determined on the COX samples extracted from different distances of 0.5-13.0 m to the wall of the main shaft. They were more or less disturbed and de-saturated before testing. In case of full water-saturation, the effective gas permeability will be lower and the clay rock practically impermeable for gas when the gas entry pressure is below the sum of the capillary pressure and the swelling pressure acting in adsorbed water-films between particles.

- **Damage**: The permeability increases dramatically by several orders of magnitude up to $10^{-18}$ – $10^{-17}$ $m^2$ when a stress criterion (percolation threshold) is exceeded, at which micro-cracks are growing sufficiently to be interconnected, forming macro-fractures and preferential pathways. The increased permeability depends on the minor confining stress dominating the fracture aperture. At high confining stresses over ~6 MPa, no significant permeability changes take place. Shear fracturing after failure does not change the permeability very much due to the limited variation of the fracture geometry.

- **Re-compaction**: The high permeability of the damaged clay rock decreases significantly when increasing the confining stresses applied along the different loading paths, isotropic loading $\sigma_1 = \sigma_2 = \sigma_3$, deviatoric loading at $\sigma_2 = \sigma_3$ = const. or $\sigma_1/\sigma_3$-ratio = const.. In fact, all the loading paths generate normal stress on the fracture surfaces, which dominates the fracture aperture and permeability. At confining stresses over 15 MPa (corresponding to a depth of ~500 m), the permeability of compacted clay rock shows very low values of $10^{-19}$ – $10^{-20}$ $m^2$ which is close to the intact state.

**Thermal effects**

Thermal impact on the hydro-mechanical properties and the integrity of clay host rocks is the key concern for disposal of heat-emitting nuclear waste. This issue was experimentally studied on the COX claystone in various respects of thermal expansion and contraction, changes in pore pressure, alteration of swelling capacity, variations in stiffness and strength. The maximum temperatures of 100 to 150 °C applied to the samples are higher than the upper limit of 90 °C designed for the clay host rock around repositories. The following significant thermal effects are observed:

- The thermal expansion of the claystone depends on both the water saturation and the hydro-mechanical boundary conditions. In saturated and undrained conditions, the thermal expansion is predominantly controlled by the pore water because of its much higher expansion coefficient compared to that of the solid grains. In unsaturated and/or drained conditions, heating causes mobilisation and expulsion of the pore water from the rock, giving rise to pore collapse and thus consolidation. The thermally-induced consolidation enhances the stiffness and strength of the clay rock. No thermal fracturing was observed by heating the nearly-saturated samples even at a deviatoric stress of $\sigma_1$ = 15 MPa and $\sigma_3$ = 3 MPa.
- Heating increases the pore-water pressure in the saturated claystone. The maximum pore pressure up to 12 MPa was recorded by heating the nearly-saturated samples up to 90 °C, but still lower than the externally applied confining stress of 15 MPa. At elevated temperatures, the pore pressure decreases with time. The same phenomenon is also observed in the clay rock mass during the TER and HED heating experiments performed in the MHM- and MT-URLs. This is attributed to the dissipation of the thermally-mobilized pore water outward seepage in drained conditions.
- Heating to 100 – 120 °C dries up the claystone leading to a maximum shrinkage of ~1 % without appearance of visual fractures even in unconfined conditions.

- The claystone, even though previously exposed to high temperatures to 100 – 120 °C, still exhibits a remarkable swelling potential with free expansion up to 12 % and swelling pressure up to 5 MPa during wetting.

Generally, no negative thermal impact on the integrity of the clay rock was found.

**Development / recovery of EDZ around boreholes**

Regarding damage development and recovery in the clay host rock around disposal boreholes, a number of large hollow cylinder tests were designed and carried out in a big triaxial apparatus by simulation of the relevant processes such as borehole excavation, ventilation, backfilling/lining, water flow, heating, and cooling. The COX hollow cylinders were prepared to an outer diameter of 280 mm and lengths of 460 – 610 mm with axially-drilled central boreholes of 50/100 mm diameter. The main observations are summarized below:

- The **borehole excavation** by reducing the borehole pressure from 15 MPa down to 1 MPa resulted in borehole convergence but not any increase in permeability in direction parallel to the borehole. Further increasing the external confining stress beyond 20 MPa generated fractures forming pathways and thus a drastic increase in gas permeability from $10^{-21}$ $m^2$ to $10^{-14}$ $m^2$.

- The **ventilation** by flowing relatively dry air through the borehole led to desaturation and shrinkage of the claystone and thus the borehole divergence appeared. In contrast, the ventilation with wet air re-saturated the claystone leading to its swelling and the borehole convergence.

- The **backfill support** by increasing the borehole pressure from 1 to 15 MPa compressed the fractures leading to a strong reduction of the permeability down to $10^{-17}$ – $10^{-21}$ $m^2$, depending on the initial characteristics of the fractures in the clay rock.

- The **water flow** through the fractures induced a strong swelling of clay minerals into the interstices and sealing them. The determined water permeability of $2 \cdot 10^{-18}$ $m^2$ is more than three orders of magnitude lower than the gas permeability before water flowing.

- **Heating** a damaged hollow cylinder from 29 °C to 74 °C accelerated the borehole convergence. The thermal impact on the water conductivity of the fractured claystone is governed by the change of the water viscosity, while the intrinsic permeability is less affected by heating.

- **Cooling down** slowed the deformation and the water transport in the damaged claystone. The permeability estimated after cooling is nearly the same as that before heating.

**Properties of crushed claystone as backfill material**

Crushed claystone produced during excavation of the repository is a favourable alternative as backfill/sealing material, because of many advantages such as a) chemical-mineralogical compatibility with the host rock, b) availability, c) low material and transport costs in comparison to the use of expensive bentonite, d) shortfall of the recycling of excavated tailings and thus no occupancy of the ground surface, and e) little effort for environmental conservation of the repository site. However, the EBS-relevant properties of such a material have not systematically been investigated so far. In the frame of this project, the hydro-mechanical properties of the crushed COX claystone were preliminarily characterized.

The air-dried aggregate with grain sizes smaller than 10 mm and 16 mm exhibits a relatively high porosity of ~45 % (dry density of 1.5 g/cm$^3$) after the normal proctor compaction. The porosity decreases non-linearly with increasing the load. In oedometer compaction tests, the porosity reached 23 – 30 % by loading to 15 MPa, depending on the applied loading rates of $1.5 \cdot 10^{-7}$ – $1.5 \cdot 10^{-5}$ s$^{-1}$. In case of the very slow drift convergence (< $10^{-10}$ s$^{-1}$ in the MHM-URL /ARM 10/), the resistance of the backfill will build up slowly. The hydraulic conductivity of the backfill decreases exponentially with porosity. Low permeability values of $10^{-16}$ – $10^{-18}$ m$^2$ were determined at porosities of 30 – 16 %. The compacted aggregate with a porosity of 19 % shows a swelling pressure of 2.5 MPa.

Further investigations on the crushed claystone as EBS material are continuing in another project (THM-TON) which is in progress /THM 07/.

## 4.3 Numerical modelling

The purpose of the modelling exercises performed in this project was to validate the capabilities of the constitutive models in the computer code CODE-BRIGHT /UPC 04/ for analysis of coupled THM processes in clay host rocks, particularly the predictability of the development and recovery of the EDZ around HLW disposal boreholes in clay formations. The model validation was conducted by simulation of the following laboratory and *in situ* experiments:

- EDZ laboratory tests performed on large COX hollow cylinders;
- REP experiment monitoring hydro-mechanical responses of the COX clay rock to shaft sinking;
- TER experiment investigating hydro-mechanical processes of the COX clay rock to thermal loading;
- Predictive calculations of THM processes in a rock–buffer system around a HLW disposal drift.

The THM processes occurring in the clay rock during the above mentioned experiments are calculated generally in a coupling way by solving a series of balance equations for energy, solid, water, air and stress with selected constitutive equations which link between the state variables and the dependent variables. The following assumptions are made:

- The COX clay rock is assumed isotropic and homogeneous;
- Heat transport includes conduction (Fourier's law) through the porous medium, advection of liquid water and vapour flow;
- Water transport is controlled by liquid water advection (Darcy's law), vapour diffusion in air (Fick's law), and liquid / gas phase changes (psychrometric law);
- Gas pressure remains at atmospheric;
- The mechanical behaviour of the clay rock is approached by the damage-elastoplastic model developed by Vaunat et al. /VAU 03/.

The damage-elastoplastic model considers a clay rock being composed of a clay matrix connected by cement bonds. The clay matrix behaves like a typical elastoplastic soil adapting the Hoek & Brown's criterion as yield surface, while the bonds behave like a typical quasi-brittle material that is represented by a damage elastic law. Bond damage or degradation occurs as the result of apparition of micro-fissures within the bonds, which reduces the surface on which stresses and strains are active. Any load applied to an element of the cemented material is distributed itself between the clay matrix and the bonds according to a ratio that depends on the geometric arrangement of both components. Totally 18 parameters are associated to the model. They are established for the COX clay rock based on our own test results and the data from literature.

The relation of intrinsic permeability with porosity is approached by the Kozeny's model being more suitable for porous media without damage effects.

**Benchmark simulation of large hollow cylinder tests**

Two large hollow cylinder tests with and without heating were simulated by coupled THM and HM calculations, respectively. The results indicate that

- The short-term deformation behaviour of the hollow cylinders is reasonably represented by the model with indication of micro-damage evolution, but the post-failure behaviour could not be modelled due to uncontrolled termination of the computation as the failure criterion is exceeded.
- The damage-induced drastic increase in permeability and the permeability decrease with re-compaction can not be captured by the Kozeny's permeability – porosity model for porous media without considering fracture effects. Thus, the water flow into the fractures is significantly underestimated by the model.
- The significant responses of deformation to heating and cooling are underestimated by the model.

**Simulation of REP shaft sinking experiment**

To investigate the hydro-mechanical behaviour of the rock observed during shaft sinking at the MHM-URL modelling exercises were carried out. Interpretive calculations were performed and compared with selected measurement data of the REP experiment in order to validate the applied basic hydro-mechanical coupled modelling approach.

The results of the hydro-mechanical simulation could represent the basic reaction of pore water pressure measured in borehole REP2102 due to the shaft excavation process, which comprises

- Level of pore water pressure below hydrostatic value before shaft excavation,
- Overpressure due to compressive loading resulting from shaft excavation process,

- Pressure decrease due to extensional deformation when shaft excavation front passes, though the total value of the pressure decrease is underestimated because rock damage has not been considered.

With respect to the experimental findings of borehole REP2202 the results of the hydro-mechanical simulation could represent the basic deformation behaviour of the clay rock due to the shaft excavation process, though the displacements related to the shaft convergence process could not be simulated with the applied modelling approach, because mechanical time-dependent viscous behaviour has not been considered in the adopted model.

**Simulation of TER heating experiments**

The TER heating experiment performed in the MHM-URL from 2006 to 2009 was simulated with a 2D axisymmetric model. The modelling results are compared with the measurements of temperature, pore-water pressure and deformation in the rock mass surrounding the heater. The heat power input was optimized for the modelling with respect to the temperature on the heater surface, because of the uncertainty with the recorded data. The comparison between the modelling results and the measured data suggests that

- The temperature evolution at most measuring positions during multiple heating-cooling cycles is reasonably represented by the model. Some differences at several positions may be caused by the adopted isotropic model for the heat transfer in the anisotropic rock mass.
- The response of the pore-water pressure to the thermal loading, i. e., pressure rising by heating and conversely pressure falling down during cooling, can be very well captured by the model.
- The rock deformations at all the measuring positions are remarkably underestimated by the model, even if using unreasonably large values of thermal expansion coefficient. The reasons remain unclear.

**Prediction of THM processes in a rock-buffer system**

The predictive modelling of THM processes in a rock-buffer system was carried out by taking into account the drift disposal concept. A horizontal drift of 2.2 m diameter and 20 m length is assumed to be excavated at a depth of 500 m. Four HLW containers of

0.39 m diameter and 1.7 m length each are emplaced in the 13.6 m long middle space. The remaining 0.9 m wide annulus between drift and container is backfilled with compacted bentonite. A 2D axisymmetric model is adopted by involving a rock mass of 100 m radius and 100 m length. The drift excavation and ventilation with 85 % air humidity is simulated for the first 100 days. The following heating period over 1000 years is modelled with application of the delayed heat output from the real spent fuel canisters. Because of the very complex THM coupled calculations with two different materials and the limited capacity of the computer used, calculation of only the first 5 years results in 3 months computing time. Nevertheless, the most important phenomena can be highlighted from the modelling for the crucial thermal transient phase:

- The drift excavation induces a redistribution of the rock stress with a minimum radial component, a maximum tangential component, and an intermediate component in the axial direction. The deviatoric stress results in deformation of the rock towards the open drift. The damaged zone around the drift extends into the rock mass to a distance of ~1.5 m.

- The drift ventilation and the subsequent backfill with unsaturated bentonite lead to a reduction of the pore pressure and even to a de-saturation in the surrounding rock to a depth of ~0.3 m. On the other side, the water saturation in the backfill increases gradually by taking up water from the initially saturated rock. The re-saturation results in build-up of the swelling pressure in the backfill against the deformation and the damage of the surrounding rock.

- The heat from the HLW containers transfers gradually into the buffer and the rock, increasing the temperatures there. The maximum temperature of 157 °C is reached at the interface between the backfill and the container after 2.5 years. The temperatures in the rock are limited below the conceptual criterion of 90 °C.

- Heating causes evaporation of the pore water in the buffer near the containers and thus de-saturation. At the opposite side, the water saturation in the buffer near the rock increases.

- The increase of temperature in the saturated rock generates a significant rise of the pore pressure up to 9 MPa due to the very low porosity and permeability as well as the large difference of the water expansion and the solid expansion. Simultaneously, the total rock stress increases, too. Since the effective stresses are still compressive, no fracturing occurs during the heating period.

## 4.4 Enhancement of model predictability

Based on the results and conclusions from our own model validation work and also from the extensive benchmark exercises made by the other TIMODAZ project partners using various kinds of constitutive models and computer codes, it is identified that further improvement of the model predictability is necessary for evaluating the significance of EDZ in PA studies of the long-term safety of repositories in argillaceous formations. This is of paramount importance for the new German approach of the proof of the safe containment of nuclear waste in an isolating rock zone (IRZ) instead of considering release scenarios as has been done preferentially in the past. The following aspects shall be taken into account in the improvement and development of constitutive models, particularly in case of using CODE-BRIGHT:

- Mechanical damage evolution and criteria for permeability changes
- Self-sealing process of EDZ with permeability decrease due to both effects of mechanical re-compaction and moisture-induced swelling / slaking of clay matrix
- Time dependence of the rock deformation and compaction
- Relation of swelling with suction or water saturation and confining stress
- Thermal effects on the sealing of EDZ
- Anisotropic effects on the THM behaviour of EDZ

The improvement and development of constitutive models requires various kinds of laboratory experiments to provide high quality data for understanding of the mechanisms dominating the coupled THM processes, for formulation of constitutive equations, for determination of model parameters, and for validation of the developed models by comparing with the test results obtained under specially-designed and well-controlled conditions.

The implementation of the models in the code has to be verified by laboratory and in-situ experiments. Additionally, the computing power has to be enhanced for predictive modelling of the long-term THM processes in the geological and engineered barriers within acceptable computing time.

The improvement of the applied models and/or development of new models for prediction of the sealing process of EDZ in clay host rocks will be conducted in a newly suggested research programme /THM 10/.

## Acknowledgements

The work described in this report was co-funded by the German Federal Ministry of Economics and Technology (BMWi) under contract number 02 E 10045 and by the European Commission (EC) as part of the sixth Euratom research and training Framework Programme (FP6) on nuclear energy (2002-2006) under contract number FP6-CT-036449. The authors would like to thank for this support. The support from the French Agence Nationale Pour la Gestion de Déchets Radioactifs (ANDRA) for providing the test material and the support from the Geotechnical Engineering Department of the Technical University of Catalonia in Barcelona (UPC) with regard to the modelling work is also gratefully acknowledged.

## References

/AND 99/ ANDRA: REFERENTIEL GEOLOGIQUE DU SITE DE L'EST. A RP ADS 99-005, 1999.

/AND 00/ ANDRA (2000): Experimental programme at the Meuse/Haute-Marne Underground Research Laboratory – A short view. 2000 – 2006.

/AND 03/ ANDRA: HLW CLAY REPOSITORY PROJECT–SIENTIFIC PROGRAMME 2002-2005.

/AND 05/ ANDRA: DOSSIER 2005. Synthesis – Evaluation of the feasibility of a geological repository in an argillaceous formation.

/AND 06/ ANDRA: Expression of need concerning coupled processes involved in the mechanical behaviour of repository structures, ANDRA internal report - CCCASMG060034, 2006.

/ARM 10/ Armand, G., Morel, J., Noiret, A.: Short and long term behaviour of drifts in the Callovo-Oxfordian claystone, The 4th international meeting – Clays in Natural & Engineered Barriers for Radioactive Waste Confinement, Nantes, 2010.

/BLU 07/ Blümling, P., Bernier, F., Lebon, P., Martin, C.D.: The excavation damaged zone in clay formations: time-dependent behaviour and influence on performance assessment. Physics and Chemistry of the Earth, 32 (2007) 588-599.

/BMU 09/ BMU: Safety Requirements Governing the Final Disposal of Heat-Generating Radioactive Waste.- Bundesministerium für Umwelt, Naturschutz und Reaktorsicherheit (BMU). Berlin, July 2009.

/BOC 01/ Bock, H.: RA Experiment – Rock mechanics analyses and synthesis: Data Report on Rock Mechanics. Technical Report 2000-02.

/BOC 10/ Bock, H., Dehandschutter, B., Martin, C.D., Mazurek, M., Haller, A.D., Skoczylas, F., Davy, C.: Self-Sealing of Fractures in Argillaceous Formations in the Context of Geological Disposal of Radioactive Waste – Review and Synthesis, OECD 2010, NEA No. 6184.

/BOS 03/ Bossart, P., Wermeille, S.: The Stress Field in the Mont Terri Region – Data Compilation. In: Heitzmann, P. & Tripet, J.-P. (ed.): Mont Terri Project – Geology, Paeohydrology and Stress Field of the Mont Terri Region – Reports of Federal Office for Water and Geology (FOWG), Geology Series 4, 65-92.

/BUE 05/ Bure Hauptprojekt zur Beteiligung am Forschungsprogramm der ANDRA im Untertagelabor Bure, GRS – Vorhabensbeschreibung, Juni 2005.

/D02 07/ Deliverable D02 of the work package WP5.1 of the EC TIMODAZ project: State of the art on THMC of Clay Host Rocks, F16W-CT-036449, 2007.

/D05 10/ Deliverable D05 of the work package WP5.1 of the EC TIMODAZ project: THM Characterization of Clay Rocks and Input for Modelling, F16W-CT-036449, 2010.

/D07 10/ Deliverable D07 of the work package WP5.1 of the EC TIMODAZ project: Laboratory simulation tests, F16W-CT-036449, 2010.

/D10 10/ Deliverable D10 of the work package WP5.1 of the EC TIMODAZ project: Constitutive models development, F16W-CT-036449, 2010.

/D13 10/ Deliverable D13 of the work package WP5.1 of the EC TIMODAZ project: Simulation of lab and in situ tests, F16W-CT-036449, 2010.

/DAV 03/ Davies, C., Bernier, F.: Impact of the Excavation Disturbed or Damaged Zone (EDZ) on the Performance of Radioactive Waste Geological Repositories. Proceedings of an European Commission Cluster Conference and Workshop Luxemburg, 3 to 5 November 2003. EUR 21028 EN.

/DAV 07/ Davy, C.A., Skoczylas, F., Barnichon, F.-D., Lebon, P.: Permeability of macro-cracked argillite under confinement: Gas and water testing. Physics and Chemistry of the Earth, 32 (2007) 667-680.

/DEL 07/ Delay, J., Vinsot, A., Krieguer, J.M., Rebours, H., Armand, G.: Making of the underground scientific experimental programme at Meuse/Haute-Marne underground research laboratory, north eastern France. Physics and Chemistry of the Earth 32 (2007) 2-18.

/DEL 09/ Delay, J., Lebon, P., Rebours, H.: The Meuse/Haute-Marne Centre: Next Steps towards a Deep Disposal Facility. Journal of Rock Mechanics & Geotechnical Engineering, 2010, 2(1): 52-70.

/FRE 93/ Fredlund, D.G., Rahardjo, H.: Soil Mechanics for Unsaturated Soils. John Wiley & Sons, INC. 1993.

/GEN 98/ Gens, A.A., Garcia-Molina, A.J., Olivella, S., Alonso, E.E., Huertas, F.: Analysis of a Full Scale in-situ Test Simulating Repository Conditions. Int. J. Numer. Anal. Meth. Geomech., 22, 515-548, 1998.

/GEN 06/ Gens, A. A., Olivella, S.: Coupled Thermo-Hydro-Mechanical Analysis of Engineered Barriers for High-Level Radioactive Waste. Chinese Journal of Rock Mechanics and Engineering, 2006, 25(4), 670 -680.

/GEN 07/ Gens, A.A., Vaunat, J., Gartitte, B., Wileveau, Y.: In situ behaviour of a stiff layered clay subject to thermal loading – observations and interpretation. Geotechnique (2007) 57, No.2, 207-228.

/GRA 09/ Gräsle,W., Plischke,I.: Laboratory testing of Opalinus Clay (LT) Experiment: Strength and Deformation of Opalinus Clay. Technical Note 2008-81. 2009.

/HOR 96/ Horseman, S.T., Higgo, J.J.W., Alexander, J., Harrington, J.F.: Water, Gas and Solute Movement through Argillaceous Media. Report CC-96/1, 1996.

/ISR 81/ ISRM: Rock Characterization Testing & Monitoring – IRSM suggested methods, 1981.

/KUL 07/ Kull, H., Jockwer, N., Zhang, C.L., Wileveau, Y., Pepa, S.: Measurement of Thermally-Induced Pore-water Pressure and Gas Migration in the Opalinus clay at Mont Terri – HE-D heating Experiment, Physics and Chemistry of the Earth, Vol. 32, 2007, 937-946.

/LEB 00/ Lebon P, Ghoreychi M.: French Underground Research Laboratory of Meuse/Haute-Marne: THM Aspects of Argillite Formation. EUROCK2000, Aachen, 27-31, March 2000.

/LEB 10/ Lebon, P., Landais, P.: On the Way to Siting and Licensing a Deep Disposal: What about the Research Programme on the Callovo-Oxfordian Formation, on the 4th international meeting – Clays in Natural & Engineered Barriers for Radioactive Waste Confinement, Nantes, 2010.

/LI 09/ Li, X.-S.: Modelling of THM Processes in Rock-Buffer-Barriers around High Level Radioactive Waste, Master Thesis, Institut für Endlagerforschung der Technischen Universität Clausthal, 2009.

/MAZ 08/ Mazurek, M., Gautschi, A., Marschall, P., Vigneron, G., Lebon, P., Delay,J.: Transferability of geoscientific information from various sources (study sites, underground rock laboratories, natural analogues) to support safety cases for radioactive waste repositories in argillaceous formations. Physics and Chemistry of the Earth, Vol. 33 (2008), 95-105.

/MIT 76/ Mitchell, J.K.: Fundamentals of soil Behavior. University of California, Berkeley, USA, 1976.

/MIT 92/ Mitchell, J.K.: Characteristics and Mechanisms of Clay Creep and Creep Rupture, in “Clay-water interface and its rheological implications, Clay Mineral society”, 1992. Vol.4, 212-244.

/MOD 06/ MODEX-REP – Hydromechanical Modelling of the argillites response to shaft sinking, EC-Deliverable 5-6-7, Kun Su, ANDRA 2006.

/NAG 02/ NAGRA: Project Opalinus Clay, Models, Codes and Data for Safety Assessment – Demonstration of disposal feasibility for spent fuel, vitrified high-level waste and long-lived intermediate-level waste. 2002.

/NAU 07/ Naumann, M., Hunsche, U., Schulze, O.: Experimental investigations on anisotropy in dilatancy, failure and creep of Opalinus clay. Physics and Chemistry of the Earth, 32 (2007) 889-895.

/NOY 00/ Noynaert, L. et al.: Heat and radiation effects on the near field of a HLW or spent fuel repository in a clay formation (CERBERUS Project). EUR 19125EN, Contract No F14W-CT95-0008.

/OLI 94/ Olivella, S., Carrera, J., Gens, A.A., Alonso, E.E.: Nonisothermal Multi-phase Flow of Brine and Gas through Saline Media. Transport in Porous Media, 15, 271-293, 1994.

/POP 07/ Popp, T., Salzer, K.: Anisotropy of seismic and mechanical properties of Opalinus clay during triaxial deformation in a multi-anvil apparatus. Physics and Chemistry of the Earth, 32 (2007) 879-888.

/ROD 99/ Rodwell, W.R., Harris, A.W., Horseman, S.T., Lalieux, P., Müller, W., Ortiz Amaya, L., Pruess, K.: Gas Migration and Two-Phase Flow through Engi-neered and Geological Barriers for a Deep Repository for Radioactive Waste. A Joint EC/NEA Status Report, European Commission, 1999, EUR 19122 EN.

/SCH 09/ Schulze, O.: Untersuchung von Endlager relevanten Gesteins-eigenschaften von Steinsalz und Tonstein, Energie und Rohstoffe 2009, Goslar.

/SU 07/ Su, K.: Synthesis of the EC MODEX-REP project – Development and Vali-dation of the Constitutive Hydromechanical Models for the Callovo-Oxfordian Argillites, FIKW-CT2000-00029, 2007.

/THM 07/ THM-TON Projekt zur Untersuchung der THM-Prozesse im Nahfeld von Endlagern in Tonformationen, GRS – Vorhabensbeschreibung, Juli 2007.

/THM 10/ Aufstockungsantrag zum THM-TON Projekt zur Erweiterung der Stoffmo-delle zur Schädigung und Verheilung von Tonstein, GRS – Vorhabensbe-schreibung, Nov. 2010.

/THU 99/ Thury, M., Bossart, P.: Mont Terri Rock Laboratory, Results of the Hydro-geological, Geochemical and Geotechnical Experiments performed in 1996 and 1997. Geological Report Nr. 23, 1999, Bern.

/TIM 06/ TIMODAZ project: Thermal Impact on the Damaged Zone around a Radioactive Waste Disposal in Clay Host Rocks. FI6W, Contract Number 036449, 2006.

/TOU 07/ Tournassat C, Gaucher E C, Fattahi M, Grambow B.: On the mobility and potential retention of iodine in the Callovian-Oxfordian formation. Physics and Chemistry of the Earth, Vol 32, 8-14, 2007, p. 539-551.

/UPC 04/ UPC: CODE-BRIGHT, A 3-D program for thermo-hydro-mechanical analysis in geological media, 2004.

/VAU 03/ Vaunat, J., Alonso, E.E., Gens, A.: Constitutive model of short and long term behaviour of the Meuse/Haute-Marne argillite. Deliverable 2&3 of the project MODEX-REP, FIKW-CT2000-00029, 2003.

/VAU 04/ Vaunat, J., Gens, A.: Aspects of modelling geotechnical problems in hard soils and soft argillaceous rocks. Proc. In. Symp. on Numerical Models in Geomechanics, 2004.

/VAU 09/ Vaunat, J.: Damage-elastoplastic model for argillaceous rocks. CODE-BRIGHT Seminar 2009, GRS Braunschweig.

/WIE 08/ Wieczorek, K., Zhang, C.-L., Rothfuchs, T.: Ventilation Test at Mont Terri – Part of NF-PRO Project. May 2008, GRS – report, GRS-235.

/WIL 03/ Wileveau, Y., Rothfuchs, T.: HE-D Experiment: Test Plan. Mont Terri Project, Technical Note 2004-20, September 2003.

/WIL 07/ Wileveau, Y., Su, K., Ghoreychi, M.: A Heating experiment in the argillaceous rocks in the Meuse/Haute-Marne Underground Research Laboratory. Proceedings of the 11th International conference on Enviromental Remediation and Radioactive Waste Management, ICEM2007, 2007, Bruges, Belgium.

/ZHA 02/ Zhang, C.L., Dittrich, J., Müller, J., Rothfuchs, T.: Experimental Study of the Hydromechanical Behaviour of the Callovo-Oxfordian Argillites – Part of the MODEX-REP Project. 2002, GRS-187.

/ZHA 04a/ Zhang, C.L., Rothfuchs, T.: Experimental Study of Hydromechanical Behaviour of the Callovo-Oxfordian Argillites. Applied Clay Science 26 (2004) 325-336.

/ZHA 04b/ Zhang, C.L., Rothfuchs, T., Moog, H., Dittrich, J., Müller, J.: Thermo-Hydro-Mechanical and Geochemical Behaviour of the Callovo-Oxfordian Argillite and the Opalinus Clay. June 2004, GRS-202.

/ZHA 04c/ Zhang C.L, Rothfuchs T, Jockwer N, et al.: Results of Laboratory Investigations on Clays, Proc. International Conference on Radioactive Waste Disposal – DisTec 2004, Berlin 26-28 April 2004.

/ZHA 05/ Zhang, C.L., Wileveau, Y., Rothfuchs, T.: A Heating Experiment in the Opalinus Clay at the Mont Terri Rock Laboratory. The 10th International Conference on Environmental Remediation and Radioactive Waste Management, September 4–8 2005, Glasgow, Scotland.

/ZHA 06/ Zhang, C.L., Rothfuchs, T., Wieczorek, K., Jockwer, N., Wileveau, Y.: Monitoring and Modelling of Responses of the Opalinus Clay to Heating. Chinese Journal of Rock Mechanics and Engineering, 2006, 25(4), 659-669.

/ZHA 07a/ Zhang, C.L., Rothfuchs, T., Jockwer, N., Wieczorek, K., Dittrich, J., Müller, J., Hartwig, L., Komischke, M.: Thermal Effects on the Opalinus Clay – A Joint Heating Experiment of ANDRA and GRS at the Mont Terri URL (HE-D Project), GRS-224, February 2007.

/ZHA 07b/ Zhang C.L, Rothfuchs T.: Moisture Effects on Argillaceous Rocks, Proc. 2nd International Conference of Mechanics of Unsaturated Soils (ed. T. Schanz), Springer Proceedings in Physics 112, Springer-Verlag Berlin Heidelberg 2007, p. 319-326.

/ZHA 07c/ Zhang, C.L., Rothfuchs, T., Su, K., Hoteit, N.: Experimental Study of the thermo-hydro-mechanical behaviour of indurated Clays, Physics and Chemistry of the Earth, Vol. 32, 2007, p. 957-965.

/ZHA 08a/ Zhang, C.L., Rothfuchs, T., Dittrich, J., Müller, J.: Investigations on self-sealing of indurated clay – part of the EC NFPRO project, GRS-230, 2008.

/ZHA 08b/ Zhang, C.L., Rothfuchs, T.: Damage and sealing of clay rocks detected by measurements of gas permeability. Physics and Chemistry of the Earth, Vol. 33 (2008), 363-373.

/ZHA 08c/ Zhang, C.L, Rothfuchs, T., Su, K.: Laboratory Experiments on the Thermal Effects on Clay Rocks, The 3rd the international conference on Coupled THMC processes in Geo-Systems, GEOPRO2008, Lille in France.

/ZHA 09a/ Zhang, C.L., Wieczorek, K., Rothfuchs, T., Armand, G., Lebon, P.: Responses of the Opalinus Clay to Heating during the HE-D Experiment at Mont Terri. The international conference and workshop in the framework of the EC TIMODAZ and THERESA projects, 2009, Luxembourg.

/ZHA 09b/ Zhang C.L.: Self-sealing of Fractures in Argillites under Repository conditions, The international conference and workshop in the framework of the EC TIMODAZ and THERESA projects, Sept. 2009, Luxembourg.

/ZHA 10a/ Zhang, C.L, Wieczorek, K., Xie, M.L.: Swelling experiments on mudstones, Journal of Rock Mechanics & Geotechnical Engineering, 2010, 2(1): 41-47.

/ZHA 10b/ Zhang C.L.: Experimental Evidence for Self-sealing of Fractures in Claystone, The 4th international meeting – Clays in Natural & Engineered Barriers for Radioactive Waste Confinement, Nantes, 2010.

## List of Tables

## Table of Figures

**Gesellschaft für Anlagen-
und Reaktorsicherheit
(GRS) mbH**

Schwertnergasse 1
**50667 Köln**
Telefon +49 221 2068-0
Telefax +49 221 2068-888

Forschungszentrum
**85748 Garching b. München**
Telefon +49 89 32004-0
Telefax +49 89 32004-300

Kurfürstendamm 200
**10719 Berlin**
Telefon +49 30 88589-0
Telefax +49 30 88589-111

Theodor-Heuss-Straße 4
**38122 Braunschweig**
Telefon +49 531 8012-0
Telefax +49 531 8012-200

www.grs.de

**ISBN 978-3-939355-42-7**